May 2013

Functional Organic Nanomaterials

Ryan R. Kohlmeyer
University of Wisconsin-Milwaukee

FUNCTIONAL ORGANIC NANOMATERIALS

by

Ryan R. Kohlmeyer

A Dissertation Submitted in

Partial Fulfillment of the

Requirements for the Degree of

Doctor of Philosophy

in Chemistry

at

The University of Wisconsin-Milwaukee

May 2013

ABSTRACT

FUNCTIONAL ORGANIC NANOMATERIALS

by

Ryan R. Kohlmeyer

The University of Wisconsin-Milwaukee, 2013
Under the Supervision of Professor Jian Chen

π-Conjugated polymers have a wide range of applications such as photovoltaics, light-emitting diodes, and sensors. To gain a better understanding of these systems, monodisperse oligomers can be used as a more simplistic model to generate predictive structural and physical properties of corresponding polymers. A divergent/convergent synthetic approach to synthesis of monodisperse π-conjugated oligomers has been developed. These well-defined, thiophene-containing molecular building blocks have been successfully coupled to a ferrocene hinge, which has been found to be highly efficient in the transport of gold atoms using a gold scanning tunneling microscopy tip.

Carbon nanotubes (CNTs) represent a rare class of materials, which exhibit a number of outstanding properties in a single material system, such as high aspect ratio, small diameter, light weight, high mechanical strength, high electrical and thermal conductivities, and near-IR optical and optoelectronic properties. Aerogels are highly porous, low-density materials comprised of a solid, three-dimensional (3D) nanoscale network fully accessible to ions and molecules. By combining the extraordinary properties of CNTs with those of aerogels, a new class of materials becomes accessible

with unique multifunctional material properties. CNT aerogels that are mechanically stable and stiff, highly porous, and exhibit excellent electrical conductivity and large specific surface area have been developed.

CNTs are recognized as the ultimate carbon fibers for high-performance, multifunctional materials, where an addition of only a small amount of CNTs, if engineered appropriately, could lead to simultaneously enhanced mechanical strength and electrical conductivity. For the first time, using core-shell multi-walled CNTs as a filler to increase the dielectric constant and reduce the dielectric loss of nanotube-polymer composites has been demonstrated.

While most efforts in the field of CNT-polymer composites have been focused on passive material properties such as mechanical, electrical, and thermal, there is growing interest in harnessing active material functions such as actuation, sensing, and power generation in designed CNT-polymer materials. The synergy between CNTs and the polymer matrix has been judiciously exploited to create highly desirable active material functions in smart material systems. By incorporating CNTs in a Nafion matrix, multi-shape memory healable composites capable of reversible remote, local, and chemical programming have been developed.

To

My Parents Rick and Janet Kohlmeyer

and

My Wife Megan Kohlmeyer

and

My Son Brayden Kohlmeyer

TABLE OF CONTENTS

LIST OF FIGURES

LIST OF TABLES

LIST OF SCHEMES

ACKNOWLEDGEMENTS

This PhD degree would not have been possible without the support and guidance of many people. First, I would like to thank my advisor Dr. Jian Chen, for his enthusiastic supervision and patience during this work. Dr. Chen is an exceptionally gifted individual and scientist and will always be an inspiration to me as I begin new chapters in my life. I would also like to acknowledge all past and current members of the Chen Group for their help along the way.

I would like to express my sincere gratitude to members of my doctoral committee, Dr. James Cook, Dr. Mark Dietz, Dr. Guilherme Indig, and Dr. Alan Schwabacher for their time and meaningful discussions. I appreciate the help and insightful conversations from Dr. Wilfred Tysoe as well as Dr. Alan Thompson throughout my PhD studies. I am very grateful to Dr. Heather Owen for her help and knowledge about SEM and to Dr. Steven Hardcastle for his assistance and meaningful conversations regarding materials characterization. I would also like to acknowledge Dr. Benjamin Feinberg for many invaluable thoughts concerning electrochemistry and Dr. Holger Föersterling for his guidance with NMR studies. Thanks as well to Elise Nicks, Mary Eckert, and Wendy Grober for all their help during my graduate studies at UWM.

I am also grateful to the UWM Research foundation for the Research Fellowship Award and to the UWM Graduate School for the Dissertation Fellowship Award.

Finally, I would like to thank my parents, family, and friends for their continuous and unconditional support. I would like to thank my wife Megan Kohlmeyer who has always encouraged and supported me during this endeavor.

Chapter 1: Synthesis and Length-Dependent Properties of Monodisperse Oligo[(*p*-phenyleneethynylene)-*alt*-(2,5-thienyleneethynylene)]s

1.1 Introduction

π-Conjugated polymers have a wide range of applications such as photovoltaics, thin-film transistors, light-emitting diodes, optoelectronic memory devices, electrochromic windows, photochromic devices, electrochemical capacitors, and sensors.[1-3] Poly(aryleneethynylene)s (PAEs) are a class of polymers in which arene groups are separated by alkyne linkers.[4] The unique optical and electronic properties of PAEs make them promising candidates for chemical- and bio-sensors, and light-emitting diodes.[5,6] The incorporation of thiophene moieties into a poly-*p*-phenyleneethynylene main chain leads to better electron delocalization and therefore lower band gap materials.[7-10] Recently, monodisperse π-conjugated oligomers have attracted increasing interest, because they represent model systems to generate predictive structural and physical properties of corresponding polymers and also serve as conductive wires in molecular electronics.[11-18]

We are interested in using monodisperse thienyl iodide terminated oligo[*p*-phenyleneethynylene)-*alt*-(2,5-thienyleneethynylene)]s (OPETEs, Scheme 1.1) as molecular building blocks to construct more complex, well defined π-conjugated architectures. Li and coworkers reported the first synthesis of OPETEs via an iterative divergent/convergent doubling strategy in solution as well as on Merrifield's resin.[19] Although this method could prepare monodisperse oligomers in high yields, it only produces phenyl iodide terminated OPETEs. Li and coworkers also tried to prepare

thienyl iodide terminated OPETEs, but "failed because the products of the iodination reaction were too complicated to purify".[19] Here we report the first synthesis of thienyl iodide terminated OPETEs and the subsequent coupling of the tetrameric OPETE to a 1,1' ferrocene derivative to synthesize a molecular hinge. The length-dependent optical and electrochemical properties of OPETE family and molecular hinge were studied.

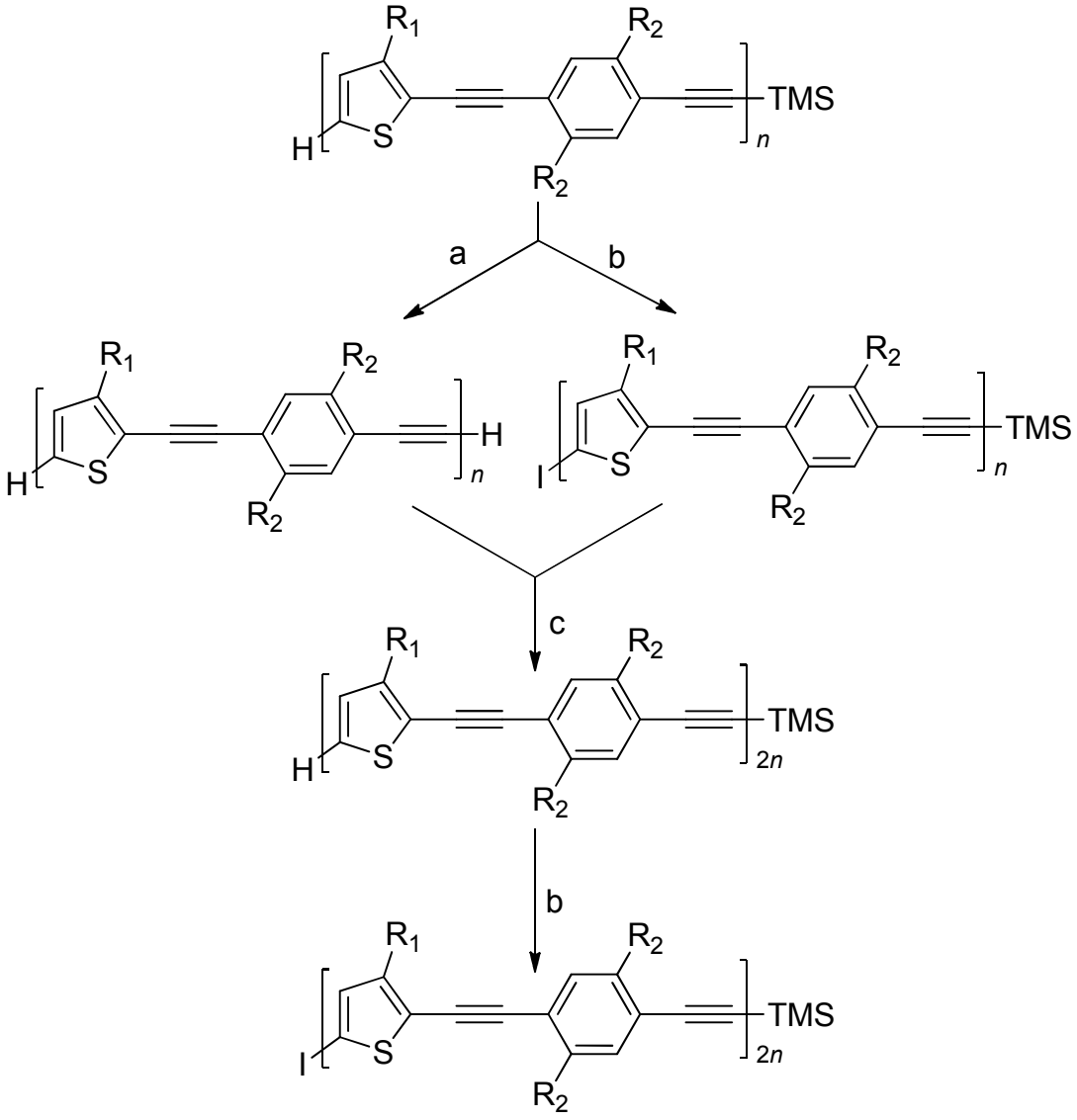

Scheme 1.1. Divergent/convergent approach used in this study. (a) KOH, THF, H_2O, MeOH; (b) LDA, THF, -78 ˚C followed by I_2, THF, -78 ˚C; (c) $PdCl_2(PPh_3)_2$, CuI, Et_3N, THF.

1.2 Results and Discussion

1.2.1 Oligomer Synthesis

The synthetic route to thienyl iodide terminated OPETEs is given in Scheme 1.2. All of the target oligomers were found to be stable towards air and moisture and are soluble in many common organic solvents such as $CHCl_3$, CH_2Cl_2, and THF. The monomeric unit **3** was prepared in 87% yield by a Sonogashira coupling reaction of 2-ethynyl-3-methylthiophene **(2)** and 2,5-dihexyloxy-4-[(trimethylsilyl)ethynyl] iodobenzene in the presence of $PdCl_2(PPh_3)_2$ and CuI. The synthetic strategy of our method for doubling oligomer length was based on a previous divergent/convergent Approach to produce thiophene-ethynylene oligomers.[11] Monomer **3** was partitioned into two parts. One portion was deprotected in 94% yield to give deprotected monomer **4**.

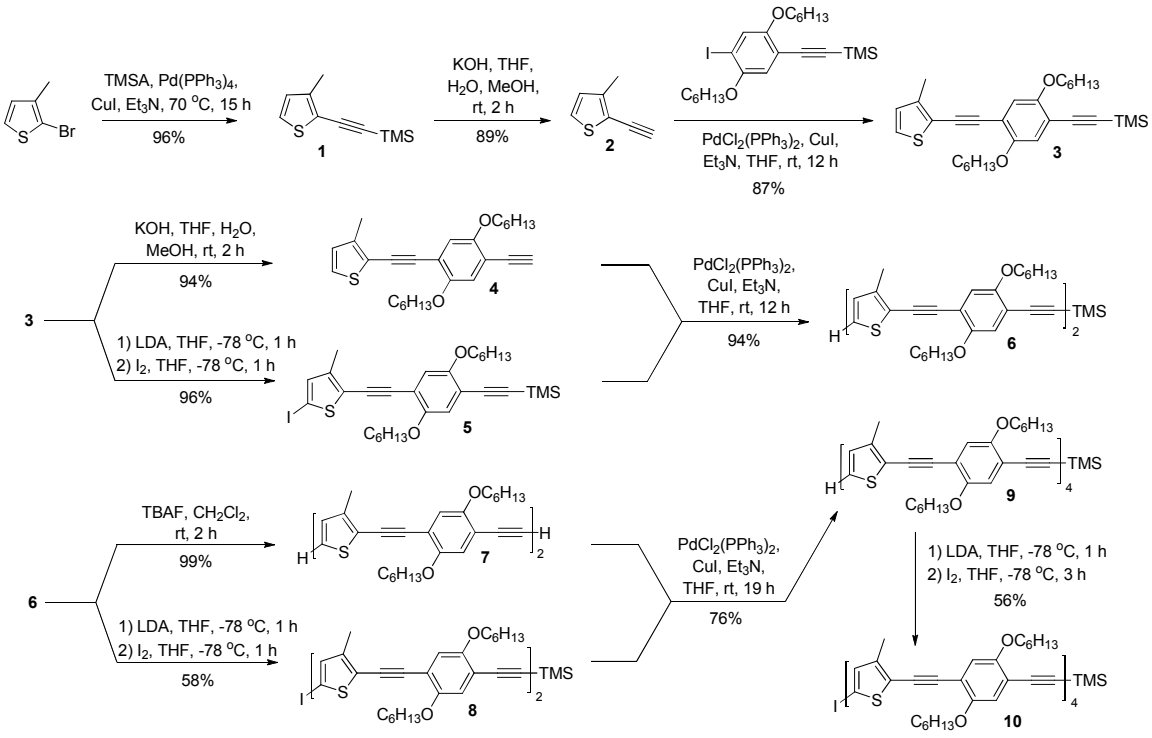

Scheme 1.2. Synthesis of monodisperse thienyl iodide terminated OPETEs; TMSA = trimethylsilylacetylene, LDA = lithium diisopropylamide, TBAF = tetrabutylammonium fluoride.

Another portion was selectively iodinated in the presence of LDA followed by the addition of iodine in THF to give iodinated monomer **5** in 96% yield. Deprotected monomer **4** and iodinated monomer **5** were then coupled via a Sonogashira reaction to produce dimer **6** in 94% yield. This divergent/convergent approach was continued to double dimer **6** into tetramer **9**, which was then successfully converted to iodinated tetramer **10** in 56% yield. There was a decrease in iodination reaction yield as oligomer length increased (96% for monomer **5**, 58% for dimer **8**, 56% for tetramer **10**). Although the thiophene α-position is significantly more reactive than the β-position, there are more β-sites present in larger oligomers, which is one likely cause of the decreased yield in compounds **8** and **10**.[20]

1.2.2 Deprotected 1,1′-ditetramericferrocene Synthesis

After synthesizing the family of thienyl iodide terminated OPETEs, a plan to couple tetrameric oligomer arms to ferrocene in a 1,1′ fashion was devised, creating a large conjugated molecule that takes advantage of ferrocene's hinge. The initial thought was to couple a tetrameric oligomer directly to either 1,1′-diiodoferrocene or 1,1′-diethynylferrocene. Both of these routes were avoided due to the low reactivity of 1,1′-diiodoferrocene and the likely [4]ferrocenophane formation from 1,1′-diethynylferrocene.[21,22] Therefore, the chosen route to synthesize 1,1′-ditetramericferrocene is outlined in Scheme 1.3. A Sonogashira coupling of iodinated tetramer **10** and **11** catalyzed by $PdCl_2(PPh_3)_2$ and CuI gave the protected 1,1′-ditetramericferrocene **12** in 69% yield. TBAF deprotection of **12** afforded the deprotected 1,1′-ditetramericferrocene **13** in 92% yield.

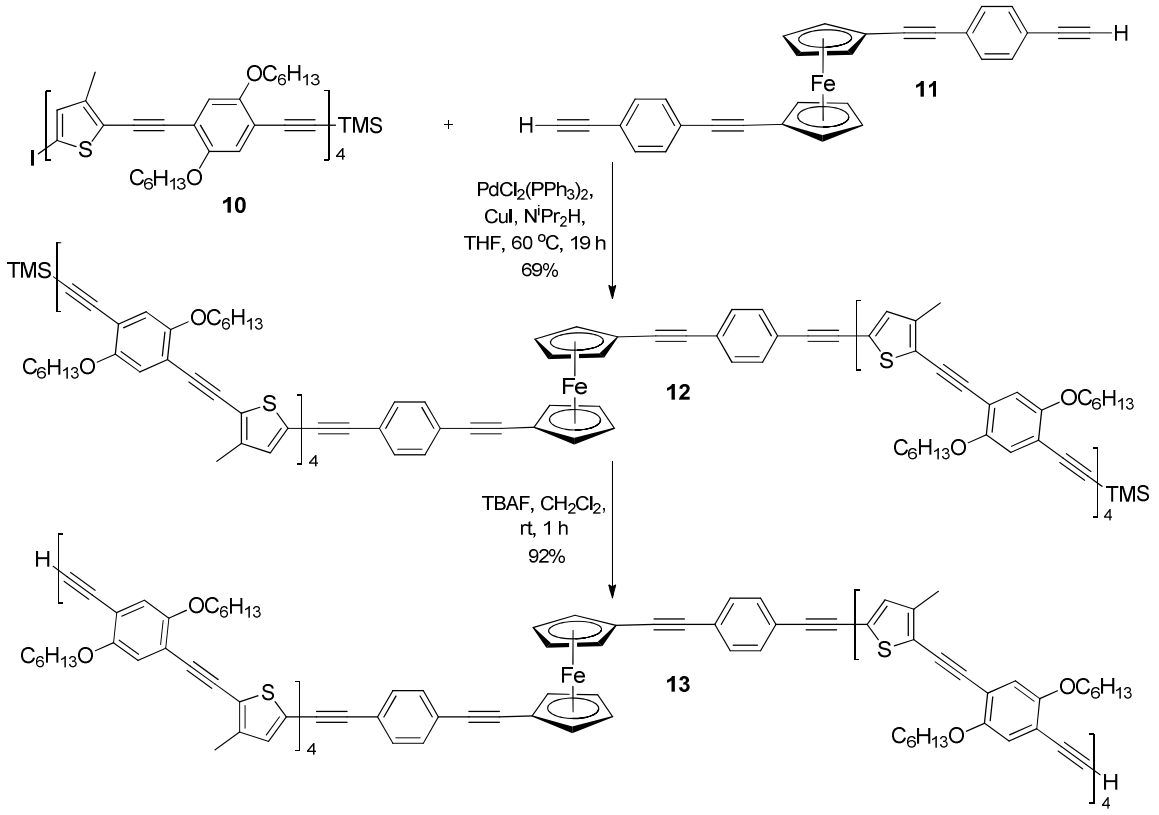

Scheme 1.3. Synthesis of Deprotected 1,1′-ditetramericferrocene.

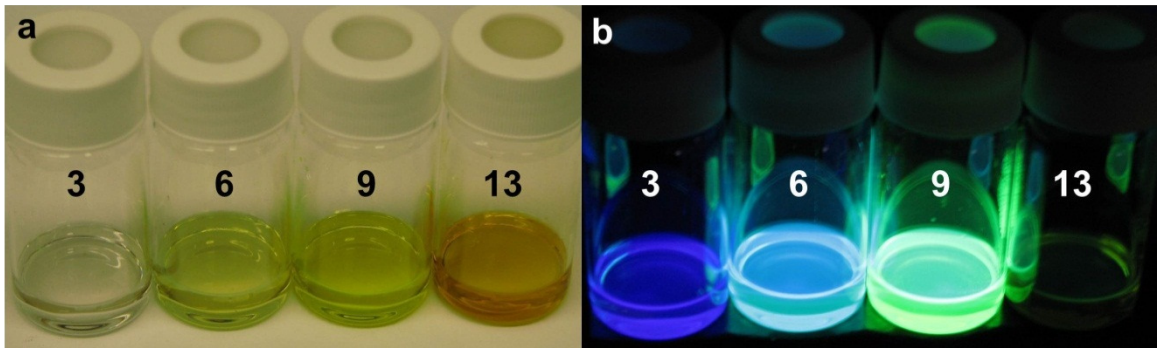

Figure 1.1. Photographs of CH_2Cl_2 solutions of **3** (1.6 mM), **6** (0.8 mM), **9** (0.4 mM), and **13** (0.2 mM) without excitation (a) and under 365 nm UV light (b). Different concentrations were used to keep the number of benzene rings, thiophene rings, and alkyne linkers constant for a better comparison of the conjugation effect.

1.2.3 Optical Properties

The length-dependent optical properties of monomer **3**, dimer **6**, tetramer **9**, and deprotected 1,1'-ditetramericferrocene **13** are shown in Figure 1.1. Unlike the monodisperse OPETEs, deprotected 1,1′-ditetramericferrocene **13** appears dark when

irradiated under 365 nm UV light. This is likely because of fluorescence quenching due to charge transfer from the central ferrocene unit to its conjugated arms.[23,24]

1.2.4 Cyclic Voltammetry

The electrochemical properties of iodinated monomer **5**, iodinated dimer **8**,

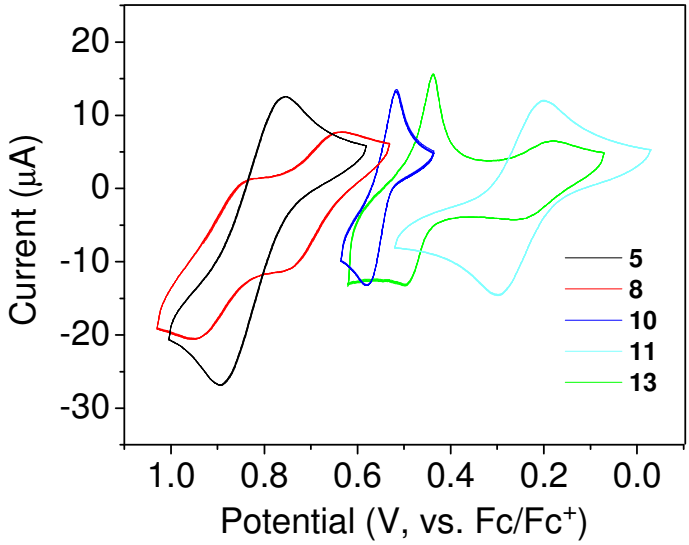

Figure 1.2. Cyclic voltammograms of **5** (1.6 mM), **8** (0.8 mM), **10** (0.4 mM), **11** (0.5 mM), and **13** (0.2 mM) in CH_2Cl_2 containing 0.1 M Bu_4NPF_6 at a scan rate of 0.1 V s^{-1}. All potentials were referenced to the internal standard Fc/Fc^+.

Table 1.1. Oxidation potentials ($E^{0\prime}$) and anodic-cathodic potential peak separation (ΔE) of various oligomers and ferrocene compounds.[a]

Compound	*First oxidation* $E^{0\prime}$ *(V)*	*ΔE (V)*	*Second oxidation* $E^{0\prime}$ *(V)*	*ΔE (V)*
5	0.824	0.139		
8	0.697	0.124	0.895	0.109
10	0.549	0.063		
11	0.250[b]	0.099		
13	0.221[b]	0.077	0.468	0.060

[a] Measurements were carried out in CH_2Cl_2 with a glassy carbon working electrode, a platinum wire auxiliary electrode, and a Ag/AgCl wire quasi-reference electrode using supporting electrolyte 0.1 M Bu_4NPF_6. Experiments were run at room temperature at a scan rate of 0.1 V s^{-1}.

[b] Oxidation due to ferrocenyl core.

iodinated tetramer **10**, **11**, and deprotected 1,1´-ditetramericferrocene **13** were measured using cyclic voltammetry. The results are summarized in Table 1.1 and Figure 1.2. All of the compounds summarized showed fully reversible redox behavior when scanned in the in the regions shown in Figure 1.2. Iodinated monomer **5** shows a quasi-reversible oxidation peak at 0.824 V vs Fc/Fc^+ due to the thiophene unit. As conjugation length increases, the first oxidation potential has been reported to decrease.[25] This held true for our system, as the first oxidation peak of dimer **8** and tetramer **10** were 0.697 V and 0.549 V respectively. The tetrameric arms of deprotected 1,1´-ditetramericferrocene **13** showed a first oxidation peak at 0.468 V. Although not fully understood at this time, dimer **8** was the only oligomer found to have more than one thiophene based oxidation, with a second quasi-reversible oxidation peak at 0.895 V. Surprisingly, tetramer **10** and deprotected 1,1´-ditetramericferrocene **13** only showed one thiophene based oxidation peak. Tetramer **10** was probed past 1 V vs Fc/Fc^+, but the voltammogram became complex with the formation of a new compound likely due to oxidative electropolymerization.[26,27] Both **11** and deprotected 1,1´-ditetramericferrocene **13** have a ferrocenyl core oxidation of 0.250 and 0.221 V, respectively. This shows an anodic shift for both compounds compared to pure ferrocene, suggesting that ferrocene is acting as an electron donor to the conjugated arms.[28,29] Interestingly, the increased conjugation length of deprotected 1,1´-ditetramericferrocene **13** compared with **11** has little effect on the oxidation potential of the ferrocenyl core.

1.3 Conclusion

Monodisperse thienyl iodide terminated OPETEs were successfully synthesized by a divergent/convergent doubling approach using a series of iodination, deprotection,

and Sonogashira coupling reactions. We have reported the first synthesis of thienyl iodide terminated OPETEs and the subsequent coupling of the tetrameric OPETE to a 1,1' ferrocene derivative to synthesize a molecular hinge. The length-dependent optical and electrochemical properties of OPETE family and molecular hinge were studied. By incorporating ferrocene as a molecular hinge, a longer structure can be synthesized without interrupting the conjugation length.

1.4 Experimental

1.4.1 General

All reagents and solvents were used as received unless otherwise noted. THF was distilled under nitrogen from Na-benzophenone, triethylamine was distilled under nitrogen from CaH_2, and diisopropylamine (N^iPr_2H) was distilled under nitrogen from KOH. Compound **11** was prepared according to literature procedures.[3,30] All Pd-catalyzed cross-coupling and iodination reactions were carried out under an atmosphere of argon using standard Schlenk and vacuum line techniques. Flash column chromatography was performed on silica gel (Silicycle, 40-63μm). Thin layer chromatography (TLC) was performed on 200 micron silica gel F_{254} plates. All reported ^1H and ^{13}C NMR spectra were collected in $CDCl_3$ using a Bruker Spectrospin 300 MHz or Bruker 500 MHz instrument (^{13}C were obtained at 125 MHz) with shifts recorded relative to $CHCl_3$. Electrospray Ionization (ESI) mass spectrometry was performed using an Applied Biosystems Voyager-PE SCIEX QSTAR mass spectrometer. Matrix-Assisted Laser Desorption/Ionization-Time of Flight (MALDI-TOF) was performed using an Applied Biosystems Voyager-DE STR mass spectrometer. All MALDI-TOF samples used the matrix 2,4,6-trihydroxyacetophenone (THAP), except compounds **9**, **10**, and **12** used 2,5-

dihydroxybenzoic acid (DHB), and compound **13** used anthracene. Cyclic voltammetry was carried out using a BASi Epsilon three-electrode potentiostat in CH_2Cl_2 containing 0.1 M tetrabutylammonium hexafluorophosphate (Bu_4NPF_6) as the supporting electrolyte. Experiments were performed at room temperature at a scan rate of 0.1 V s^{-1} with a three electrode cell containing a glassy carbon working electrode (0.07 cm^2), a platinum wire auxiliary electrode, and a Ag/AgCl wire quasi-reference electrode. Cyclic voltammetry was conducted under nitrogen and the CH_2Cl_2 solution was deoxygenated by bubbling with nitrogen for at least 10 min. The internal standard Fc/Fc^+ was used to correct all potentials. ^{1}H-NMR, ^{13}C-NMR, and mass spectra of compounds **1**, **3-10**, **12**, **13** can be found in Appendix A.

*1.4.1.1. 3-methyl-2-[(trimethylsilyl)ethynyl]thiophene **(1)***

Et_3N (75 mL) and trimethylsilylacetylene (3.60 g, 36.65 mmol) were added to a degassed mixture of 2-bromo-3-methylthiophene (5.00 g, 28.24 mmol), $Pd(PPh_3)_4$ (1.00 g, 0.87 mmol), and CuI (0.20 g, 1.05 mmol) under argon. The mixture was stirred at 70 ^oC for 15 h, poured into $CHCl_3$, and washed with saturated NH_4Cl aq, HCl aq, $NaHCO_3$ aq, and water. The mixture was dried over $MgSO_4$ and solvent was removed via rotary evaporation. The residue was purified via flash column chromatography (silica gel, hexanes, R_f = 0.30) giving the title compound as a colorless liquid (5.25 g, 96%). ^{1}H NMR (500 MHz, $CDCl_3$) δ 7.11 (d, J = 5.5 Hz, 1H), 6.81 (d, J = 5.0 Hz, 1H), 2.33 (s, 3H), 0.28 (s, 9H). ^{13}C (125 MHz, $CDCl_3$) δ 143.71, 129.32, 126.11, 119.01, 101.16, 97.85, 15.23, 0.37. MS (ESI): *m/z* calcd for $C_{10}H_{14}SSi$ $[M+H]^+$: 195.0664, found: 195.0663.

*1.4.1.2. 2-ethynyl-3-methylthiophene **(2)***[31,32]

KOH (8.00 g, 142.58 mmol) in H_2O (70 mL) was added to a solution of **1** (5.54 g, 28.50 mmol) in THF (100 mL). Methanol was added until the solution was homogenous. After stirring for 2 h at room temperature, the mixture was washed with water and dried over $MgSO_4$. Solvent was removed carefully by rotary evaporation to give the title compound as a yellow liquid (3.10 g, 89%). ^{1}H NMR (500 MHz, $CDCl_3$) δ 7.14 (d, J = 5.1 Hz, 1H), 6.83 (d, J = 5.1 Hz, 1H), 3.45 (s, 1H), 2.33 (s, 3H).

*1.4.1.3. Monomer **(3)***

Et_3N (15 mL) and THF (30 mL) were added to a degassed mixture of 2,5-dihexyloxy-4-[(trimethylsilyl)ethynyl]iodobenzene (2.70 g, 5.39 mmol), **2** (0.87 g, 7.12 mmol), $PdCl_2(PPh_3)_2$ (0.0840 g, 0.120 mmol), and CuI (0.0450 g, 0.236 mmol). The mixture was degassed at -78 ˚C and refilled with argon three times, then stirred for 12 h at room temperature. Solvent was removed and the resulting brown residue was dissolved in $CHCl_3$ and washed with saturated NH_4Cl aq and water. The mixture was dried over $MgSO_4$ and solvent was removed via rotary evaporation. A pale yellow solid (2.32 g, 87%) was obtained by recrystallizing from $CHCl_3/CH_3OH$. ^{1}H NMR (300 MHz, $CDCl_3$) δ 7.17 (d, J = 5.5 Hz, 1H), 6.93 (s, 1H), 6.92 (s, 1H), 6.86 (d, J = 5.0 Hz, 1H), 3.98 (t, J = 6.5 Hz, 4H), 2.40 (s, 3H), 1.84-1.77 (m, 4H), 1.55-1.49 (m, 4H), 1.37-1.32 (m, 8H), 0.93-0.87 (m, 6H), 0.26 (s, 9H). ^{13}C (125 MHz, $CDCl_3$) δ 154.51, 153.51, 143.05, 129.58, 126.42, 119.20, 117.27, 116.78, 114.56, 113.85, 101.59, 100.36, 92.31, 88.32, 69.91, 69.81, 31.98, 29.71, 29.68, 26.13, 26.06, 22.99, 22.97, 15.34, 14.42, 14.40, 0.33. MS (MALDI-TOF): *m/z* calcd for $C_{30}H_{42}O_2SSi$ $[M+H]^+$: 495.2753, found: 495.2432.

*1.4.1.4. Deprotected Monomer **(4)***

KOH (0.85 g, 15.15 mmol) in H_2O (9 mL) was added to a solution of **3** (1.50 g, 3.03 mmol) in THF (30 mL). Methanol was added until the solution was homogenous. The mixture was stirred at room temperature for 2 h, then washed with water and dried over $MgSO_4$. Solvent was removed via rotary evaporation to afford the title compound as a yellow solid (1.20 g, 94%). ^{1}H NMR (500 MHz, $CDCl_3$) δ 7.18 (d, J = 5.0 Hz, 1H), 6.96 (s, 2H), 6.87 (d, J = 5.5 Hz, 1H), 4.02-3.97 (m, 4H), 3.33 (s, 1H), 2.40 (s, 3H), 1.84-1.79 (m, 4H), 1.53-1.48 (m, 4H), 1.37-1.33 (m, 8H), 0.93-0.87 (m, 6H). ^{13}C NMR (125 MHz, $CDCl_3$) δ 154.61, 153.60, 143.11, 129.59, 126.46, 119.22, 117.99, 117.03, 115.14, 112.93, 92.19, 88.38, 82.52, 80.50, 70.19, 69.99, 31.98, 31.90,, 29.74, 29.54, 26.13, 25.97, 22.94, 15.32, 14.34. MS (MALDI-TOF): *m/z* calcd for $C_{27}H_{34}O_2S$ $[M+H]^+$: 422.2280, found: 422.2346.

*1.4.1.5. Iodinated Monomer **(5)***

LDA (6.54 mmol, 3.63 mL, 1.8 M) was added dropwise into degassed solution of **3** (1.08 g, 2.18 mmol) in THF (17 mL) at -78˚C under argon. After stirring for 1 h at -78 ˚C, a separate solution of iodine (1.66 g, 6.54 mmol) in THF (12 mL) was added slowly. The mixture was stirred for an additional 1 h at -78 ˚C, poured into water, and extracted with THF. The organic layer was washed with $Na_2S_2O_3$ aq and water, then dried over $MgSO_4$. Solvent was removed by rotary evaporation, and a yellow solid (1.30 g, 96%) was obtained by recrystallizing from $CHCl_3/CH_3OH$. ^{1}H NMR (300 MHz, $CDCl_3$) δ 7.01 (s, 1H), 6.92 (s, 1H), 6.90 (s, 1H), 3.99-3.95 (m, 4H), 2.35 (s, 3H), 1.85-1.75 (m, 4H), 1.54-1.49 (m, 4H), 1.36-1.32 (m, 8H), 0.93-0.87 (m, 6H), 0.26 (s, 9H). ^{13}C

NMR (125 MHz, $CDCl_3$) δ 154.48, 153.54, 144.49, 139.40, 125.31, 117.17, 116.70, 114.19, 114.03, 101.49, 100.60, 94.01, 86.96, 74.22, 69.91, 69.74, 31.97, 29.67, 26.12, 26.05, 22.98, 14.99, 14.41, 0.31. MS (MALDI-TOF): *m/z* calcd for $C_{30}H_{41}IO_2SSi$ $[M+K]^+$: 659.1278, found: 659.1262.

1.4.16. Dimer ***(6)***

Et_3N (15 mL) and THF (30 mL) were added into a degassed mixture of **4** (0.75 g, 1.77 mmol), **5** (1.10 g, 1.77 mmol), $PdCl_2(PPh_3)_2$ (0.0246 g, 0.035 mmol), and CuI (0.0135 g, 0.071 mmol). The mixture was degassed at -78 ˚C and refilled with argon three times, then stirred at room temperature for 12 h. The brown solid obtained after removing solvent was dissolved in $CHCl_3$ and washed with saturated NH_4Cl aq and water. The mixture was dried over $MgSO_4$ and solvent was removed via rotary evaporation. The residue was purified by flash column chromatography (silica gel, CH_2Cl_2/hexanes = 1/2, R_f = 0.24) giving the title compound as a yellow solid (1.53 g, 94%). ^{1}H NMR (300 MHz, $CDCl_3$) δ 7.18 (d, J = 5.1 Hz, 1H), 7.02 (s, 1H), 6.97 (s, 1H), 6.95 (s, 1H), 6.93 (s, 2H), 6.87 (d, J = 5.1 Hz, 1H), 4.04-3.96 (m, 8H), 2.41 (s, 3H), 2.36 (s, 3H), 1.88-1.76 (m, 8H), 1.57-1.48 (m, 8H), 1.40-1.32 (m, 16H), 0.93-0.87 (m, 12H), 0.28 (s, 9H). ^{13}C NMR (125 MHz, $CDCl_3$) δ 154.49, 153.94, 153.66, 153.62, 143.12, 142.95, 134.02, 129.61, 126.48, 123.73, 120.96, 119.20, 117.16, 116.81, 116.73, 116.48, 114.64, 114.17, 114.12, 113.56, 101.53, 100.63, 93.50, 92.38, 91.24, 88.61, 88.38, 88.05, 70.07, 69.91, 69.84, 69.75, 31.96, 29.71, 29.67, 29.62, 26.14, 26.11, 26.07, 22.98, 15.33, 14.41, 0.31. MS (MALDI-TOF): *m/z* calcd for $C_{57}H_{74}O_4S_2Si$ $[M+H]^+$: 915.4876, found: 915.4835.

*1.4.1.7. Deprotected Dimer **(7)***

TBAF (1.70 mmol, 1.70 mL, 1M in THF) was added to a solution of **6** (1.30 g, 1.42 mmol) in CH_2Cl_2 (80 mL) and stirred for 2 h at room temperature. The mixture was passed through a short silica plug, and solvent was removed to afford a yellow solid (1.18 g, 99%). ^{1}H NMR (500 MHz, $CDCl_3$) δ 7.18 (d, J = 5.0 Hz, 1H), 7.02 (s, 1H), 6.97 (s, 1H), 6.96 (s, 2H), 6.956 (s, 1H), 6.87 (d, J = 5.0 Hz, 1H), 4.03-3.97 (m, 8H), 3.35 (s, 1H), 2.41 (s, 3H), 2.37 (s, 3H), 1.85-1.81 (m, 8H), 1.53-1.48 (m, 8H), 1.39-1.33 (m, 16H), 0.93-0.88 (m, 12H). ^{13}C NMR (125 MHz, $CDCl_3$) δ 154.46, 153.92, 153.63, 153.57, 143.13, 143.05, 134.02, 129.61, 126.49, 123.80, 120.84, 119.16, 117.60, 116.75, 116.70, 116.42, 114.63, 114.50, 113.49, 112.99, 93.27, 92.35, 91.26, 88.63, 88.34, 88.10, 82.77, 80.39, 70.04, 69.81, 69.77, 31.98, 31.94, 31.88, 29.70, 29.65, 29.61, 29.46, 26.14, 26.11, 26.07, 25.94, 22.97, 15.33, 14.41. MS (MALDI-TOF): *m/z* calcd for $C_{54}H_{66}O_4S_2$ $[M+H]^+$: 843.4481, found: 843.4449.

*1.4.1.8. Iodinated Dimer **(8)***

LDA (3.28 mmol, 1.82 mL, 1.8 M) was added dropwise to a degassed solution of **6** (0.75 g, 0.82 mmol) in THF (72 mL) at -78 ˚C under argon. After stirring for 1 h at -78 ˚C, a separate solution of iodine (0.83 g, 3.28 mmol) in THF (6 mL) was added slowly. The mixture was stirred for an additional 1 h at -78 ˚C, poured into water, and extracted with $CHCl_3$. The organic layer was washed with $Na_2S_2O_3$ aq and water. The mixture was dried over $MgSO_4$ and solvent was removed via rotary evaporation. A yellow solid (0.49 g, 58%) was obtained via flash column chromatography (silica gel, CH_2Cl_2/hexanes = 1/2, R_f = 0.32). ^{1}H NMR (500 MHz, $CDCl_3$) δ 7.02 (s, 2H), 6.95 (s,

2H), 6.93 (s, 2H), 4.02-3.97 (m, 8H), 2.36 (s, 6H), 1.85-1.79 (m, 8H), 1.55-1.49 (m, 8H), 1.38-1.33 (m, 16H), 0.93-0.88 (m, 12H), 0.26 (s, 9H). ^{13}C NMR (125 MHz, $CDCl_3$) δ 154.48, 153.90, 153.69, 153.62, 144.55, 142.96, 139.41, 134.08, 125.30, 123.64, 121.03, 117.15, 116.73, 116.37, 116.33, 114.18, 114.09, 113.92, 101.51, 100.64, 94.07, 93.54, 91.16, 88.58, 88.02, 87.24, 74.29, 70.07, 69.90, 69.75, 31.96, 29.67, 29.60, 26.12, 26.06, 22.99, 15.32, 15.00, 14.41, 0.31. MS (MALDI-TOF): *m/z* calcd for $C_{57}H_{73}IO_4S_2Si$ $[M+H]^+$: 1041.3842, found: 1041.3870.

*1.4.1.9. Tetramer **(9)***

Et_3N (25 mL) and THF (50 mL) were added to a degassed mixture of **7** (0.59 g, 0.70 mmol), **8** (0.72 g, 0.70 mmol), $PdCl_2(PPh_3)_2$ (0.0098 g, 0.014 mmol), and CuI (0.0053 g, 0.028 mmol). The mixture was degassed at -78 ˚C and refilled with argon three times, then stirred at room temperature for 19 h. The brown solid obtained after removing solvent was dissolved in $CHCl_3$ and washed with saturated NH_4Cl aq, and water. The mixture was dried over $MgSO_4$ and solvent was removed via rotary evaporation. The residue was purified by flash column chromatography (silica gel, CH_2Cl_2/hexanes = 1/2, R_f = 0.05) giving the title compound as an orange solid (0.92 g, 76%). ^{1}H NMR (500 MHz, $CDCl_3$) δ 7.18 (d, J = 5.0 Hz, 1H), 7.034 (s, 1H), 7.030 (s, 1H), 7.026 (s, 1H), 6.97-6.96 (m, 6H), 6.93 (s, 2H), 6.87 (d, J = 5.0 Hz, 1H), 4.03-3.97 (m, 16H), 2.41 (s, 3H), 2.38 (s, 6H), 2.37 (s, 3H), 1.87-1.78 (m, 16H), 1.57-1.50 (m, 16H), 1.38-1.34 (m, 32H), 0.93-0.88 (m, 24H), 0.27 (s, 9H). ^{13}C NMR (125 MHz, $CDCl_3$) δ 154.52, 153.96, 153.82, 153.69, 143.12, 143.01, 142.95, 134.08, 129.61, 126.48, 123.82, 123.75, 123.68, 121.06, 120.97, 119.22, 117.58, 117.22, 116.82, 116.53,

116.42, 114.70, 114.25, 114.14, 113.96, 113.60, 101.54, 100.64, 93.64, 93.60, 92.39, 91.30, 91.22, 88.62, 88.35, 88.02, 70.11, 69.95, 69.84, 31.96, 29.68, 29.63, 26.13, 26.08, 22.98, 15.34, 14.40, 0.31. MS (MALDI-TOF): *m/z* calcd for $C_{111}H_{138}O_8S_4Si$ $[M+H]^+$: 1755.9122, found: 1755.9132.

*1.4.1.10. Iodinated Tetramer **(10)***

LDA (0.95 mL, 1.71 mmol, 1.8 M) was added dropwise to a degassed solution of **9** (0.50 g, 0.29 mmol) in THF (15 mL) at -78 ˚C under argon. After stirring for 1 h at -78 ˚C, a separate solution of iodine (0.43 g, 1.71 mmol) in THF (10 mL) was added slowly. The mixture was stirred for an additional 3 h at -78 ˚C, poured into water, and extracted with $CHCl_3$. The organic layer was washed with $Na_2S_2O_3$ aq and water. The mixture was dried over $MgSO_4$ and solvent was removed via rotary evaporation. A dark orange solid (0.30 g, 56%) was obtained by flash column chromatography (silica gel, CH_2Cl_2/hexanes = 1/2, R_f = 0.07). ^{1}H NMR (500 MHz, $CDCl_3$) δ 7.032 (s, 1H), 7.029 (s, 1H), 7.02 (s, 2H), 6.97 (s, 2H), 6.962 (s, 1H), 6.960 (s, 1H), 6.952 (s, 1H), 6.949 (s, 1H), 6.93 (s, 2H), 4.04-3.97 (m, 16H), 2.38 (s, 6H), 2.37 (s, 6H), 1.87-1.79 (m, 16H), 1.54-1.50 (m, 16H), 1.38-1.33 (m, 32H), 0.93-0.89 (m, 24H), 0.27 (s, 9H). ^{13}C NMR (125 MHz, $CDCl_3$) δ 154.48, 153.90, 153.77, 153.68, 153.61, 144.56, 143.03, 142.97, 139.42, 134.09, 125.29, 123.70, 123.64, 121.03, 117.11, 116.72, 116.33, 114.15, 114.09, 114.06, 113.88, 101.50, 100.65, 94.07, 93.62, 93.54, 91.25, 91.21, 88.63, 88.59, 88.33, 88.03, 87.26, 74.31, 70.06, 69.88, 69.77, 31.96, 29.67, 29.61, 26.13, 26.07, 22.99, 15.34, 15.01, 14.42, 0.31. MS (MALDI-TOF): *m/z* calcd for $C_{111}H_{137}IO_8S_4Si$ $[M+H]^+$: 1881.8088, found: 1881.8071.

*1.4.1.11. Protected 1,1′-ditetramericferrocene **(12)***

THF (1.7 mL) and N^iPr_2H (0.4 mL) were added to a degassed mixture of **11** (10.42 mg, 0.024 mmol), iodinated tetramer **10** (100.00 mg, 0.053 mmol), $PdCl_2(PPh_3)_2$ (0.68 mg, 0.00097 mmol), and CuI (0.18 mg, 0.00097 mmol). After cooling to -78 ˚C, the mixture was degassed and filled with argon three times. The mixture was warmed to 60 ˚C and stirred for 19 h. Rotary evaporation was used to remove solvent. A dark red solid was obtained by recrystallizing from CH_2Cl_2/ethanol (65 mg, 69%). ^{1}H NMR (500 MHz, $CDCl_3$) δ 7.35 (d+d, J = 8.0 Hz, 8H), 7.032 (s, 2H), 7.029 (s, 2H), 7.025 (s, 2H), 7.00 (s, 2H), 6.97-6.94 (m, 12H), 6.93 (s, 4H), 4.56 (t, J = 1.8 Hz, 4H), 4.35 (t, J = 1.8 Hz, 4H), 4.02-3.97 (m, 32H), 2.38-2.36 (m, 24H), 1.89-1.78 (m, 32H), 1.58-1.47 (m, 32H), 1.38-1.34 (m, 64H), 0.93-0.87 (m, 48H), 0.26 (s, 18H). ^{13}C (125 MHz, $CDCl_3$) δ 154.5, 153.9, 153.8, 153.6, 143.0, 143.2, 134.1, 131.6, 131.5, 124.2, 123.7, 123.6, 123.4, 122.1, 121.0, 117.1, 116.7, 116.3, 116.2, 114.1, 113.9, 101.5, 100.6, 94.3, 93.6, 93.5, 91.3, 89.7, 88.6, 88.3, 88.0, 87.1, 84.7, 73.3, 71.3, 70.2, 70.0, 69.9, 69.7, 67.5, 32.0, 29.7, 29.5, 26.13, 26.08, 26.0, 23.0, 15.3, 14.4, 0.3. MS (MALDI-TOF): *m/z* calcd for $C_{252}H_{290}FeO_{16}S_8Si_2$ $[M]^+$: 3939.8533, found: 3939.4543.

*1.4.1.12. Deprotected 1,1′-ditetramericferrocene **(13)***

12 (70.00 mg, 0.018 mmol) was dissolved in CH_2Cl_2 (16.8 mL). TBAF (0.043 mmol, 0.43 mL, 0.1 M in THF) was added and the mixture was stirred at room temperature for 1 h. The mixture was passed through a 4 cm dry silica plug and was recrystallized from CH_2Cl_2/ethanol to give the title compound as a dark red solid (62 mg, 92%). ^{1}H NMR (500 MHz, $CDCl_3$) δ 7.35 (d+d, J = 8.5 Hz, 8H), 7.03 (m, 6H), 7.00 (s, 2H), 6.97-6.94

(m, 16H), 4.56 (t, J = 1.8 Hz, 4H), 4.35 (t, J = 1.8 Hz, 4H), 4.02-3.97 (m, 32H), 3.35 (s, 2H), 2.38-2.36 (m, 24H), 1.87-1.80 (m, 32H), 1.56-1.49 (m, 32H), 1.38-1.33 (m, 64H), 0.93-0.89 (m, 48H). ^{13}C (125 MHz, $CDCl_3$) δ 154.5, 153.9, 153.8, 153.6, 143.0, 134.2, 134.1, 131.6, 131.5, 124.2, 123.7, 123.4, 122.1, 121.1, 121.0, 120.9, 117.6, 117.5, 116.7, 116.35, 116.28, 114.5, 114.20, 114.16, 113.9, 113.0, 94.3, 93.6, 93.3, 91.3, 89.7, 88.6, 88.3, 88.1, 87.1, 84.7, 82.8, 80.4, 73.3, 71.3, 70.3, 70.1, 69.8, 67.5, 32.0, 31.9, 29.7, 29.6, 29.5, 26.13, 26.09, 26.0, 23.0, 15.3, 14.4. MS (MALDI-TOF): *m/z* calcd for $C_{246}H_{274}FeO_{16}S_8$ $[M]^+$: 3795.7742, found: 3795.8464.

1.5 References

(1) *Conjugated Polymers: Theory, Synthesis, Properties, and Characterization*; Skotheim, T. A., Reynolds, J. R., Eds.; CRC Press: Boca Raton, FL, **2007**.
(2) *Functional Organic Materials*; Müller, T. J. J., Bunz, U. H. F., Eds.; Wiley-VCH: Weinheim, Germany, **2007**.
(3) *Handbook of Thiophene-Based Materials: Applications in Organic Electronics and Photonics*; Perepichka, I. F., Perepichka, D. F., Eds.; Wiley: West Sussex, United Kindom, **2009**.
(4) Bunz, U. H. F. *Adv. Polym. Sci.* **2005**, *177*, 1-52.
(5) Zheng, J.; Swager, T. M. *Adv. Polym. Sci.* **2005**, *177*, 151-179.
(6) Voskerician, G.; Weder, C. *Adv. Polym. Sci.* **2005**, *177*, 209-248.
(7) Morley, J. O.; Pugh, D. *J. Chem. Soc. Faraday Trans.* **1991**, *87*, 3021-3025.
(8) Wu, I.-Y.; Lin, J. T.; Li, C.-S.; Wang, W. C.; Huang, T. H.; Wen, Y. S.; Chow, T.; Tsai, C. *Tetrahedron* **1999**, *55*, 13973-13982.
(9) Rodríguez, J. G.; Lafuente, A.; Rubio, L.; Esquivias, J. *Tetrahedron Lett.* **2004**, *45*, 7061-7064.
(10) Bunz, U. H. F. *Chem. Rev.* **2000**, *100*, 1605-1644.
(11) Wu, R.; Schumm, J. S.; Pearson, D. L.; Tour, J. M. *J. Org. Chem.* **1996**, *61*, 6906-6921.
(12) Kukula, H.; Veit, S.; Godt, A. *Eur. J. Org. Chem.* **1999**, 277-286.
(13) Hensel, V.; Godt, A.; Popovitz-Biro, R.; Cohen, H.; Jensen, T. R.; Kjaer, K.; Weissbuch, I.; Lifshitz, E.; Lahav, M. *Chem. Eur. J.* **2002**, *8*, 1413-1423.
(14) Pang, Y.; Li, J.; Barton, T. J. *J. Mater. Chem.* **1998**, *8*, 1687-1690.
(15) Ickenroth, D.; Weissmann, S.; Rumpf, N.; Meier, H. *Eur. J. Org. Chem.* **2002**, 2808-2814.
(16) Zhou, C.-Z.; Liu, T.; Xu, J.-M.; Chen, Z.-K. *Macromolecules* **2003**, *36*, 1457-1464.
(17) Xue, C.; Luo, F.-T. *Tetrahedron* **2004**, *60*, 6285-6294.

(18) Rodríguez, J. G.; Esquivias, J.; Lafuente, A.; Rubio, L. *Tetrahedron* **2006**, *62*, 3112-3122.
(19) Li, G.; Wang, X.; Li, J.; Zhao, X.; Wang, F. *Tetrahedron* **2006**, *62*, 2576-2582.
(20) Izumi, T.; Kobashi, S.; Takimiya, K.; Aso, Y.; Otsubo, T. *J. Am. Chem. Soc.* **2003**, *125*, 5286-5287.
(21) Engtrakul, C.; Sita, L. R. *Organometallics* **2008**, *27*, 927-937.
(22) Pudelski, J. K.; Callstrom, M. R. *Organometallics* **1994**, *13*, 3095-3109.
(23) Tan, L.; David Curtis, M.; Francis, A. H. *Macromolecules* **2002**, *35*, 4628-4635.
(24) Xue, C.; Chen, Z.; Wen, Y.; Luo, F.-T.; Chen, J.; Liu, H. *Langmuir* **2005**, *21*, 7860-7865.
(25) Jestin, I.; Frére, P.; Mercier, N.; Levillain, E.; Stievenard, D.; Roncali, J. *J. Am. Chem. Soc.* **1998**, *120*, 8150-8158.
(26) Zhu, Y.; Wolf, M. O. *Chem. Mater.* **1999**, *11*, 2995-3001.
(27) Audebert, P.; Catel, J.-M.; Coustumer, G. L.; Duchenet, V.; Hapiot, P. *J. Phys. Chem. B* **1998**, *102*, 8661-8669.
(28) Sailer, M.; Rominger, F.; Mùller, T. J. J. *J. Organomet. Chem.* **2006**, *691*, 299-308.
(29) Butler, I. R.; Hobson, L. J.; Coles, S. J.; Hursthouse, M. B.; Abdul Malik, K. M. *J. Organomet. Chem.* **1997**, *540*, 27-40.
(30) Li, H.; Powell, D. R.; Hayashi, R. K.; West, R. *Macromolecules* **1998**, *31*, 52-58.
(31) Beny, J.-P.; Dhawan, S. N.; Kagan, J.; Sundlass, S. *J. Org. Chem.* **1982**, *47*, 2201-2204.
(32) Carpita, A.; Rossi, R.; Veracini, C. A. *Tetrahedron* **1985**, *41*, 1919-1929.

Chapter 2: Efficient Transport of Gold Atoms with a Scanning Tunneling Microscopy Tip and a Linker Molecule

2.1 Introduction

The controlled manipulation of atoms and molecules is crucial to fabricating nanoarchitectures. One approach has been to use scanning probe microscopy to achieve such manipulation.[1,2] It has been found that features such as islands, mounds, and pits on metallic surfaces often coarsen naturally because of adatom, cluster, and vacancy diffusion. These processes have strong temperature dependences, and a significant amount of experimental work[3-8] and kinetic modeling[9-11] has been carried out to understand them. An extensive review of the research on collective and single-particle diffusion has been published by Ala-Nissila et al.[12] The restructuring of Au(111) steps to form so-called "gold magic fingers" under the influence of a scanning tunneling microscope (STM) tip by using high tip voltages to produce a high electric field has been reported by Guo et al.[13,14] Monte Carlo simulations of the formation of these structures reported by Totó et al. have suggested that the high electric field between the tip and substrate induces the detachment of atoms from steps to deposit adatoms close to the step, which then nucleate to form the gold fingers when the experiment is carried out at ~300 K.[15,16]

It has also been found that the presence of molecules on the surface can affect the coarsening mechanism as demonstrated for the formation of silver islands when there is sulfur present on the surface, which is facilitated by the formation of sulfur–silver complexes.[4] Also, the etching of terraces to form pits has been reported when sulfur is

deposited on gold.[17] This is not surprising considering that there is a large amount of literature showing that sulfur bonds strongly to coinage metals. A well-known example of this is the formation of thiolate self-assembled monolayers (SAMs) on gold surfaces that induces the formation of pits and islands,[18] and the extraction of gold atoms from the surface to form thiolate–gold adatom complexes has been recently demonstrated.[19] This raises the possibility of being able to drag metallic atoms across a surface using a functionalized tip, and something similar has been accomplished recently by using an STM tip to push molecules with gold atoms attached.[20,21] Here, it was found that the preadsorption of a HS-ssDNA self-assembled monolayer (SAM) on Au(111) enhances the formation of gold fingers when the surface is subsequently scanned with an STM tip.[20] This was achieved using a Pt/Ir tip, and it was proposed that the tip penetrates the molecules in the SAM and mechanically pushes them, thereby dragging the attached gold atoms and enhancing the formation of the gold fingers, similarly to what was previously proposed by Keel et al. for dodecanethiol on Au(111).[21] The following proposes an alternative approach, which involves manipulating surface gold atoms by using an STM tip that has been functionalized by a sulfur-containing molecule as the gold atom transporter. To accomplish such a manipulation, the Au–S bond has to be sufficiently strong that when the tip moves laterally it causes the Au–Au bonds to break rather than cleaving those between the gold and sulfur or between the molecule and the tip. Kiguchi et al. demonstrated qualitatively by means of break-junction experiments that the Au–Au bond is in fact weaker than the Au–S bond.[22] The strength of the S–Au interaction will also depend on the chemical state of the sulfur. Sulfur in an alkylthiolate formed by either the deprotonation of an alkylthiol[18,19,23,24] or by S–S bond scission of a dialkyl disulfide[25]

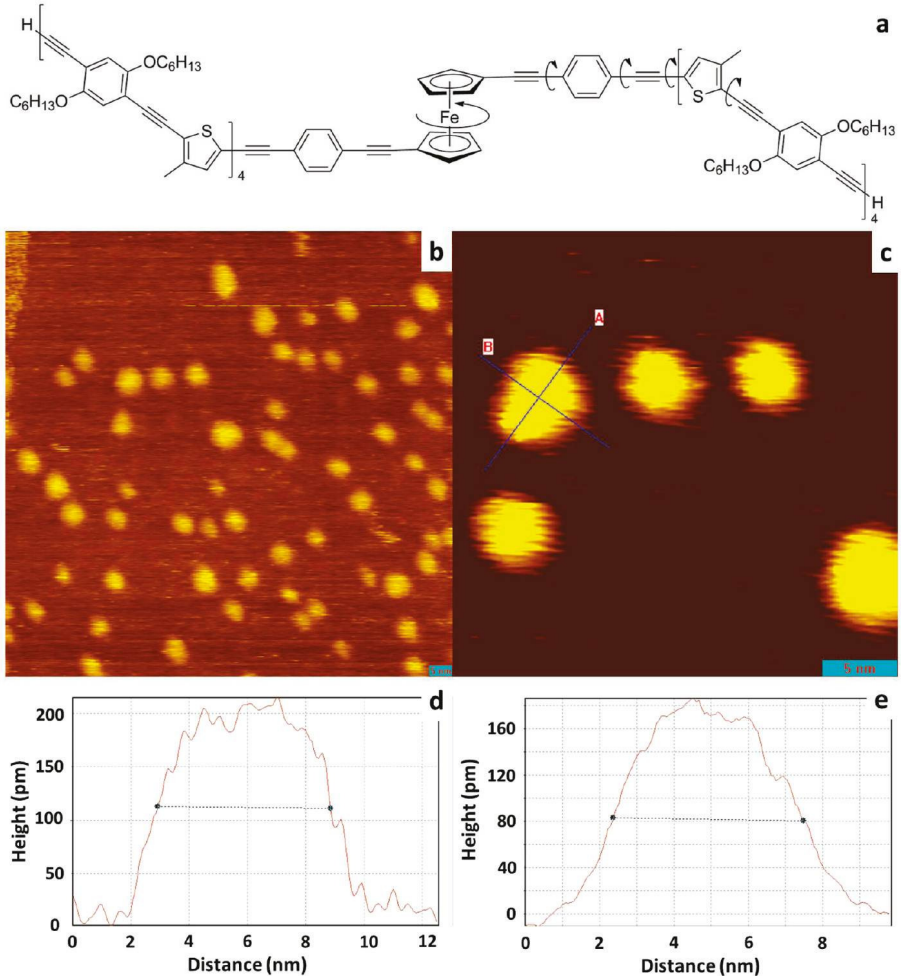

Figure 2.1. (a) Structure of the CTFH molecule and (b) 100 nm × 100 nm^2 image of the functionalized ferrocene molecules adsorbed on Au(111) and imaged with a Pt/Ir tip. Vb = -102 mV, It = 7.4 pA, and scanning speed = 500 nm/s. Different shapes and sizes are observed, corresponding to some of the many different conformations expected for the molecule. (c) A 30 nm × 30 nm^2 image from which height profiles were obtained to estimate the apparent dimensions of the molecules. Vb = -102 mV, It = 7.3 pA, and scanning speed = 150 nm/s. (d, e) Profiles corresponding to sections A and B, respectively, in c. The average length and width measured at half-height of the protrusions are 5.2 ± 0.8 and 4.6 ± 0.3 nm, respectively. The average height is 180 ± 11 pm.

binds with a strength of 1.31 eV to gold.[26] For sulfur in a dialkyl sulfide, where no S–S bond scission occurs, the S–Au interaction is weaker although still significant.[26,27] Thus, for gold atoms to be redistributed during scanning, energetically allowed pathways must also be available to redeposit the gold atom on the surface, presumably at surface defects

such as steps. It is proposed, on the basis of the above considerations, that this can occur when gold is bonded to sulfur in a thiophene molecule, and this process is discussed in some detail below on the basis of our experimental observations. Experiments are carried out using a functionalized ferrocene molecule that contains eight thiophene groups, each contributing one sulfur atom (a conjugated thiophene-containing ferrocene hinge, CTFH, shown in Figure 2.1a) as the transporter molecule with a Au(111) surface as the metal substrate. Although thiophenes adsorbed on Au(111) surfaces have been extensively reported in the literature, this effect has not been previously explored.[27-40] The rationale for choosing this molecule will be discussed in greater detail below.

2.2 Experimental

A Au(111) single crystal (Princeton Scientific) was cleaned with cycles of ion bombardment using 1 keV argon ions for 30 min (1 $\mu A/cm^2$), annealing to 900 K for 5 min and then to 600 K for 30 min. Cleanliness was verified by obtaining a perfectly defined herringbone reconstruction by STM. The experiments were carried out in an ultrahigh vacuum (UHV) chamber operating at a base pressure of 2×10^{-10} Torr following bakeout. After being cleaned, the Au(111) sample was removed from the chamber and dipped for 30 s in a 0.2 μM solution of a functionalized ferrocene molecule containing eight thiophene groups (CTFH: conjugated thiophene-containing ferrocene hinge) in its structure. Chloroform was used as a solvent. The structure of the molecule is shown in Figure 2.1 and was synthesized as reported by Chen et al.[41] The sample was dried by gently blowing with dry nitrogen gas and immediately reinserted into the vacuum chamber. The transfer both in and out of the chamber was achieved without breaking vacuum in the STM chamber by means of a load-lock cell. The same procedure

was used for the experiment using the molecule shown as an inset in Figure 2.5, except that the concentration was 0.4 μM. STM images were acquired at a sample temperature of 300 K. During scanning, the tip rasters back and forth, and each image consists of 512 scan lines. Experiments were performed using a scanning tunneling microscope (RHK UHV350 dual AFM/STM) as described elsewhere.[42] The gold-coated tip was fabricated by dipping a sharp tungsten tip a controlled distance of 10 nm into a clean gold sample. Gold is much softer than tungsten, and plastic deformation of the substrate occurs when the tip indents the surface. When the tip is pulled away from the surface, a significant number of gold atoms remain attached to the tip. This procedure is widely used for tip conditioning. A simulation of this process has been recently reported for a Ni tip on a Cu substrate.[43] This is analogous to the W/Au system in the sense that a hard tip indents a softer material producing plastic deformation in the latter and carrying along some of the soft material when the tip retracts from the surface. The W STM tip was fabricated from a recrystallized tungsten wire by electrochemical etching with 4 M NaOH(aq), and the oxide was removed by Ar^+ bombardment.[44] The Pt/Ir tip was prepared with pliers by simultaneously pulling and cutting a Pt/Ir wire at a ~15° angle with respect to the long direction of the wire. The results of the experiments were reproduced with two different gold-coated tips made using identical methods and with two different Pt/Ir tips. Image analysis was done either with WXSM5.0 software or with XPMPro 2.0 software, including plane subtraction and noise filtering for easier visualization of the features of interest. Some of the thermal drift corrections were also made using WSXM5.0 software.[45]

2.3 Results and Discussion

Typical STM images of CTFH on the Au(111) surface taken with a Pt/Ir tip are shown in Figure 2.1. Figure 2.1b shows a 100 × 100 nm^2 image, where protrusions with different shapes and sizes are observed, presumably corresponding to the many expected conformations of this molecule. Figure 2.1c shows a smaller region, 30 × 30 nm^2, from which height profiles of the molecules were obtained in order to estimate their dimensions. Two of these profiles, corresponding to sections A and B of inset c, are shown in insets d and e, respectively. The average apparent dimensions are 5.2 ± 0.8 nm, 4.6 ± 0.3 nm, and 180 ± 11 pm for the length, width, and height, respectively. These are assigned to the presence of CTFH deposited on the surface from solution. Control experiments using the pure solvent alone were carried out, and no such features were detected by STM, excluding the possibility that the features are due to the solvent or impurities. In addition, the number of such features increases with increasing solution concentration.

When the surface is scanned using a gold-terminated tip, not only are the particles that were observed using the Pt/Ir tip not seen but also the surface within the scanning area is eroded as a result of scanning. This is shown in the sequence of images in Figure 2.2 where a peninsula, denoted by a blue (dark-gray) dashed oval, and a screw dislocation, denoted by a red (light-gray) solid oval in Figure 2.2a, are sequentially etched by repeated scans over that area. Some of the atoms that are removed from the scanned area are deposited at the line defined by the points at which the tip changes its scanning direction (i.e., at the edges of the images). In the following text, this line is referred to as the turning-point line (TPL). This effect is clearly seen in Figure 2.3. After subsequent scans over the area shown in Figure 2.3a, an image was taken to include

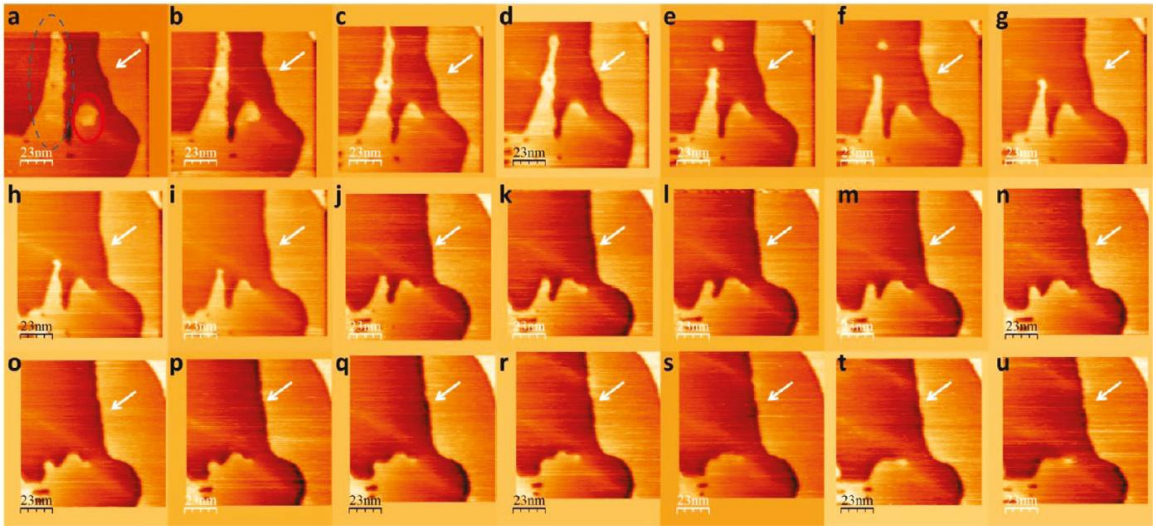

Figure 2.2. Series of 21 consecutive scans of a 100 × 100 nm^2 region showing the coarsening of a peninsula by scanning the surface with a gold-covered tungsten tip. Imaging conditions: Vb = -11 mV, It = 9 pA, and scanning speed = 1 μm/s.

the TPL, and this is displayed in Figure 2.3b.

A deposit of connected islands of gold atoms can be observed at the TPL. Moreover, this deposit is thicker at the upper part of the image, where it connects to a step edge. When the TPL coincides with a step edge (step down, Figure 2.4), the growth of stripes of gold originating from the step edge toward the lower terrace is observed. The substrate lattice directions were obtained from images taken on the clean Au(111) surface, and by comparison, it was found that the stripes always grow along one of the $<1\bar{1}0>$ directions (data not shown). Experiments were also carried out by adsorbing only the sulfur-containing oligomer (molecular structure shown in Figure 2.5) to gauge the effect of changing the number of thiophene groups and the effect of the ferrocene hinge. The transport of gold atoms was also observed, but at a much lower rate than when the longer chain was used under similar imaging conditions. Only when using tunneling currents 10 to 30 times larger than that used for CTFH was a significant transport of atoms observed. Figure 2.5 shows the variation of the area of a terrace (labeled B in the

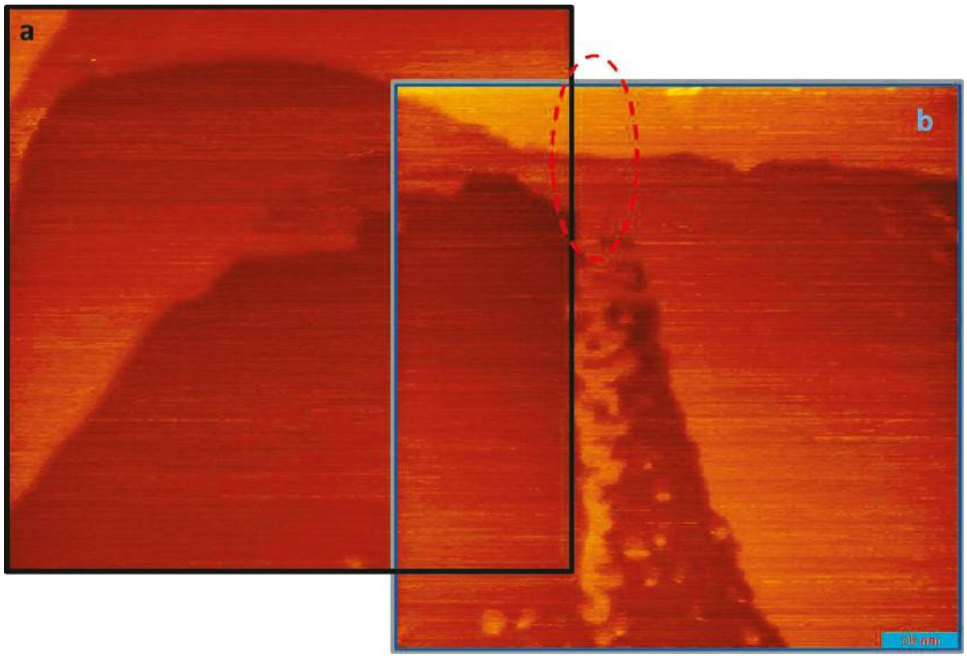

Figure 2.3. (a) When the surface is scanned with a gold-covered tungsten tip, the molecules cannot be observed. (b) An area that includes the turning points of the tip when scanning the area shown in image a. It can be observed that gold atoms are deposited along the line defined by the turning points. The height of these deposits corresponds to islands of gold atoms. Imaging conditions: Vb = -7.63 mV, It = 29.4 pA, and scanning speed = 500 nm/s.

image in the top-left corner) as a function of the number of image scans. A linear rate of terrace-area growth of 993 nm^2/scan is observed. Also, control experiments were carried out by performing identical experiments with only the pure solvent, and no mobility of gold atoms or growth of stripes was observed, thereby excluding effects due to the solvent alone. Experiments were also carried out to test the influence of the bias on the transport of atoms, and it was found that positive and negative bias showed the same effect for both molecules (data not shown).

It is postulated that it is possible to transport gold atoms mechanically and efficiently on a surface using a sulfur-containing molecule as the transporter. The CTFH molecules are necessary for this to occur, as at low tip bias voltages the herringbone

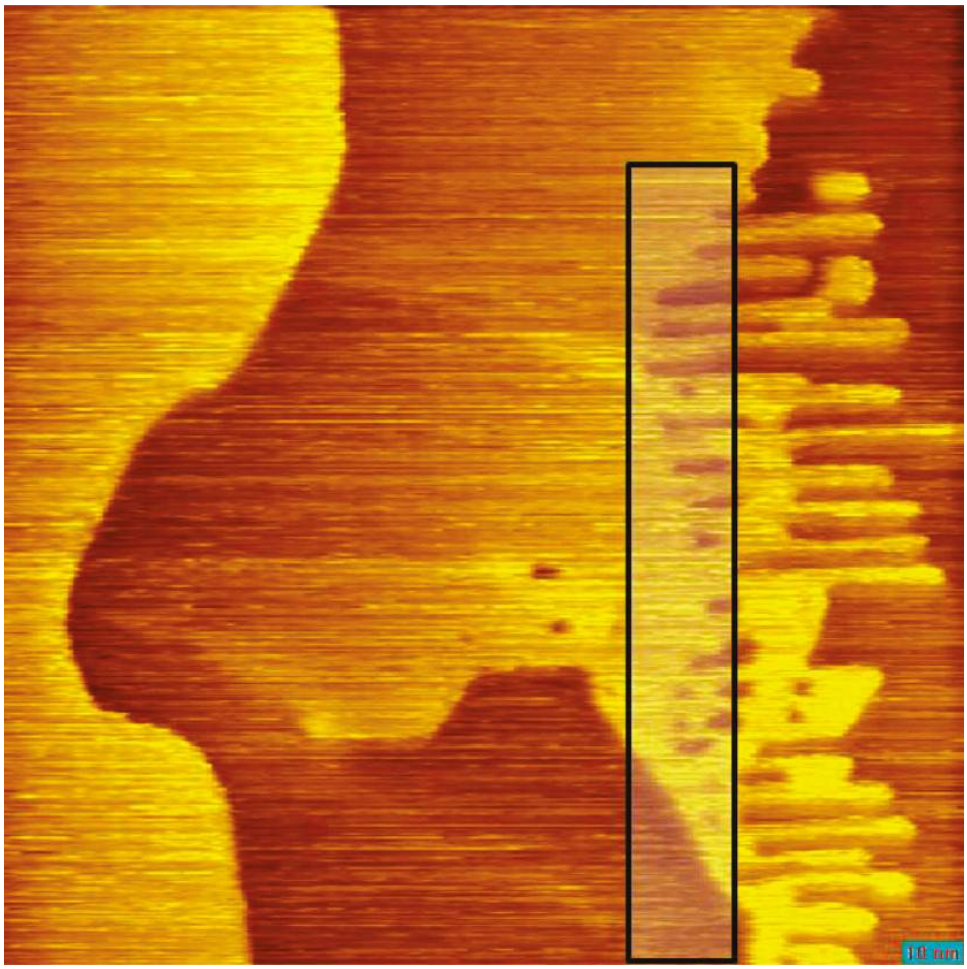

Figure 2.4. A 100 nm × 100 nm^2 image showing the growth of stripes (gold magic fingers) from a step edge formed when previous scans are made such that the line defined by the turning points in the image coincides with a step edge. Imaging conditions were Vb = -100 mV, It = 9.16 pA, and scanning speed = 500 nm/s.

reconstruction of the surface is clearly visible and no evidence of step flow is seen on the Au(111) surface without adsorbed CTFH molecules (not shown). The conductivity of the clean surface is much larger than that of a CTFH-covered surface, indicating that the tip has been functionalized. Note that the thiophene functionalities of the hinge molecule are linked by acetylide groups, thus maintaining π conjugation throughout the molecules and facilitating electron transport through the molecule. The molecule itself is reasonably flexible because of the ability to rotate around the acetylide–thiophene bonds, and the

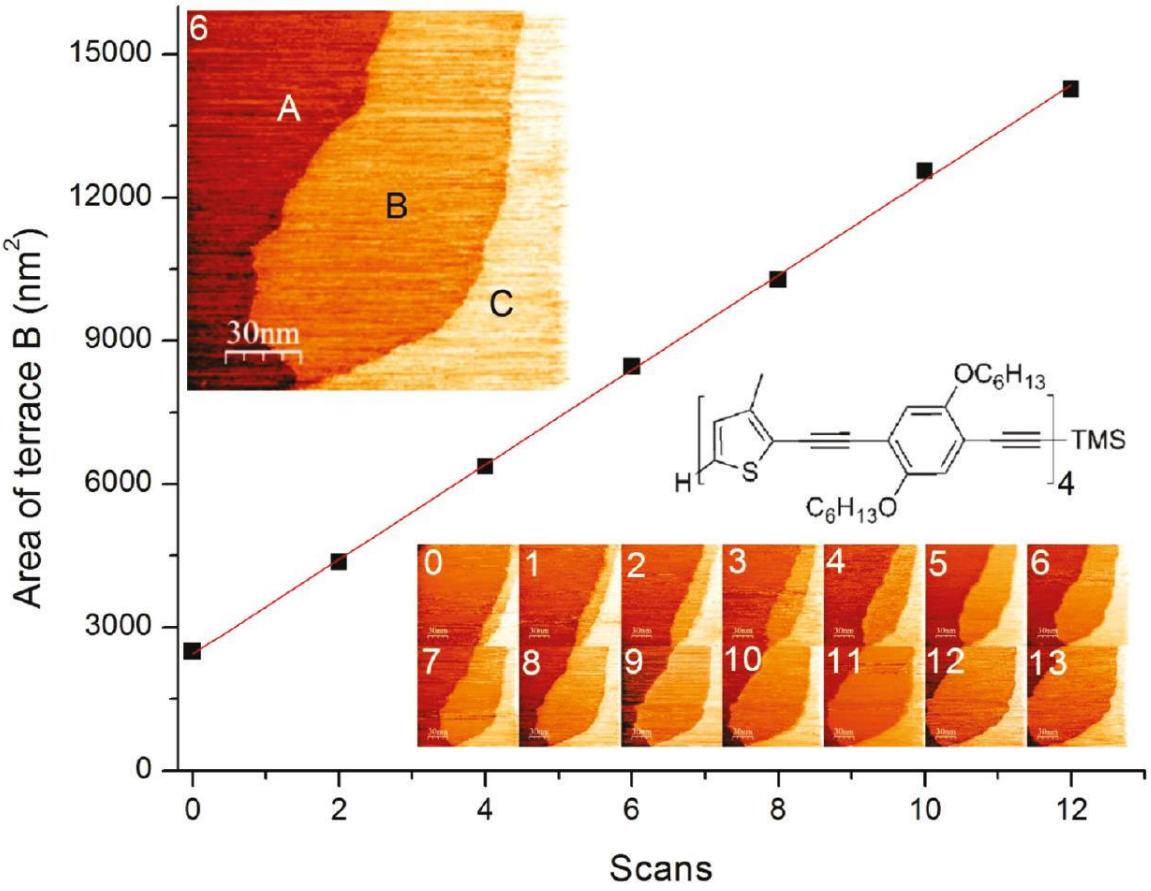

Figure 2.5. Area (9) of terrace labeled B in the inset at the top left as a function of the number of scans. The measurements correspond to the even numbered frames of the series of images shown in the inset below the curve. The growth rate of terrace B (slope of the curve) is 993 nm^2/scan. The images in the inset are 150 nm × 150 nm^2 scans taken under the following tunneling conditions: Vb = 102 mV, It = 280 pA, and scanning speed = 0.76 μm/s.

ferrocene "hinge" imparts additional flexibility to facilitate the thiophene's bonding both to the tip and the surface.

The presence of CTFH molecules on the Au(111) surface is verified from images using a Pt/Ir tip (Figure 2.1), finding an average particle size of 5.2 nm in length and 4.6 nm in width. Note that no such features are detected on surfaces exposed to the solvent alone. On the basis of standard bond lengths, the CTFH molecule would be expected have a size of 12.8 × 2.2 nm^2 in a linear anti conformation in which the organic moieties

rotate about the thiophene hinge so that they are opposite to each other. This is clearly larger than the longest distance measured by STM (Figure 2.1). Rotation around the hinge in a linear *syn* conformation suggests that the size would be 6.5×2.2 nm^2, which is also somewhat different from the experimental value. The formation of an almost circular conformation would yield an elliptical backbone with dimensions of 4.5×4.9 nm^2, which are somewhat closer to the measured values. These structures are illustrated in Figure 2.6. However, this measurement does not account for the alkyl chains that extend outside this perimeter. The motions of the side chains will be rapid compared to the STM collection time at the temperature at which the surface was imaged (~300 K), so they are unlikely to be resolved by STM. In addition, it has been found that the STM images of large molecules tend to be somewhat smaller than would be anticipated on the basis of their expected molecular sizes, as exemplified by recent studies of human insulin adsorbed on gold. (See ref 46 and references therein.)

When this surface is scanned using a gold-terminated tip, it is found that gold atoms are deposited at the end of the scan line when the direction of motion of the tip changes. A mechanism for this process is proposed in which the tip is functionalized by the transporter molecule (in this case, CTFH) as shown above. This is achieved by coating a tungsten tip with gold as described in the Experimental Section. It is proposed that when a gold-coated tip scans the surface the low-coordination gold atoms at the end of the tip can bind to some of the sulfur atoms of the CTFH. However, if all of the sulfur atoms of the molecule were to bind to the tip, then there would then be no sulfur atoms available to transport the gold atoms, whereas it is evident from Figures 2.2-2.4 that gold atom transport does occur. This effect is likely due to steric constraints that allow some of

the sulfur atoms of the molecule to remain uncoordinated and thus also be available to bind to surface gold atoms.

It can be seen in Figure 2.2 that when the tip rasters the surface during image collection, a peninsula is subsequently eroded. For this to occur, gold atoms located at one edge of a peninsula must be attached to the (functionalized) tip. The scan speeds range from 500 to 1000 nm/s. This indicates that, considering the diameter of a gold atom to be ~0.29 nm, the tip spends in average of ~300 to 600 μs over each atom. This is sufficient time for the proposed Au–S bond to form because typical bond-formation times range from a nanosecond to a few femtoseconds.[47]

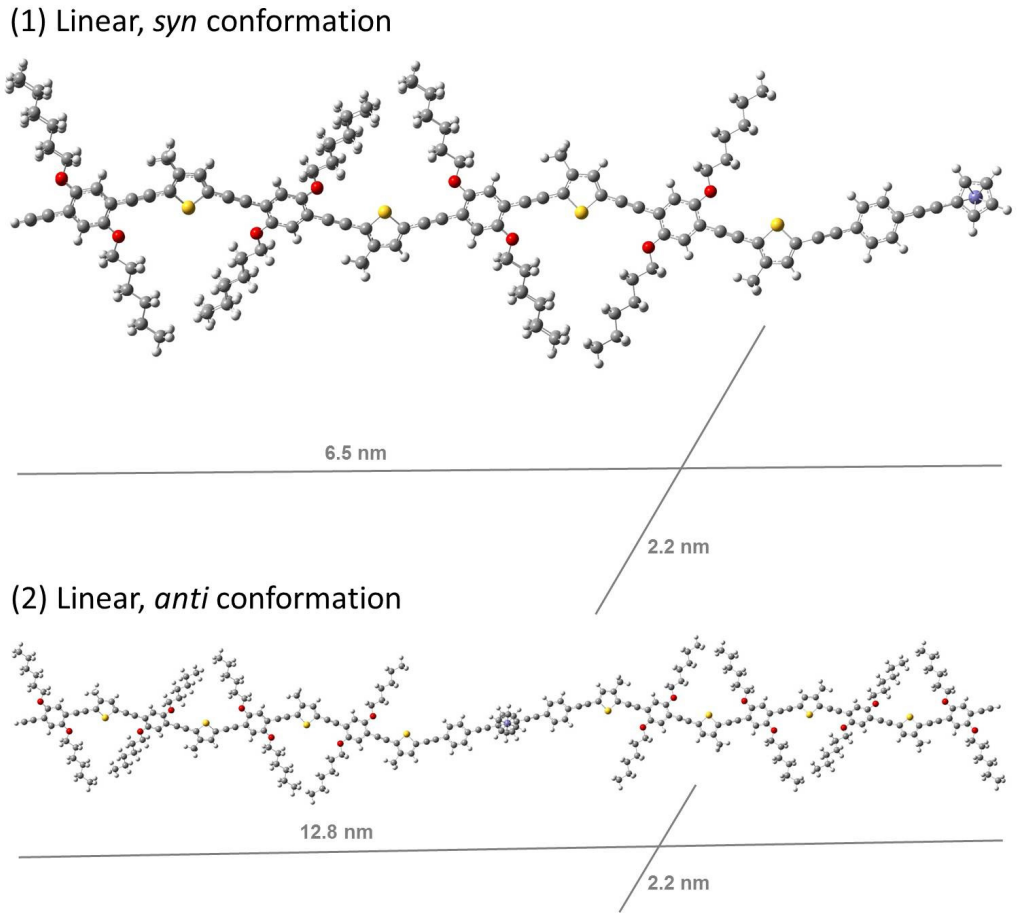

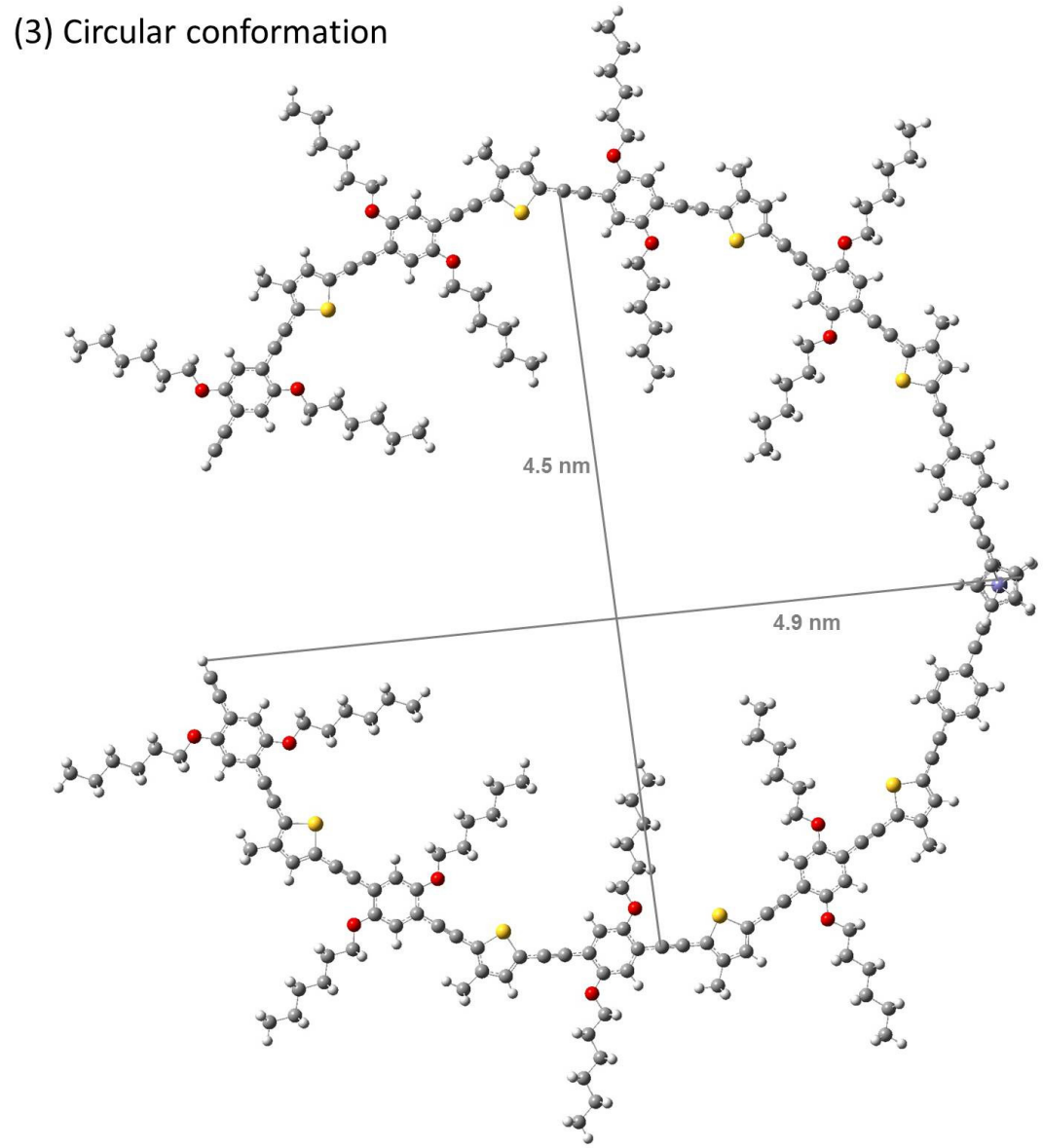

Figure 2.6. Potential conformations of CTFH molecule.

Because the tip oscillates back and forth along each line during scanning, erosion could occur when a tip goes up a step, down a step, or both. This will be addressed in greater detail below. It can also be seen that the step edge indicated by the white arrow in the images (Figure 2.2) changes shape along the scans, although is it not evident whether it is being eroded or the atoms are just being redistributed. Again, this point will be addressed later. Nevertheless, it is clear that the atoms are removed from the peninsula

during scanning. The image in Figure 2.3, showing the surfaces after repeated scanning over region 3a of the TPL (3b), reveals that atoms removed from the previously scanned area are deposited in the region where the tip changes direction. Furthermore, this deposition is thicker in the upper region, where it attaches to a step edge. This implies that the release of gold atoms is favored by the presence of the step edge. It is therefore inferred that the barrier for gold atoms attached to the functionalized tip to surmount a step is sufficiently high that, at least in some cases, the Au–S bonds cleave and the gold atoms are deposited onto the step edge. Note that in the region marked with the red (gray) dashed oval it can be seen that no deposit is present in the TPL on the upper terraces. This means that none of the atoms that are carried by the tip can pass a step-up barrier because if that were the case some of them would be deposited on the TPL of the upper terraces.

The above considerations can be summarized as follows:

(i) Atoms are removed from the step when the functionalized tip moves in a step-down direction.

(ii) Atoms are added to the step edge when the tip moves in a step-up direction.

(iii) Atoms that are carried by the transporter molecule can be released upon a change in the scanning direction of the tip even on the flat surface.

It is evident from the sequence of images shown in Figure 2.2 that the step edges change in shape from initially convex to a straight line (white arrows). This indicates that the average coordination number of the gold atoms increases during scanning, leading to an energetically more favorable structure. Also, a small step flow can be observed as the peninsula is etched, and this is consistent with the above postulates because the atoms

removed from the right side of the peninsula should be incorporated into the step edge. In accord with this idea, it can also be observed that the step flow stops when the peninsula has been completely eroded.

When the TPL coincides with a step edge, as in the case shown in Figure 2.4, the formation of gold stripes oriented along the scanning direction is observed. Their widths are mostly between 2 and 5 nm, although in some cases stripes of widths of up to 15 nm were also observed (data not shown). Such features have been previously reported and are named gold magic fingers.[13,14,20,48] A shaded rectangle is drawn on the image to show the TPL from which the stripes originate. It is worth noting that in none of the images could the herringbone reconstruction be observed. This could be due to a lifting of the reconstruction either by CTFH adsorption or by the presence of flexible CTFH molecules on the tip that could significantly degrade the image resolution. The latter is most likely because the low resolution is also evident from the ill-defined borders of the step edges in the images.

Moving gold atoms from a step edge to form stripes has been accomplished previously using an STM tip by using high-field scanning conditions (with a tip voltage of 1.5 V and a tunneling current of 30 nA). There it was found that the fingers grew only along the $<1\bar{1}0>$ directions, and no fingers were found for scanning along the $<11\bar{2}>$ directions.[13,14] Kinetic Monte Carlo simulations of the formation of fingers induced by kinetic instabilities generated by this strong field were performed by Totó et al.,[15] and the diffusion energetics of the elemental surface processes were described. In this work, stripes were also oriented along the $<1\bar{1}0>$ directions. This is not surprising because the

directions of the step edges of such stripes are thermodynamically more stable than for other directions.

The mobility of the gold atoms on the surface and their attachment or detachment from step edges and terraces can be also thought of as assisted diffusion. It is therefore instructive to analyze the energetics of such processes compared to the strength of the Au–S bond. The interaction energy with which the transported gold atoms are attached to the thiophene sulfur must be large enough to overcome the energy needed to transit a stepdown barrier but small enough not to be able to surmount the step-up barrier. The Au–S bond should also be sufficiently strong to detach gold atoms from the step edges. Although alkylthiols dehydrogenate[23,24] and dialkyl disulfides cleave the S–S bond[25] to give chemisorbed thiolate species, dialkyl sulfides and thiophenes49 are thought to bond to the surface without bond breaking. Lavrich has reported an adsorption energy of thiophene on Au(111) of 0.62 eV,[26] and Zhou et al. have found adsorption energies for thiophene ranging from 0.46 and 0.7 eV depending on the orientation of the molecules.[27] Because this is due to a Au–S interaction, this energy will be referred as E_{Au_S}.

Work by Kim et al. calculates the minimum-energy pathways and activation barriers for atomic diffusion processes on the surfaces of fcc crystals, including the Au(111) surface plane[9,50] along both terraces and along and across steps for both step-up and step-down directions for different diffusion paths. For the single-adatom diffusion along a terrace, values of the diffusion activation energies E_{diff} of 0.117, 0.135, and 0.861 eV were reported for motion along the $<11\bar{2}>$ and $<10\bar{1}>$ directions and exchange along the $<2\bar{1}\bar{1}>$ direction, respectively. (The lattice directions are depicted in the upper-left corner of Figure 2.7.) On (111) surfaces, the thermodynamically most stable steps run

along the <1$\bar{1}$0> directions. However, there are two kinds of steps along this direction, commonly referred as A and B. The structures of both steps are shown in Figure 2.7 (upper left). For step-up diffusion, different mechanisms and pathways that are close in energy were analyzed, yielding average values of E_{upA} = 0.680 eV for a step-up diffusion on type-A steps and E_{upB} = 0.647 eV for type B. For step-down motion, barrier E_{down} is significantly smaller, being 0.164 and 0.155 eV for A- and B-type steps, respectively. These rationalize the observation that transported atoms are released when transiting a (high-energy) step-up barrier because the step-up energies are larger than the Au–S bond strength for thiophene. Interestingly, it was found that a gold atom exchange mechanism between a diffusing atom and a step atom is slightly more favorable than the more intuitive hopping mechanism. These energetics render thiophenes ideal for scanning-induced gold atom transport processes. In the case of alkylthiols, the much larger interaction energy (1.31 eV)[26] would easily overcome the step-up energy barriers ($E_{up} \approx$ 0.66 eV) reported by Kim et al.[9] and therefore would simply transport the gold atoms across the surface without releasing them.

These considerations provide a plausible rationale for gold atom transport across steps and for atom release when moving up a step on the basis of the energy barriers for these processes to occur. They do not explain how gold atoms are transported when the erosion process begins. Totó et al. preformed kinetic Monte Carlo simulations of gold-nanofinger formation on step edges using high tip voltages. To consider all of the possible events leading to this phenomenon, the energy barriers for diffusion processes were calculated using the Gupta potential as a function of the change in the coordination number.[15] The cases of interest for the current study involve the removal of gold atoms

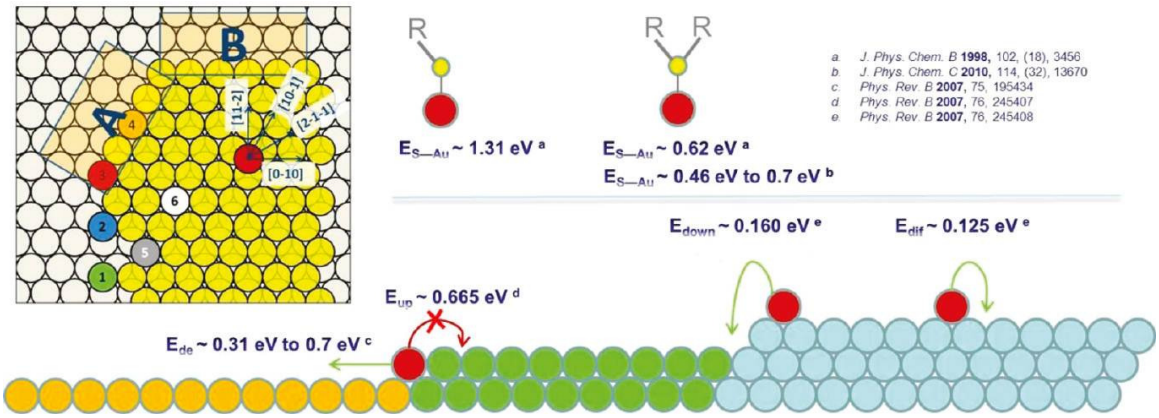

Figure 2.7. (Top left) Depiction of the different types of gold atoms that can be extracted from a step edge on the basis of the coordination number, the two different types of steps A and B along the <1$\bar{1}$0> surface directions, and the different directions along which an adatom can diffuse. The energies that are relevant to the proposed model are included (Au–S interaction energy E_{Au_S}, step detachment barrier E_{de}, terrace diffusion barrier E_{dif}, step-down diffusion barrier E_{down}, and step-up diffusion barrier E_{up}), as are the references from which they were taken. The energetically favorable processes are marked with green (light-gray) arrows, and the unfavorable, with a red (dark-gray), crossed arrow.

from steps. The calculated detachment-energy barriers (E_{de}) ranged from 0.31 to 0.7 eV and were mostly lower than the gold–sulfur bond energy, E_{Au_S}, of 0.62 eV reported for the thiophene S–Au bond, except for the following changes in coordination number: 3→0, 0.7 eV; 4→1 (on type-B steps), 0.67 eV; and 4→2 (on type-B steps), 0.63 eV. The latter values are very close in energy so that detachment could also occur because of statistical fluctuations or further weakening of the Au–Au interaction induced by the electric field generated by the tip. Figure 2.7 summarizes these energy considerations. The favorable gold atom motions (detachment from a step, stepdown diffusion, and terrace diffusion) are illustrated by green (light-gray) arrows, and the unfavorable (step-up diffusion) motion is marked by a red (dark-gray) arrow. The tunneling conditions influence the ease of gold atom detachment from the step edge, and a similar effect has been reported under high fields (Vb = 1.5 V, It = 30 nA) using a bare tip on Au(111).[13,14]

In our case, atom transport occurred under much lower field conditions. It is therefore inferred that the tip-functionalizing molecules assist the transport of atoms. However, the field generated by the tip does have an important effect in our experiments. Higher-field conditions (Vb = 102 mV, It = 280 pA) are needed to induce a rapid step atom detachment using the shorter oligomer (Figure 2.5) compared with CTFH (Vb = -11 mV, It = 9 pA) and to erode the peninsula (Figure 2.2). Thus, the nature of functional groups will affect the rate at which the gold atoms are transported. The ferrocene hinge is expected to enhance the flexibility of the CTFH molecule, which could influence its ability to coordinate to both the tip and the surface. However, conclusive statements cannot be made about the influence of the functional groups and the number of thiophene rings in the molecule because the shape and radius of the tip can also change between experiments and these morphological and size changes will significantly affect the number of molecules attached to the tip and therefore the rate of gold atom transport.

A mechanism for the transport of gold atoms by pushing molecules with the tip, similar to the ones previously reported,[20,21] could also be considered in our case. However, this is unlikely considering that, if that were the case, scanning using the Pt/Ir tip would have had the same effect. The solvent can be ruled out as being responsible for the transport effect because the control experiment did not show surface mobility or the formation of stripes.

The average number of gold atoms transported per pass can be estimated from the kinetic data in Figure 2.5. Scanning back and forth 512 times to obtain the image increases the area of the terrace by ~990 nm^2, suggesting that an area of gold atoms occupying ~1.9 nm^2 is moved per pass of the tip. The average area occupied per gold

atom on Au(111) is 0.072 nm^2, suggesting that ~25 atoms are transported per pass of the tip. This indicates that gold atoms are rather efficiently transported on the surface irrespective of the mechanism by which this occurs. This value is also substantially larger than the number of thiophene groups per molecule and indicates that the tip is functionalized by several molecules that enable multiple gold atoms to be picked up and deposited while transiting the steps. It also accounts for the relatively low resolution of the images. The large number of transported atoms also indicates that other mechanisms, such as a weakening of the gold bonding at steps due to adsorption, can be excluded because at the relatively low coverage of the modifier molecules on the surface (Figure 2.1) a sharp tip would not be able to move so many gold atoms.

2.4 Conclusion

It was found that gold atoms can be transported on a Au(111) surface when a thiophene-containing molecule attached to a gold-coated STM tip is used to scan the surface. A model is proposed to explain this phenomenon by means of a gold atom drag-and-drop mechanism. Using an STM tip, a molecule attached to the tip can raster the surface and bind to gold atoms sufficiently strongly to detach them from step sites and drag them along with the tip to then drop them at a different point on the surface. The atom, or group of atoms, can be released at a step edge when the tip is scanning in the step-up direction, or if there are no "up steps" in the scanning area they can also be dropped at the point at which the tip changes its scanning direction. The energy of the Au–S bond in thiophene (0.62 eV) is, in most cases, greater than that of the Au–Au bond, so the attachment of gold to the functionalized tip is energetically favored. Furthermore, this energy is greater than the diffusion barriers across a terrace (~0.13 eV),

so the gold atoms will move with the tip. This bond strength is also greater than the energy barrier of moving down a step (~0.16 eV) but slightly lower than that required to move up a step (~0.66 eV), indicating that gold atoms attached to the thiophene-functionalized tip will move down the steps but will be deposited on up steps.

2.5 References

(1) Otero, R.; Rosei, F.; Besenbacher, F. *Annu. Rev. Phys. Chem*. **2006**, 57, 497-525.
(2) Auwarter, W.; Schiffrin, A.; Weber-Bargioni, A.; Pennec, Y.; Riemann, A.; Barth, J. V. *Int. J. Nanotechnol*. **2008**, 5, 1171-1193.
(3) Gonzalez-Carrazco, A.; Valenzuela-Benavides, J. J. *Nanosci. Nanotechnol*. **2008**, 8, 6603-6607.
(4) Thiel, P. A.; Shen, M.; Liu, D. J.; Evans, J. W. *J. Phys. Chem. C* **2009**, 113, 5047-5067.
(5) Morgenstern, K.; Laegsgaard, E.; Besenbacher, F. *Phys. Rev. B* **2005**, 71, 155426.
(6) Shen, M. M.; Jenks, C. J.; Evans, J. W.; Thiel, P. A. *J. Phys.: Condens. Matter* **2010**, 22, 215002.
(7) Shen, M. M.; Wen, J. M.; Jenks, C. J.; Thiel, P. A.; Liu, D. J.; Evans, J. W. *Phys. Rev. B* **2007**, 75, 245409.
(8) Michely, T.; Kalff, M.; Comsa, G.; Strobel, M.; Heinig, K. H. *J. Phys.: Condens. Matter* **2002**, 14, 4177-4185.
(9) Kim, S. Y.; Lee, I.-H.; Jun, S. *Phys. Rev. B* **2007**, 76, 245408.
(10) Luque, N. B.; Ibach, H.; Pötting, K.; Schmickler, W. *Electrochim. Acta* **2010**, 55, 5411-5413.
(11) Yildirim, H.; Rahman, T. S. *Phys. Rev. B* **2009**, 80, 235413.
(12) Ala-Nissila, T.; Ferrando, R.; Ying, S. C. *Adv. Phys*. **2002**, 51, 949-1078.
(13) Yin, F.; Palmer, R. E.; Guo, Q. *Surf. Sci*. **2006**, 600, 1504-1509.
(14) Guo, Q. M.; Yin, F.; Palmer, R. E. *Small* **2005**, 1, 76-79.
(15) Totó, N.; Ferrando, R.; Guo, Q. M.; Johnston, R. L. *Phys. Rev. B* **2007**, 75, 195434.
(16) Totó, N.; Ferrando, R.; Johnston, R. L.; Guo, Q. M. *Surf. Sci*. **2007**, 601, 4175-4179.
(17) Biener, M. M.; Biener, J.; Friend, C. M. *Langmuir* **2005**, 21, 1668-1671.
(18) Li, F. S.; Zhou, W. C.; Guo, Q. M. *Phys. Rev. B* **2009**, 79, 113412.
(19) Kautz, N. A.; Kandel, S. A. *J. Phys. Chem. C* **2009**, 113, 19286-19291.
(20) Chen, F.; Zhou, A. H.; Yang, H. *Appl. Surf. Sci*. **2009**, 255, 6832-6839.
(21) Keel, J. M.; Yin, J.; Guo, Q.; Palmer, R. E. *J. Chem. Phys*. **2002**, 116, 7151.
(22) Kiguchi, M.; Miura, S.; Hara, K.; Sawamura, M.; Murakoshi, K. *Appl. Phys. Lett*. **2006**, 89, 213104.
(23) Kodama, C.; Hayashi, T.; Nozoye, H. *Appl. Surf. Sci*. **2001**, 169-170, 264-267.
(24) Torres, E.; Blumenau, A. T.; Biedermann, P. U. *Phys. Rev. B* **2009**, 79, 075440.
(25) Noh, J.; Kato, H. S.; Kawai, M.; Hara, M. *J. Phys. Chem. B* **2002**, 106, 13268-13272.

(26) Lavrich, D. J.; Wetterer, S. M.; Bernasek, S. L.; Scoles, G. *J. Phys. Chem. B* **1998**, 102, 3456-3465.
(27) Zhou, J.; Yang, Y. X.; Liu, P.; Camillone, N.; White, M. G. *J. Phys. Chem. C* **2010**, 114, 13670-13677.
(28) Ito, E.; Hara, M.; Kanai, K.; Ouchi, Y.; Seki, K.; Noh, J. *Bull. Korean Chem. Soc*. **2009**, 30, 1755-1759.
(29) Pasquali, L.; Terzi, F.; Montecchi, M.; Doyle, B. P.; Lukkari, J.; Zanfrognini, B.; Seeber, R.; Nannarone, S. *J. Electron Spectrosc. Relat. Phenom*. **2009**, 172, 114-119.
(30) Glowatzki, H.; Duhm, S.; Braun, K. F.; Rabe, J. P.; Koch, N. *Phys. Rev. B* **2007**, 76, 125425.
(31) Han, J. W.; Noh, J. *Mol. Cryst. Liq. Cryst*. **2007**, 464, 787-791.
(32) Sako, E. O.; Kondoh, H.; Nakai, I.; Nambu, A.; Nakamura, T.; Ohta, T. *Chem. Phys. Lett*. **2005**, 413, 267-271.
(33) Matsuura, T.; Sakaguchi, H.; Shimoyama, Y. *J. Mater. Sci.: Mater. Electron*. **2003**, 14, 353.
(34) Noh, J.; Ito, E.; Araki, T.; Hara, M. *Surf. Sci*. **2003**, 532, 1116-1120.
(35) Su, G. J.; Zhang, H. M.; Wan, L. J.; Bai, C. L. *Surf. Sci*. **2003**, 531, L363-L368.
(36) Kondoh, H.; Nakamura, T.; Matsui, F.; Yokoyama, T.; Ohta, T.; Matsumoto, M. *Mol. Cryst. Liq. Cryst*. **2002**, 377, 45-48.
(37) Liu, G.; Rodriguez, J. A.; Dvorak, J.; Hrbek, J.; Jirsak, T. *Surf. Sci*. **2002**, 505, 295-307.
(38) Matsuura, T.; Shimoyama, Y. *Eur. Phys. J. E* **2002**, 7, 233-240.
(39) Noh, J.; Ito, E.; Nakajima, K.; Kim, J.; Lee, H.; Hara, M. *J. Phys. Chem. B* **2002**, 106, 7139-7141.
(40) Dishner, M. H.; Hemminger, J. C.; Feher, F. J. *Langmuir* **1996**, 12, 6176-6178.
(41) Kohlmeyer, R. R.; Chen, J. To be submitted for publication.
(42) Burkholder, L.; Stacchiola, D.; Boscoboinik, J. A.; Tysoe, W. T. *J. Phys. Chem. C* **2009**, 113, 13877-13885.
(43) Mei, J. F.; Li, J. W.; Ni, Y. S.; Wang, H. T. *Nanoscale Res. Lett.* **2010**, 5, 692-700.
(44) Yu, Z. Q.; Wang, C. M.; Du, Y.; Thevuthasan, S.; Lyubinetsky, I. *Ultramicroscopy* **2008**, 108, 873-877.
(45) Horcas, I.; Fernandez, R.; Gomez-Rodriguez, J. M.; Colchero, J.; Gomez-Herrero, J.; Baro, A. M. *Rev. Sci. Instrum*. **2007**, 78, 013705.
(46) Welinder, A. C.; Zhang, J.; Steensgaard, D. B.; Ulstrup, *J. Phys. Chem. Chem. Phys*. **2010**, 12, 9999-10011.
(47) Zewail, A. H. *J. Phys. Chem. A* **2000**, 104, 5660-5694.
(48) Yin, F.; Palmer, R. E.; Guo, Q. *J. Phys.: Condens. Matter* **2009**, 21, 445001.
(49) Beulen, M. W. J.; Huisman, B. H.; vanderHeijden, P. A.; vanVeggel, F.; Simons, M. G.; Biemond, E.; deLange, P. J.; Reinhoudt, D. N. *Langmuir* **1996**, 12, 6170-6172.
(50) Kim, S. Y.; Lee, I. H.; Jun, S. *Phys. Rev. B* **2007**, 76, 245407.

Chapter 3: Preparation of Stable Carbon Nanotube Aerogels with High Electrical Conductivity and Porosity

3.1 Introduction

Aerogels are highly porous, low-density materials comprising a solid, three-dimensional (3D) nanoscale network completely accessible to ions and molecules.[1-5] Aerogels have already demonstrated orders of magnitude faster response for sensing, energy storage, and energy conversion than other pore-solid architectures.[6-8] Carbon nanotubes (CNTs) represent a rare material that exhibits a number of outstanding properties in a single material system, such as high aspect ratio, small diameter, light weight, high mechanical strength, high electrical and thermal conductivities, and unique optical and optoelectronic properties. By combining extraordinary properties of CNTs with those of aerogels, a new class of materials becomes accessible with unique multifunctional material properties, which may find applications in fuel cells, super capacitors, 3D batteries, advanced catalyst supports, energy absorption materials, multifunctional composites, chemical and biological sensors, etc.

Bryning and coworkers created CNT aerogels from wet CNT-surfactant gel precursors, and they showed that polyvinyl alcohol-reinforced CNT aerogels (typical CNT loadings range from 25 to 33 wt.%) are strong and electrically conductive ($\sim 10^{-2}$ S/cm).[9] Worsley and coworkers fabricated carbon- reinforced single-walled CNT (SWCNT) aerogels (SWCNT loading up to 55 wt.%) by pyrolysis of a dried gel mixture of SWCNTs, resorcinol, and formaldehyde at 1050 °C under nitrogen.[10-12] These carbon-reinforced SWCNT aerogels are mechanically robust and highly electrically conductive

(up to 1.12 S/cm) and show specific surface area up to 184 m^2/g, which are excellent fillers for high-performance polymer composites.[12] Worsley and coworkers were also able to use the similar approach to incorporate double-walled CNTs (DWCNTs) into a carbon aerogel, which was, however, limited in the amount of DWCNTs (up to 8 wt.%) that could be incorporated into the carbon aerogel framework and in its ability to achieve monolithic densities below 70 mg/cm^3.[13] Kwon and coworkers fabricated multi-walled CNT (MWCNT)-based aerogels with aligned porous structures using an ice-templating process.[14] These anisotropic MWCNT aerogels are electrically conductive (up to 1.9×10^{-2} S/cm) and have specific surface area up to 181 m^2/g. Very recently, Gui and coworkers synthesized highly porous CNT sponges containing large-diameter MWCNTs (30–50 nm) by a chemical vapor deposition method.[15] These MWCNT sponges display exceptional structural flexibility, excellent electrical conductivity (~1.7 S/cm), and good specific surface area (300–400 m^2/g). While this paper was in preparation, Zou and coworkers reported the synthesis of an ultralight MWCNT aerogel, which shows large specific surface area (580 m^2/g) and has an electrical conductivity of 3.2×10^{-2} S/cm that can be further increased to 0.67 S/cm by a high-current pulse method.[16]

In this article we report a new approach to the synthesis of stable CNT aerogels. Our method involves following two distinctive aspects: (1) 3D chemical assembly of CNTs in solution to form a stable gel using a chemical cross-linker such as ferrocene-grafted poly(p-phenyleneethynylene) (Fc-PPE, Figure 3.1),[17] followed by a CO_2 supercritical drying to create stable aerogels; (2) thermal annealing of these aerogels in air to significantly improve their electrical and mechanical properties and enhance their surface area and porosity. We have demonstrated the preparation of thermally annealed

CNT aerogels containing small-diameter CNTs such as SWCNTs and DWCNTs, which are mechanically stable and stiff, highly porous (~99%), and exhibit excellent electrical conductivity (~1–2 S/cm) and large specific surface area (~590–680 m^2/g).

3.2 Experimental

Two chemical cross-linkers (Fc-PPE and Fc-PPETE, Figure 3.1) were synthesized and characterized according to literature methods.[18,19] Purified $SWCNTs_{HiPco}$ and DWCNTs were purchased from Carbon Nanotechnologies Inc. and were used without further purification. Fc-PPE–CNT and Fc-PPETE–CNT gels were prepared in

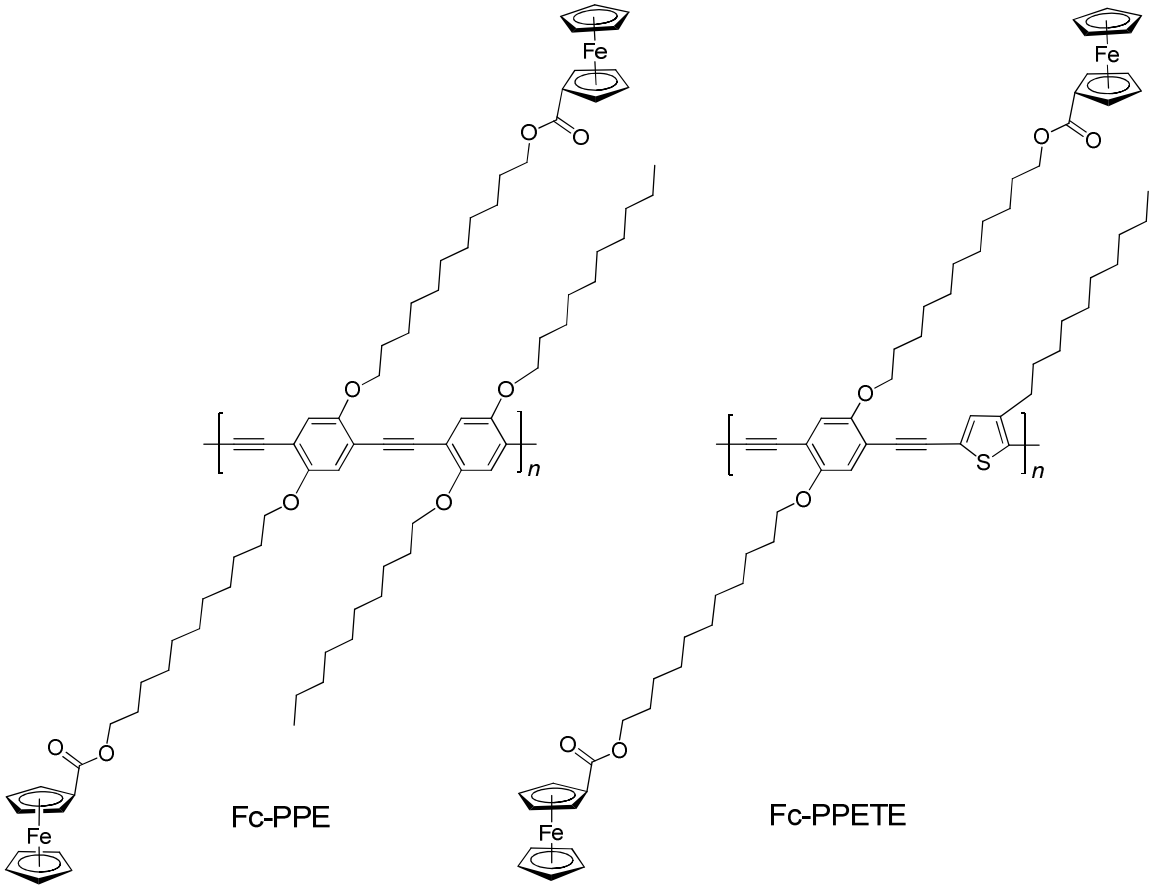

Figure 3.1. Chemical structures of two chemical cross-linkers used in this study: (1) ferrocene-grafted poly(pphenyleneethynylene) (Fc-PPE); (2) ferrocene-grafted poly[(p-phenyleneethynylene)-alt-(2,5-thienyleneethynylene)] (Fc- PPETE).

Table 3.1. Properties of CNT aerogels.

Sample no.[a]	CNT	CCL (wt.%)[b]	S_{BET} (m^2/g)	V_{meso} (cm^3/g)	D_{meso} (nm)	Porosity[c] (%)	σ[d] (S/cm)
$1_{as\text{-}prepared}$	SWCNT	Fc-PPE (20%)	327	0.88	11.2	99.4	Fragile[e]
$1_{annealed\ I}$	SWCNT		635	0.93	9.4		Fragile
$2_{as\text{-}prepared}$	DWCNT	Fc-PPETE (20%)	464	1.20	11.4	99.3	Fragile
$2_{annealed\ I}$	DWCNT		679	1.44	9.2		Fragile
$3_{as\text{-}prepared}$	SWCNT	Fc-PPE (33%)	176	0.49	13.8	98.6	1.81×10^{-1}
$3_{annealed\ I}$	SWCNT		507	0.63	9.2		1.96
$3_{annealed\ II}$	SWCNT		596	0.85	9.9		8.85×10^{-1}
$4_{as\text{-}prepared}$	DWCNT	Fc-PPE (33%)	237	0.76	14.4	99.1	2.91×10^{-1}
$4_{annealed\ II}$	DWCNT		684	1.22	8.6		1.78
$5_{as\text{-}prepared}$	DWCNT	Fc-PPETE (33%)	276	0.84	13.5	99.1	1.22×10^{-1}
$5_{annealed\ I}$	DWCNT		447	1.08	10.8		1.58
$5_{annealed\ II}$	DWCNT		587	1.32	10.4		1.10
$6_{as\text{-}prepared}$	SWCNT	Fc-PPE (50%)	145	0.50	17.3	98.9	3.37×10^{-2}
$7_{as\text{-}prepared}$	DWCNT	Fc-PPE (50%)	141	0.46	15.8	98.8	2.57×10^{-2}

[a] Annealed I samples: mass loss ~20–25 wt.% relative to as-prepared aerogels; annealed II samples: mass loss ~41–43 wt.% relative to as-prepared aerogels.
[b] CCL (wt.%): the chemical cross-linker and its loading.
[c] Porosity: calculated from the aerogel density, assuming a density of 1.1 g/cm^3 for SWCNT [39] and DWCNT [40] and 1.2 g/cm^3 for Fc-PPE and Fc-PPETE.
[d] Electrical conductivity.
[e] The sample is fragile and the conductivity cannot be measured reliably.

chlorobenzene according to our previous procedure.[17] The mass ratio of CNT:chemical crosslinker (CCL) was kept at 1, 2, and 4, respectively (Table 3.1). The freestanding monolithic gel was soaked in anhydrous ethanol for solvent exchange to remove the chlorobenzene. The resulting wet gel in ethanol was transferred to a Tousimis SAMDRI-PVT-3D critical point dryer. The ethanol in the wet gel was exchanged with liquid CO_2 several times to remove the ethanol. The CO_2 supercritical drying of the wet gel was carried out for 24 h above the critical temperature and pressure of CO_2 (31.1 °C, 1072 psi) and then the chamber pressure was slowly released overnight to obtain the aerogel. No significant sample shrinkage was observed after supercritical drying. The as-prepared CNT aerogels were annealed in air at 350 °C until the mass loss reached either ~20–25 wt.% (annealed I CNT aerogels) or ~41–43 wt.% (annealed II CNT aerogels) relative to the original mass of the as prepared CNT aerogel.

The surface and porosity data of CNT aerogel samples were calculated by Brunauer–Emmett–Teller (BET) and Barrett–Joyner–Halenda (BJH) methods based on N_2 adsorption–desorption isotherms at 77 K obtained using an ASAP 2020 surface area

and porosimetry analyzer (Micromeritics Instrument Corporation). Samples were heated at 100 °C under vacuum for at least 12 h to remove any potential adsorbed species such as air, water, or organic solvents prior to the measurement. For an accurate characterization of the microporous region, a separate measurement was performed at low relative pressure ($P/P_0 < 0.01$), and the micropore volume was calculated by t-plot theory. The two-point probe measurement for direct current electrical conductivity study was performed using a Keithley 2400 source meter instrument through the computer controlled LabVIEW program. Electrical contacts to aerogel samples were made with silver paste. The Lucas Laboratories Pro4 system was used for the four-point probe measurement to verify the two-point probe measurement. Scanning electron microscopy (SEM) was performed using a Hitachi S-4800 field emission scanning electron microscope (accelerating voltage: 3 kV). SEM samples were imaged without coating to avoid potential metal coating artifacts. Energy-dispersive X-ray spectroscopy (EDS) was performed with the same SEM instrument and was calibrated with ferrocenecarboxylic acid. Transmission electron microscopy (TEM) was performed using a Hitachi H 9000 NAR transmission electron microscope (operated at 300 kV). Attenuated total reflectance-Fourier transform infrared (ATR-FTIR) measurements were obtained on a Nexus 670 FTIR spectrometer with a Smart OMNI-Sampler accessory containing a Germanium crystal.

3.3 Results and Discussion

3.3.1 CNT Organogels

Stable CNT gels are critical precursors to stable, highly porous, 3D interconnected CNT aerogels.[14,17,20–29] Pristine SWCNTs and DWCNTs are not soluble in

most solvents and do not form stable, freestanding monolithic gels because of weak physical interactions among CNTs.

We recently developed a versatile and nondamaging chemistry platform that enabled us to engineer specific CNT surface properties, while preserving CNT's intrinsic properties. We discovered that rigid conjugated macromolecules such as PPEs could be used to noncovalently functionalize and solubilize CNTs, and disperse CNTs homogeneously in polymer matrices.[17,30–38] In an organogel, gelling agents (gelators) form a fibrous 3D network whose interstitial spaces solvents to form a freestanding organogel that cannot be redispersed in any organic solvents, indicating the robustness of a 3D nanotube network.[17] When the concentration of the Fc-PPE–SWCNT is sufficiently high, the ferrocenyl groups act as "anchoring" units to cross-link SWCNTs and enable the formation of the 3D nanotube network, which, in turn, gelates the organic solvent. It appears that the strong, yet noncovalent interaction between the ferrocenyl group and the neighboring nanotube surface allows the concerted cross-linking among SWCNTs during the formation of the 3D nanotube network, therefore avoiding the nanotube precipitation from solution, which is a common and highly undesirable competing process in chemical cross-linking of nanotubes in solution.

In this study, we used this gelation method to prepare a series of SWCNT and DWCNT organogels, which allowed us to investigate effects of different CCLs (Fc-PPE vs. Fc-PPETE, Figure 3.1) and different mass ratios of CNT:CCL on the stability of CNT organogels and corresponding aerogels. We found that the Fc-PPE could solubilize CNTs better than the Fc-PPETE at the same nanotube concentration. As a result, Fc-PPE–CNT organogels are more robust than Fc-PPETE–CNT organogels. We observed a strong

correlation in mechanical stability between the CNT organogels and corresponding CNT aerogels. Fc-PPE–CNT aerogels consistently show better mechanical stability than corresponding Fc-PPETE–CNT aerogels.

The mass ratio of CNT:CCL has even more dramatic effects on the mechanical stability of CNT organogels and corresponding CNT aerogels and surface area and porosity of as-prepared CNT aerogels. Pristine CNTs (0 wt.% of CCL) do not form freestanding organogels. When the mass ratio is 4 (20 wt.% of CCL), CCL–CNT organogels are quite fragile. As the mass ratio decreases to 2 (33 wt.% of CCL), CCL–CNT organogels become mechanically stable. As the mass ratio further decreases to 1 (50 wt.% of CCL), CCL–CNT organogels become mechanically robust. Similarly, mechanical properties of corresponding CNT aerogels increases as the mass ratio of CNT:CCL decreases.

3.3.2 As-Prepared CNT Aerogels

The CO_2 supercritical drying of CNT organogels prevents the 3D nanotube network from significant shrinkage and leads to low-density (7–16 mg/cm^3), highly porous (~99%), monolithic CNT aerogels (Table 3.1). SEM confirms the highly porous 3D nanotube network in CNT aerogels (Figure 3.2). As-prepared CNT aerogels are quite conductive considering the extremely low density: ~0.1–0.3 S/cm for CNT aerogels with 33 wt.% of CCL and ~0.03 S/cm for CNT aerogels with 50 wt.% of CCL (Table 3.1). The electrical conductivity of CNT aerogels decreases with the increase of the semiconducting CCL.

The specific surface area (S_{BET}) of an as-prepared CNT aerogel increases with the decrease of CCL loading (Table 3.1): ~140 m^2/g for SWCNT and DWCNT aerogels with

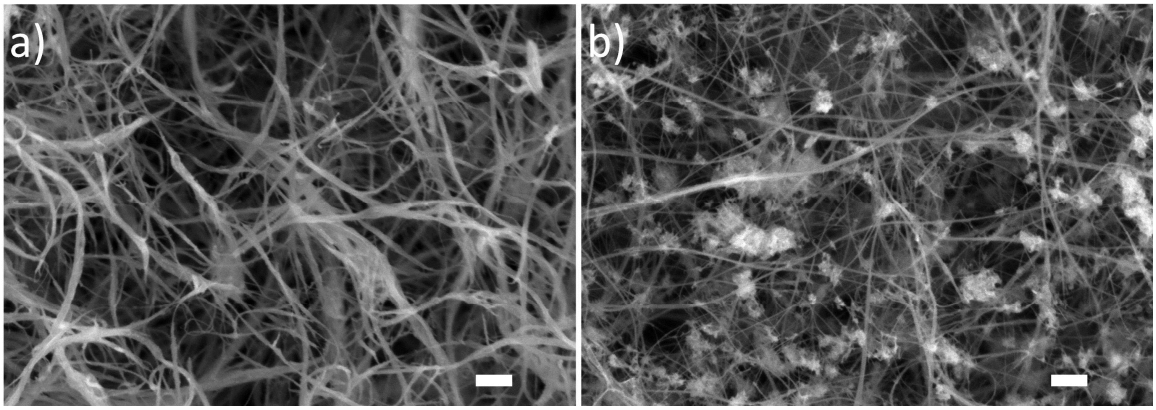

Figure 3.2. SEM images of (a) the $\mathbf{3}_{\text{as-prepared}}$ SWCNT aerogel and (b) $\mathbf{4}_{\text{as-prepared}}$ DWCNT aerogel. Scale bar: 200 nm.

50 wt.% of CCL; ~180 m^2/g for SWCNT aerogels and ~240–280 m^2/g for DWCNT aerogels with 33 wt.% of CCL; ~330 m^2/g for SWCNT aerogels and ~460 m^2/g for DWCNT aerogels with 20 wt.% of CCL. Similarly, Worsley and coworkers reported that carbon reinforced SWCNT aerogels (SWCNT loading up to 55 wt.%) exhibited specific surface area up to 184 m^2/g.[10–12] According to IUPAC, micropores are pores with diameters less than 2 nm, mesopores have diameters between 2 and 50 nm, and macropores have diameters greater than 50 nm. The N_2 adsorption and desorption isotherms of as-prepared CNT aerogels at 77 K are shown in Figure 3.3a and b. The hysteresis, suggesting pore structures are predominated by mesopores. A steep isotherms of as-prepared CNT aerogels resemble type IV IUPAC isotherms with a small increase in N_2 adsorption at low relative pressure ($P/P_0 < 0.01$) is characteristic of the presence of micropores. As shown in Figure 3.3a and b, both micropore and mesopore volumes significantly decrease with the increase of CCL. Figure 3.3c and d show the pore size distribution in as-prepared CNT aerogels. When the CCL increases from 20% to 33% and 50%, small mesopores (2–3 nm in SWCNT aerogels; 2–4 nm in DWCNT aerogels)

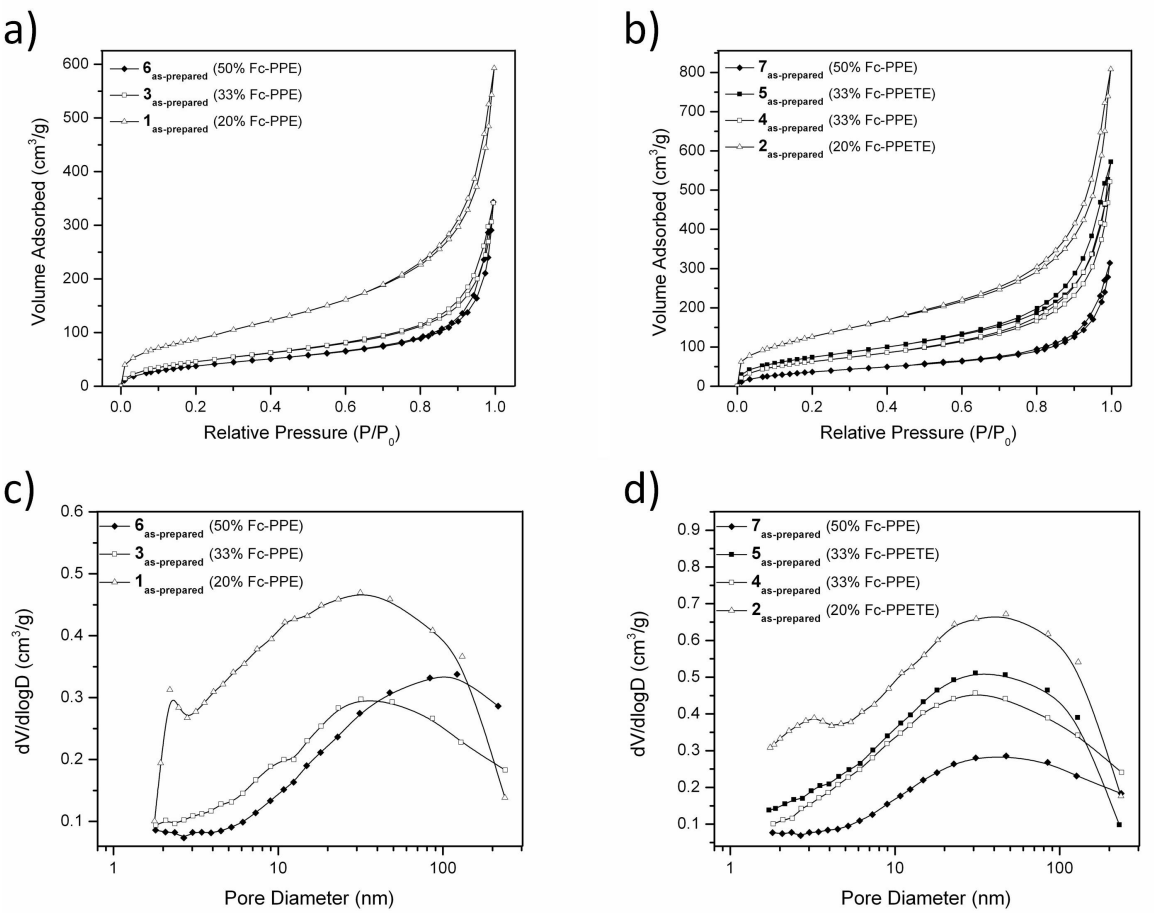

Figure 3.3. N_2 adsorption and desorption isotherms of (a) as-prepared SWCNT aerogels and (b) as-prepared DWCNT aerogels. Pore size distributions of (c) as-prepared SWCNT aerogels and (d) as-prepared DWCNT aerogels.

significantly diminish in as-prepared CNT aerogels (Figure 3.3c and d), which also leads to the increase of average mesopore size (D_{meso}) of as-prepared CNT aerogels with the increase of CCL (Table 3.1). The collective information from Figure 3.3 clearly indicates that, as the CCL increases, both micropores and small mesopores are blocked, hence considerably reducing the S_{BET} of as-prepared CNT aerogels.

Table 3.1 also reveals another clear but somewhat unexpected trend: a DWCNT aerogel consistently outperforms the corresponding SWCNT aerogel with the same type of CCL and loading in S_{BET} and V_{meso} (mesopore volume) when the CCL loading is at

either 33 wt.% or 20 wt.%. The theoretical specific surface area of an individual SWCNT is generally much larger than an individual DWCNT.[41] According to SEM of CNT aerogels (Figure 3.2) and TEM of as-received, purified CNTs (Figure 3.4), however, $SWCNTs_{HiPco}$ form much larger bundles than DWCNTs. Theoretical calculation shows that the external specific surface area decreases dramatically with the increase of the CNT bundle size.[41,42] Therefore the much smaller bundle sizes of DWCNTs are probably responsible for their superior surface area and porosity observed in this study.

Both SWCNT and DWCNT materials contain some impurities. According to calibrated EDS, the SWCNT material has ~9.5 wt.% (2.2 at.%) of Fe and the DWCNT material has ~0.2 wt.% (<0.1 at.%) of Fe. Bright-field TEM shows the major impurity in $SWCNTs_{HiPco}$ to be iron-rich nanoparticles that produce dark contrast with white Fresnel fringe at their rim (Figure 3.4c), while the main impurity in the DWCNT material is hollow, graphitic carbon nanoparticles (Figure 3.4f). Both impurities have a negative impact on the S_{BET} of CNT aerogels because such nanoparticle impurities have higher densities and lower specific surface areas than SWCNTs and DWCNTs.

It is worth mentioning that the nitrogen adsorption–desorption analysis mainly measures micropores and mesopores, therefore the large macropores observed in SEM (Figure 3.2) can not be experimentally evaluated using this analytical approach.[43] Although CNT aerogels with 20 wt.% of CCL demonstrate the best S_{BET} and V_{meso} among as-prepared CNT aerogels (Table 3.1), their mechanical weakness makes them less attractive materials. Conversely, CNT aerogels with 50 wt.% of CCL display the best mechanical robustness, but have low specific surface areas. Hence as-prepared CNT aerogels with 33 wt.% of CCLs are the focus of further investigations in this study.

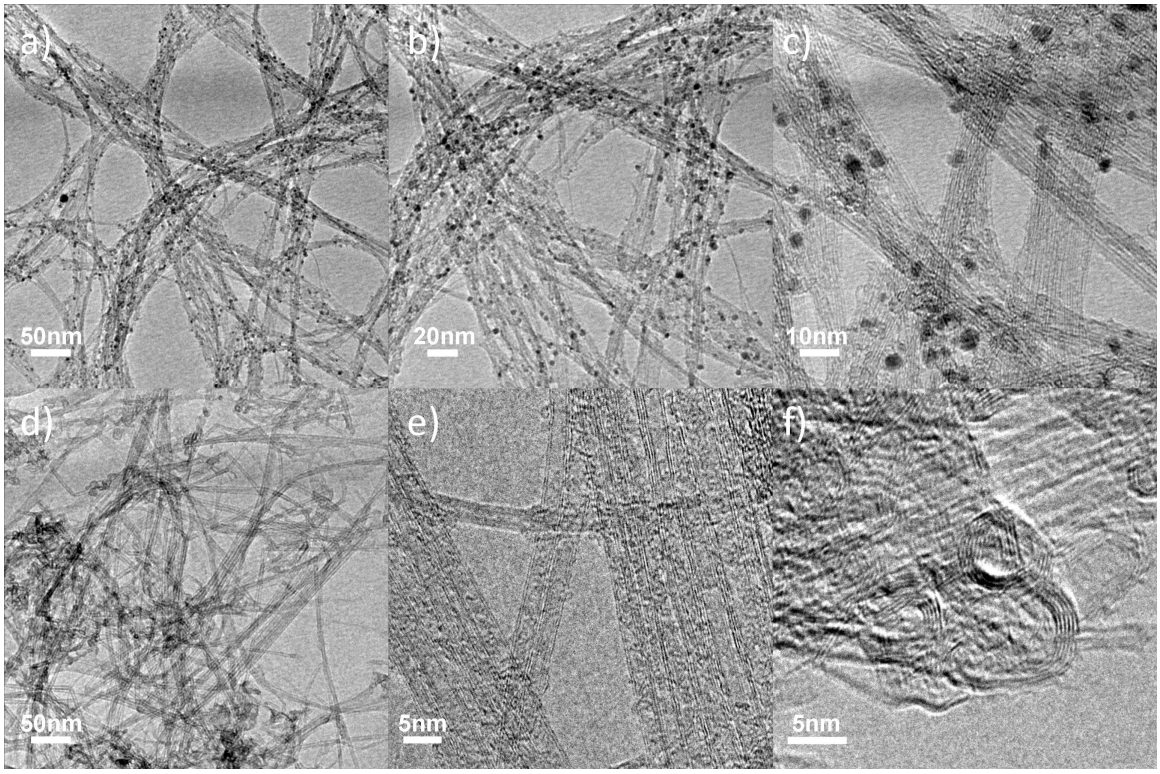

Figure 3.4. TEM images of (a–c) $SWCNTs_{HiPco}$ and iron nanoparticles, and (d–f) DWCNTs and graphitic carbon nanoparticles.

3.3.3 Thermally Annealed CNT Aerogels

While the CCL is crucial to form stable CNT organogels and aerogels, we found that it could substantially block micropores (<2 nm) and small mesopores (2–4 nm) and reduce the specific surface area and mesopore volume of CNT aerogels. To solve this dilemma, we developed a simple yet effective post annealing approach, which can significantly enhance the electrical and mechanical properties and enhance the surface area and porosity of CNT aerogels. Thermal annealing is particularly effective for CNT aerogels because aerogels have 3D interconnected porous networks, which ensure a uniform heat treatment.

Thermal decomposition of dialkoxy-PPEs in air involves two steps: a rapid cleavage of polymer side chains starting at 220 °C followed by a slow decomposition of

conjugated polymer backbones.[44,45] As shown in Figures 3.5 and 3.6, as prepared CNT aerogels with 33% of Fc-PPE could undergo uniform and stepwise annealing in air at 350 °C, which is below the decomposition temperatures of purified SWCNTs and DWCNTs,[46,47] to generate annealed I and II CNT aerogels with either reduced or similar density, respectively. The average mass-loss rate of as-prepared CNT aerogels with 33% of Fc-PPE in the annealing I step is relatively fast and insensitive to CNT materials: ~1.2 wt.% loss/min for the $\mathbf{3}_{\text{as-prepared}}$ SWCNT aerogel and ~1.4 wt.% loss/min for the $\mathbf{4}_{\text{as-prepared}}$ DWCNT aerogel. As-prepared CNT aerogels with 33% of Fc- PPE have ~28 wt.% of polymer side chains. These data suggest that the removal of polymer side chains predominates in the annealing I step with typical 20–25 wt.% loss. The average mass-loss rate of annealed I CNT aerogels in the annealing II step is much slower: ~0.3 wt.%

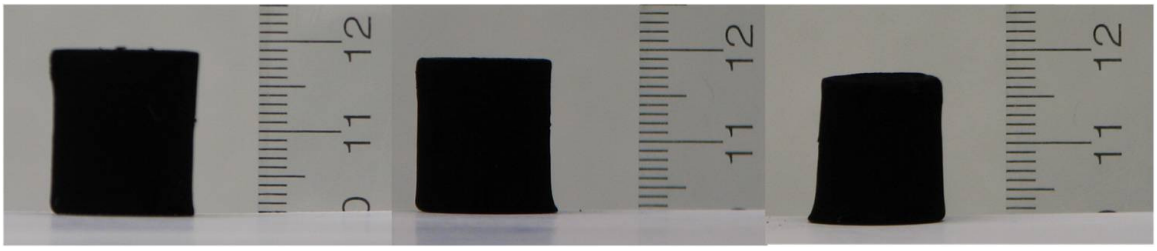

Figure 3.5. Stepwise annealing of a $\mathbf{3}_{\text{as-prepared}}$ SWCNT aerogel with 33 wt.% of Fc-PPE (left, mass: 29.6 mg; density: 9.9 mg/cm^3) in air at 350 °C, which led to the $\mathbf{3}_{\text{annealed I}}$ aerogel (middle, mass: 22.8 mg; density: 9.3 mg/cm^3) and $\mathbf{3}_{\text{annealed II}}$ aerogel (right, mass: 17.4 mg; density: 9.8 mg/cm^3), sequentially.

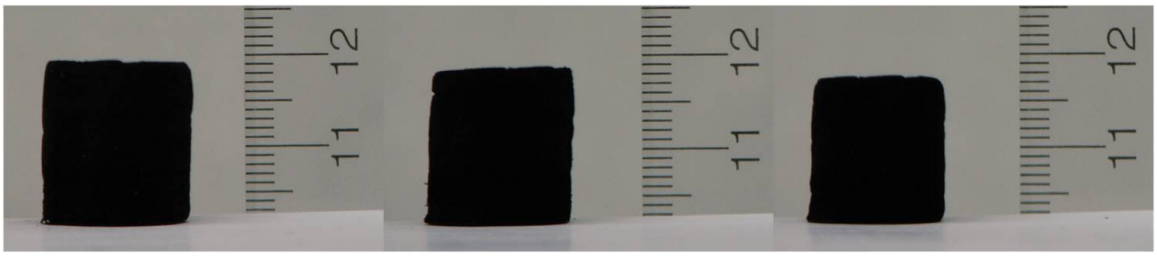

Figure 3.6. Stepwise annealing of a $\mathbf{4}_{\text{as-prepared}}$ DWCNT aerogel with 33 wt.% of Fc-PPE (left, mass: 29.3 mg; density: 9.8 mg/cm^3) in air at 350 °C, which led to the $\mathbf{4}_{\text{annealed I}}$ aerogel (middle, mass: 21.9 mg; density: 8.9 mg/cm^3) and $\mathbf{4}_{\text{annealed II}}$ aerogel (right, mass: 17.3 mg; density: 8.0 mg/cm^3), sequentially.

loss/min for the **3**$_{\textbf{annealed I}}$ SWCNT aerogel and ~0.2 wt.% loss/min for the **4**$_{\textbf{annealed II}}$ DWCNT aerogel. This suggests that the decomposition of polymer backbones, carbon impurities associated with CNTs, and defective CNTs probably predominates in the annealing II stage.

The FTIR spectroscopy has proven to be an important tool to investigate the interaction between CNTs and molecules/ macromolecules. We found previously that the infrared vibrations of adsorbed molecules/macromolecules that give rise to dipole changes parallel to the highly polarizable CNT surface are diminished significantly in intensity.[34] The CNT surface attenuated infrared absorption (CNT SAIRA) therefore provides a mechanism to probe and compare the overall surface qualities of various bulk CNT materials as well as the interaction strength between CNTs and molecules/macromolecules.[34,48] The IR spectrum of pure Fc-PPE shows a number of characteristic vibration modes (Figure 3.7): (1) $\nu_{as}(CH_2)$ (2922 cm^{-1}) from polymer side chains; (2) ν(C=O) (1713 cm^{-1}), side chains; (3) ν_{as}(COC) (1275 and 1213 cm^{-1}), side chains; (4) ν(cyclopentadienyl ring (Cp ring)) (1136 cm^{-1}), side chains; (5) $\delta_s(CH_2)$ (1463 cm^{-1}), side chains; (6) $\delta_s(CH_3)$ (1388 cm^{-1}), side chains; (7) ν(C=C) (1514 and 1429 cm^{-1}), backbones. As compared to pure PPE, most of IR absorptions arising from Fc-PPE in the **3**$_{\textbf{as-prepared}}$ SWCNT aerogel diminish significantly in intensity (Figure 3.7a), thanks to the CNT SAIRA.[34] Since the $\nu_{as}(CH_2)$ mode causes primarily a dipole change perpendicular to the CNT surface, its IR intensity is expected to remain unchanged. In contrast, the ν(C=C), $\delta_s(CH_2)$, $\delta_s(CH_3)$, and ν_{as}(COC) modes all give rise to net dipole changes parallel to the CNT surface and, therefore, their IR intensities are reduced dramatically. Most importantly, the relatively sharp ν(C=O) and ν(Cp ring) modes, which

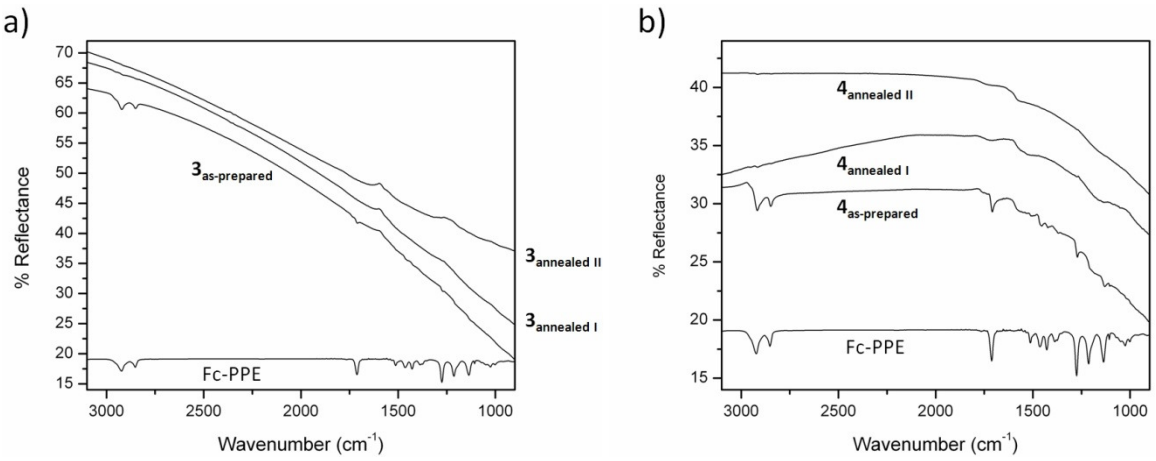

Figure 3.7. ATR-FTIR spectra of pure Fc-PPE and (a) $\mathbf{3}_{\mathbf{as\text{-}prepared}}$ SWCNT aerogel and (b) $\mathbf{4}_{\mathbf{as\text{-}prepared}}$ DWCNT aerogel before and after thermal annealings. The spectra of pure Fc-PPE and as-prepared CNT aerogel were normalized at the 2922 cm^{-1} peak and were offset vertically for better visual comparison in each series, respectively.

are associated with ferrocenyl groups at the end of polymer side chains (Figure 3.1), also diminish significantly. This indicates a substantial interaction between ferrocenyl groups and neighboring SWCNT surfaces in the $\mathbf{3}_{\mathbf{as\text{-}prepared}}$ SWCNT aerogel.

The CNT SAIRA is highly sensitive to the distance between adsorbed molecules/macromolecules and the CNT surface as well as the degree of nanotube conjugation and surface cleanliness.[34] Unlike $SWCNTs_{HiPco}$, as-received, purified DWCNTs have detectable amount of carbonyl groups based on previous study.[34] These carbonyl groups could be covalently attached to CNT surfaces, or could arise from residual carbon impurities (e.g. oxidized amorphous carbon after purification) that are noncovalently adsorbed on CNT surfaces.[34] The existence of these carbonyl groups, which show a very broad IR absorption in the region of 1800–1650 cm^{-1},[34] on DWCNT surfaces can considerably interfere with the p–p interaction between Fc-PPE and the nanotube surface and, as a result, increase their distance of separation. Therefore DWCNTs could only partially reduce IR intensities of adsorbed Fc-PPE in the $\mathbf{4}_{\mathbf{as\text{-}prepared}}$

DWCNT aerogel between 1800 and 1000 cm^{-1} (Figure 3.7b). The substantial intensity of the relatively sharp ν(C=O) and ν(Cp ring) modes, which are associated with ferrocenyl groups (Figure 3.7b), suggests the interaction between ferrocenyl groups and neighboring DWCNT surfaces is weaker in the $\mathbf{4}_{\mathbf{as\text{-}prepared}}$ DWCNT aerogel than that in the $\mathbf{3}_{\mathbf{as\text{-}prepared}}$ SWCNT aerogel (Figure 3.7a). There is little free Fc-PPE in the $\mathbf{4}_{\mathbf{as\text{-}prepared}}$ DWCNT aerogel because the Fc-PPE is only 33 wt.%, which is far less than the experimental saturation loading (~50 wt.% of Fc-PPE).Hence it is unlikely that IR signals observed in the region of 1800–1000 cm^{-1} in the $\mathbf{4}_{\mathbf{as\text{-}prepared}}$ DWCNT aerogel arise primarily from free Fc-PPEs.

After the thermal annealing I, the $\nu_{as}(CH_2)$ mode, which is associated with polymer side chains and not affected by the CNT SAIRA effect, disappears as expected. This lends further support to the notion that the removal of polymer side chains predominates in the annealing I step. The interpretation of the change in the region of 1800–1000 cm^{-1} is complicated by the CNT SAIRA effect. We do notice, however, that all sharp IR signals below 1800 cm^{-1} in the DWCNT aerogel either disappear and/or convert to new broad features, which are not due to DWCNTs, after the thermal annealing I (Figure 3.7b). These new broad features disappear after the thermal annealing II. The IR spectra of CNT aerogels after the thermal annealing II are essentially identical to those of as-received, purified SWCNTs and DWCNTs, respectively.

Figure 3.8 shows that thermal annealing has a dramatic impact on pore structures of CNT aerogels. As shown in Figure 3.8a and b, thermal annealing substantially increases the micropore volume at low relative pressure ($P/P_0 < 0.01$) in CNT aerogels, particularly in the thermal annealing I phase, which is predominated by the removal of

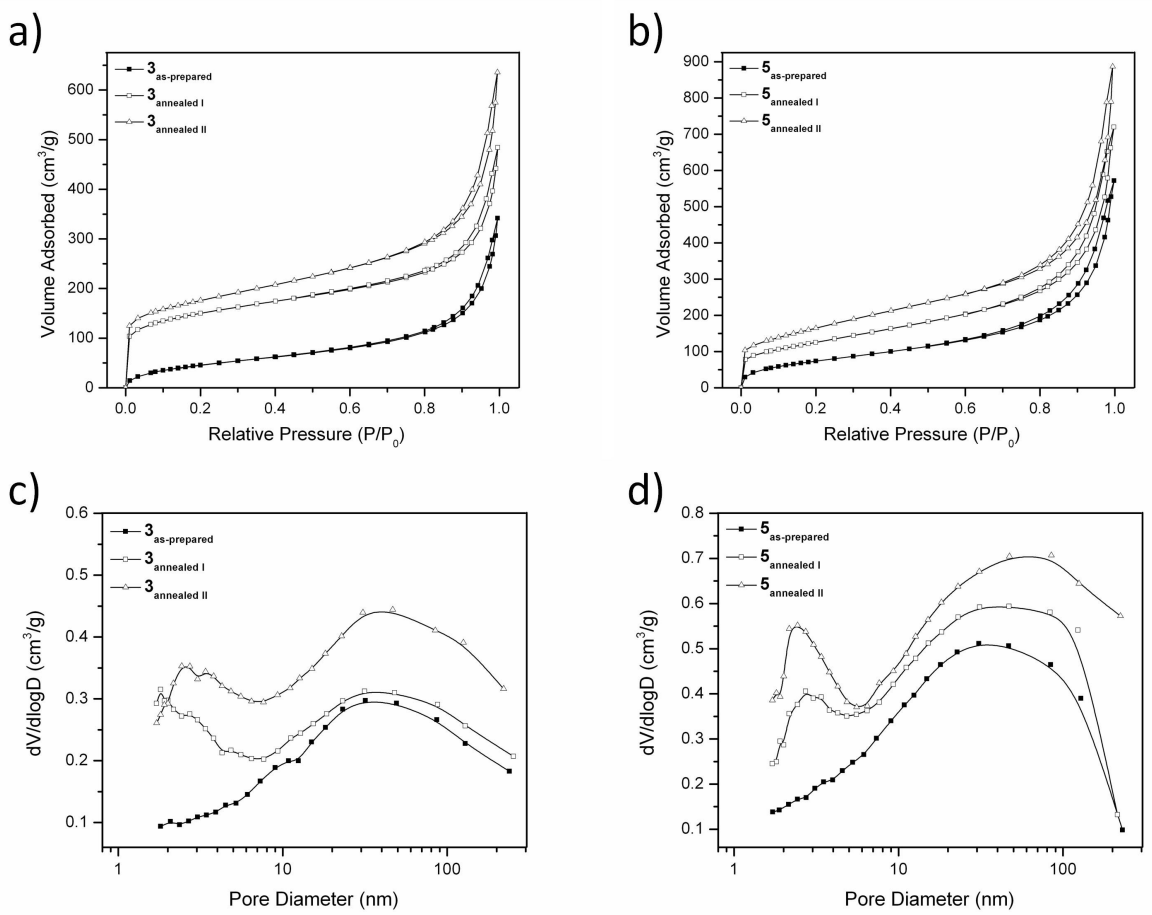

Figure 3.8. N_2 adsorption and desorption isotherms of (a) as-prepared SWCNT aerogels and (b) as-prepared DWCNT aerogels before and after thermal annealings. Pore size distributions of (c) as prepared SWCNT aerogels and (d) as-prepared DWCNT aerogels before and after thermal annealings.

polymer side chains. The data in Figure 3.8a and b as well as Figure 3.3a and b indicate clearly that polymer side chains of CCL block most micropores and thermal annealing re-opens these blocked micropores by removing polymer side chains. The micropore volumes for $\mathbf{3}_{\mathbf{annealed\ II}}$ SWCNT aerogel and $\mathbf{4}_{\mathbf{annealed\ II}}$ DWCNT aerogel are 0.17 and 0.12 cm^3/g, respectively. Although thermal annealing significantly increases the micropore volumes, the pore structures in annealed aerogel samples are still predominated by mesopores.

Thermal annealing's effects on mesopore sizes of CNT aerogels are also

significant and, again, most dramatic changes occur in the thermal annealing I phase (Figure 3.8c and d). After the annealing I in air at 350 °C, small mesopores (2–3 nm in SWCNT aerogels; 2–4 nm in DWCNT aerogels) reappear, thanks to the removal of polymer side chains. Upon further heat treatment in the annealing II, the peak pore size of small mesopores become larger in SWCNT aerogels (from 1.8 to 2.5 nm) but smaller in DWCNT aerogels (from 2.7 to 2.4 nm). The origin of such difference is not fully understood at present.

Figure 3.8 reveals that thermal annealing in air is a simple yet effective method for re-opening the originally blocked micropores and small mesopores in as-prepared CNT aerogels. As a result, specific surface areas of annealed CNT aerogels increase dramatically by ~50–240% (Table 3.1).

Despite losing ~41–43 wt.% of the original mass, the light density, annealed II SWCNT and DWCNT aerogels could still support the same amount of weight as corresponding as- prepared aerogels do without deformation. This corresponds to ~1150 times the annealed II SWCNT aerogel's weight and ~870 times the annealed II DWCNT aerogel's weight, respectively (Figures 3.9 and 3.10). The thermal annealing also

Figure 3.9. A $\mathbf{3}_{\text{annealed II}}$ SWCNT aerogel (left, 17.4 mg, density: 9.8 mg/cm^3); the same sample supporting a 20 g weight (middle, ~1150 times its own weight); the same sample after removal of the weight (right).

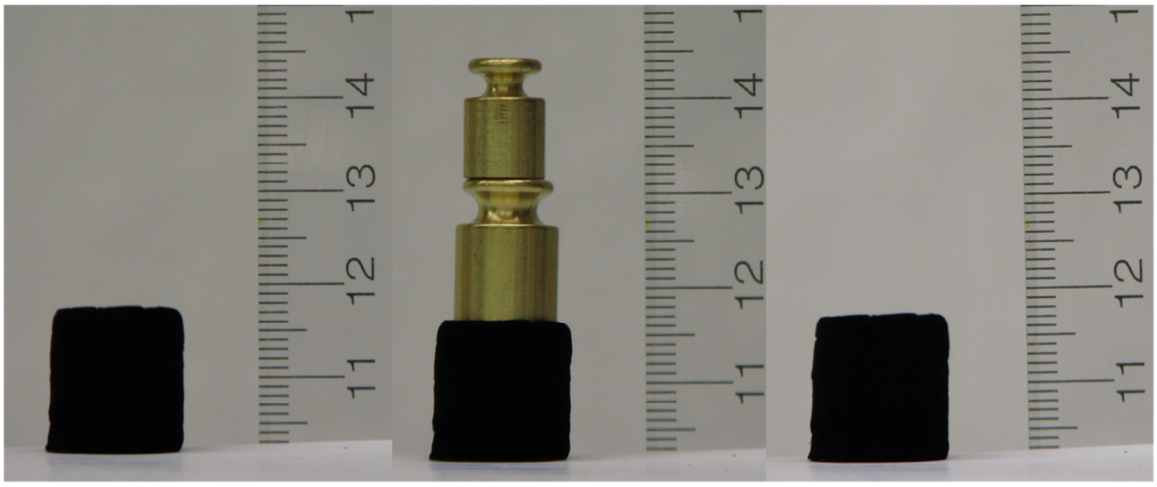

Figure 3.10. A $\mathbf{4}_{\text{annealed II}}$ aerogel (left, 17.3 mg, density: 8.0 mg/cm^3); the same sample supporting 15 g of total weights (middle, ~870 times its own weight); the same sample after removal of weights (right).

substantially increases the electrical conductivity of CNT aerogels by a factor of 6–13 (Table 3.1). The two-probe measurement results have been confirmed by the four-probe measurement. For example, the two-point probe/four-point probe conductivities of the $\mathbf{4}_{\text{annealed II}}$ DWCNT aerogel are 1.78/1.84 S/cm. These combined observations strongly suggest the annealing induced reinforcement of CNT–CNT junctions in CNT aerogels, which will be a subject of future study.

3.4 Conclusion

We have developed a new approach to the synthesis of stable CNT aerogels. The approach involves three steps: (1) 3D chemical assembly of CNTs in solution to form a stable gel using a chemical cross-linker; (2) CO_2 supercritical drying of CNT gels to create stable aerogels; (3) thermal annealing of these aerogels in air to significantly enhance their electrical and mechanical properties, and enhance their surface area and porosity. We have demonstrated the preparation of thermally annealed CNT aerogels containing small-diameter CNTs such as SWCNTs and DWCNTs, which are

mechanically stable and stiff, highly porous (~99%), and exhibit excellent electrical conductivity (~1–2 S/cm) and large specific surface area (~590– 680 m^2/g). We have found that thermal annealing in air is a simple yet effective method for re-opening the originally blocked micropores and small mesopores in the as-prepared CNT aerogels.

3.5 References

(1) Gesser, H. D.; Goswami, P. C. *Chem. Rev.* **1989**, 89, 765–788.
(2) Hüsing, N; Schubert, U. *Angew. Chem. Int. Ed.* **1998**, 37, 23–45.
(3) Pierre, A. C.; Pajonk, G. M. *Chem. Rev.* **2002**, 102, 4243–4265.
(4) Rolison, D. R. *Science* **2003**, 299, 1698–1701.
(5) Long, J. W.; Rolison, D. R. *Acc. Chem. Res.* **2007**, 40, 854–862.
(6) Long, J. W.; Dunn, B.; Rolison, D.R.; White, H. S. *Chem. Rev.* **2004**, 104, 4463–4492.
(7) Aerogels 7. In: Rolison, D. R., editor. *J. Non-Cryst. Solids* **2004**, 350, 1–404.
(8) Rolison, D. R.; Dunn, B. *J. Mater. Chem.* **2001**, 11, 963–980.
(9) Bryning, M. B.; Milkie, D. E.; Islam, M. F.; Hough, L. A.; Kikkawa, J. M.; Yodh, A. G. *Adv. Mater.* **2007**, 19, 661–664.
(10) Worsley, M. A.; Kucheyev, S. O.; Satcher, J. H.; Hamza, A. V.; Baumann, T. F. *Appl. Phys. Lett.* **2009**, 94, 073115.
(11) Worsley, M. A.; Pauzauskie, P. J.; Kucheyev, S. O.; Zaug, J. M.; Hamza, A. V.; Satcher, J. H.; et al. *Acta. Mater.* **2009**, 57, 5131–5136.
(12) Worsley, M. A.; Kucheyev, S. O.; Kuntz, J. D.; Hamza, A. V.; Satcher, J. H.; Baumann, T. F. *J. Mater. Chem.* **2009**, 19, 3370–3372.
(13) Worsley, M. A.; Satcher, J. H.; Baumann, T. F. *Langmuir* **2008**, 24, 9763–9766.
(14) Kwon, S. M.; Kim, H. S.; Jin, H. J. *Polymer* **2009**, 50, 2786–2792.
(15) Gui, X.; Wei, J.; Wang, K.; Cao, A.; Zhu, H.; Jia, Y.; et al. *Adv. Mater.* **2010**, 22, 617–621.
(16) Zou, J.; Liu, J.; Karakoti, A. S.; Kumar, A.; Joung, D.; Li, Q.; et al. *ACS Nano* **2010**, 4, 7293–7302.
(17) Chen, J.; Xue, C.; Ramasubramaniam, R.; Liu, H. Y. *Carbon* **2006**, 44, 2142–2146.
(18) Xue, C.; Chen, Z.; Wen, Y.; Luo, F. T.; Chen, J.; Liu, H. Y. *Langmuir* **2005**, 21, 7860–7865.
(19) Pang, Y.; Li, J.; Barton, T. J. *J. Mater. Chem.* **1998**, 8, 1687–1690.
(20) Fukushima, T.; Kosaka, A.; Ishimura, Y.; Yamamoto, T.; Takigawa, T.; Ishii, N.; et al. *Science* **2003**, 300, 2072–2074.
(21) Kovtyukhova, N. I.; Mallouk, T. E.; Pan, L.; Dickey, E. C. *J. Am. Chem. Soc.* **2003**, 125, 9761–9769.
(22) Hough, L. A.; Islam, M. F.; Janmey, P. A.; Yodh, A. G. *Phys. Rev. Lett.* **2004**, 93, 168102.
(23) Sabba, Y.; Thomas, E. L. *Macromolecules* **2004**, 37, 4815–4820.

(24) Wang, Z.; Chen, Y. *Macromolecules* **2007**, 40, 3402–3407.
(25) Srinivasan, S.; Babu, S. S.; Praveen, V. K.; Ajayaghosh, A. *Angew. Chem. Int. Ed.* **2008**, 47, 5746–5749.
(26) Klink, M.; Ritter, H. *Macromol. Rapid Commun* .**2008**, 29, 1208–1211.
(27) Moniruzzaman, M.; Sahin, A.; Winey, K. I. *Carbon* **2009**, 47, 645–650.
(28) You, Y. Z.; Yan, J. J.; Yu, Z. Q.; Cui, M. M.; Hong, C. Y.; Qu, B. J. *J. Mater. Chem.* **2009**, 19, 7656–7660.
(29) Oh, H.; Jung, B. M.; Lee, H. P.; Chang, J. Y. *J. Colloid Interface Sci.* **2010**, 352, 121–127.
(30) Chen, J.; Liu, H.; Weimer, W. A.; Halls, M. D.; Waldeck, D. H.; Walker, G. C. *J. Am. Chem. Soc.* **2002**, 124, 9034–9035.
(31) Ramasubramaniam, R.; Chen, J.; Liu, H. *Appl. Phys. Lett.* **2003**, 83, 2928–2930.
(32) Chen, J.; Ramasubramaniam, R.; Xue, C.; Liu, H. *Adv. Funct. Mater.* **2006**, 16, 114–119.
(33) Sankapal, B.; Setyowati, K.; Chen, J.; Liu, H. *Appl. Phys. Lett.* **2007**, 91, 173103.
(34) Setyowati, K.; Piao, M. J.; Chen, J.; Liu, H. *Appl. Phys. Lett.* **2008**, 92, 043105.
(35) Pradhan, B.; Setyowati, K.; Liu, H.; Waldeck, D. H.; Chen, J. *Nano. Lett.* **2008**, 8, 1142–1146.
(36) Yang, L.; Setyowati, K.; Li, A.; Gong, S.; Chen, J. *Adv. Mater.* **2008**, 20, 2271–2275.
(37) Pradhan, B.; Kohlmeyer, R. R.; Setyowati, K.; Chen, J. *Appl. Phys. Lett.* **2008**, 93, 223102.
(38) Pradhan, B.; Kohlmeyer, R. R.; Setyowati, K.; Owen, H. A.; Chen, J. *Carbon* **2009**, 47, 1686–1692.
(39) Arnold, M.; Green, A.; Hulvat, J.; Stupp, S.; Hersam, M. *Nature Nanotech.* **2006**, 1, 60–65.
(40) Green, A.; Hersam, M. *Nature Nanotech.* **2009**, 4, 64–70.
(41) Peigney, A.; Laurent, Ch.; Flahaut, E.; Bacsa, R. R.; Rousset, A. *Carbon* **2001**, 39, 507–514.
(42) Williams, K. A.; Eklund, P. C. *Chem. Phys. Lett.* **2000**, 320, 352–358.
(43) Zhang, X.; Chang, D.; Liu, J.; Luo, Y. *J. Mater. Chem.* **2010**, 20, 5080–5085.
(44) Moroni, M.; Le Moigne, J.; Luzzati, S. *Macromolecules* **1994**, 27, 562–571.
(45) Bunz, U. H. F. *Chem. Rev.* **2000**, 100, 1605–1644.
(46) Chiang, I. W.; Brinson, B. E.; Huang, A. Y.; Willis, P. A.; Bronikowski, M. J.; Margrave, J. L.; et al. *J. Phys. Chem. B* **2001**, 105, 8297–8301.
(47) Muramatsu, H.; Hayashi, T.; Kim, Y. A.; Shimamoto, D.; Kim, Y. J.; Tantrakarn, K.; et al. *Chem. Phys. Lett.* **2005**, 414, 444–448.
(48) Kamarás, K.; Botka, B.; Pekker, .Á; Ben-Valid, S.; Zeng, A.; Reiss, L.; et al. *Phys. Status Solidi B* **2009**, 246, 2737–2739.

Chapter 4: Remote, Local, and Chemical Programming of Healable Multishape Memory Polymer Nanocomposites

4.1 Introduction

Traditional shape memory polymers (SMP) are materials that can memorize one or two temporary shapes (dual- or triple-shape memory effect) and are able to return to their permanent shape upon exposure to an external stimulus such as heat, light, or magnetic field.[1–6] Multishape memory effect, i.e., memorizing three or more temporary shapes in one cycle, is extremely rare because of enormous difficulty in synthesizing a SMP with more than two discrete reversible shape memory transitions.[7] Recent discovery of the tunable multishape memory effect in a single component polymer with a broad thermal transition such as Nafion opens the door to new designs and applications of SMPs.[7] Any multishape memory polymer (MSMP) based on the single broad glass transition platform, however, presents new challenges in thermal programming of the multishape memory effect because of increased thermal vulnerability of any temporary shape. This ultimately limits the complexity and number of shapes a MSMP could reliably memorize in the long term. Here we show that the combination of remote, local, and chemical programming of the multishape memory effects offers unparalleled shape and function control in carbon nanotube (CNT)−Nafion composites. This strategy not only allows the high-fidelity encoding and extraction of designed material shapes at different length scales (macro, micro, and nano) but also enables the reversible tunability of material functions, such as shape memorizability, mechanical properties, surface hydrophobicity, and material resealability, in a single nanocomposite.

In a thermoresponsive MSMP such as Nafion, the thermal programming using a direct heating source (e.g., oven) must be monotonic in both shape fixing (from higher to lower deformation temperature, T_d) and recovery (from lower to higher recovery temperature, T_r) because the whole sample is exposed to the external heat. In other words, the higher temperature temporary shape is always fixed first, and the lower temperature temporary shape is always recovered first. Such monotonic programming considerably limits the complexity and number of shapes a MSMP could memorize. These limitations can be resolved, in principle, by applying the heat remotely to just a selected region of a MSMP sample. Macroscale localized shape memory effect has only been recently demonstrated in a metallo-supramolecular polymer by UV light[8] and in a SMP (epoxy-based polymer) multicomposite consisting of a Fe_3O_4−SMP region and a CNT−SMP region separated by the neat SMP via selective radio frequency.[9] Although SMP composites with thermally conductive fillers, such as multiwalled CNTs (MWNTs) in a polyurethane matrix, have shown remote shape memory effect via IR irradiation,[10] it was thought these composites tend not to have localized effects because of enhanced thermal conductivity.[8] While CNT−Nafion composites are known, previous efforts were focused on electrochemistry of CNT−Nafion composites in aqueous electrolyte solutions for fuel-cell and actuator applications.[11,12] Here we show remote-controlled, localized shape memory effects at both macroscale and microscale in a uniform CNT−SMP composite.

4.2 Experimental

Amide functionalized SWNTs (P9-SWNT) were purchased from Carbon Solutions, Inc. and solubilized in ethanol with bath sonication. The resulting SWNT

solution was then mixed with a 5% w/w Nafion$_{H^+}$ alcohol solution (Alfa Aesar) to produce a homogeneous SWNT-Nafion$_{H^+}$ composite solution, which was cast on a PTFE dish and dried slowly to give a freestanding film after peeling from the substrate. The SWNT loading was kept at 0.5 wt.% . All as-prepared SWNT-Nafion$_{H^+}$ films were annealed at 140 °C for 2 h to reach their equilibrium states. Chemical "locking" refers to the process of converting the SWNT-Nafion$_{H^+}$ composite to the SWNT-Nafion$_{Na^+}$ composite by soaking in a 1M NaOH solution, followed by washing with deionized water and drying. Chemical "unlocking" refers to the process of converting the SWNT-Nafion$_{Na^+}$ composite back to the SWNT-Nafion$_{H^+}$ composite by soaking in a 1M HCl solution, followed by washing with deionized water and drying. Microscale surface patterning was performed by pressing either Pelco 400 mesh square or Veco 200 mesh hexagonal TEM grids to the top of a SWNT-Nafion$_{H^+}$ film in oven followed by cooling to room temperature under the load. Nanoscale surface patterning was created by pressing a Whatman Anodisc membrane filter with 0.2 μm pore size to the top of a SWNT-Nafion$_{H^+}$ film in oven followed by cooling to room temperature under the load. The resulting nanopatterned film was first soaked in 1 M NaOH for 1 h to remove the alumina membrane, which also simultaneously converted the film to SWNT-Nafion$_{Na^+}$ composite, followed by washing with deionized water and drying.

Additional details of shape memory and healing experiments were described in the figure captions in both the text and supporting information. IR irradiation sources include an 808 nm, 300 mW laser and a 250 W IR lamp. The power intensity and/or temperature of the IR laser and lamp were controlled by varying the distance from the sample. Sample temperatures in shape memory and healing experiments were measured

with a MICRO-EPSILON thermoMETER LS noncontact infrared thermometer, which was found to be in good agreement (within ±2 °C) with a traditional thermometer. IR laser irradiation times for macroscale experiments were between 5 sec and 2 min, and IR lamp irradiation time for macroscale experiments was 10 min. IR laser irradiation times for microscale experiments were between 1 and 10 min, and IR lamp irradiation time for nanoscale experiments was 30 min. Typical IR lamp irradiation time for healing experiments ranged from 5 to 20 min. SEM was performed using a Hitachi S-4800 field emission scanning electron microscope. SEM samples were imaged without coating to avoid potential metal coating artifacts. Two different imaging conditions were used in order to better image the film surface and SWNT dispersion, respectively. Film surface characteristics were best imaged using a 3 kV accelerating voltage and the lower secondary electron detector (Figure 4.1a). To see the SWNT distribution in a Nafion matrix, however, it was necessary to use higher accelerating voltage (10 kV) and the upper secondary electron detector (Figures 4.1b and 4.2). Optical microscopy was performed using a LOMO LA-MI-POLAM-312 light microscope without a polarizer. DSC thermograms were acquired using a TA Instruments DSC Q10 under Ar. The heating range was between 30 and 300 °C with a rate of 10 °C/min. Thermograms were recorded after first heating a sample up to 130 °C inside the DSC instrument and cooling back down to 30 °C to remove residual moisture in the sample. Water contact angles of SWNT-Nafion films were measured using a ramé-hart Model 250 Standard Contact Angle Goniometer/Tensiometer. Mechanical testing was performed using a Shimadzu Autograph AGS-J universal tester with a 500 N cell load and pneumatic side-action grips. The tensile tests were carried out at 0.5 mm/min. Film thicknesses were measured using a

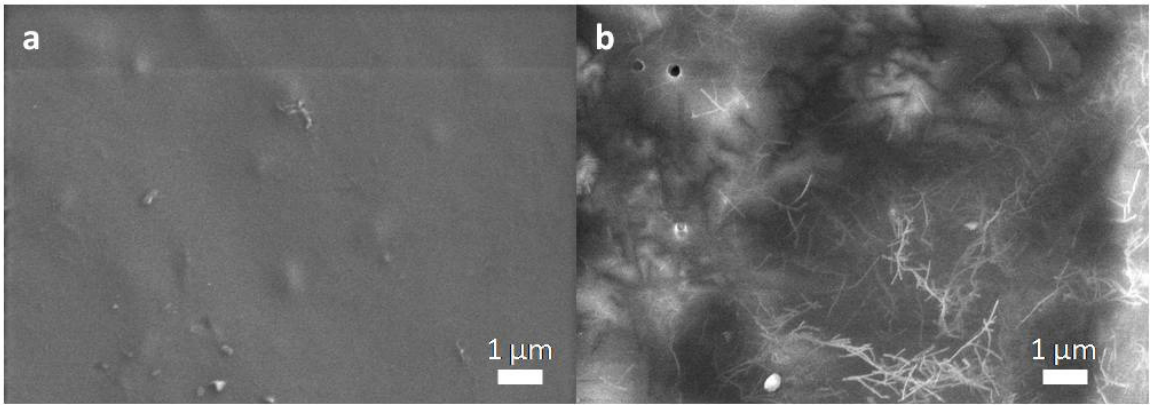

Figure 4.1. SEM images of a 0.5 wt.% SWNT-Nafion$_{H^+}$ film showing the same region with two different imaging conditions. (a) Surface characteristics imaged using a 3 kV accelerating voltage and the lower secondary electron detector. (b) SWNT dispersion imaged using a 10 kV accelerating voltage and the upper secondary electron detector.

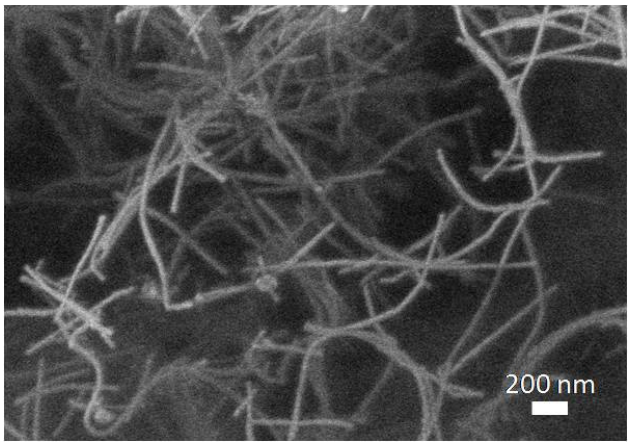

Figure 4.2. Higher magnification SEM image of a 0.5 wt.% SWNT-Nafion$_{H^+}$ film using a 10 kV accelerating voltage and the upper secondary electron detector.

Mitutoyo Digital Micrometer. The UV-Vis- NIR absorption spectrum was recorded with a Cary 5000 UV-Vis-NIR spectrophotometer. Attenuated total reflectance-FTIR spectra were obtained via a Nexus 670 FTIR spectrometer with a Smart OMNI-Sampler accessory containing a Germanium crystal.

4.3 Results and Discussion

In contrast to MWNTs, which have featureless visible–near- IR absorption, single-walled CNTs (SWNTs) display strong and specific absorptions in the vis–near-IR

region owing to the diameter-dependent band gap transitions and can absorb near- IR light much better than MWNTs.[13] We have previously shown the reversible IR actuation of SWNT−liquid crystalline elastomer nanocomposites at the very low nanotube loadings (0.1−0.2 wt.%).[14] In this study, we chose commercially available amide-functionalized SWNTs as a filler because they are soluble in alcohols and can be uniformly dispersed in a Nafion matrix. Protonated and deprotonated Nafion polymers are denoted as $Nafion_{H^+}$ and $Nafion_{Na^+}$, respectively (Figure 4.7e). All results in this study were based on 0.5 wt.% SWNT−Nafion composites. Scanning electron microscopy (SEM) confirmed the excellent dispersion of nanotubes in a Nafion matrix (Figures 4.1 and 4.2). The SWNT−$Nafion_{H^+}$ film exhibits two strong and broad absorptions in the near-IR region (Figure 4.3), which originate from the S_{11} and S_{22} optical transitions of arc-produced semiconducting SWNTs.[13] In SWNT−Nafion composites, the semiconducting SWNTs can efficiently absorb and transform near-IR light into thermal energy, thereby serving as

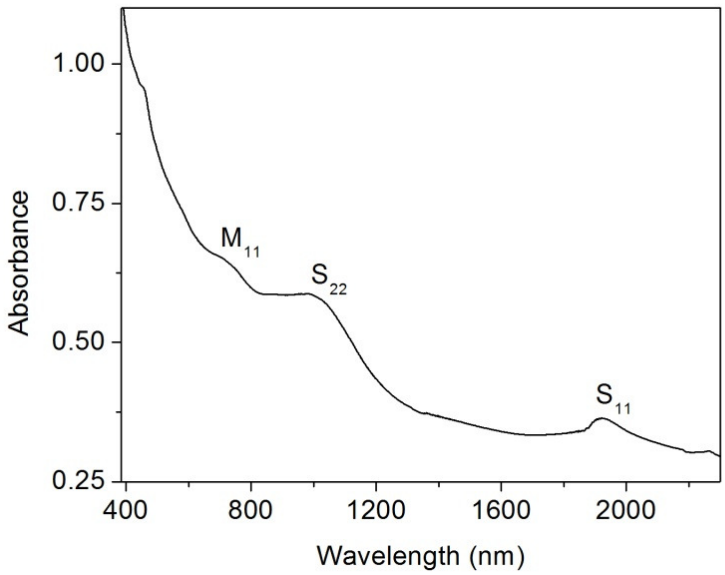

Figure 4.3. UV–Vis–NIR spectrum of a 0.5 wt.% SWNT-$Nafion_{H^+}$ film. M_{11}, S_{11}, and S_{22} represent optical transitions in metallic and semiconducting SWNTs, respectively.

numerous nanoscale heaters uniformly embedded in the Nafion matrix. As a result, our IR heating approach does NOT hinge on dramatically improved thermal conductivity of a composite as a whole. Recent studies have shown that although CNTs impart great electrical conductivity to polymers, a similar degree of thermal conductivity enhancement is NOT achieved due to phonon scattering.[15,16] In fact, the lack of dramatic thermal conductivity enhancement in CNT−polymer composites is essential to successful remote and local programming of CNT−Nafion composites by focused IR beam at both macro and microscale. (Figure 4.4).

Figure 4.4 shows thermal response of various films upon IR irradiation. Samples were suspended in order to measure the temperature on both sides of the film. A 0.5 wt.% SWNT-Nafion$_{H^+}$ film irradiated with 808 nm laser at spot A shows similar thermal profiles on both sides of the film at spot A (Figure 4.4c), which were characterized by initial rapid temperature boost followed by gradual temperature increase at the late stage. Heat is basically not transferred across the length of the film, as no significant temperature increase is observed at either spot B or C (Figure 4.4c). A neat Nafion$_{H^+}$ film irradiated with 808 nm laser at the same intensity at spot A shows no significant heating throughout the entire film (Figure 4.4d). Figure 4.4e shows the effect of thickness on heating of 0.5 wt.% SWNT-Nafion$_{H^+}$ films upon IR laser irradiation. Although the thinner film (83 μm) shows a faster rate of heating than the thicker film (290 μm) at the initial stage, the thicker film reaches higher temperature than the thinner film at the late stage. Both films show similar temperature profiles on both sides of the film upon IR irradiation, respectively, showing that thermal conduction is sufficiently fast across the thickness of both films. In order to try to increase thermal conduction in our films, we

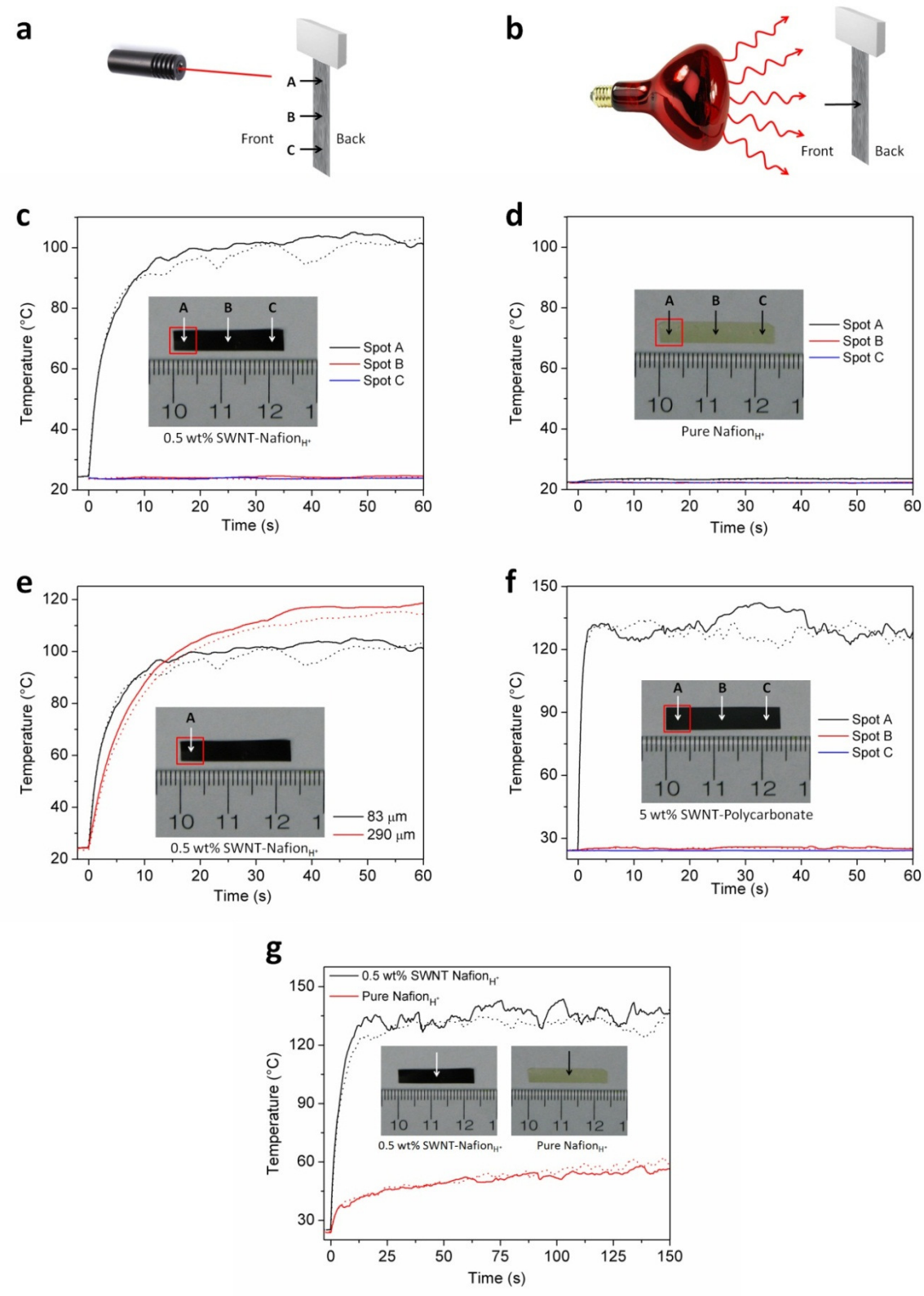

Figure 4.4. Temperature profiles of IR induced heating of various films. (a) Schematic drawing of the setup used to measure 808 nm laser induced heating. The laser beam (10

mW/mm^2) was focused on spot A on the front of the film (highlighted by a red square in following figure insets) and temperatures were measured at spots A, B, and C (indicated by solid lines in following temperature profiles) using a noncontact IR thermometer. To test IR induced heating through the thickness of the film, temperature profiles were collected on the back of the films right behind spots A and B (indicated by dotted lines in following temperature profiles). (b) Schematic drawing of the setup used to measure 250 W IR lamp induced heating. Irradiation from the lamp covered the entire film and temperature profiles were collected on both the front (solid line) and back (dotted line) of the film at the position indicated by an arrow. (c) Laser induced heating of a 0.5 wt.% SWNT-Nafion$_{H^+}$ film (thickness: 83 μm, measured by a Mitutoyo Digital Micrometer). (d) Laser induced heating of a pure Nafion$_{H^+}$ film (thickness: 64 μm). (e) Effect of thickness on laser induced heating of 0.5 wt.% SWNT-Nafion$_{H^+}$ films. (f) Laser induced heating of 5% SWNT-polycarbonate film (thickness: 25 μm). (g) 250 W IR lamp induced heating of a 0.5 wt.% SWNT-Nafion$_{H^+}$ film (thickness: 83 μm) and a pure Nafion$_{H^+}$ film (thickness: 64 μm).

decided to make a 5 wt.% SWNT-polycarbonate film. Since the low solubility of amide functionalized P9-SWNTs prevents us from making a good quality 5 wt.% SWNT-Nafion composite film, we prepared a uniform 5 wt.% SWNT-polycarbonate film via noncovalent functionalization of P2-SWNTs using poly(*p*phenylene ethynylene)s.[17-19] Although both are purified arc-produced SWNTs from Carbon Solutions, Inc., P2-SWNTs have much lower degree of functionalization than P9-SWNTs, which were covalently functionalized by amide groups. Therefore P2-SWNT material is a better choice if we want to increase thermal conduction in our films. Despite increasing the SWNT loading by 10 times, heat is still basically not transferred across the length of the film, as no significant temperature increase is observed at either spot B or C (Figure 4.4f). These experiments further support the notion that the lack of dramatic thermal conductivity enhancement in CNT-polymer composites is essential to successful remote and local programming of CNT-Nafion composites by focused IR beam.

The remote, local programming of the multishape memory effects enables extraordinary flexibility in shape fixing and recovery. In one example (Figure 4.5a–e), it

was possible to form the second temporary shape (a bend) of a SWNT−Nafion$_{H^+}$ film at higher temperature (T_d = 140−150 °C) via IR laser (Figure 4.5c) without reverting the

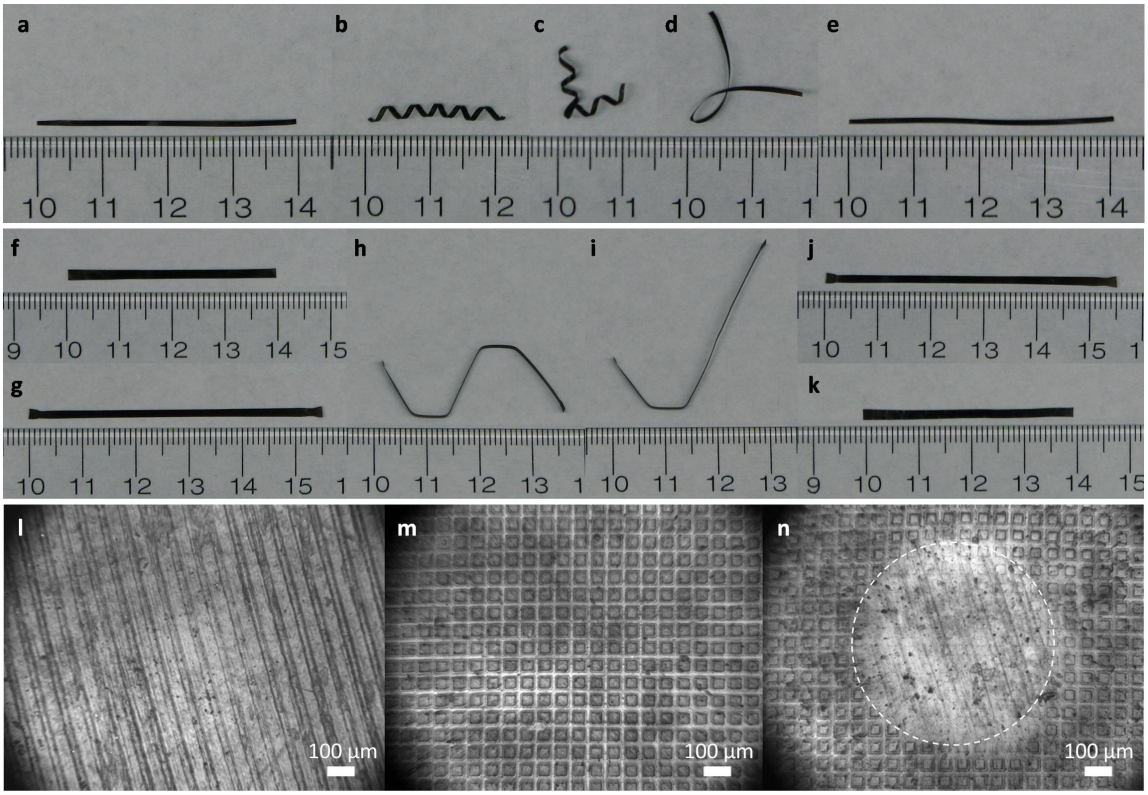

Figure 4.5. Macroscale and microscale shape memory effects in 0.5 wt.% SWNT−Nafion$_{H^+}$ films. (a–e) Macroscale multiple-shape memory cycle 1. (a) Permanent shape. (b) Coiling via 808 nm IR laser (6 mW/mm^2, T = 70–75 °C) and then cooling. (c) Localized bending via 808 nm IR laser (25 mW/mm^2, T = 140–150 °C) and then cooling. (d) Removing coiling at 75 °C in oven. (e) Removing the localized bend and recovering the original shape via 808 nm IR laser (T = 140–150 °C). (f–k) Macroscale multiple-shape memory cycle 2. (f) Permanent shape. (g) Stretching at 100 °C in oven and then cooling. (h) Localized bending via 808 nm IR laser (25 mW/mm^2, T = 140–150 °C) and then cooling (side view). (i) Localized removal of two bends via 808 nm IR laser (T = 140–150 °C, side view). (j) Localized removal of remaining two bends via 808 nm IR laser (T = 140–150 °C). (k) Recovering the original shape via IR lamp (T = 120 °C). (l–n) Microscale localized shape memory effect. (l) Optical microscopy image before patterning. The line pattern in all optical microscopy images is due to the permanent molding impression of the PTFE substrate during film preparation. (m) After TEM grid patterning at 110 °C in oven and then cooling. (n) After selective removal of the microscale pattern via 808 nm IR laser (48 mW/mm^2) through a circular mask. The removed region is highlighted by a dashed circle.

first temporary shape (a coil) (T_d = 70−75 °C, Figure 4.5b) to the original, permanent shape (Figure 4.5a). Subsequent removal of the coil at 75 °C in oven while keeping the bend intact led to the creation of the third temporary shape (Figure 4.5d). In another example (Figure 4.5f− k), we not only made the second temporary shape (four bends) at higher temperature (T_d = 140−150 °C) via IR laser (Figure 4.5h) but also selectively removed only two of four bends to generate the third temporary shape (T_r = 140−150 °C) via IR laser (Figure 4.5i); both localized shape transformations occurred at higher temperature (140−150 °C) than the first temporary shape (T_d = 100 °C, Figure 4.5g) without switching back to the permanent shape (Figure 4.5f). Such nonmonotonic shape programming is simply impossible for pure Nafion$_{H^+}$. Although not demonstrated here, more than three temporary shapes could be formed (e.g., one localized deformation at a time) in SWNT−Nafion$_{H^+}$ composites using IR laser.

Various temporary micropatterns were created on the surface of a SWNT−Nafion$_{H^+}$ composite in oven using different transmission electron microscopy (TEM) grids as molds at different deformation temperatures and then were removed one at a time via IR light (Figure 4.6). Remote-controlled, localized shape memory effect is also feasible at microscale. For instance, we were able to selectively remove part of the micropattern via IR laser through a mask (Figure 4.5l−n).

One main concern about a MSMP based on the broad continuous glass transition is the thermal stability of temporary shapes, especially those deformed at relatively lower temperatures and/or at microscale and nanoscale. We have found that a temporary shape could be chemically "locked" by exposing it to a dilute NaOH solution. After the basic

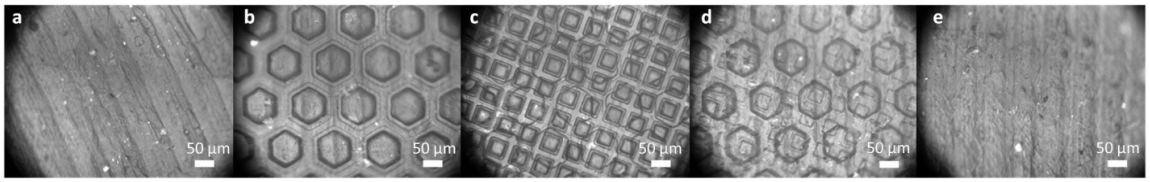

Figure 4.6. Optical microscopy images of a microscale triple-shape memory cycle in a 0.5 wt.% SWNT-Nafion$_{H^+}$ film. (a) before patterning. (b) After 200 mesh hexagonal TEM grid patterning at 130 °C in oven and then cooling. (c) After 400 mesh TEM grid patterning at 40 °C in oven and then cooling. (d) After removal of 400 mesh TEM grid pattern via 808 nm IR laser (19 mW/mm^2, T = 110-115 °C). (e) After removal of 200 mesh hexagonal TEM grid pattern via 808 nm IR laser (25 mW/mm^2, T = 140-150 °C).

treatment, the sulfonic acid group (−SO_3H) in a SWNT−Nafion$_{H^+}$ composite was converted to the sulfonate group (−SO_3^-) in a SWNT−Nafion$_{Na^+}$ composite (Figure 4.7e). This chemical transformation is supported by IR spectroscopy (Figure 4.8). Differential scanning calorimetry (DSC) indicated that the molecular mobility of Nafion polymer was greatly suppressed in the SWNT−Nafion$_{Na^+}$ composite as evidenced by the substantial diminishing of the endothermic DSC peak and the upshift of the peak maximum from ~169 °C in the SWNT−Nafion$_{H^+}$ composite to ~243 °C in the SWNT−Nafion$_{Na^+}$ composite (Figure 4.7f). This observation is in agreement with prior thermal analysis of Nafion in acidic and basic forms.[20,21] The diminished molecular mobility in the SWNT−Nafion$_{Na^+}$ composite is probably due to the significantly enhanced electrostatic interactions among the Nafion chains. According to the IR (Figure 4.8) and DSC (Figure 4.7f), the molecular mobility of Nafion polymer could be fully restored by transforming the SWNT−Nafion$_{Na^+}$ composite back to SWNT−Nafion$_{H^+}$ composite through a dilute HCl solution treatment. Figure 4.8 is in agreement with previous ATR studies of Nafion$_{H^+}$ and Nafion$_{Na^+}$ membranes.[22-25] Treating a 0.5 wt.% SWNT-Nafion$_{H^+}$ film with 1 M NaOH causes the symmetric -SO_3^- stretching mode to shift from 1057 (a) to 1064 cm^{-1}

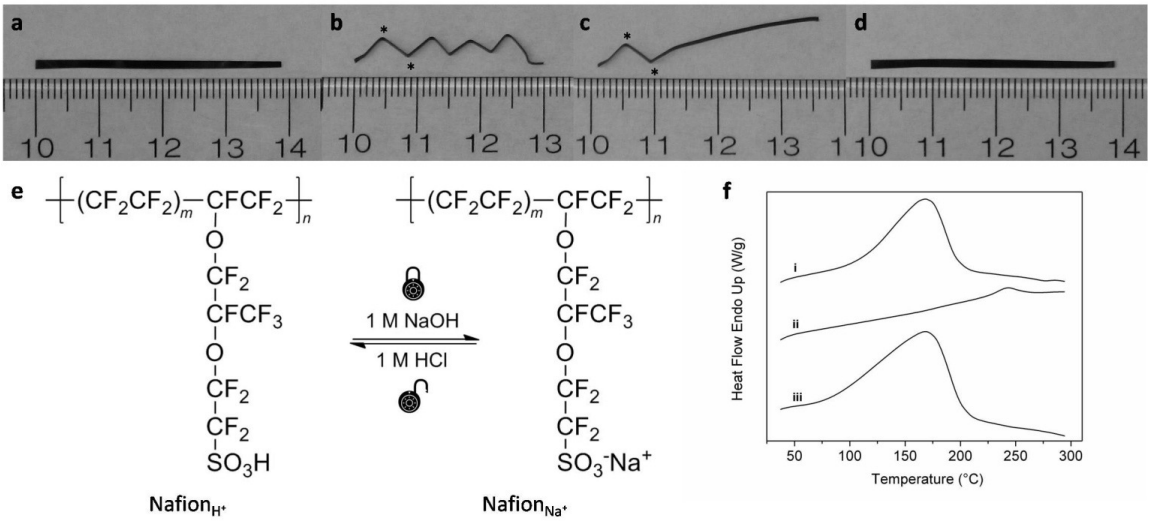

Figure 4.7. Reversible chemical "locking" and "unlocking" of 0.5 wt.% SWNT–Nafion$_{H^+}$ films. (a–d) Macroscale shape memory cycle. (a) Permanent shape. (b) After fixing 8 bends at 120 °C in oven and then cooling, followed by "locking" of two bends (indicated by asterisk) via soaking these two bends in 1 M NaOH (side view). (c) After oven heating at 130 °C to remove six pristine bends (side view). (d) Removal of the remaining two bends by first soaking in 1 M HCl and then heating at 130 °C in oven. (e) Reversible switch between acidic ("unlocked") and basic ("locked") forms of Nafion. (f) DSC thermograms of (i) 0.5 wt.% SWNT–Nafion$_{H^+}$ composite, (ii) 0.5 wt.% SWNT–Nafion$_{Na^+}$ composite obtained from 1 M NaOH treatment of (i), and (iii) recovered 0.5 wt.% SWNT–Nafion$_{H^+}$ composite obtained from 1 M HCl treatment of (ii). Thermograms were shifted along the y-axis for better visual comparison.

(b). This process is reversible, as soaking the SWNT-Nafion$_{Na^+}$ film in 1 M HCl solution renders this peak to shift back to 1057 cm^{-1} (c). Treating a 0.5 wt.% SWNT-Nafion$_{H^+}$ film with 1 M NaOH causes the symmetric C-O-C stretching mode to shift from 969 cm^{-1} (a) to higher wavenumber, becoming a shoulder on the asymmetric C-O-C stretching mode at 982 cm^{-1} (b). Soaking the SWNT-Nafion$_{Na^+}$ film in 1 M HCl renders this peak to shift back to 969 cm^{-1} (c).

Therefore, a temporary shape could be reversibly "locked" and "unlocked" with high fidelity by deprotonation and reprotonation, respectively. In Figure 4.7, all eight bends were first formed at 120 °C, and then the two bends (indicated by an asterisk) were chemically "locked" by selective NaOH treatment. Unlike the untreated bends, the two

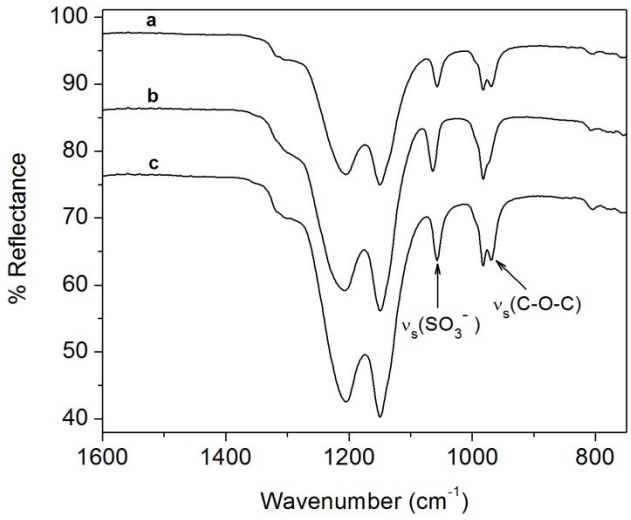

Figure 4.8. ATR-FTIR spectra. (a) 0.5 wt.% SWNT-Nafion$_{H^+}$ film. (b) 0.5 wt.% SWNT-Nafion$_{Na^+}$ film obtained from 1 M NaOH treatment of (a). (c) 0.5 wt.% SWNT-Nafion$_{H^+}$ film obtained from 1 M HCl treatment of (b). Spectra were shifted along the y-axis for better visual comparison.

"locked" bends were stable toward subsequent oven heating at 130 °C (Figure 4.7c). The two "locked" bends were then "unlocked" by HCl treatment and removed by heating at 130 °C (Figure 4.7d).

We have also found that chemical "locking" treatment dramatically increases the tensile strength and Young's modulus of the 0.5 wt.% SWNT−Nafion composite in its permanent shape by nearly 175% and 470%, respectively (Figure 4.9). This observation is in strong agreement with the notion that the diminished molecular mobility in the SWNT−Nafion$_{Na^+}$ composite most likely originates from the considerably enhanced electrostatic interactions among the Nafion chains. Simultaneous shape "locking" and mechanical enhancement are highly desirable for certain applications where shape and mechanical stabilities are critical.

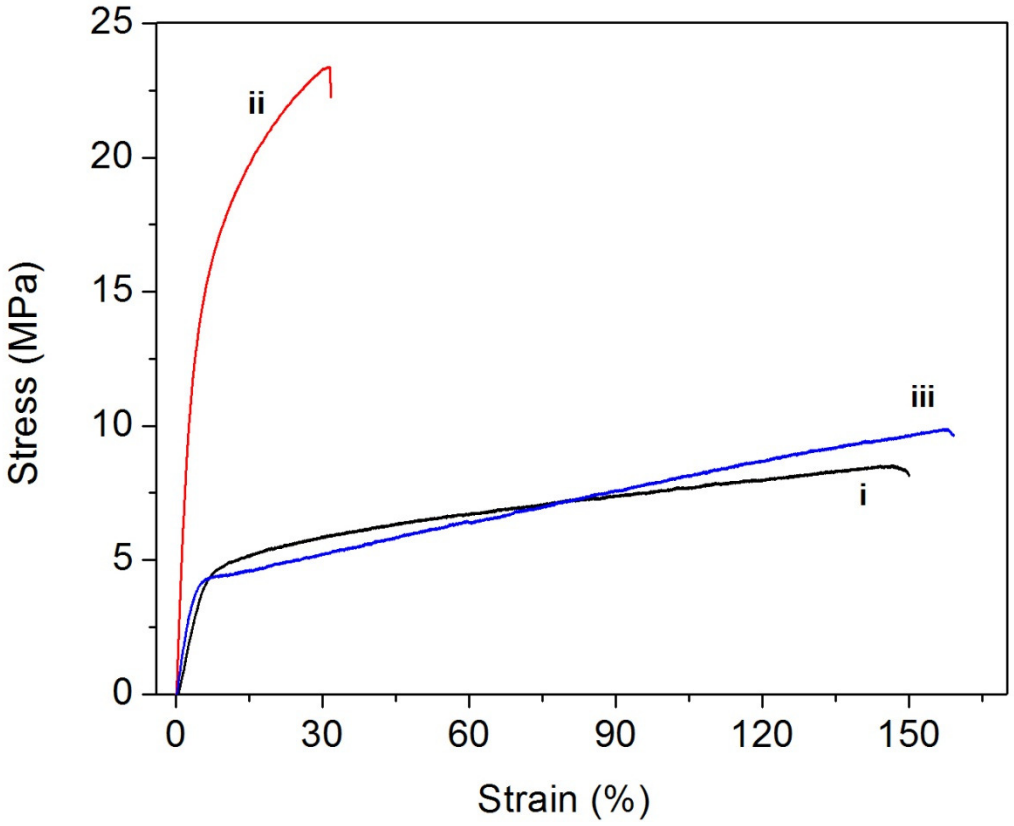

Figure 4.9. Stress-strain curves of (i) 0.5 wt.% SWNT-Nafion$_{H^+}$ film (strain: 150%; tensile strength: 8.5 MPa; Young's modulus: 82.7 MPa). (ii) 0.5 wt.% SWNT-Nafion$_{Na^+}$ film obtained from 1 M NaOH treatment of (i) (strain: 32%; tensile strength: 23.4 MPa; Young's modulus: 470.2 MPa). (iii) 0.5 wt.% SWNT-Nafion$_{H^+}$ film obtained from 1 M HCl treatment of (ii) (strain: 159%; tensile strength: 9.8 MPa; Young's modulus: 111.8 MPa).

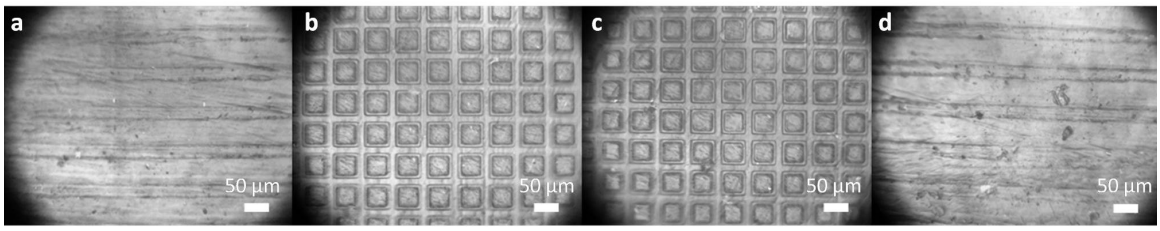

Figure 4.10. Optical microscopy images of a microscale chemical "locking" and "unlocking" cycle in a 0.5 wt.% SWNT-Nafion$_{H^+}$ composite. (a) before patterning. (b) After TEM grid patterning at 115 °C in oven and then cooling. (c) After "locking" the micropattern by soaking in 1 M NaOH. The "locked" micropattern remained unchanged after heating at 130 °C in oven. (d) Removal of the micropattern by first soaking in 1 M HCl and then heating at 130 °C in oven.

Chemical "locking" is particularly useful for stabilizing the microscale and nanoscale temporary shapes against heating to temperatures at or higher than their deformation temperature. The "locked" micropattern (T_d = 115 °C) was stable upon exposure to the 130 °C thermal treatment and could only be removed at the same temperature after "unlocking" (Figure 4.10). Even the "locked" nanowires (T_d = 150−155 °C) were found to be inert against heating at 180−190 °C (Figure 4.11b).

As shown in Figure 4.7e, Nafion has two components: hydrophobic tetrafluoroethylene backbone and perfluoroalkyl ether side chains and hydrophilic sulfonic acid groups (in $Nafion_{H^+}$) or sulfonate groups (in $Nafion_{Na^+}$). It was discovered that adsorption of water onto a Nafion surface caused the surface to switch from being hydrophobic to being hydrophilic.[26] Microscale and nanoscale patterning of the SMP surface has received increasing attention recently.[27-30] In this study, we investigated the impact of nanopatterning of SWNT−Nafion composite surfaces on their surface wettability, with the goal of enhancing the hydrophobicity and hence improving the environmental stability of Nafion-based SMPs. A temporary nanowire array pattern on the SWNT−Nafion surface was fabricated (T_d =150−155 °C) and chemically "locked" (Figure 4.11b). The contact angle of 144° indicated the near superhydrophobic surface, which was in sharp contrast to the SWNT−Nafion surface before the nanopatterning (contact angle: 118°, Figure 4.11a). The "locked" nanowire array pattern was stable toward IR lamp irradiation at 180−190 °C. Although the "unlocked" nanowire array surface showed an even higher contact angle of 153° and was therefore superhydrophobic (Figure 4.11c), it was able to switch back to the hydrophobic, unpatterned surface

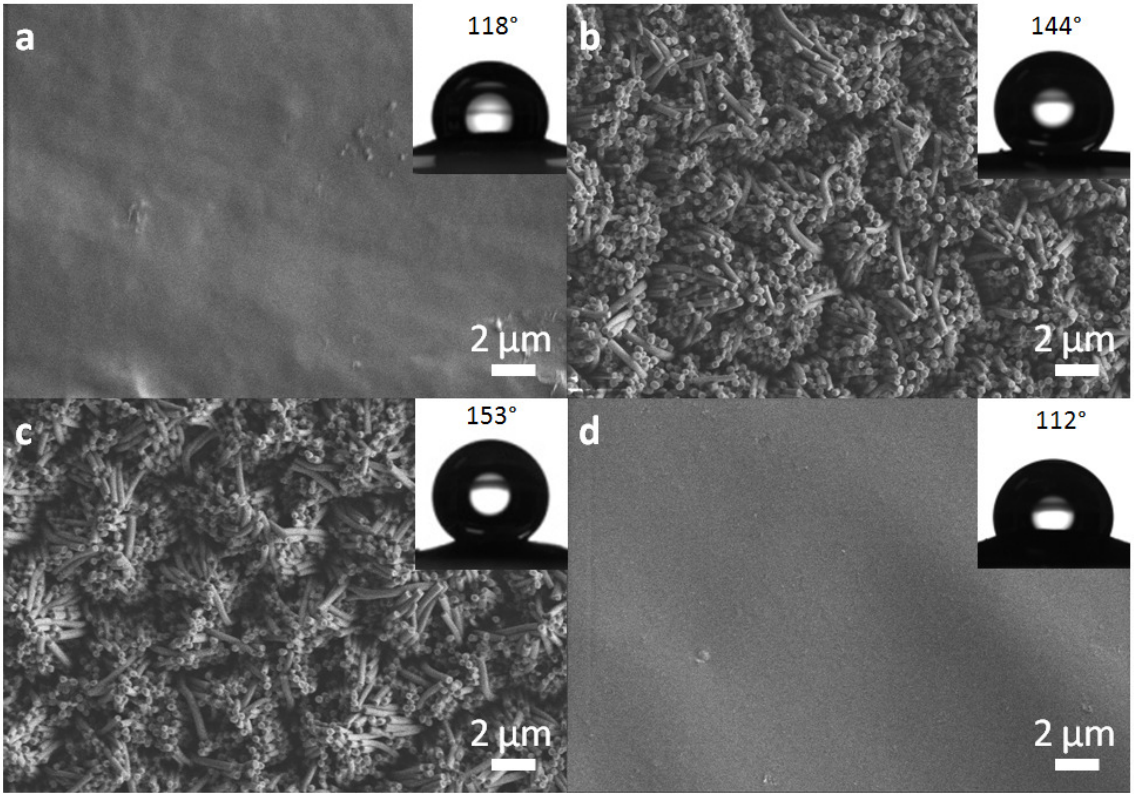

Figure 4.11. Impact of nanoscale patterning on hydrophobicity of 0.5 wt.% SWNT–Nafion films. SEM images and insets of corresponding water contact angle measurements of (a) SWNT–Nafion$_{H^+}$ surface before patterning; (b) SWNT–Nafion$_{Na^+}$ surface with nanowire array pattern, which remained unchanged after IR lamp irradiation (T = 180–190 °C); and (c) SWNT–Nafion$_{H^+}$ surface with nanowire array pattern obtained by 1 M HCl treatment of (b). (d) After pattern removal of (c) via IR lamp (T = 180–190 °C).

after IR irradiation at 180–190 °C (contact angle: 112°, Figure 4.11d). Nafion$_{H^+}$-based materials, patterned or unpatterned, were found to be slightly more hydrophobic than corresponding Nafion$_{Na^+}$-based materials. It should be possible to further enhance the hydrophobicity of the SWNT–Nafion surface by optimizing the shape and size of the patterned nanostructures.[31,32] A simple and effective "template rolling press" method could be used to fabricate nanopatterned surface on a large scale.[33]

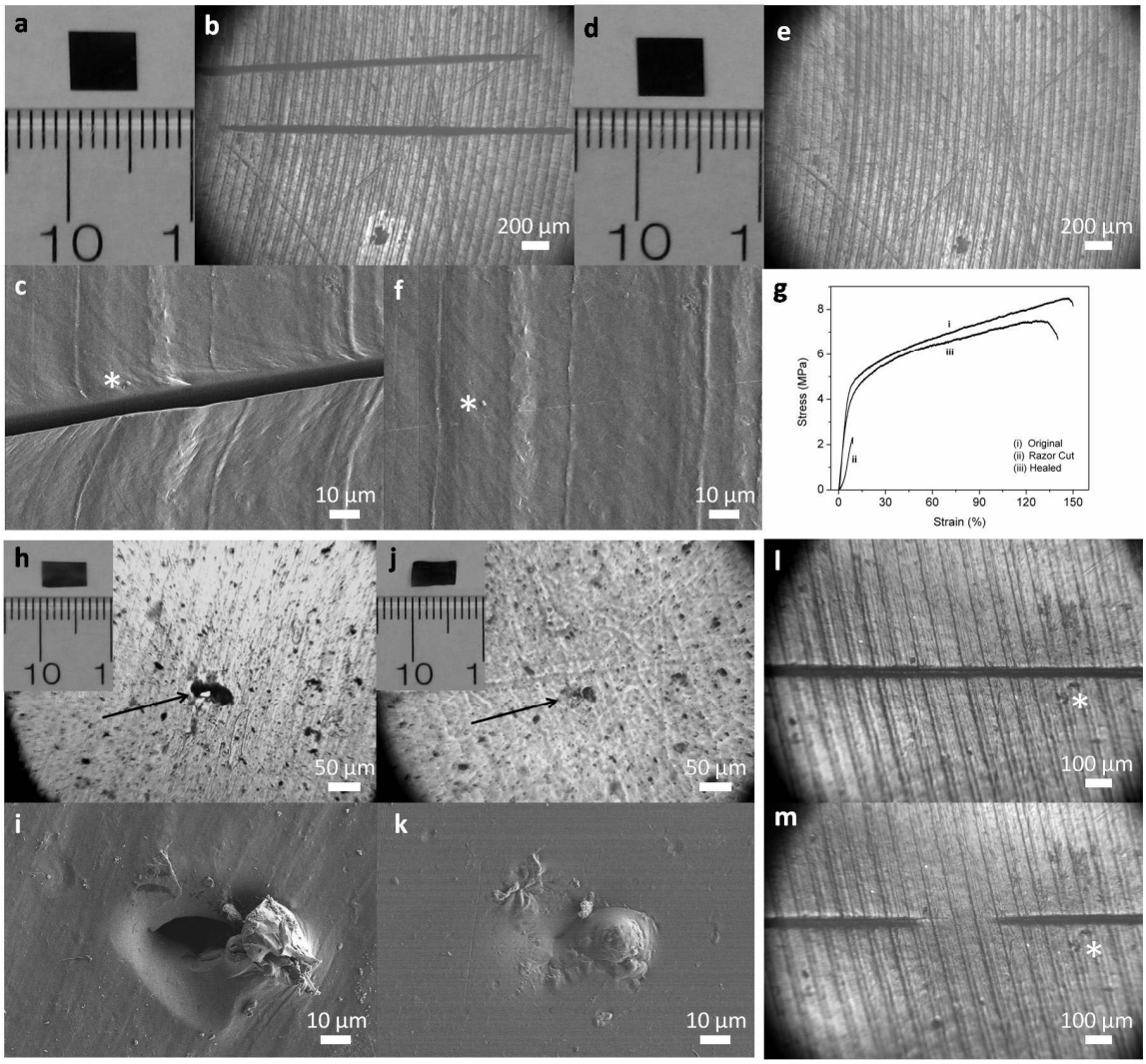

Figure 4.12. Remote-controlled and localized healing of 0.5 wt.% SWNT–Nafion$_{H^+}$ films in their permanent shapes. (a–g) Healing of razor cuts. (a) Photograph of a pristine film. (b) Optical microscopy (arrow indicates a pen mark drawn to show the same position on the film) and (c) SEM images of damaged film with two razor cuts occurred at room temperature. (d) Photograph of healed film via IR lamp (T = 140–150 °C). (e) Optical microscopy and (f) SEM images of same region of the film after healing (asterisk indicates the same position on the film). (g) Stress–strain curves of 0.5 wt.% SWNT–Nafion$_{H^+}$ films: (i) without razor cuts, (ii) after damaging with razor cuts, and (iii) after healing via IR lamp (T = 140–150 °C). All cuts were made perpendicular to the tensile direction. (h–k) Healing of a needle hole through the film. (h) Photograph (inset), optical microscopy (hole indicated by an arrow; dark dots are mainly from dust (see Figure 4.15 for more analysis)), and (i) SEM images of damaged film with a see-through needle hole occurred at room temperature. (j) Photograph (inset), optical microscopy (healed hole position indicated by an arrow), and (k) SEM images of same region after healing via IR lamp (T = 230 °C). (l, m) Localized healing of a razor cut. (l) Optical microscopy image of damaged film with a razor cut occurred at room temperature and (m) after localized

healing of only a small part of the cut via 808 nm IR laser (300 mW/mm^2, asterisk indicates the same position on the film).

The self-healing capability is particularly desirable for a multifunctional material because it could make the material more reliable in multitasking and lasting longer.[34-38] Several ionomers, such as Surlyn and Nucrel polymers, exhibited instantaneous and autonomous self-healing in response to projectile puncturing without the need of any healing agent. The healing action occurred via thermally controlled reversible hydrogen bonding of pendant acid groups in ionomers. In SWNT−Nafion$_{H^+}$ SMP composites, numerous embedded semiconducting SWNTs absorb near-IR light efficiently and convert it into thermal energy, which could trigger the healing of Nafion$_{H^+}$. It is therefore possible to perform a repair remotely by pinpointing the focused IR beam to only the damaged area.

Razor cuts were made on SWNT−Nafion$_{H^+}$ films in their permanent shape at room temperature (Figure 4.12a−c). Compared with the pristine SWNT−Nafion$_{H^+}$ film, the tensile strength and strain of the damaged film decreased by ~73% and 94%, respectively (Figure 4.12g). The damaged film was efficiently healed by IR lamp irradiation at 140−150 °C. Optical microscopy and SEM showed the disappearance of razor cuts in the IR-healed SWNT−Nafion$_{H^+}$ film (Figure 4.12d−f). The healing efficiency (tensile strength$_{healed}$/tensile strength$_{original}$) was about 88% (Figure 4.12g). In addition, the see-through, needle hole damage which occurred on the SWNT−Nafion$_{H^+}$ film in its permanent shape at room temperature could also be completely mended via IR light (Figure 4.12h−k). Moreover, the remote-controlled localized repair was demonstrated on the SWNT−Nafion$_{H^+}$ film, where only a very small part of the razor cut (~200 μm long)

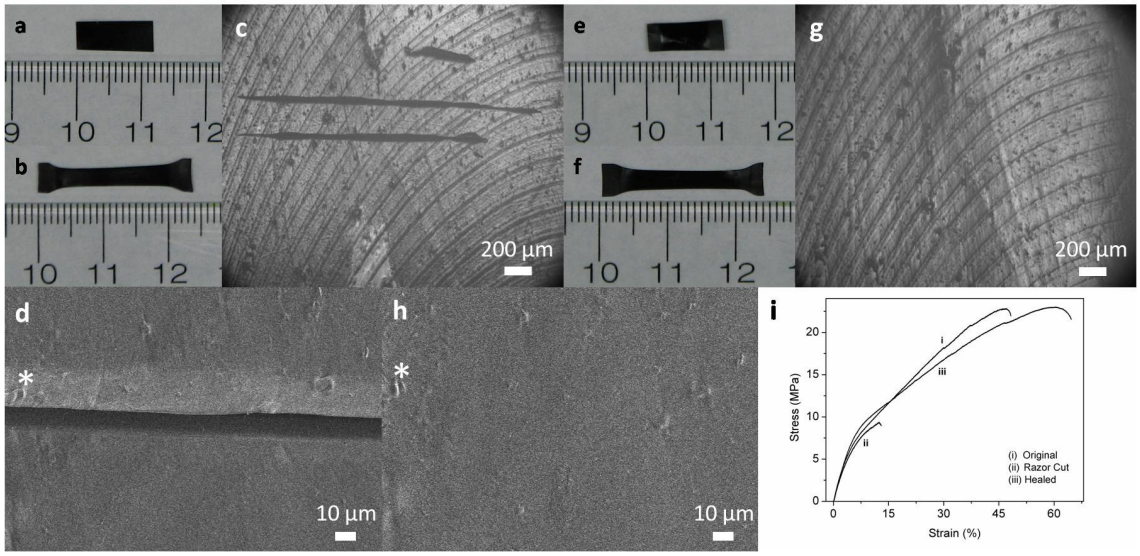

Figure 4.13. Remote-controlled healing of razor cuts in 0.5 wt.% SWNT-Nafion$_{H^+}$ films in their temporary shape. Photographs of (a) the original film and (b) the film after stretching at 110-115 °C in oven and then cooling, followed by damaging with two razor cuts at room temperature. (c) Optical microscopy and (d) SEM images of damaged film. Photographs of (e) after simultaneous healing and recovering the original shape via IR lamp (T = 170-180 °C) and (f) after restretching the healed film at 110-115 °C in oven and then cooling. (g) Optical microscopy and (h) SEM images of same regions of the stretched, healed film (* indicates the same position on the film). (i) Stress-strain curves of stretched 0.5 wt.% SWNT-Nafion films: i) without razor cuts, ii) after damaging with razor cuts, and iii) after healing via IR lamp (T = 170-180 °C) and restretching at 110-115 °C in oven and then cooling. The stretch ratio of all mechanical testing samples was between 175 and 183%, and all cuts were made perpendicular to the tensile direction.

was healed via IR laser (Figure 4.12l,m). The damaged SWNT−Nafion$_{H^+}$ films in their temporary shape could also be efficiently repaired remotely (Figures 4.13 and 4.14). IR lamp irradiation simultaneously reverted the damaged temporary shape to the healed permanent shape, which was then redeformed to the original temporary shape with the complete disappearance of the damages, as evidenced by optical microscopy and SEM (Figures 4.13 and 4.14). The healing efficiency in terms of tensile strength for the razor cuts in the SWNT−Nafion$_{H^+}$ film in its temporary shape was about 100% (Figure 4.13i). Since the molecular mobility is severely suppressed in the SWNT−Nafion$_{Na^+}$ composite film, the damage in such a film, according to our experiments, cannot be mended by the

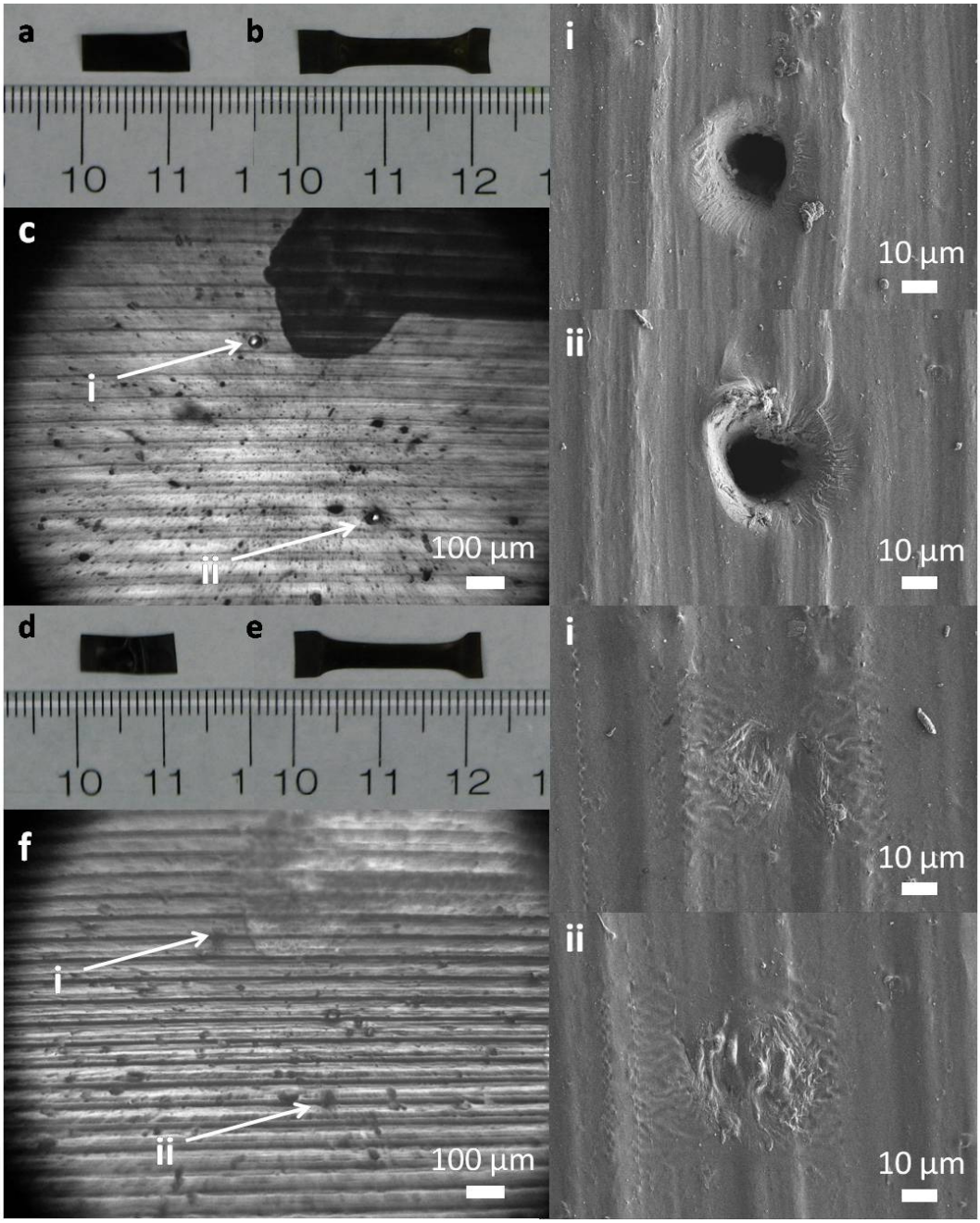

Figure 4.14. Remote-controlled healing of see-through needle holes in 0.5 wt.% SWNT-Nafion$_{H^+}$ films in their temporary shape. Photographs of (a) the original film and (b) the film after stretching at 110-115 °C in oven and then cooling, followed by damaging with two needle holes at room temperature. (c) Optical microscopy (* indicates a pen mark drawn to show the same position on the film) and corresponding SEM images showing holes i and ii (indicated by arrows). Photographs of (d) after simultaneous healing and recovering the original shape via IR lamp (T = 140-150 °C) and (e) after restretching the healed film at 110-115 °C in oven and then cooling. (f) Optical microscopy and corresponding SEM images showing the healed regions (arrows indicate the original hole positions).

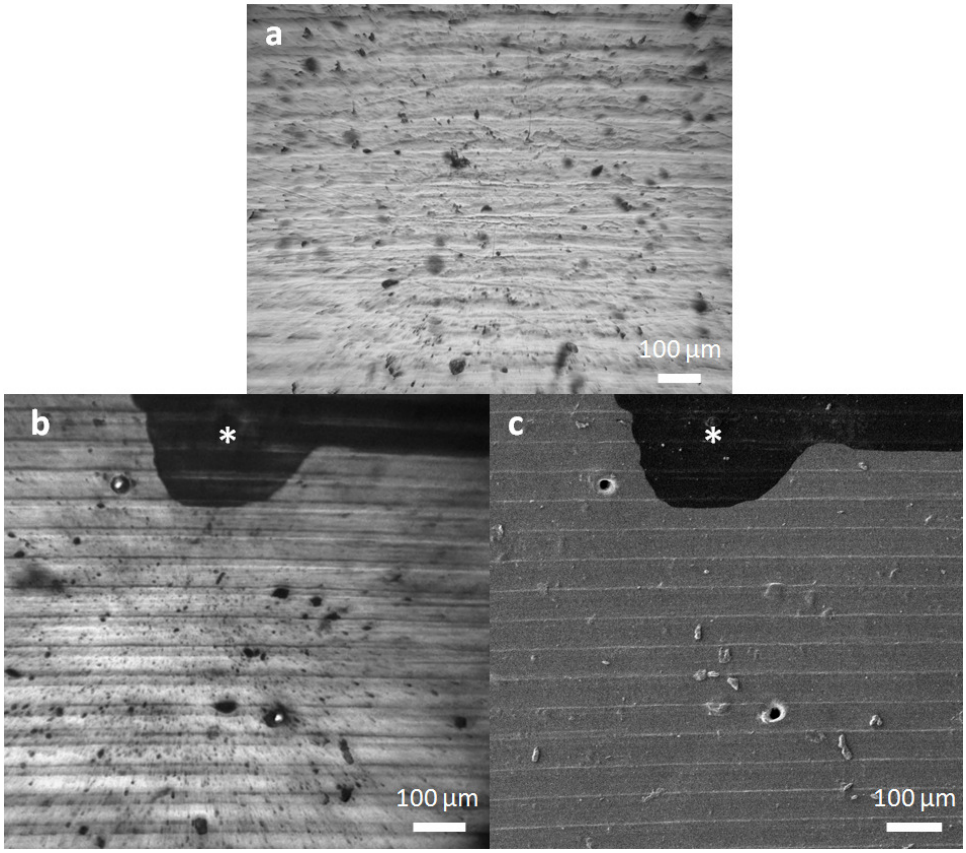

Figure 4.15. (a) Optical microscopy image of a neat $Nafion_{H^+}$ film. (b) Optical microscopy and (c) corresponding SEM images of a 0.5 wt.% SWNT-$Nafion_{H^+}$ film (* indicates a pen mark drawn to show the same position on the film).

similar IR irradiation or direct heating. The ability to reversibly tune the healability of a material, although counterintuitively, could find some useful applications. For instance, a membrane with microsized holes could be "locked" in the SWNT−$Nafion_{Na^+}$ composite, which is much more stable toward the heat. When needed, the membrane is resealed by the chemical "unlocking" into the SWNT−$Nafion_{H^+}$ composite followed by the IR healing of the holes. Such resealable membrane is valuable for controlled storage and/or transportation of liquid and gas.

Figure 4.15 shows that the dark spots present in optical microscopy images of 0.5 wt.% SWNT-$Nafion_{H^+}$ films primarily originate from dust, NOT SWNT clumps. This

conclusion is based on two key observations: 1) similar dark spots are also present in neat Nafion$_{H^+}$ films (Figure 4.15a); 2) most dark spots present in the optical microscopy of 0.5 wt.% SWNT-Nafion$_{H^+}$ film (Figure 4.15b) can also be seen at the same locations in SEM as dust particles (Figure 4.15c). We have noticed that Nafion-based films have a much greater affinity for dust than polycarbonate-based films.

4.4 Conclusion

The remote and local programming strategy established in SWNT−Nafion composites is extendable to other SMP nanocomposites.[5] The concept of the reversible switch of molecular mobility between two stable chemical states without involving dynamic covalent bonds and material shape change could be applied to other SMPs and their nanocomposites via either similar (e.g., for other ionomers) or different chemistry.

4.5 References

(1) Liu, C.; Qin, H.; Mather, P. T. *J. Mater. Chem.* **2007**, 17, 1543−1558.
(2) Mather, P. T.; Luo, X.; Rousseau, I. A. *Annu. Rev. Mater. Res.* **2009**, 39, 445−471.
(3) Leng, J.; Lu, H.; Liu, Y.; Huang, W. M.; Du, S. *MRS Bull.* **2009**, 34, 848−855.
(4) Behl, M.; Razzaq, M. Y.; Lendlein, A. *Adv. Mater.* **2010**, 22, 3388−3410.
(5) Madbouly, S. A.; Lendlein, A. *Adv. Polym. Sci.* **2010**, 226, 41−95.
(6) Xie, T. *Polymer* **2011**, 52, 4985−5000.
(7) Xie, T. *Nature* **2010**, 464, 267−270.
(8) Kumpfer, J. R.; Rowan, S. J. *J. Am. Chem. Soc.* **2011**, 133, 12866−12874.
(9) He, Z.; Satarkar, N.; Xie, T.; Cheng, Y.-T.; Hilt, J. Z. *Adv. Mater.* **2011**, 23, 3192−3196.
(10) Koerner, H.; Price, G.; Pearce, N. A.; Alexander, M.; Vaia, R. A. *Nat. Mater.* **2004**, 3, 115−120.
(11) Landi, B. J.; Raffaelle, R. P.; Heben, M. J.; Alleman, J. L.; VanDerveer, W.; Gennett, T. *Nano Lett.* **2002**, 2, 1329−1332.
(12) Kannan, R.; Kakade, B. A.; Pillai, V. K. *Angew. Chem., Int. Ed.* **2008**, 47, 2653−2656.
(13) Hamon, M. A.; Itkis, M. E.; Niyogi, S.; Alvaraez, T.; Kuper, C.; Menon, M.; Haddon, R. C. *J. Am. Chem. Soc.* **2001**, 123, 11292−11293.

(14) Yang, L.; Setyowati, K.; Li, A.; Gong, S.; Chen, J. *Adv. Mater.* **2008**, 20, 2271−2275.
(15) Rousseau, I. A. *Polym. Eng. Sci.* **2008**, 48, 2075−2089.
(16) Winey, K. I.; Kashiwagi, T.; Mu, M. *MRS Bull.* **2007**, 32, 348−353.
(17) Chen, J.; Liu, H.; Weimer, W. A.; Halls, M. D.; Waldeck, D. H.; Walker, G. C. *J. Am. Chem. Soc.* **2002**, *124*, 9034–9035.
(18) Ramasubramaniam, R.; Chen, J.; Liu, H. *Appl. Phys. Lett.* **2003**, *83*, 2928-2930.
(19) Chen, J.; Ramasubramaniam, R.; Xue, C.; Liu, H. *Adv. Funct. Mater.* **2006**, *16*, 114-119.
(20) Page, K. A.; Cable, K. M.; Moore, R. B. *Macromolecules* **2005**, 38, 6472−6484.
(21) Mauritz, K. A.; Moore, R. B. *Chem. Rev.* **2004**, 104, 4535−4585.
(22) Heitner-Wirguin, C. *Polymer* **1979**, *20*, 371-374.
(23) Lowry, S. R.; Mauritz, K. A. *J. Am. Chem. Soc.* **1980**, *102*, 4665-4667.
(24) Quezado, S.; Kwak, J. C. T.; Falk, M. *Can. J. Chem.* **1984**, *62*, 958-966.
(25) Cable, K. M.; Mauritz, K. A.; Moore, R. B. *J. Polym. Sci., Part B: Polym. Phys.* **1995**, *33*, 1065-1072.
(26) Goswami, S.; Klaus, S.; Benziger, J. *Langmuir* **2008**, 24, 8627−8633.
(27) Reddy, S.; Arzt, E.; del Campo, A. *Adv. Mater.* **2007**, 19, 3833−3837.
(28) Altebaeumer, T.; Gotsmann, B.; Pozidis, H.; Knoll, A.; Duerig, U. *Nano Lett*. **2008**, 8, 4398−4403.
(29) Xie, T.; Xiao, X.; Li, J.; Wang, R. *Adv. Mater*. **2010**, 22, 4390−4394.
(30) Wang, Z.; Hansen, C.; Ge, Q.; Maruf, S. H.; Ahn, D. U.; Qi, H. J.; Ding, Y. *Adv. Mater.* **2011**, 23, 3669−3673.
(31) Sun, T.; Feng, L.; Gao, X.; Jiang, L. *Acc. Chem. Res.* **2005**, 38, 644−652.
(32) Tuteja, A.; Choi, W.; McKinley, G. H.; Cohen, R. E.; Rubner, M. F. *MRS Bull.* **2008**, 33, 752−758.
(33) Guo, C.; Feng, L.; Zhai, J.; Wang, G.; Song, Y.; Jiang, L.; Zhu, D. *ChemPhysChem* **2004**, 5, 750−753.
(34) Blaiszik, B. J.; Kramer, S. L. B.; Olugebefola, S. C.; Moore, J. S.; Sottos, N. R.; White, S. R. *Annu. Rev. Mater. Res.* **2010**, 40, 179−211.
(35) Bergman, S. D.; Wudl, F. *J. Mater. Chem.* **2008**, 18, 41−62.
(36) Xiao, X.; Xie, T.; Cheng, Y.-T. *J. Mater. Chem.* **2010**, 20, 3508−3514.
(37) Rodriguez, E. D.; Luo, X.; Mather, P. T. *ACS Appl. Mater. Interfaces* **2011**, 3, 152−161.
(38) Burnworth, M.; Tang, L.; Kumpfer, J. R.; Duncan, A. J.; Beyer, F. L.; Fiore, G. L.; Rowan, S. J.; Weder, C. *Nature* **2011**, 472, 334−337.

Chapter 5: Electrical and Dielectric Properties of Hydroxylated Carbon Nanotube-Elastomer Composites

5.1 Introduction

High-dielectric-constant polymer composite materials may find applications in actuators for artificial muscles; capacitors for energy storage; high-*K* gate dielectric for flexible electronics; and sensors for mechanical strain, humidity, and gases. Electrically conductive carbon nanotubes (CNTs), owing to their large dielectric constant, are proven attractive fillers for high dielectric-constant nanocomposites.[1-8] However, the dramatic increase in dielectric constant in CNT-polymer composites is usually accompanied by a dramatic increase in dielectric loss and a significant decrease in dielectric strength, which are undesirable for many practical applications. How to solve this dilemma faced by electrically conductive CNTs remains a great challenge.

To realize the full potential of CNTs as a high-dielectric constant filler, innovative approaches are needed to maximize the increase in dielectric constant while minimizing the increase in dielectric loss in CNT-polymer composites. It is well-known that high-degree covalent functionalization of the CNT surface can significantly damage or even destroy the CNT's intrinsic properties, such as electrical conductivity.[9] We are interested in developing high-dielectric-constant carbon nanotube-polymer composites using core-shell multiwalled CNTs (MWNTs) as a filler, in which the outer graphene layer is covalently functionalized to become nonconducting, whereas the inner graphene layers are unfunctionalized and remain electrically conducting (Figure 5.1). This approach could ultimately allow us to dramatically increase the dielectric constant while minimizing the

amount of increase observed in the electrical conductivity and dielectric loss of the CNT-polymer composites. Although chemically functionalized MWNTs have been used previously to prepare high-dielectric-constant CNT-polymer composites in several studies, the main purpose of chemical functionalization was to achieve a better CNT dispersion in the polymer matrices.[6,8] The impact of covalent functionalization of nanotube surfaces on the dielectric constant and, most importantly, the dielectric loss of the CNT nanocomposites compared with pristine CNTs remains essentially unclear. For example, Li and co-workers reported that MWNT-poly(vinylidene fluoride) (PVDF) nanocomposites based on ester-functionalized MWNTs showed lower dielectric constants and dielectric losses than those based on pristine MWNTs ($MWNTs_{pristine}$), whereas MWNT-PVDF nanocomposites based on carboxylated MWNTs exhibited higher

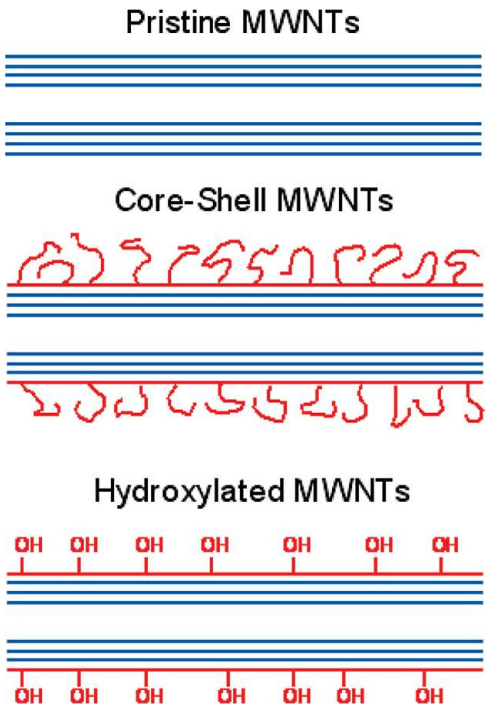

Figure 5.1. Schematic illustrations of the pristine MWNTs, core-shell MWNTs, and hydroxylated MWNTs, which represent one of the simplest types of core-shell MWNTs.

dielectric constants and dielectric losses than those based on $MWNTs_{pristine}$.[8] Previous research did not demonstrate the feasibility of using chemically functionalized MWNTs as a filler to increase the dielectric constant and reduce the dielectric loss of CNT-polymer nanocomposites. Hydroxylated MWNTs ($MWNTs_{OH}$) represent one of the simplest types of core-shell MWNTs (Figure 5.1). In this article, we report a comparative study of the electrical and dielectric properties of MWNT-polydimethylsiloxane (PDMS) composites based on $MWNTs_{pristine}$ and $MWNTs_{OH}$, respectively. We demonstrate for the first time the feasibility of using core-shell MWNTs as a filler to increase the dielectric constant and reduce the dielectric loss of CNT-polymer nanocomposites.

5.2 Experimental

$MWNTs_{pristine}$ and $MWNTs_{OH}$ were purchased from Nanostructured & Amorphous Materials, Inc. According to the manufacturer's specification sheets, the purity, outer diameter, and length of both $MWNTs_{pristine}$ and $MWNTs_{OH}$ are 95%, 10-20 nm, and 10-30 μm, respectively, and the content of -OH in $MWNTs_{OH}$ is about 1-7 wt.% . Sylgard 184 PDMS base and curing agent were supplied from Dow Corning Corporation. A suspension of MWNTs in chloroform was first sonicated in a bath sonicator for 30 min and then mixed with PDMS base by stirring. Removing part of the chloroform from the resulting mixture by evaporation produced a viscous gellike liquid, which was then mixed with PDMS curing agent by stirring. The ratio of PDMS curing agent to base was 1:10. The resulting gel-like liquid was cast into a mold and dried very slowly at room temperature overnight to remove the remaining chloroform. The resulting material was then cured at 80 °C for 4 h to give a flexible MWNT-PDMS composite disk. MWNT-PDMS composites with various MWNT types and loadings were prepared according to

the above procedure. Pure PDMS samples were made following the manufacture's procedure with the same ratio of PDMS curing agent to base (1:10) and the same curing condition (80 °C for 4 h). The two-point probe measurement for the direct current electrical conductivity study was performed using a Keithley 2400 source meter and Keithley 6485 picoammeter (for low current) instrument through the computer controlled LabVIEW program. The Lucas Laboratories Pro4 system was used for the four-point probe measurement. The dielectric properties were measured using an Agilent E4980A LCR meter at room temperature with an Agilent 16451B dielectric test fixture. Scanning electron microscopy (SEM) was performed using a Hitachi S-4800 field emission scanning electron microscope (accelerating voltage, 1 kV). No sample coating was used in the SEM experiment to avoid possible artifacts induced by the metal coating. Energy dispersive X-ray spectroscopy (EDS) was performed with the same SEM instrument and was calibrated with dibenzo-18-crown-6.

5.3 Results and Discussion

The $MWNTs_{OH}$ were chosen as the model core-shell MWNTs in this study mainly for two reasons: (1) The $MWNT_{OH}$ material is commercially available and (2) it is possible to convert the hydroxyl group to much longer linear or branched insulating polymer chains using various polymer grafting techniques (e.g., atom transfer radical polymerization) in future studies. The calibrated EDS could be used to estimate the degree of functionalization in covalently functionalized CNTs.[10-12] The EDS showed the presence of ~7.3 wt.% of O in the $MWNT_{OH}$ material, which provides an estimate of the amount of hydroxyl groups in $MWNTs_{OH}$ (~1 -OH group/17 C_{MWNT}). In contrast, no oxygen was detected by the EDS in the $MWNTs_{pristine}$.

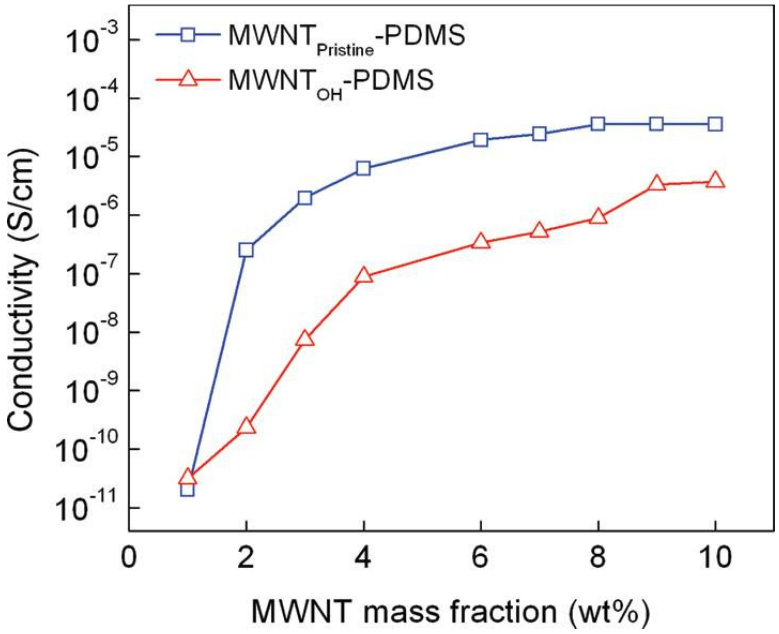

Figure 5.2. Room temperature two-point probe electrical conductivity of the MWNT-PDMS composites as a function of MWNT mass fraction (wt.%).

Figure 5.2 shows the measured two-point probe electrical conductivity of the MWNT-PDMS composites as a function of the MWNT loading. The conductivity of the $MWNT_{pristine}$-PDMS composite increases sharply between 1 and 2 wt.% of nanotube loading, indicating the formation of a percolating network. In contrast, the conductivity of the $MWNT_{OH}$-PDMS composite increases less sharply but still rapidly in a broader range between 1 and 4 wt.% of nanotube loading, suggesting a higher percolation threshold of the $MWNT_{OH}$-PDMS composites as compared with that of the $MWNT_{pristine}$-PDMS composites. In addition, the electrical conductivity of the $MWNT_{OH}$-PDMS composites is consistently 1-3 orders of magnitude lower than that of the $MWNT_{pristine}$-PDMS composites at the same MWNT loading (Figure 5.2). Although both $MWNTs_{pristine}$ and $MWNTs_{OH}$ have similar purity levels, diameters, and lengths, hydroxylation of MWNTs significantly interrupts the π-conjugation of the outer

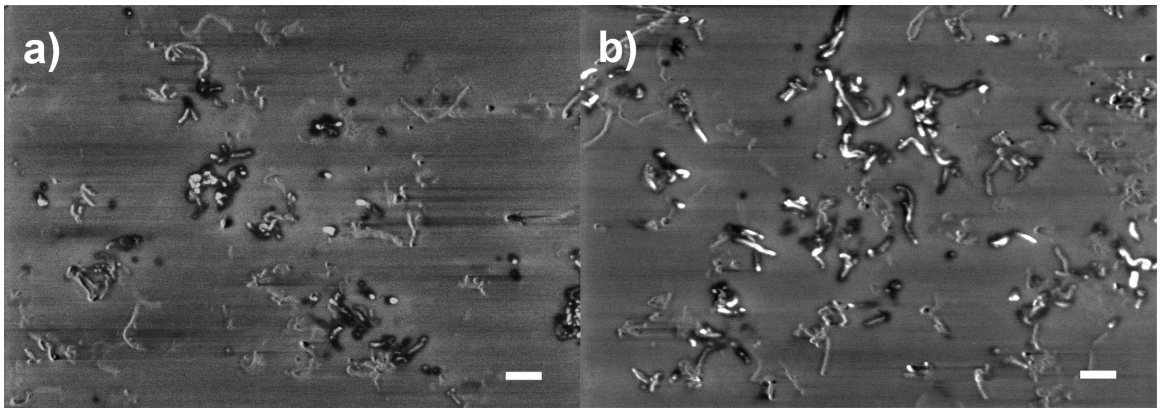

Figure 5.3. SEM images of (a) the 7 wt.% $MWNT_{pristine}$-PDMS composite and (b) the 7 wt.% $MWNT_{OH}$-PDMS composite. Scale bar: 400 nm.

graphene layer and diminishes the surface electrical conductivity of MWNTs, leading to a higher percolation threshold and dramatically lower electrical conductivity in the $MWNT_{OH}$-PDMS composites. There is no significant difference between the two-point probe and four-point probe conductivities of the same sample: for example, the two-point probe/four-point probe conductivities of the 6 and 9 wt.% $MWNT_{pristine}$-PDMS composites are $1.93 \times 10^{-5}/2.14 \times 10^{-5}$ and $3.60 \times 10^{-5}/3.70 \times 10^{-5}$ S/cm, respectively. This is consistent with our previous experimental observation on other CNT-polymer nanocomposites.[13] SEM images reveal similar dispersion of MWNTs in both $MWNT_{pristine}$-PDMS and $MWNT_{OH}$-PDMS composites at the same MWNT loading level (Figure 5.3). Prior study showed that the incorporation of MWNTs in the PDMS matrix could also increase the Young's modulus of resulting polymer composites.[14]

Figure 5.4a and d shows the room temperature dielectric constant and dielectric loss of the MWNT-PDMS composites as a function of the MWNT loading at 1 kHz, respectively. The inclusion of $MWNTs_{pristine}$ in the PDMS matrix significantly increases the dielectric constant from 3.3 (pure PDMS) to ~1554 at 1 kHz with 6 wt.% of $MWNT_{pristine}$ loading (Figure 5.4a); however, the dielectric loss also dramatically

increases from 0.01 for the pure PDMS to ~3.74 for the 6 wt.% $MWNT_{pristine}$-PDMS composite (Figure 5.4d). Compared with the $MWNT_{pristine}$-PDMS composites, the core-shell MWNT-polymer composite enables a higher MWNT loading level while still keeping the electrical conductivity relatively low (Figure 5.2). Therefore, it is possible to achieve a much higher dielectric constant in the core-shell MWNT-polymer composite while still maintaining similar or lower dielectric loss. For example, the introduction of $MWNTs_{OH}$ into the PDMS matrix dramatically increases the dielectric constant from 3.3 (pure PDMS) to ~3221 at 1 kHz with 9 wt.% of $MWNT_{OH}$ loading (Figure 5.4a), which is approximately twice the dielectric constant (~1554) of the 6 wt.% $MWNT_{pristine}$-PDMS composite. In the meantime, the dielectric loss (~4.00) of the 9 wt.% $MWNT_{OH}$PDMS composite is similar to that (~3.74) of the 6 wt.% $MWNT_{pristine}$-PDMS composite (Figure 5.4d). Although the dielectric constant of the 9 wt.% $MWNT_{pristine}$-PDMS composite approaches ~2076, its dielectric loss either reaches or exceeds our instrument's maximum measurement limit, which is 10.

The benefit of core-shell MWNT-polymer composites is even more obvious at 10 kHz. Figure 5.4b and e shows the room temperature dielectric constant and dielectric loss of the MWNT-PDMS composites as a function of the MWNT loading at 10 kHz, respectively. The inclusion of $MWNTs_{pristine}$ in the PDMS matrix significantly increases the dielectric constant from 3.3 (pure PDMS) to ~875 at 10 kHz with 6 wt.% of $MWNT_{pristine}$ loading (Figure 5.4b). As expected, the dielectric loss also dramatically increases from 0.01 for the pure PDMS to ~1.25 for the 6 wt.% $MWNT_{pristine}$-PDMS composite (Figure 5.4e). The introduction of $MWNTs_{OH}$ into the PDMS matrix

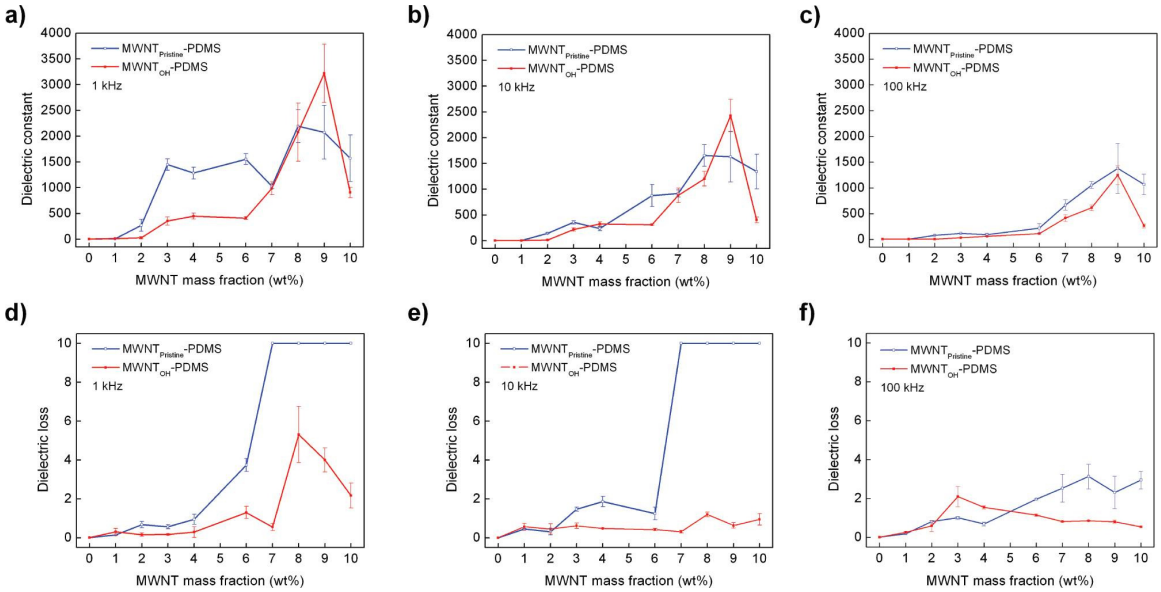

Figure 5.4. Room temperature dielectric constant of the MWNT-PDMS composites as a function of MWNT mass fraction (wt.%) at (a) 1, (b) 10, and (c) 100 kHz, respectively. Room temperature dielectric loss of MWNT-PDMS composites as a function of MWNT mass fraction (wt.%) at (d) 1, (e) 10, and (f) 100 kHz, respectively. The dielectric loss value of 10 indicates that the dielectric loss either reaches or exceeds our instrument's maximum measurement limit, which is 10.

dramatically increases the dielectric constant from 3.3 (pure PDMS) to ~2429 at 10 kHz with 9 wt.% of $MWNT_{OH}$ loading (Figure 5.4b), which is nearly 3 times the dielectric constant (~875) of the 6 wt.% $MWNT_{pristine}$-PDMS composite. Meanwhile, the dielectric loss (~0.63) of the 9 wt.% $MWNT_{OH}$-PDMS composite is much lower than that (~1.25) of the 6 wt.% $MWNT_{pristine}$-PDMS composite (Figure 5.4e). For comparison, the dielectric constant and dielectric loss of the 9 wt.% $MWNT_{pristine}$-PDMS composite are ~1631 and ≥10, respectively.

A similar trend is also observed at 100 kHz (Figure 5.4c and f). Whereas the dielectric constant (~1249) of the 9 wt.% $MWNT_{OH}$-PDMS composite is close to that (~1382) of the 9 wt.% $MWNT_{pristine}$-PDMS composite, its dielectric loss (~0.80) is much lower than that (~2.31) of the 9 wt.% $MWNT_{pristine}$-PDMS composite.

5.4 Conclusion

We demonstrate for the first time the feasibility of using core-shell MWNTs as a filler to increase the dielectric constant and reduce the dielectric loss of CNT-polymer nanocomposites. Since $MWNTs_{OH}$ represent only one of the simplest types of core-shell MWNTs (Figure 5.1), we believe optimizing the core-shell MWNTs would further maximize the increase in dielectric constant while minimizing the potential increase in dielectric loss of the core-shell MWNT-polymer composites. For example, it is possible to convert the hydroxyl group to much longer linear or branched insulating polymer chains using various polymer grafting techniques (e.g., atom transfer radical polymerization), which should considerably reduce the surface electrical conductivity of the core-shell MWNTs.

5.5 References

(1) Benedict, L. X.; Louie, S. G.; Cohen, M. L. *Phys. Rev. B* **1995**, *52*, 8541–8549.
(2) Krupke, R.; Hennrich, F.; Lohneysen, H. v.; Kappes, M. M. *Science* **2003**, *301*, 344–347.
(3) Kozinsky, B.; Marzari, N. *Phys. Rev. Lett.* **2006**, *96*, 166801.
(4) Wang, L.; Dang, Z. M. *Appl. Phys. Lett.* **2005**, *87*, 042903.
(5) Ahmad, K.; Pan, W.; Shi, S. L. *Appl. Phys. Lett.* **2006**, *89*, 133122.
(6) Dang, Z. M.; Wang, L.; Yin, Y.; Zhang, Q.; Lei, Q. Q. *Adv. Mater.* **2007**, *19*, 852–857.
(7) Jiang, M. J.; Dang, Z. M.; Xu, H. P. *Appl. Phys. Lett.* **2007**, *90*, 042914.
(8) Li, Q.; Xue, Q.; Hao, L.; Gao, X.; Zheng, Q. *Compos. Sci. Technol.* **2008**, *68*, 2290–2296.
(9) Georgakilas, V.; Kordatos, K.; Prato, M.; Guldi, D. M.; Holzinger, M.; Hirsch, A. *J. Am. Chem. Soc.* **2002**, *124*, 760–761.
(10) Chen, J.; Hamon, M. A.; Hu, H.; Chen, Y.; Rao, A. M.; Eklund, P. C.; Haddon, R. C. *Science* **1998**, *282*, 95–98.
(11) Chen, J.; Rao, A. M.; Lyuksyutov, S.; Itkis, M. E.; Hamon, M. A.; Hu, H.; Cohn, R. W.; Eklund, P. C.; Colbert, D. T.; Smalley, R. E.; Haddon, R. C. *J. Phys. Chem. B.* **2001**, *105*, 2525–2528.
(12) Hu, H.; Zhao, B.; Hamon, M. A.; Kamaras, K.; Itkis, M. E.; Haddon, R. C. *J. Am. Chem. Soc.* **2003**, *125*, 14893–14900.

(13) Sankapal, B. R.; Setyowati, K.; Chen, J.; Liu, H. *Appl. Phys. Lett.* **2007**, *91*, 173103.
(14) Ahir, S. V.; Squires, A. M.; Tajbakhsh, A. R.; Terentjev, E. M. *Phys. Rev. B* **2006**, *73*, 085420.

APPENDIX A: ^{1}H-NMR, ^{13}C-NMR, and mass spectra of compounds **1**, **3-10**, **12**, **13**

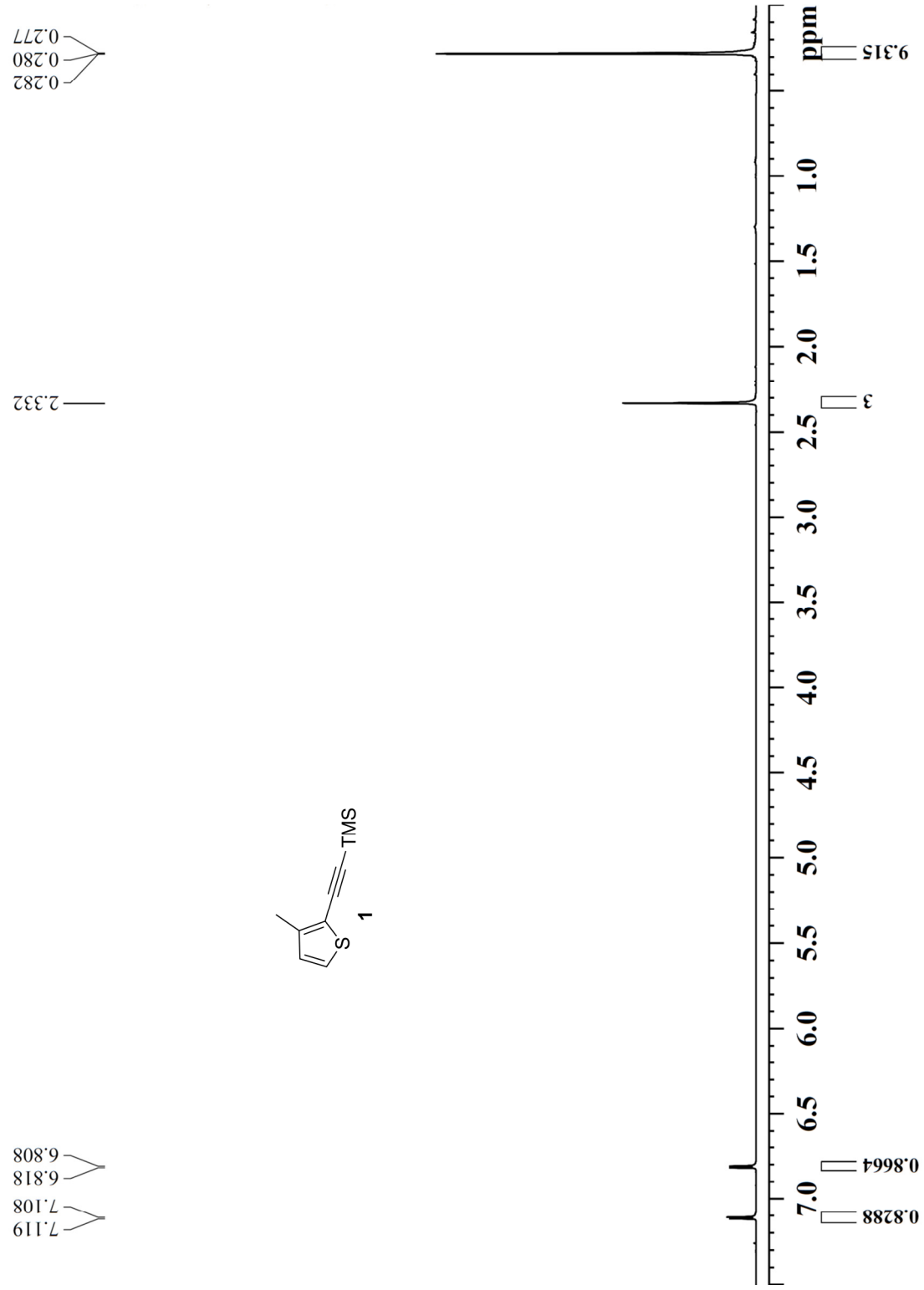

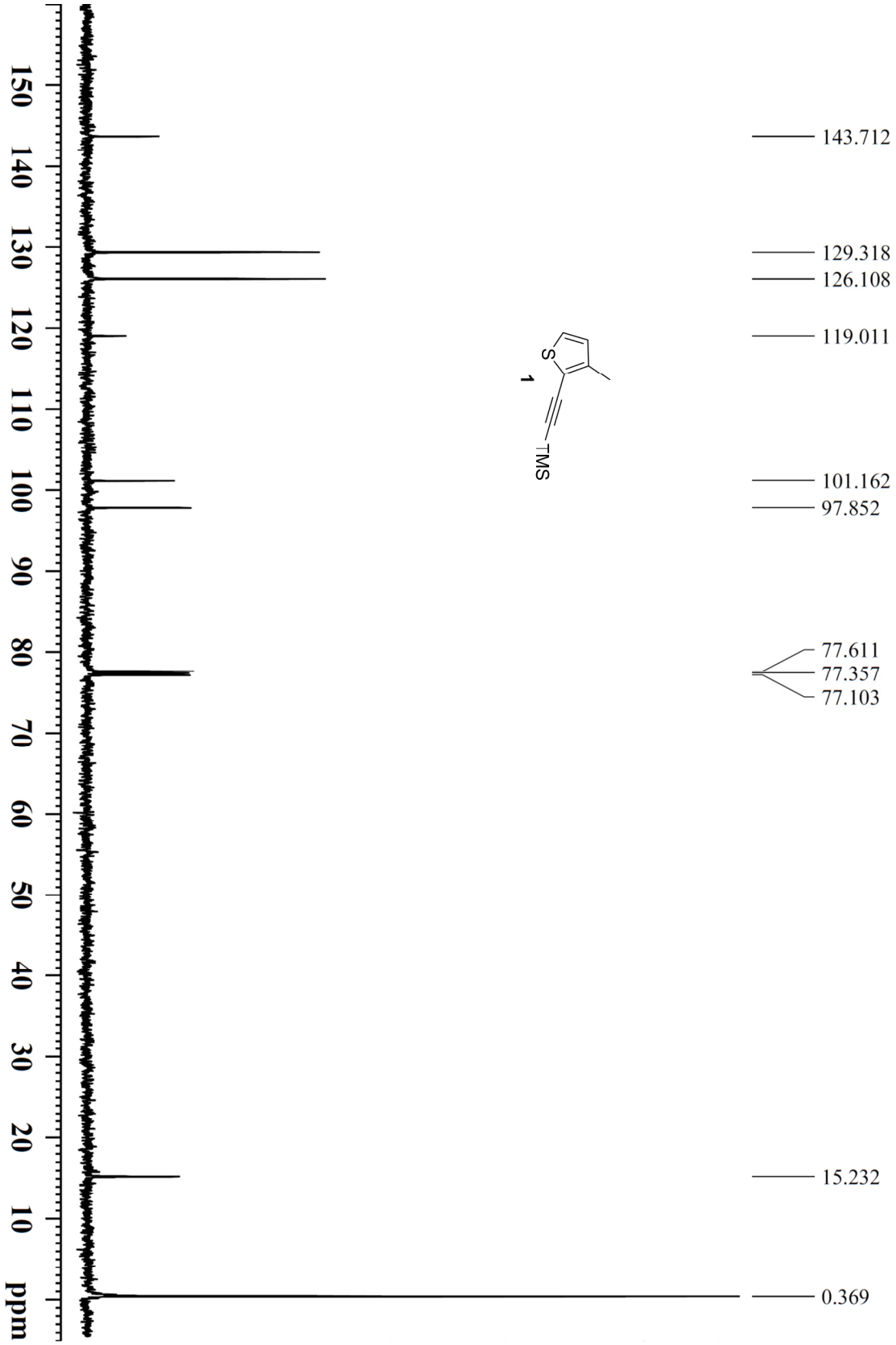
150
140
130
120
110
100
90
80
70
60
50
40
30
20
10
ppm
143.712
129.318
126.108
119.011
101.162
97.852
77.611
77.357
77.103
15.232
0.369
S
1
TMS

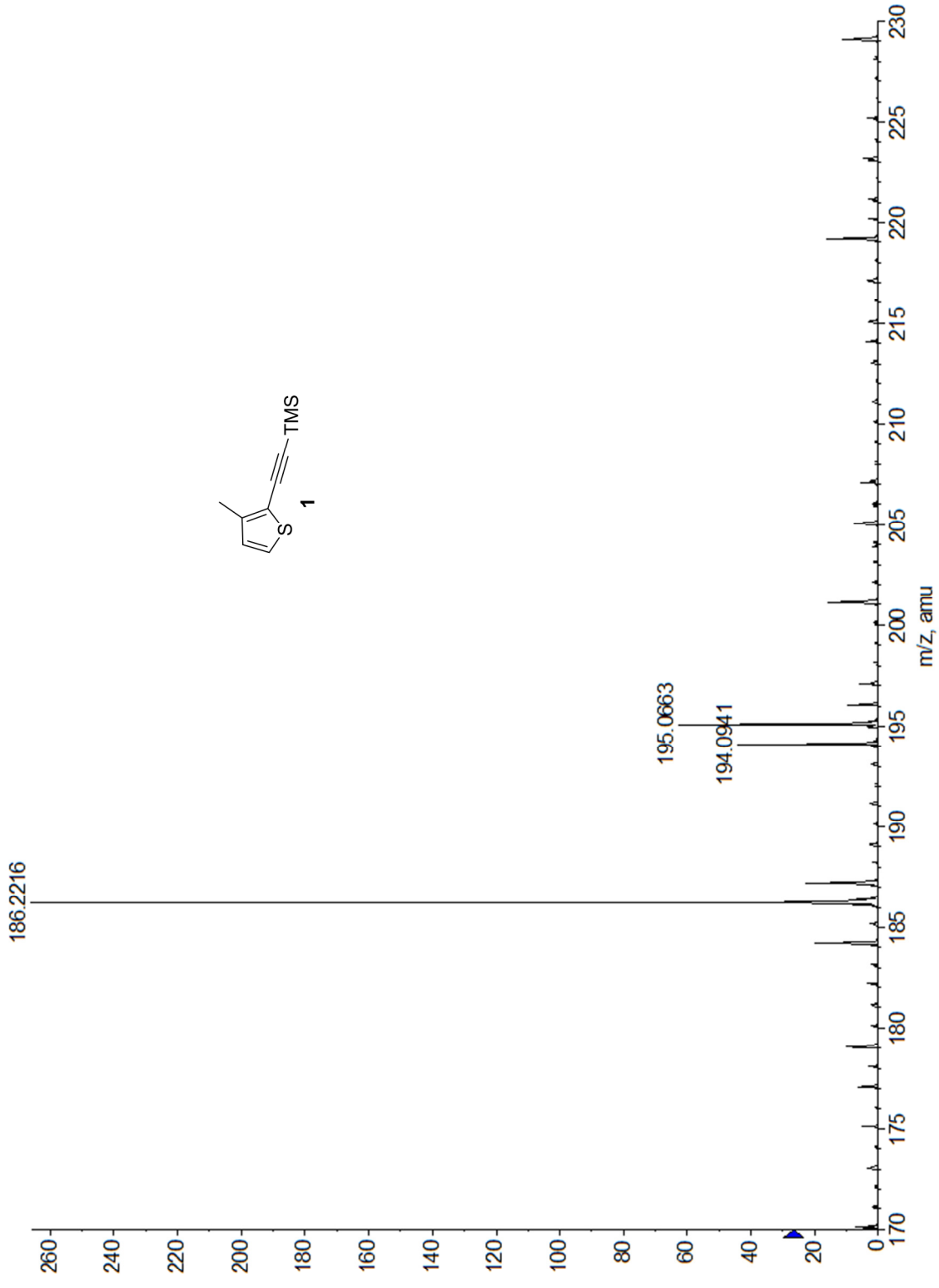
TMS
S
1
186.2216
195.0663
194.0941
m/z, amu

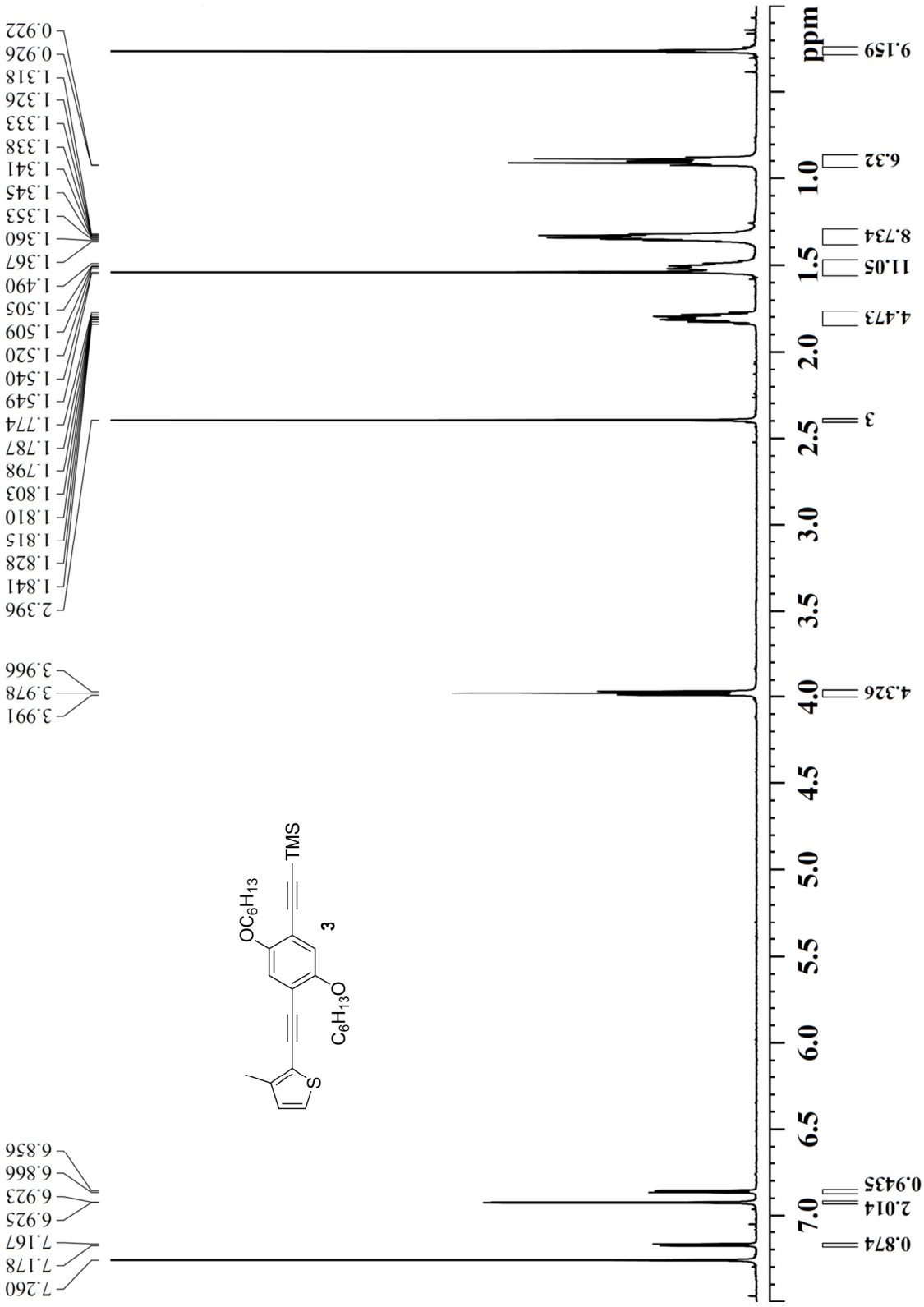
ppm
9.159
6.32
8.734
11.05
4.473
3
4.326
0.874
2.014
0.9435
7.260
7.178
7.167
6.925
6.923
6.866
6.856
3.991
3.978
3.966
2.396
1.841
1.828
1.815
1.810
1.803
1.798
1.787
1.774
1.549
1.540
1.520
1.509
1.505
1.490
1.367
1.360
1.353
1.345
1.341
1.338
1.333
1.326
1.318
0.926
0.922
TMS
OC6H13
C6H13O
S
3

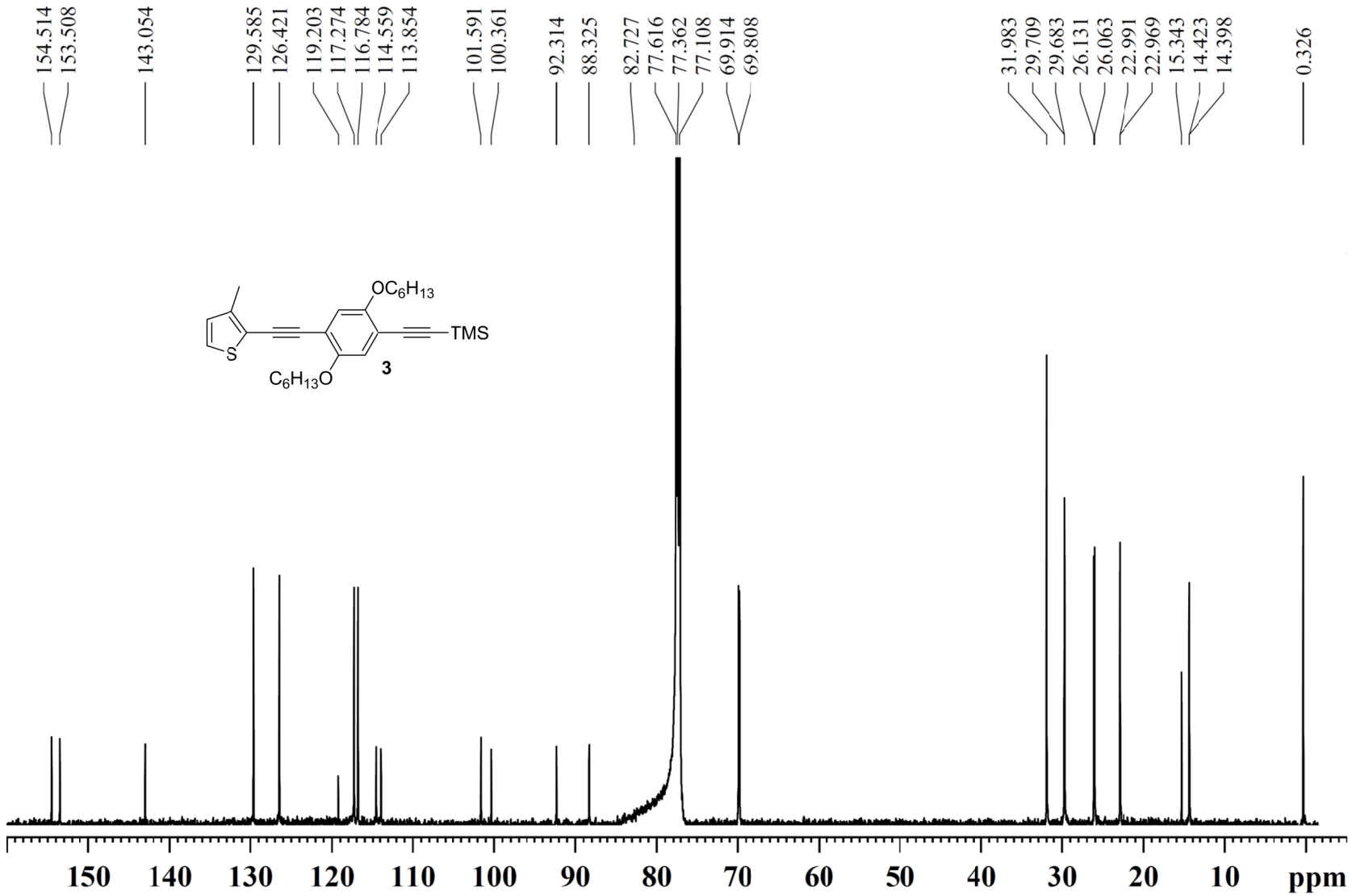
154.514
153.508
143.054
129.585
126.421
119.203
117.274
116.784
114.559
113.854
101.591
100.361
92.314
88.325
82.727
77.616
77.362
77.108
69.914
69.808
31.983
29.709
29.683
26.131
26.063
22.991
22.969
15.343
14.423
14.398
0.326
OC6H13
TMS
S
C6H13O
3
150
140
130
120
110
100
90
80
70
60
50
40
30
20
10
ppm

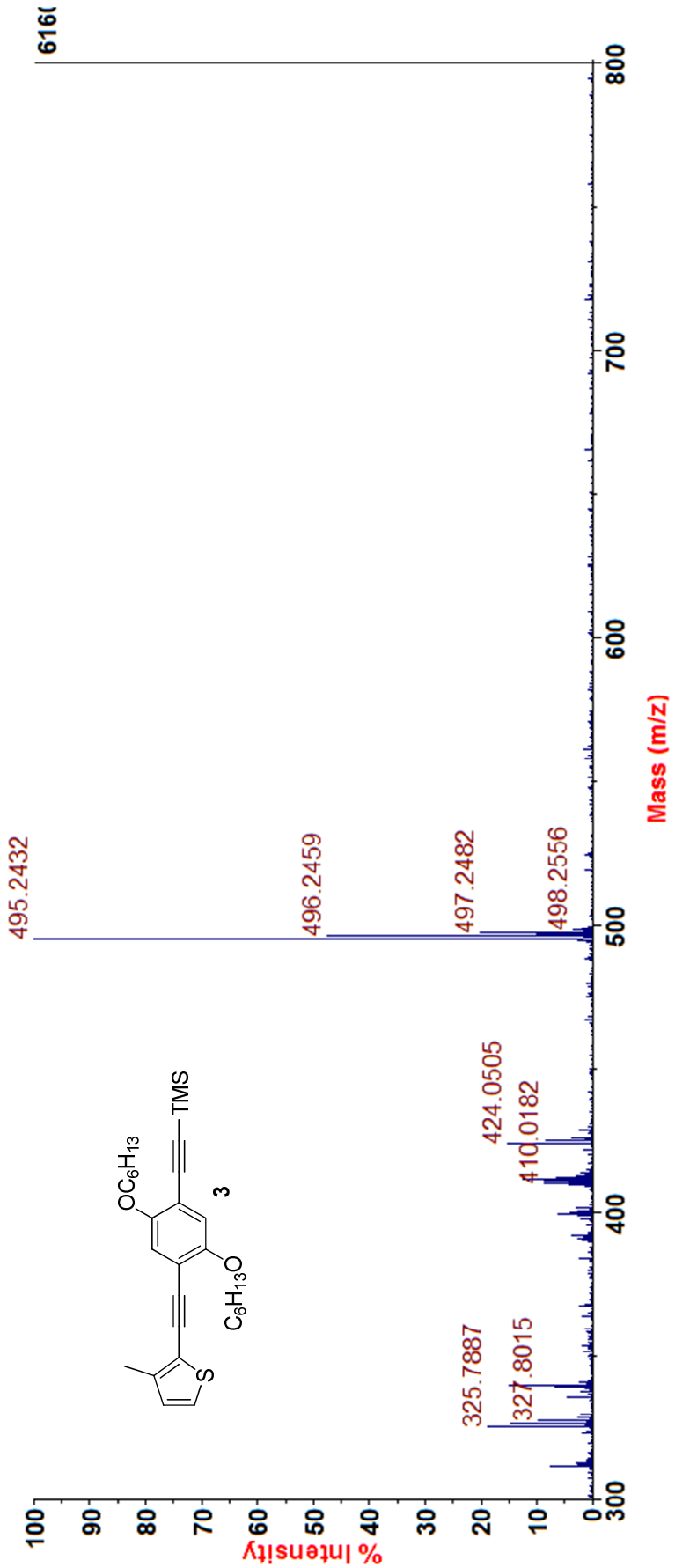
6161
495.2432
496.2459
497.2482
498.2556
424.0505
410.0182
325.7887
327.8015
TMS
OC_6H_{13}
$C_6H_{13}O$
S
3
% Intensity
Mass (m/z)
100
90
80
70
60
50
40
30
20
10
0
300
400
500
600
700
800

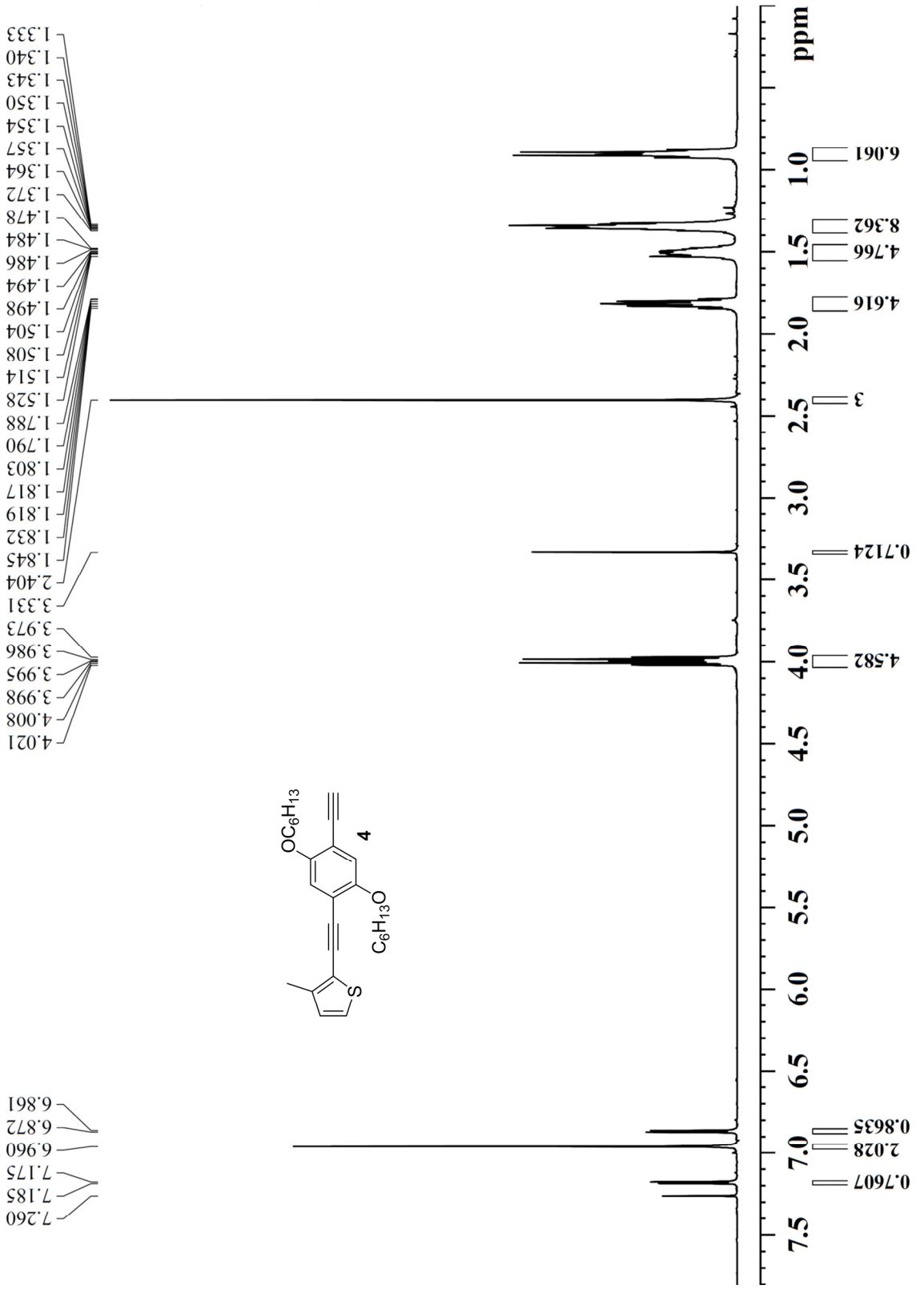
ppm
7.5
7.0
6.5
6.0
5.5
5.0
4.5
4.0
3.5
3.0
2.5
2.0
1.5
1.0
0.7607
2.028
0.8635
4.582
0.7124
3
4.616
4.766
8.362
6.061
4
OC6H13
C6H13O
S
7.260
7.185
7.175
6.960
6.872
6.861
4.021
4.008
3.998
3.995
3.986
3.973
3.331
2.404
1.845
1.832
1.819
1.817
1.803
1.790
1.788
1.528
1.514
1.508
1.504
1.498
1.494
1.486
1.484
1.478
1.372
1.364
1.357
1.354
1.350
1.343
1.340
1.333

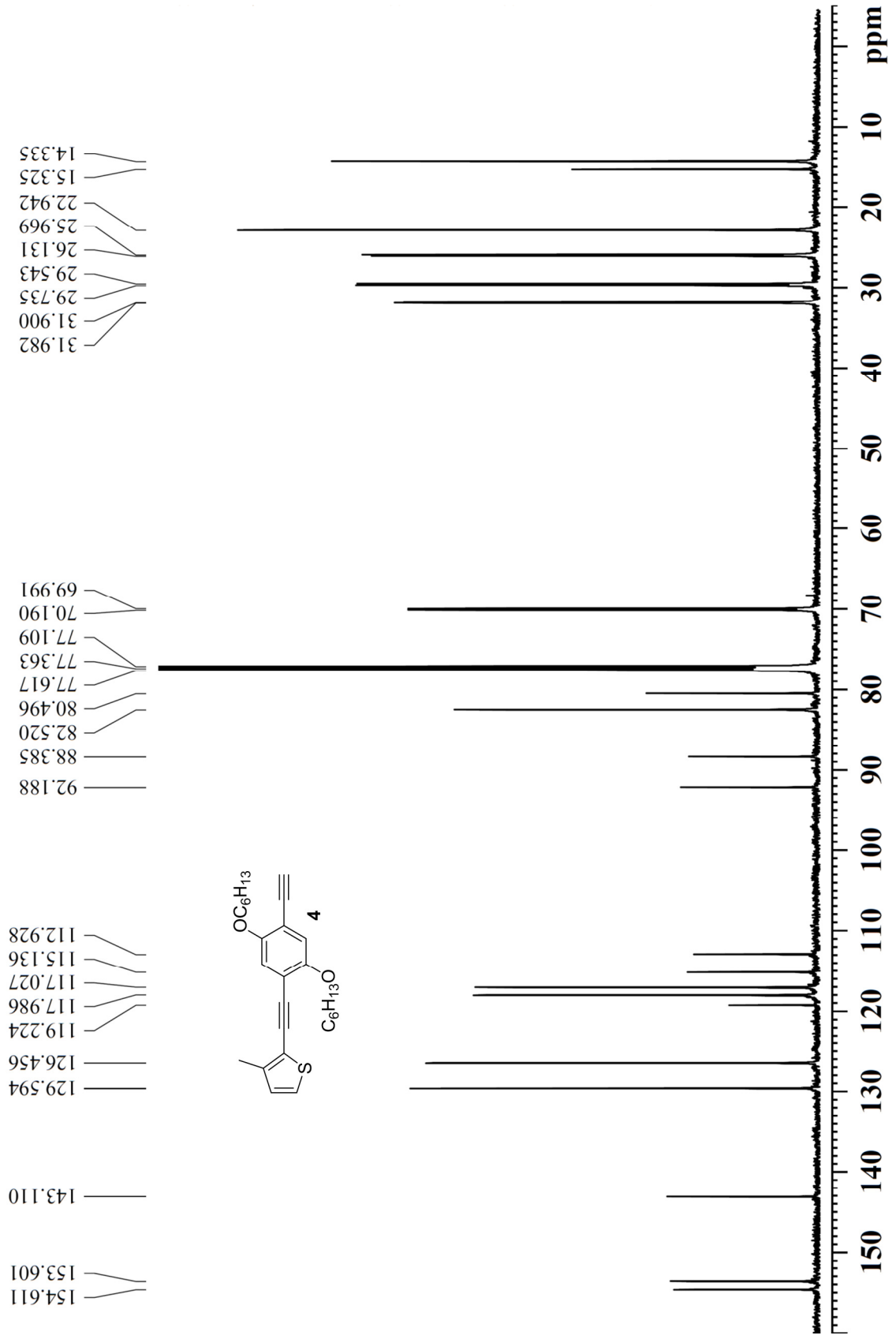
ppm
10
20
30
40
50
60
70
80
90
100
110
120
130
140
150
14.335
15.325
22.942
25.969
26.131
29.543
29.735
31.900
31.982
69.991
70.190
77.109
77.363
77.617
80.496
82.520
88.385
92.188
112.928
115.136
117.027
117.986
119.224
126.456
129.594
143.110
153.601
154.611
4
OC6H13
C6H13O
S

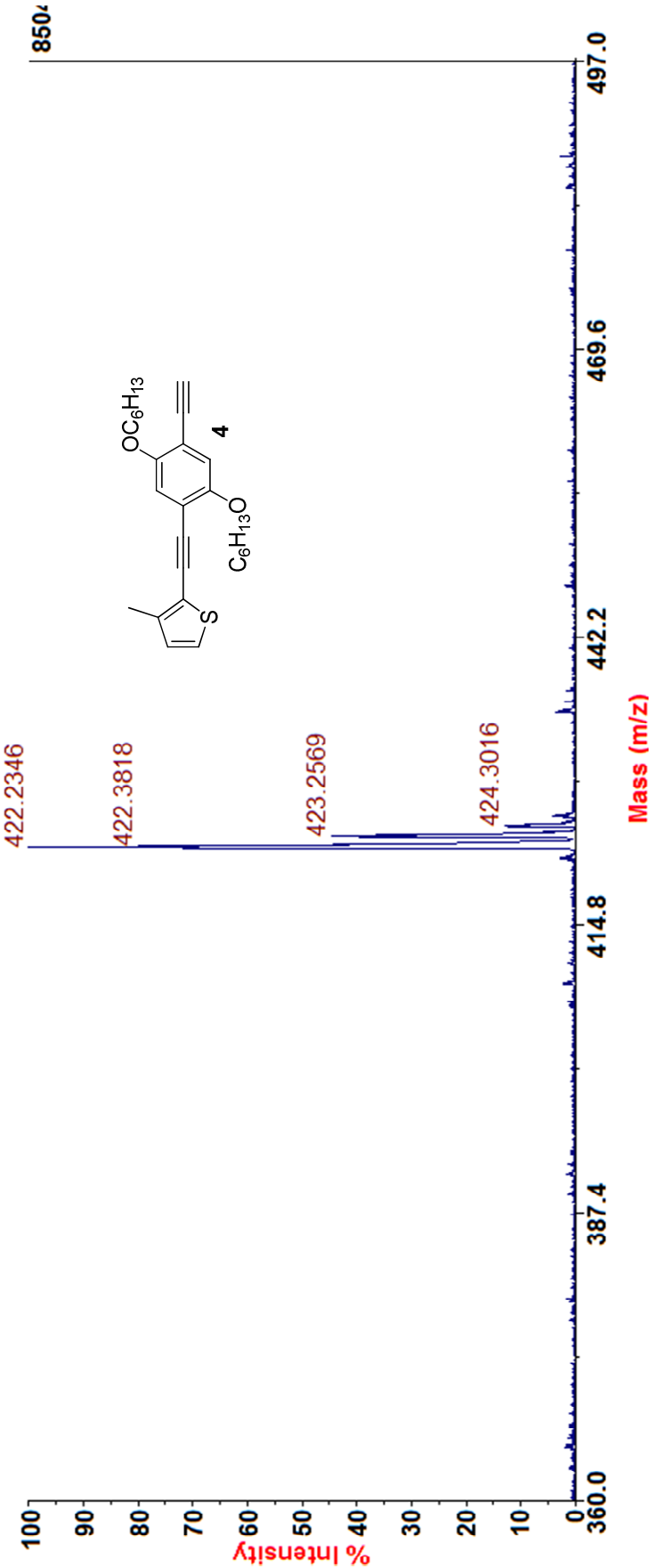
850
497.0
469.6
442.2
414.8
387.4
360.0
Mass (m/z)
422.2346
422.3818
423.2569
424.3016
100
90
80
70
60
50
40
30
20
10
0
% Intensity
OC6H13
C6H13O
S
4

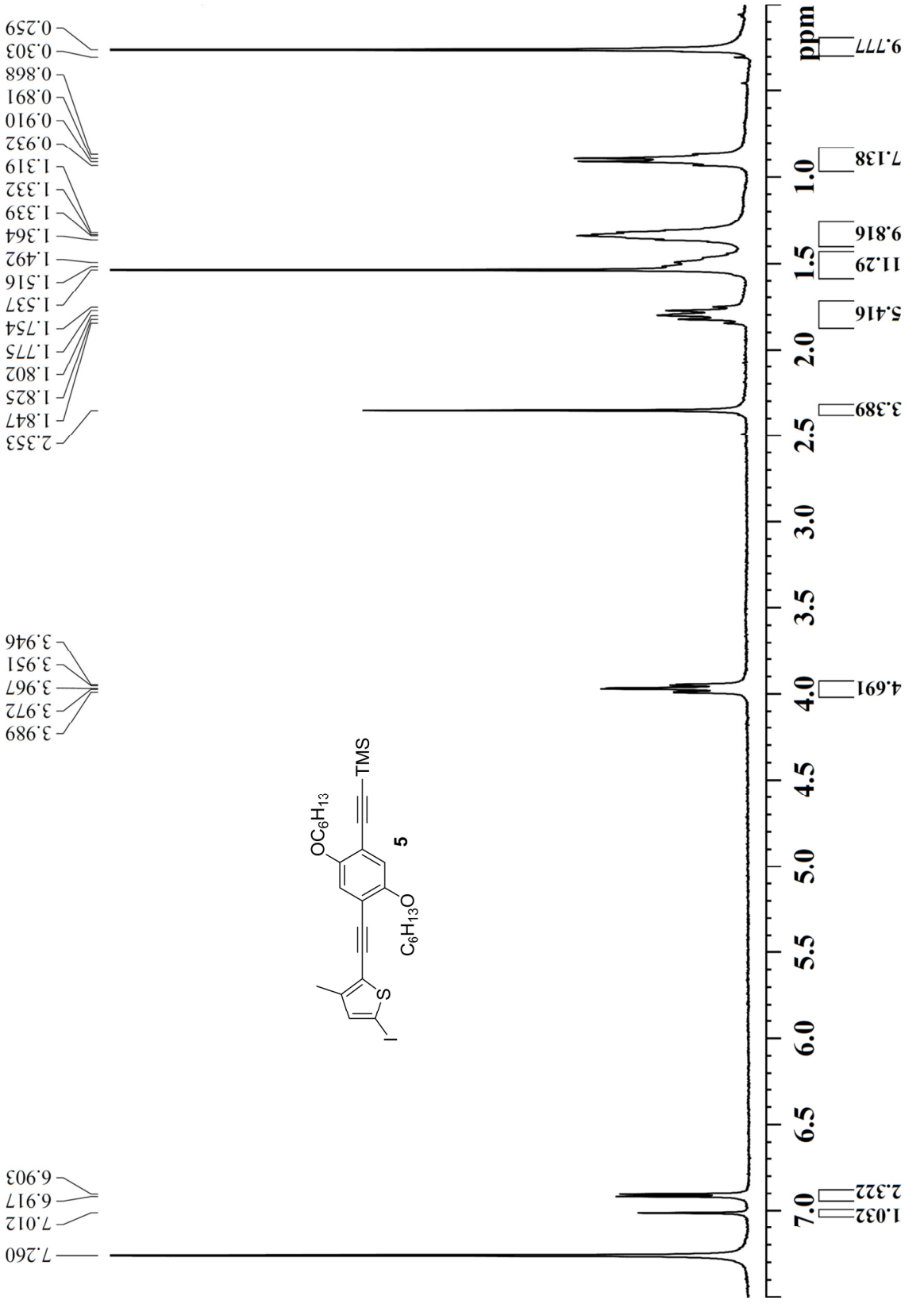
ppm
9.777
7.138
9.816
11.29
5.416
3.389
4.691
2.322
1.032
7.260
7.012
6.917
6.903
3.989
3.972
3.967
3.951
3.946
2.353
1.847
1.825
1.802
1.775
1.754
1.537
1.516
1.492
1.364
1.339
1.332
1.319
0.932
0.910
0.891
0.868
0.303
0.259
TMS
OC6H13
C6H13O
S
I
5

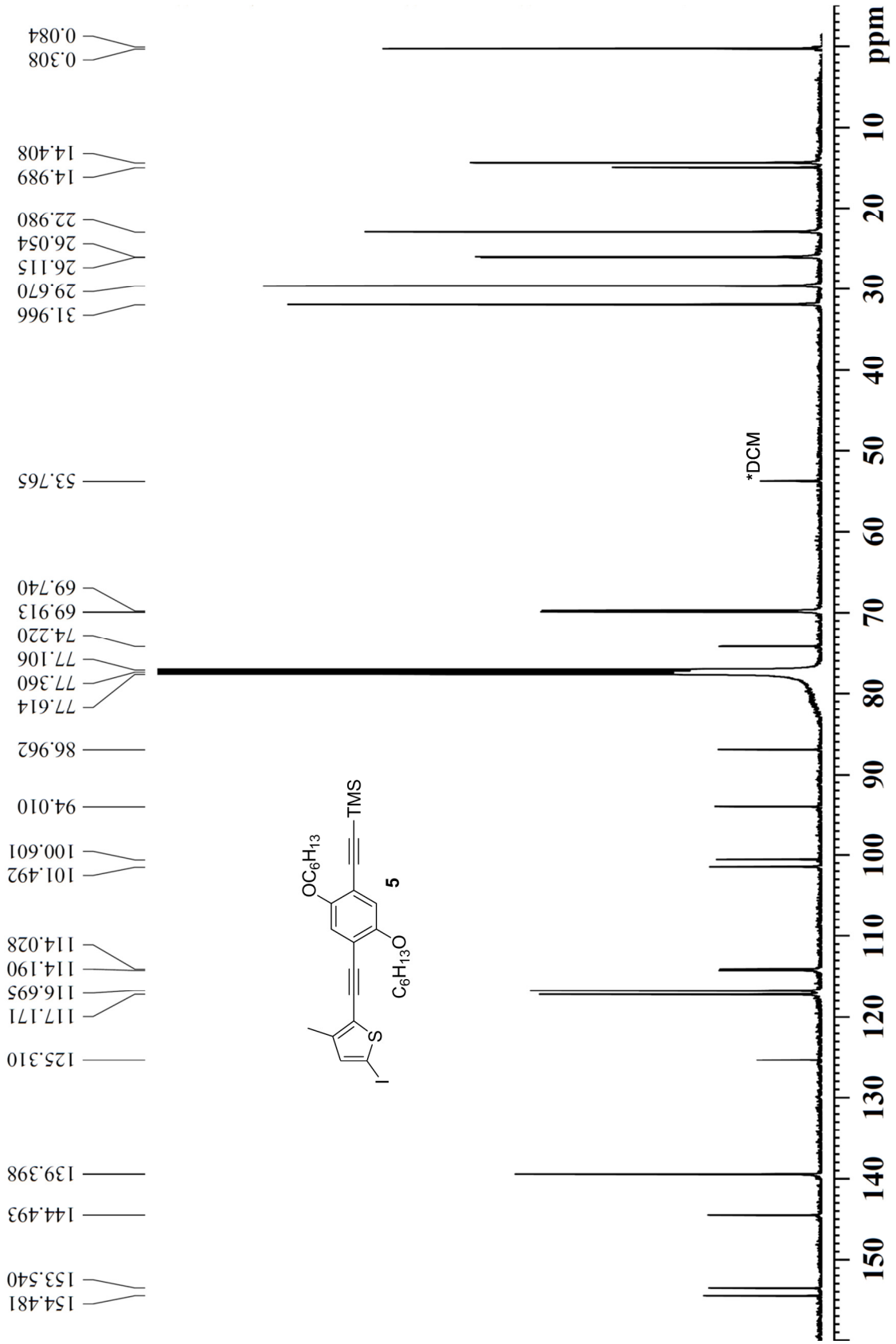
ppm
*DCM
TMS
OC_6H_{13}
$C_6H_{13}O$
S
I
5
0.084
0.308
14.408
14.989
22.980
26.054
26.115
29.670
31.966
53.765
69.740
69.913
74.220
77.106
77.360
77.614
86.962
94.010
100.601
101.492
114.028
114.190
116.695
117.171
125.310
139.398
144.493
153.540
154.481

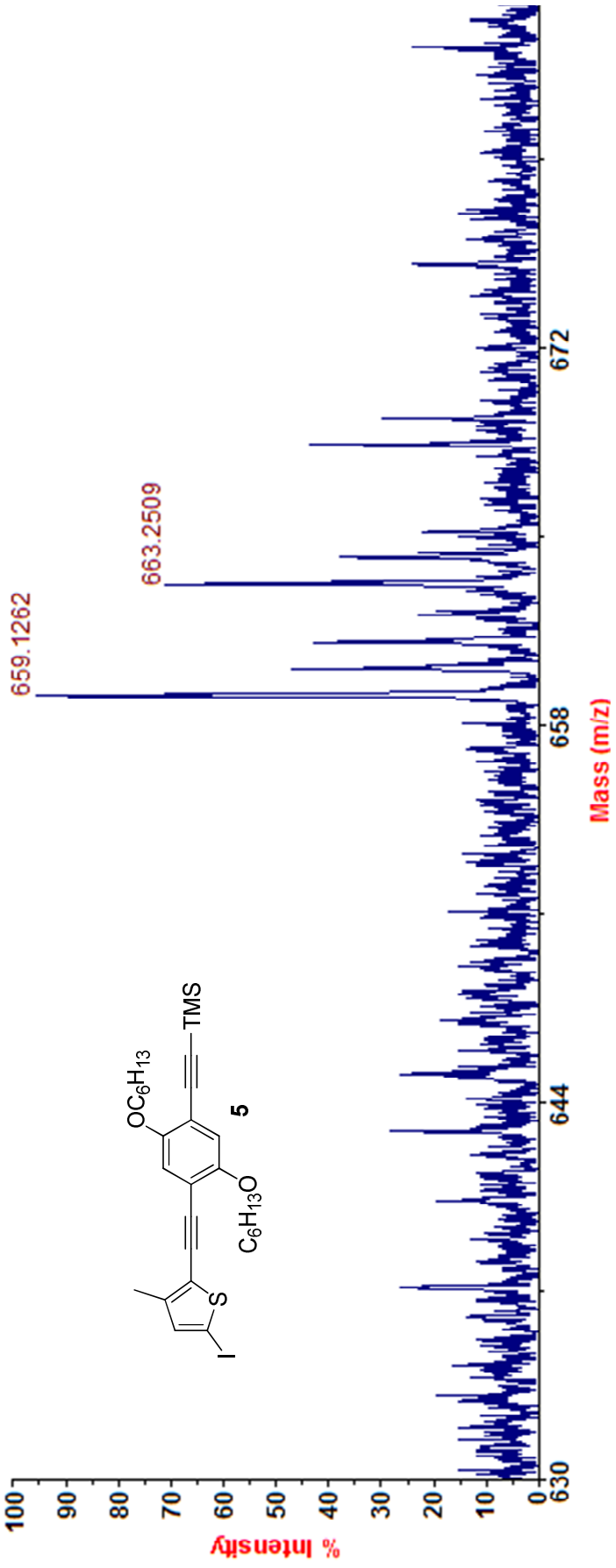
659.1262
663.2509
100
90
80
70
60
50
40
30
20
10
0
% Intensity
630
644
658
672
Mass (m/z)
OC6H13
TMS
5
C6H13O
S
I

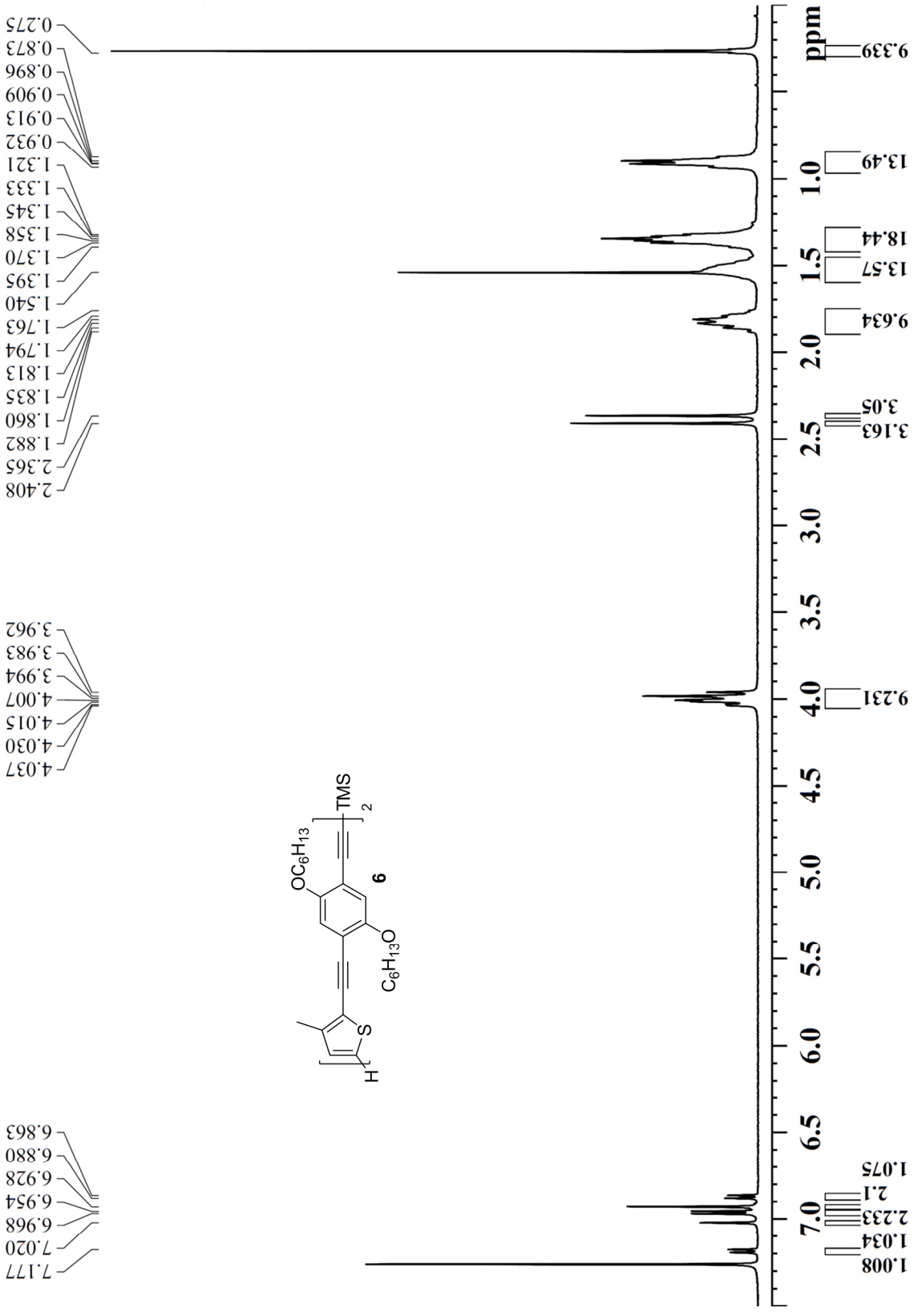
ppm
9.339
13.49
18.44
13.57
9.634
3.163
3.05
9.231
1.008
1.034
2.233
2.1
1.075
7.177
7.020
6.968
6.954
6.928
6.880
6.863
4.037
4.030
4.015
4.007
3.994
3.983
3.962
2.408
2.365
1.882
1.860
1.835
1.813
1.794
1.763
1.540
1.395
1.370
1.358
1.345
1.333
1.321
0.932
0.913
0.909
0.896
0.873
0.275
TMS
2
OC6H13
6
C6H13O
S
H

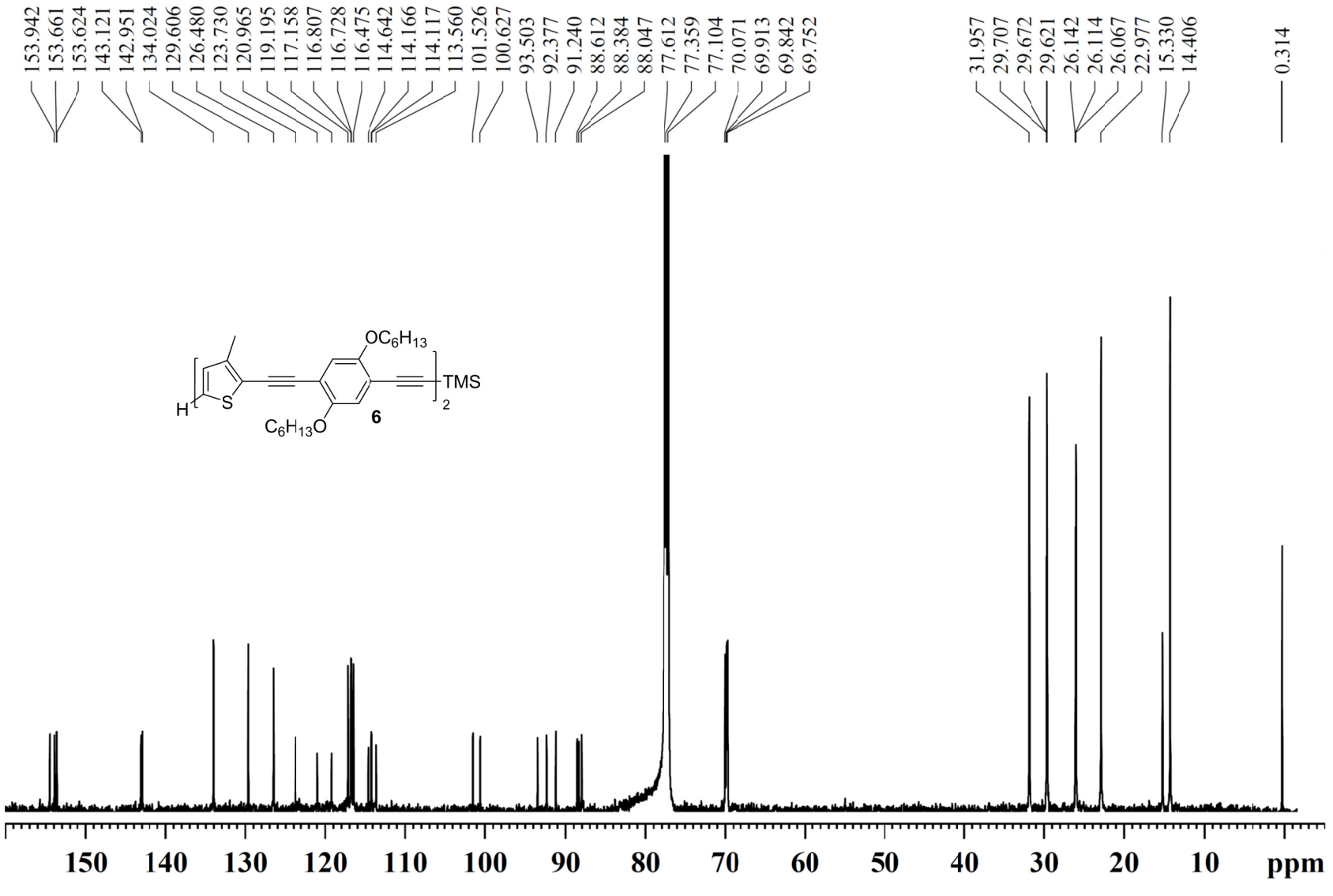
153.942
153.661
153.624
143.121
142.951
134.024
129.606
126.480
123.730
120.965
119.195
117.158
116.807
116.728
116.475
114.642
114.166
114.117
113.560
101.526
100.627
93.503
92.377
91.240
88.612
88.384
88.047
77.612
77.359
77.104
70.071
69.913
69.842
69.752
31.957
29.707
29.672
29.621
26.142
26.114
26.067
22.977
15.330
14.406
0.314
OC6H13
TMS
H
S
C6H13O
2
6
150
140
130
120
110
100
90
80
70
60
50
40
30
20
10
ppm

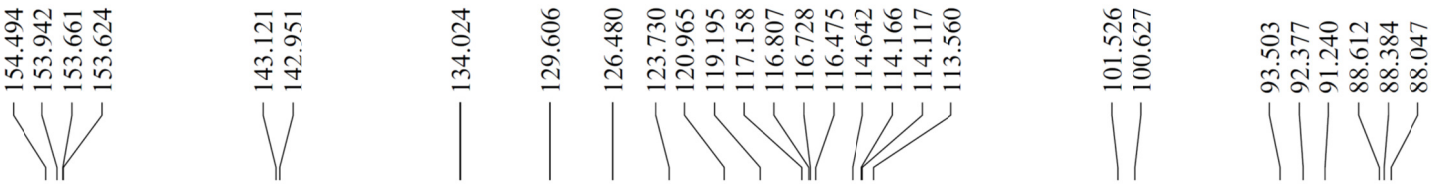
154.494
153.942
153.661
153.624
143.121
142.951
134.024
129.606
126.480
123.730
120.965
119.195
117.158
116.807
116.728
116.475
114.642
114.166
114.117
113.560
101.526
100.627
93.503
92.377
91.240
88.612
88.384
88.047

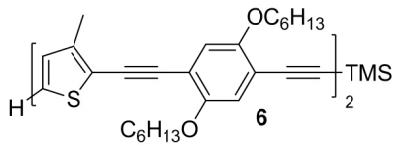
OC6H13
TMS
2
H
S
C6H13O

6

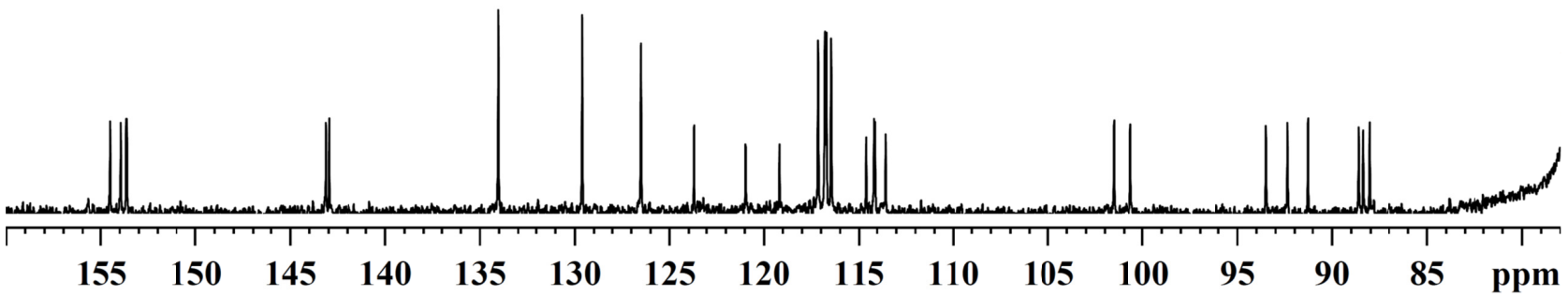
155
150
145
140
135
130
125
120
115
110
105
100
95
90
85
ppm

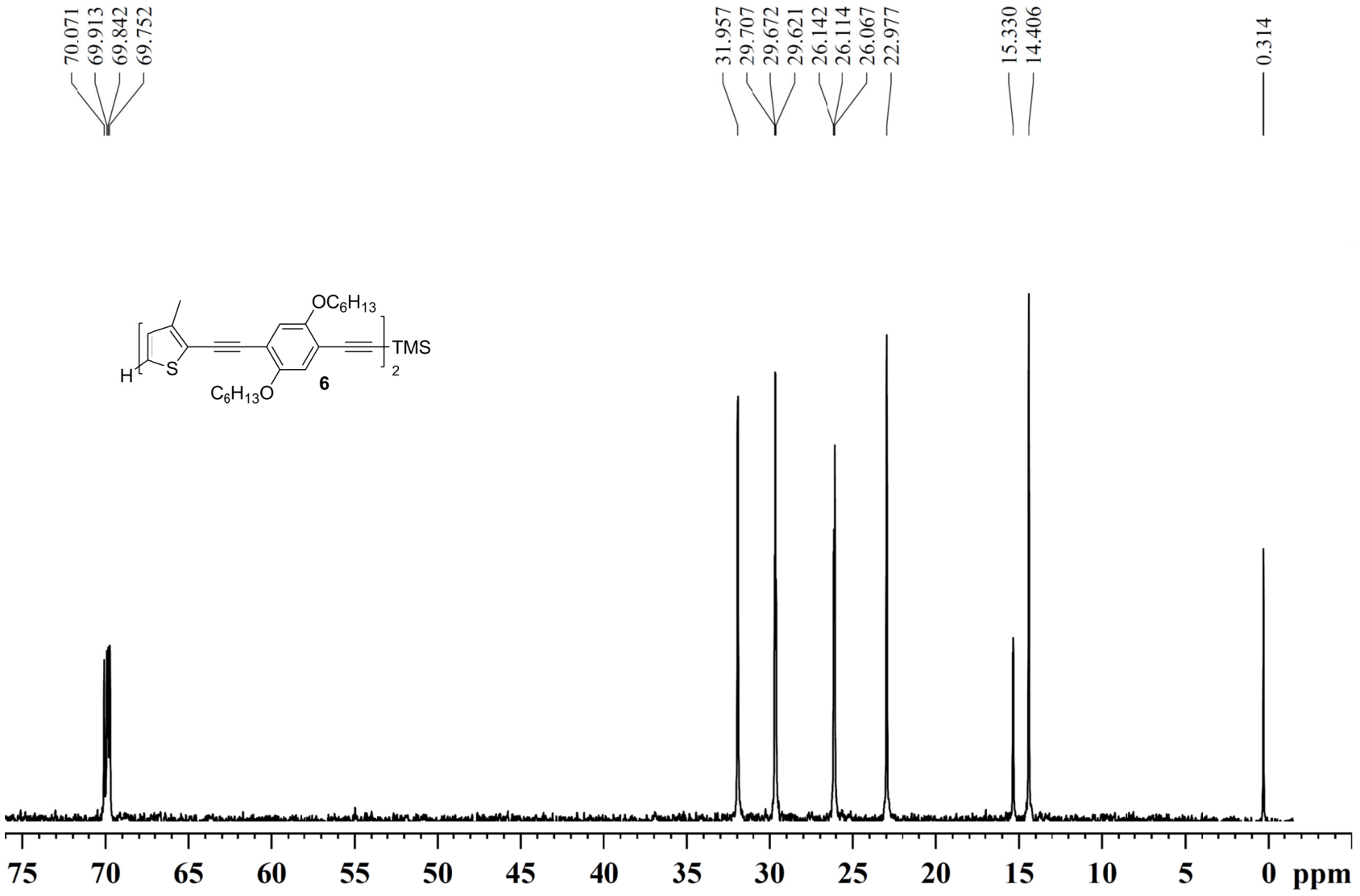
70.071
69.913
69.842
69.752
31.957
29.707
29.672
29.621
26.142
26.114
26.067
22.977
15.330
14.406
0.314
OC6H13
TMS
2
H
S
C6H13O
6
75
70
65
60
55
50
45
40
35
30
25
20
15
10
5
0
ppm

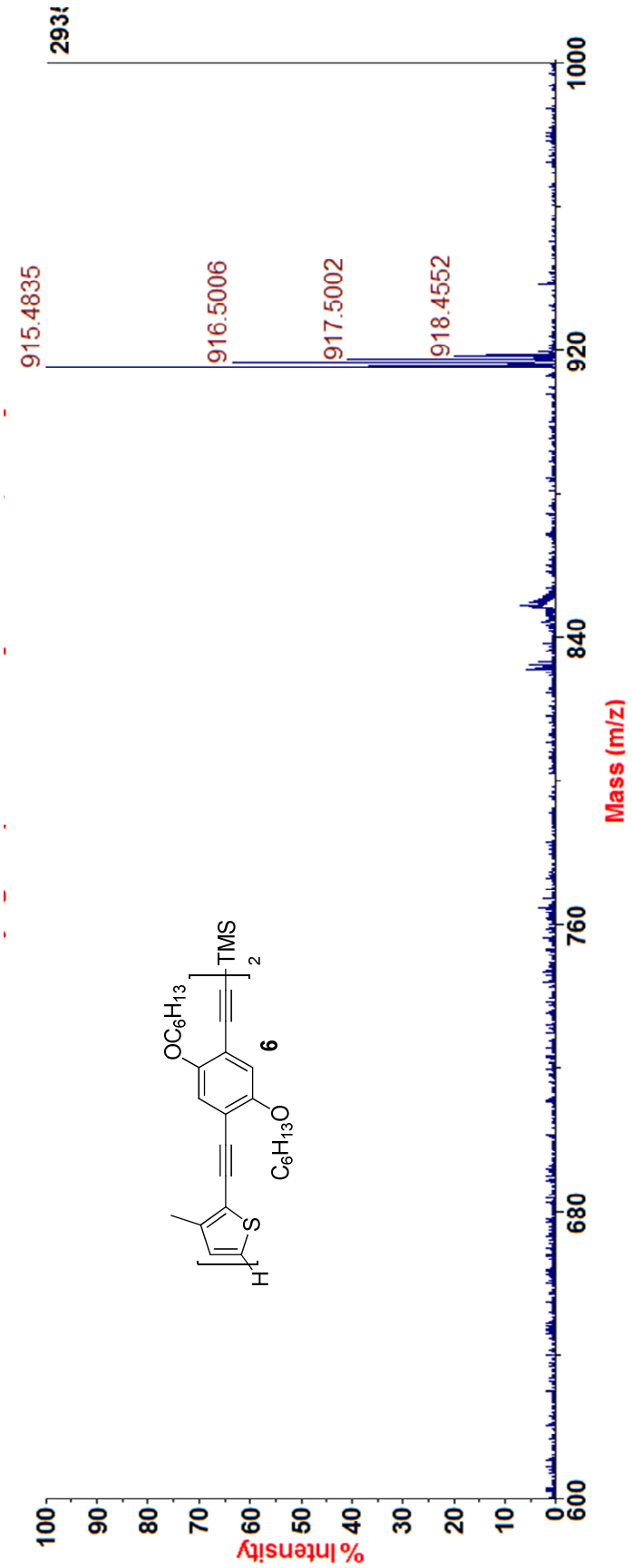
293
915.4835
916.5006
917.5002
918.4552
1000
920
840
760
680
600
Mass (m/z)
100
90
80
70
60
50
40
30
20
10
0
% Intensity
OC6H13
TMS
2
6
C6H13O
S
H

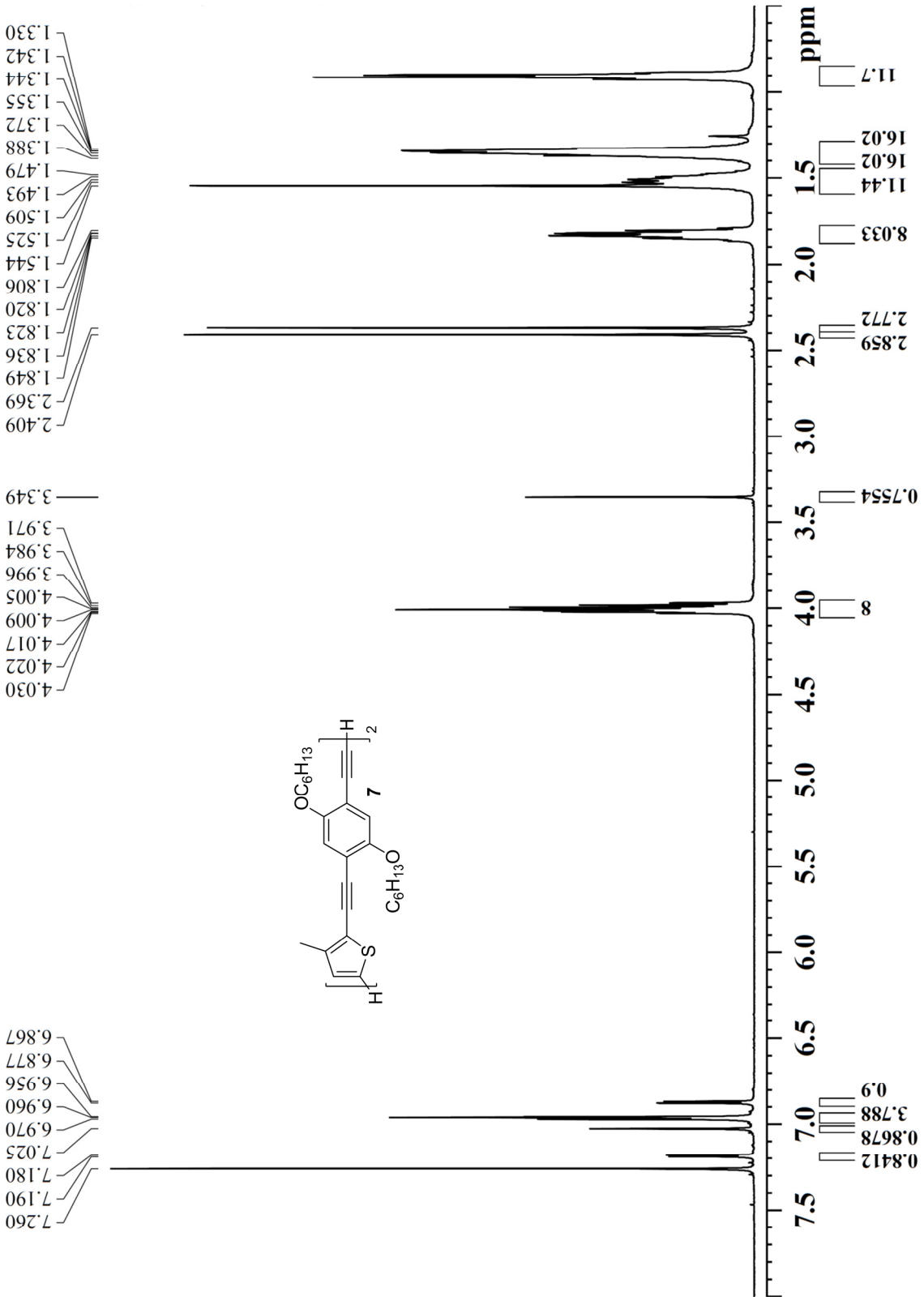
ppm
11.7
16.02
16.02
11.44
8.033
2.859
2.772
0.7554
8
0.8412
0.8678
3.788
0.9
7.260
7.190
7.180
7.025
6.970
6.960
6.956
6.877
6.867
4.030
4.022
4.017
4.009
4.005
3.996
3.984
3.971
3.349
2.409
2.369
1.849
1.836
1.823
1.820
1.806
1.544
1.525
1.509
1.493
1.479
1.388
1.372
1.355
1.344
1.342
1.330
OC6H13
7
C6H13O
S
H
2

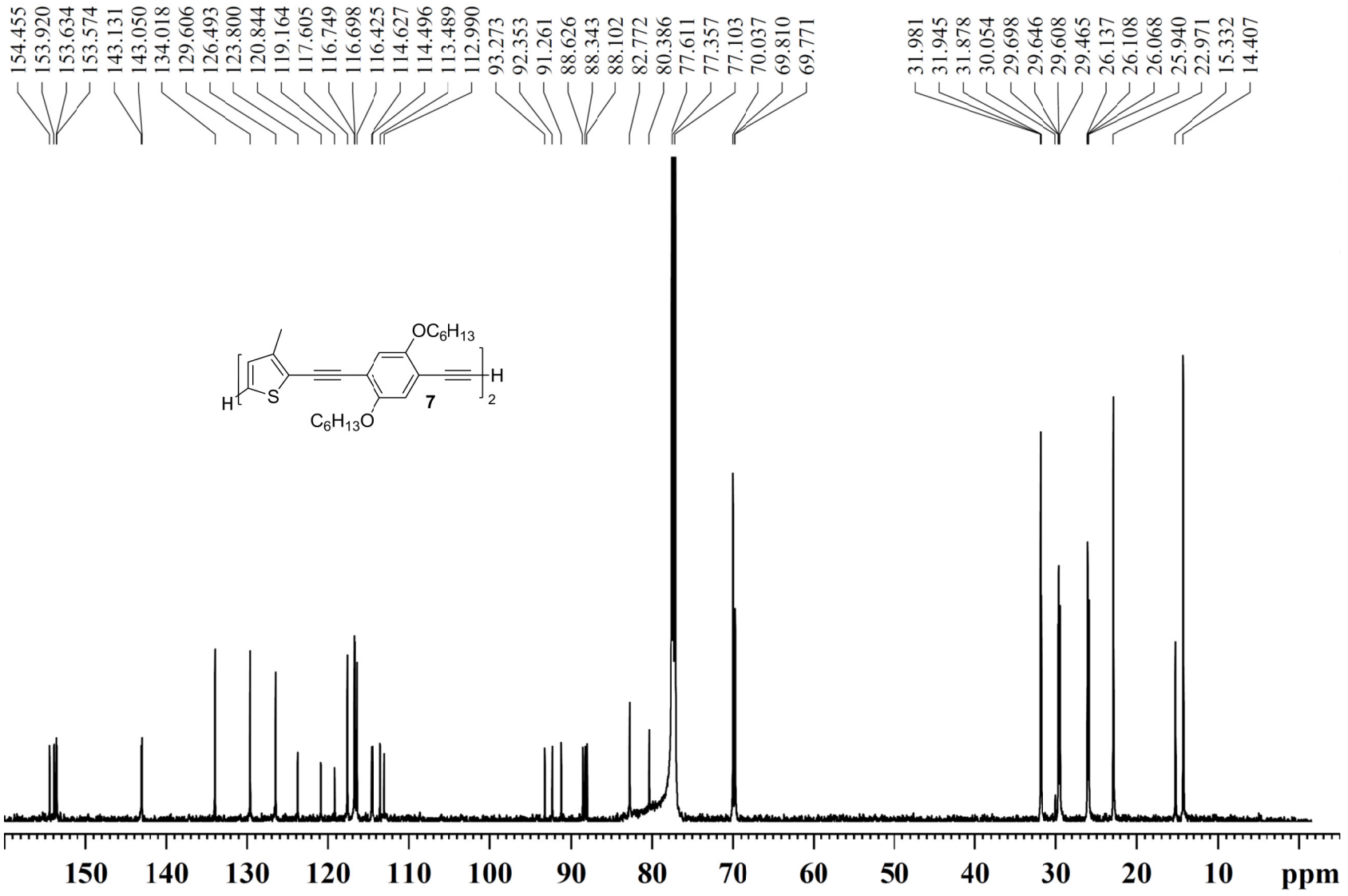
154.455
153.920
153.634
153.574
143.131
143.050
134.018
129.606
126.493
123.800
120.844
119.164
117.605
116.749
116.698
116.425
114.627
114.496
113.489
112.990
93.273
92.353
91.261
88.626
88.343
88.102
82.772
80.386
77.611
77.357
77.103
70.037
69.810
69.771
31.981
31.945
31.878
30.054
29.698
29.646
29.608
29.465
26.137
26.108
26.068
25.940
22.971
15.332
14.407
OC6H13
H
S
H
2
C6H13O
7
150
140
130
120
110
100
90
80
70
60
50
40
30
20
10
ppm

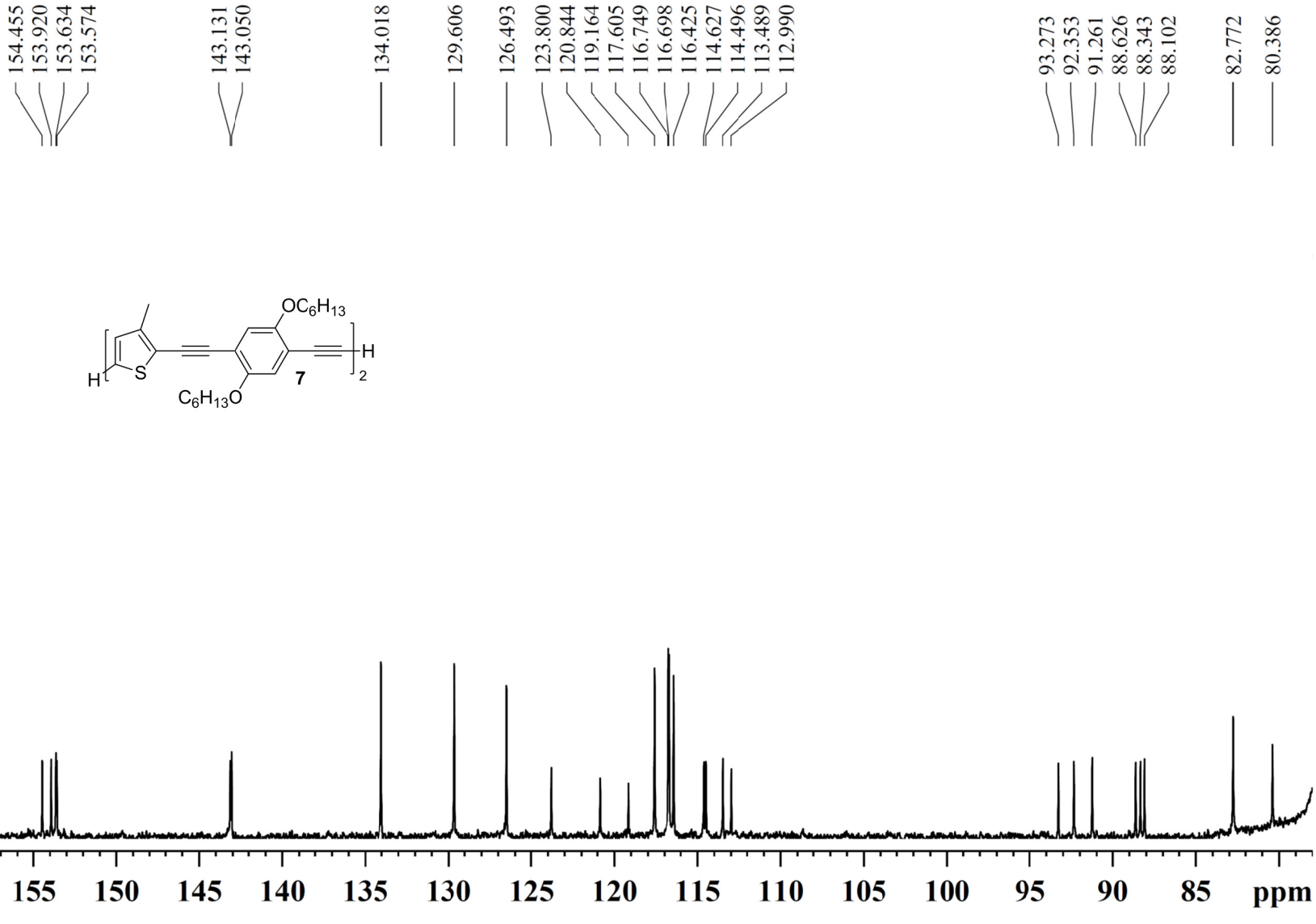
154.455
153.920
153.634
153.574
143.131
143.050
134.018
129.606
126.493
123.800
120.844
119.164
117.605
116.749
116.698
116.425
114.627
114.496
113.489
112.990
93.273
92.353
91.261
88.626
88.343
88.102
82.772
80.386
OC6H13
H
S
H
2
C6H13O
7
155
150
145
140
135
130
125
120
115
110
105
100
95
90
85
ppm

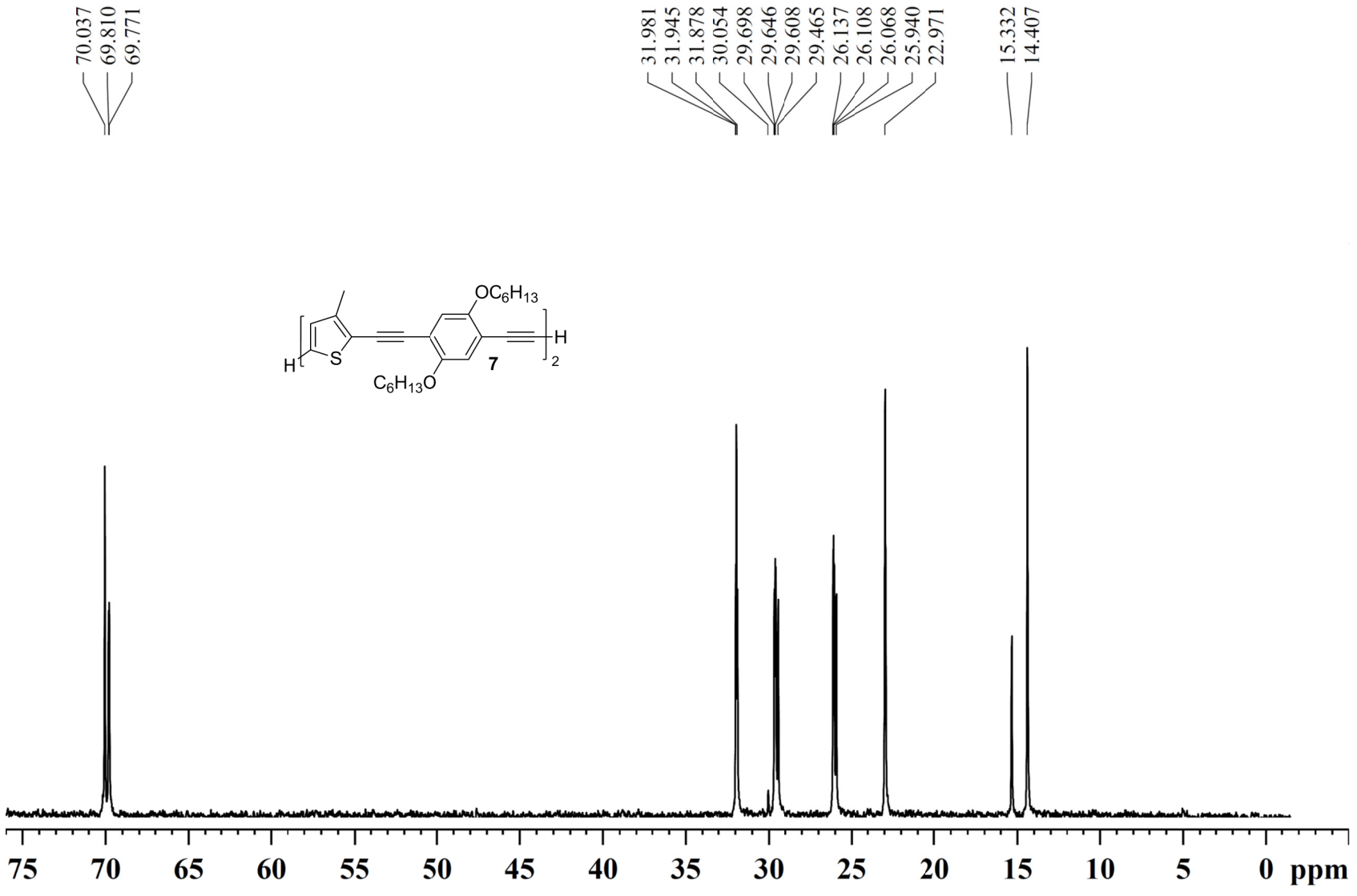
70.037
69.810
69.771
31.981
31.945
31.878
30.054
29.698
29.646
29.608
29.465
26.137
26.108
26.068
25.940
22.971
15.332
14.407
OC6H13
H
S
H
2
C6H13O
7
75
70
65
60
55
50
45
40
35
30
25
20
15
10
5
0
ppm

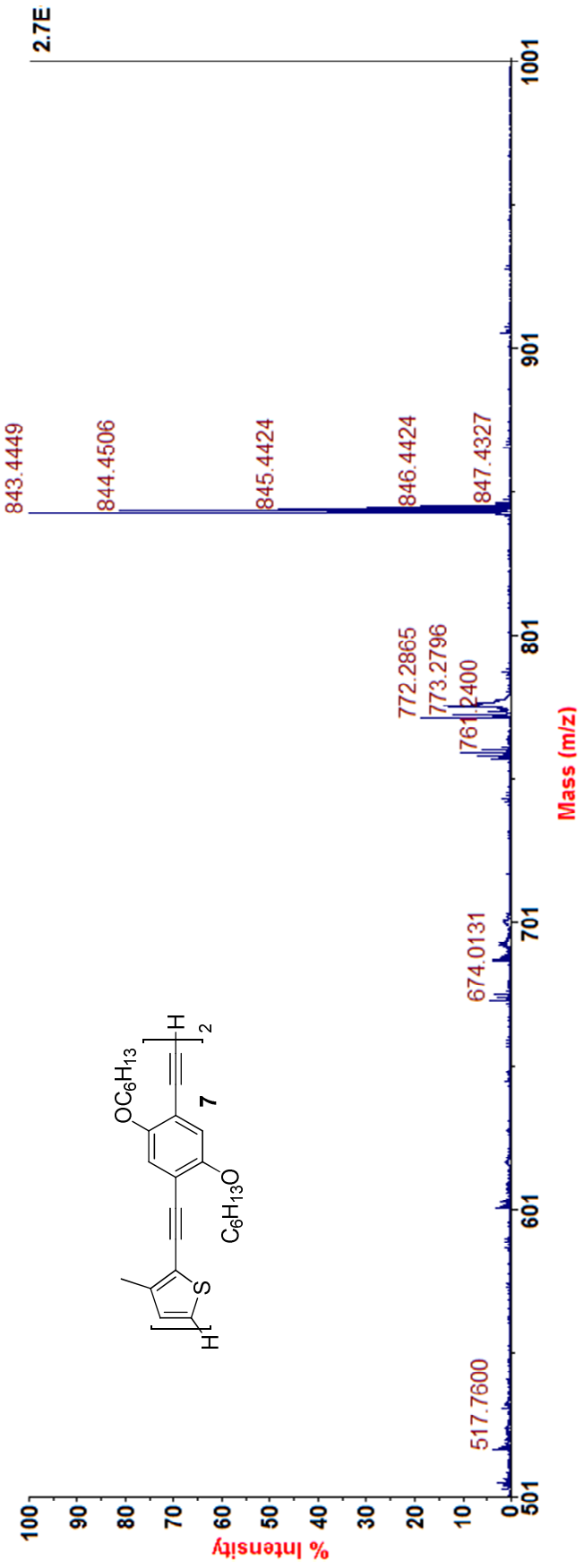
2.7E
843.4449
844.4506
845.4424
846.4424
847.4327
772.2865
773.2796
674.0131
517.7600
% Intensity
Mass (m/z)
100
90
80
70
60
50
40
30
20
10
0
501
601
701
801
901
1001
OC6H13
C6H13O
S
H
2
7

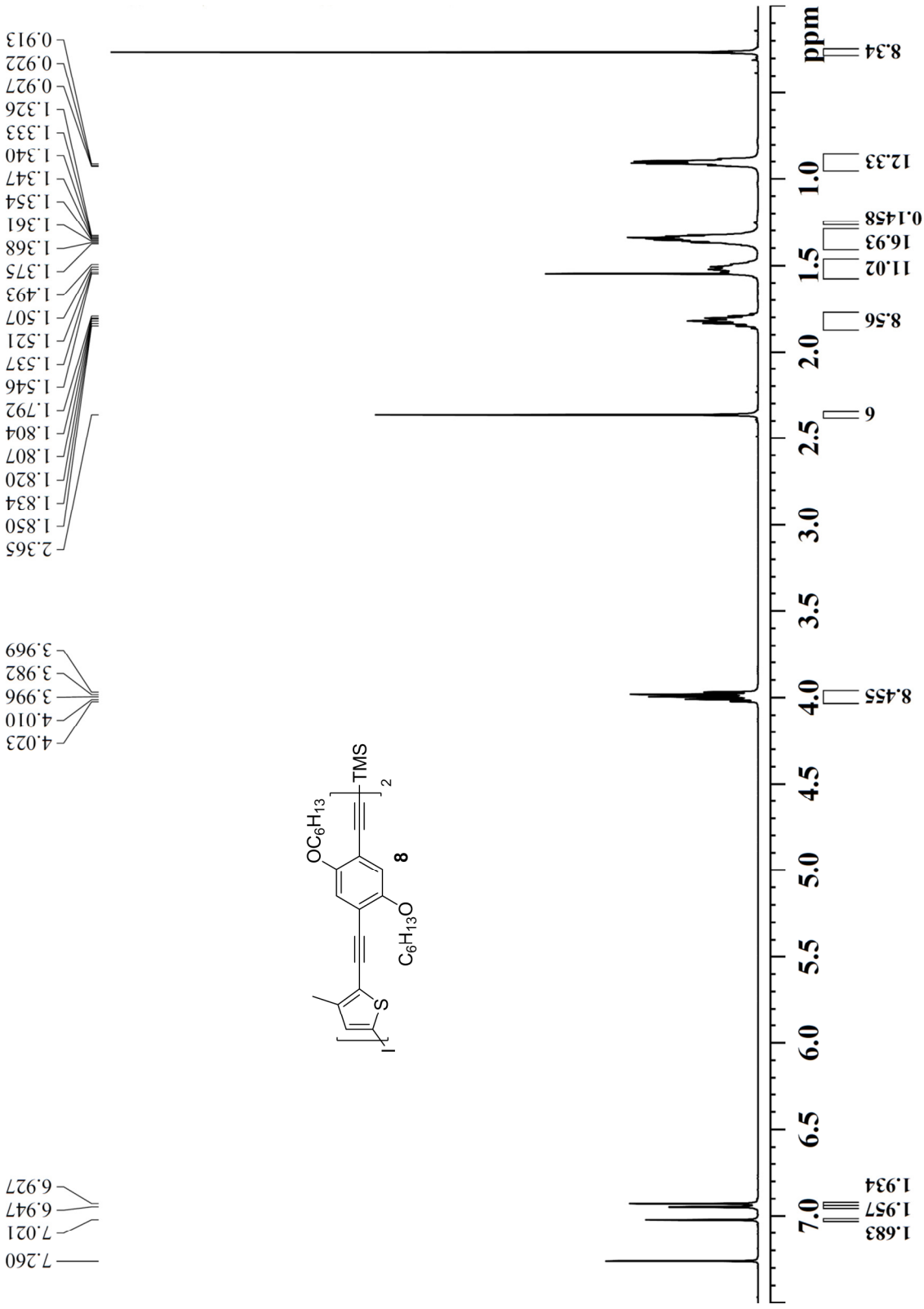
ppm
8.34
12.33
0.1458
16.93
11.02
8.56
6
8.455
1.683
1.957
1.934
7.260
7.021
6.947
6.927
4.023
4.010
3.996
3.982
3.969
2.365
1.850
1.834
1.820
1.807
1.804
1.792
1.546
1.537
1.521
1.507
1.493
1.375
1.368
1.361
1.354
1.347
1.340
1.333
1.326
0.927
0.922
0.913
8
TMS
2
OC6H13
C6H13O
S
I-

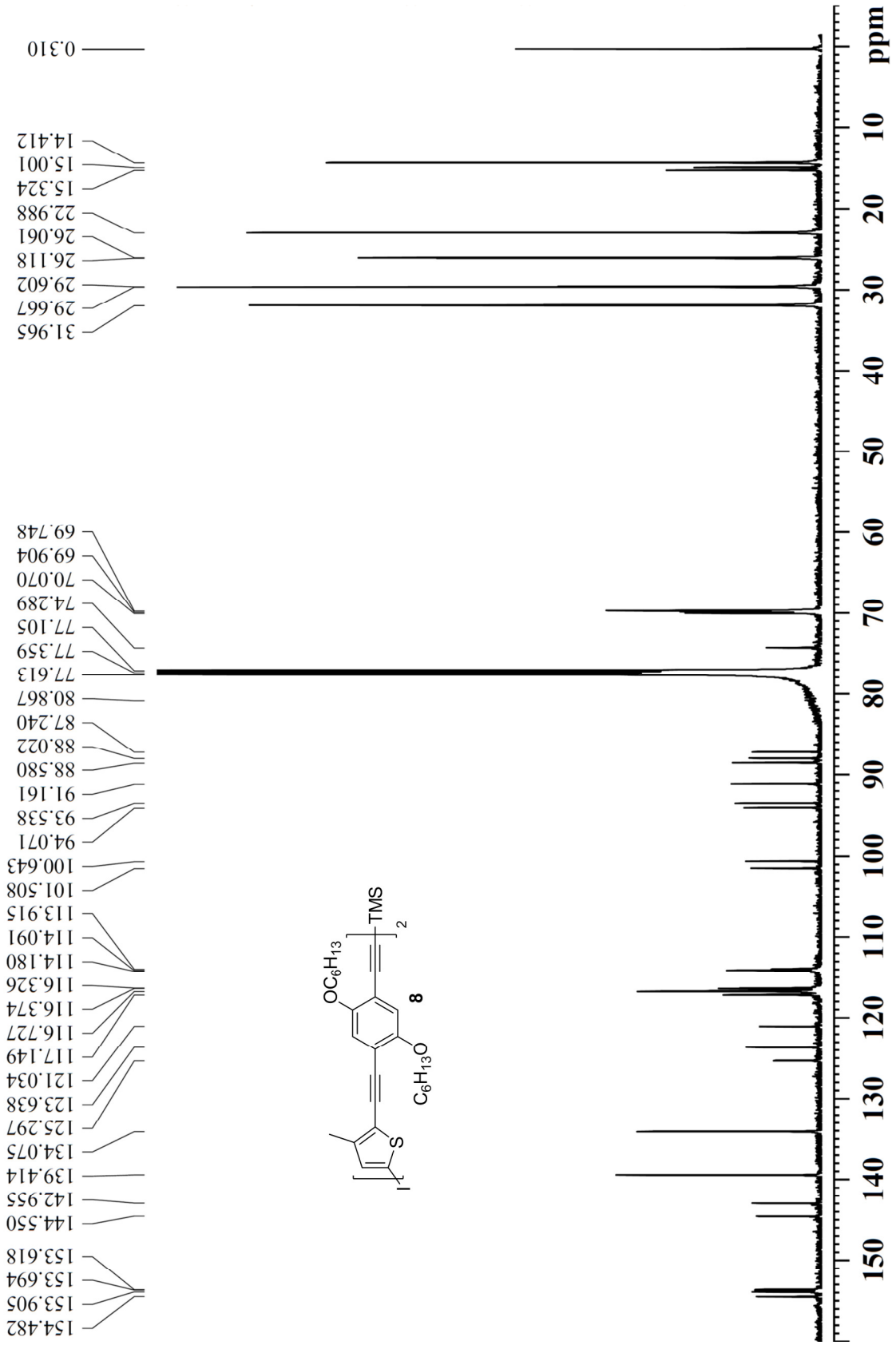
ppm
150
140
130
120
110
100
90
80
70
60
50
40
30
20
10
0.310
14.412
15.001
15.324
22.988
26.061
26.118
29.602
29.667
31.965
69.748
69.904
70.070
74.289
77.105
77.359
77.613
80.867
87.240
88.022
88.580
91.161
93.538
94.071
100.643
101.508
113.915
114.091
114.180
116.326
116.374
116.727
117.149
121.034
123.638
125.297
134.075
139.414
142.955
144.550
153.618
153.694
153.905
154.482
OC6H13
TMS
2
8
C6H13O
S
I

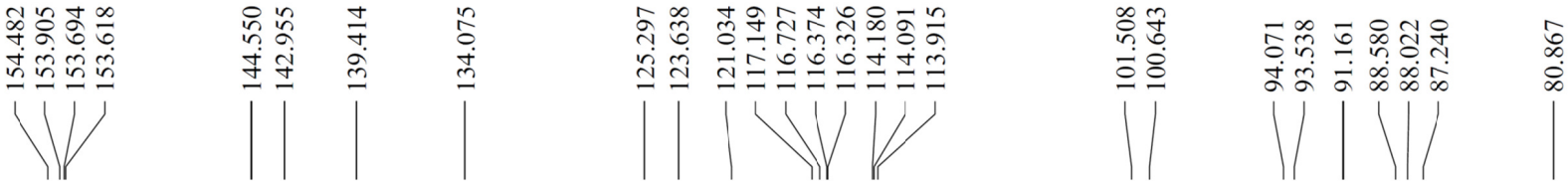
154.482
153.905
153.694
153.618
144.550
142.955
139.414
134.075
125.297
123.638
121.034
117.149
116.727
116.374
116.326
114.180
114.091
113.915
101.508
100.643
94.071
93.538
91.161
88.580
88.022
87.240
80.867

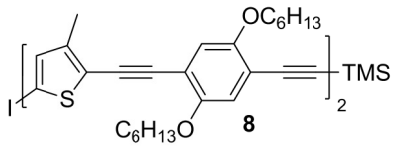
OC6H13
TMS
I
S
C6H13O
2

8

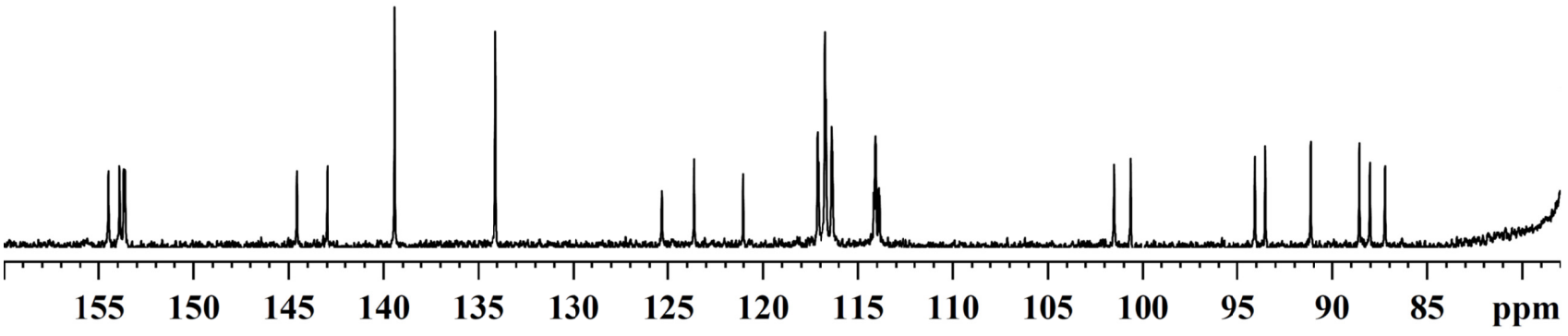
155
150
145
140
135
130
125
120
115
110
105
100
95
90
85
ppm

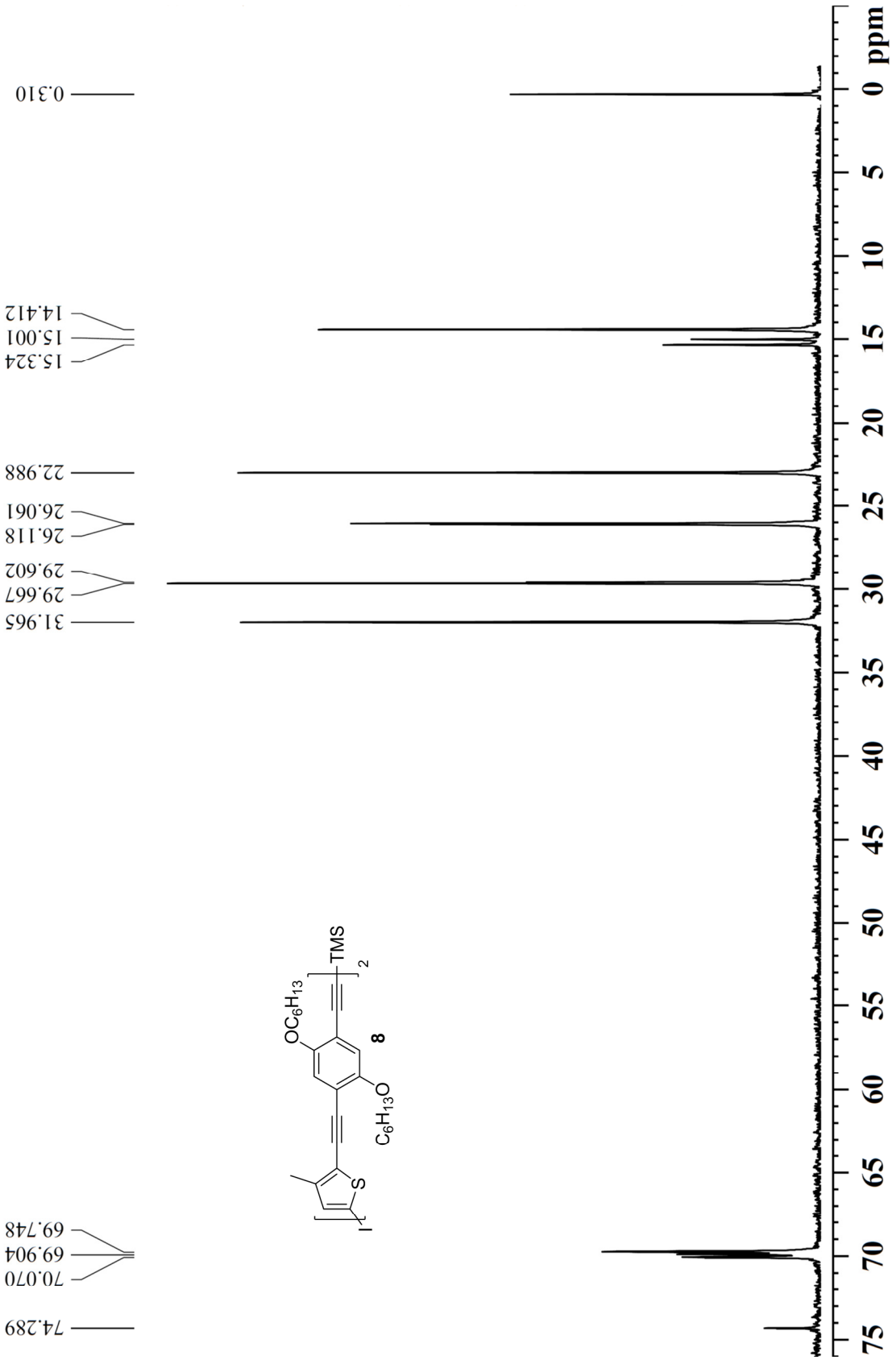
0.310
14.412
15.001
15.324
22.988
26.061
26.118
29.602
29.667
31.965
74.289
69.748
69.904
70.070
OC6H13
TMS
2
8
C6H13O
S
I
ppm

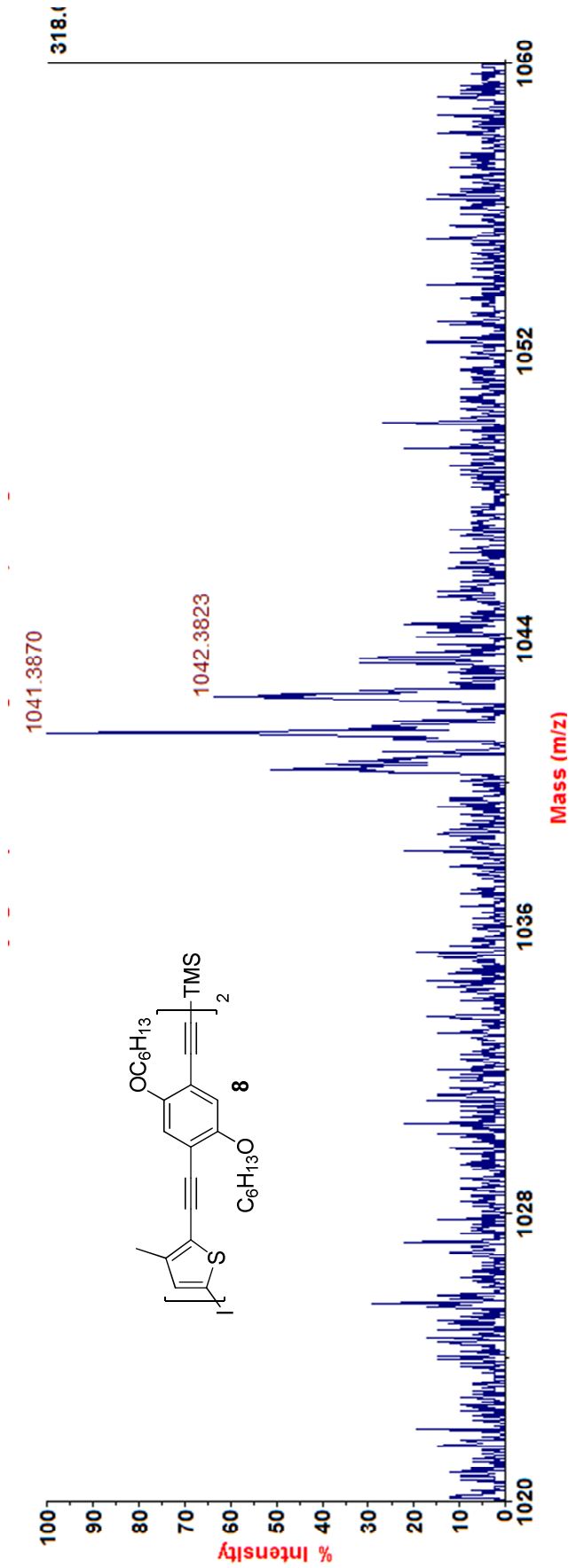
318.(
1041.3870
1042.3823
1020
1028
1036
1044
1052
1060
Mass (m/z)
% Intensity
100
90
80
70
60
50
40
30
20
10
0
OC6H13
TMS
2
8
C6H13O
S
I

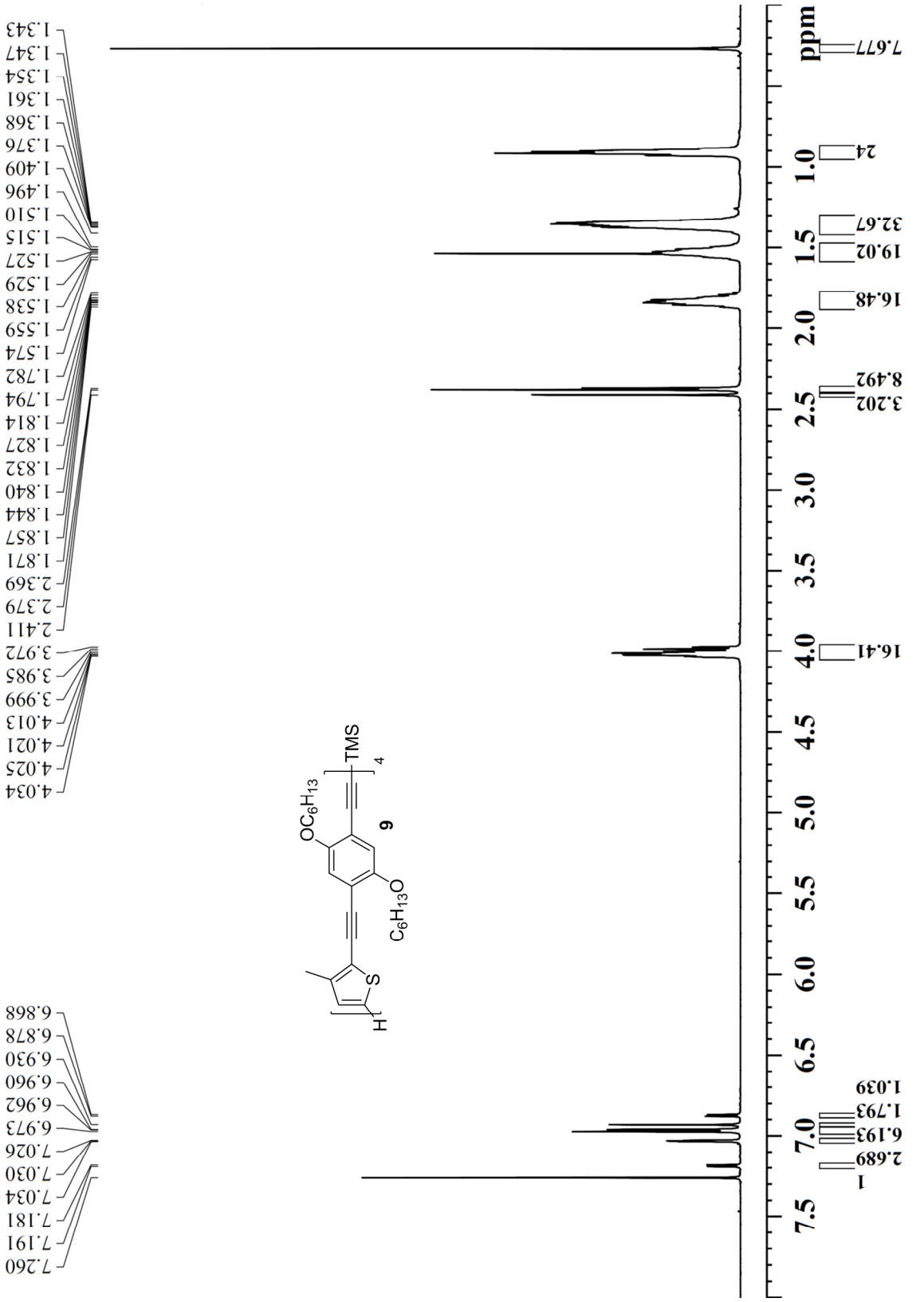
ppm
7.677
24
32.67
19.02
16.48
3.202
8.492
16.41
1
2.689
6.193
1.793
1.039
TMS
4
9
OC6H13
C6H13O
H
S
7.260
7.191
7.181
7.034
7.030
7.026
6.973
6.962
6.960
6.930
6.878
6.868
4.034
4.025
4.021
4.013
3.999
3.985
3.972
2.411
2.379
2.369
1.871
1.857
1.844
1.840
1.832
1.827
1.814
1.794
1.782
1.574
1.559
1.538
1.529
1.527
1.515
1.510
1.496
1.409
1.376
1.368
1.361
1.354
1.347
1.343

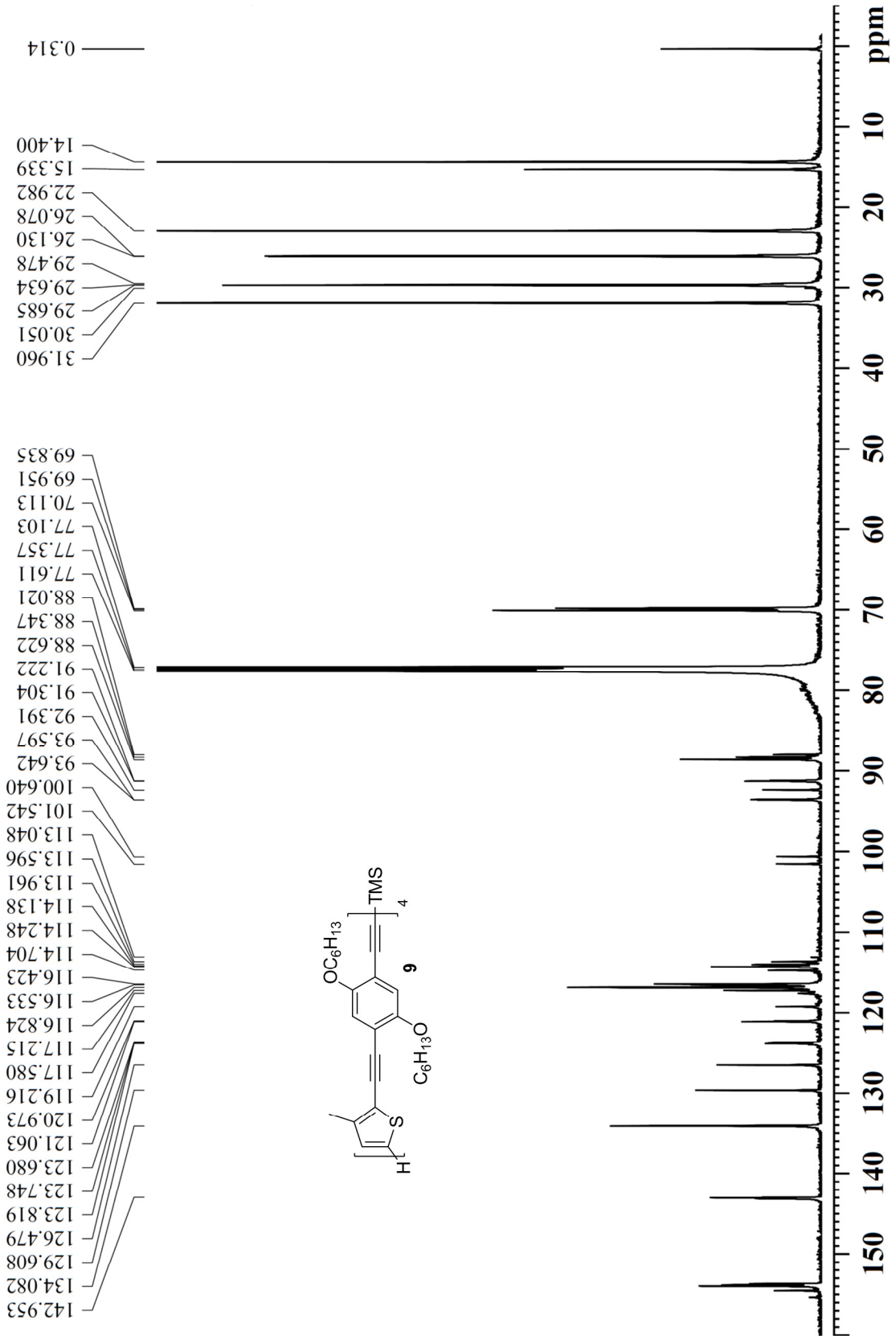
ppm
150
140
130
120
110
100
90
80
70
60
50
40
30
20
10
0.314
14.400
15.339
22.982
26.078
26.130
29.478
29.634
29.685
30.051
31.960
69.835
69.951
70.113
77.103
77.357
77.611
88.021
88.347
88.622
91.222
91.304
92.391
93.597
93.642
100.640
101.542
113.048
113.596
113.961
114.138
114.248
114.704
116.423
116.533
116.824
117.215
117.580
119.216
120.973
121.063
123.680
123.748
123.819
126.479
129.608
134.082
142.953
TMS
4
OC6H13
C6H13O
S
H
9

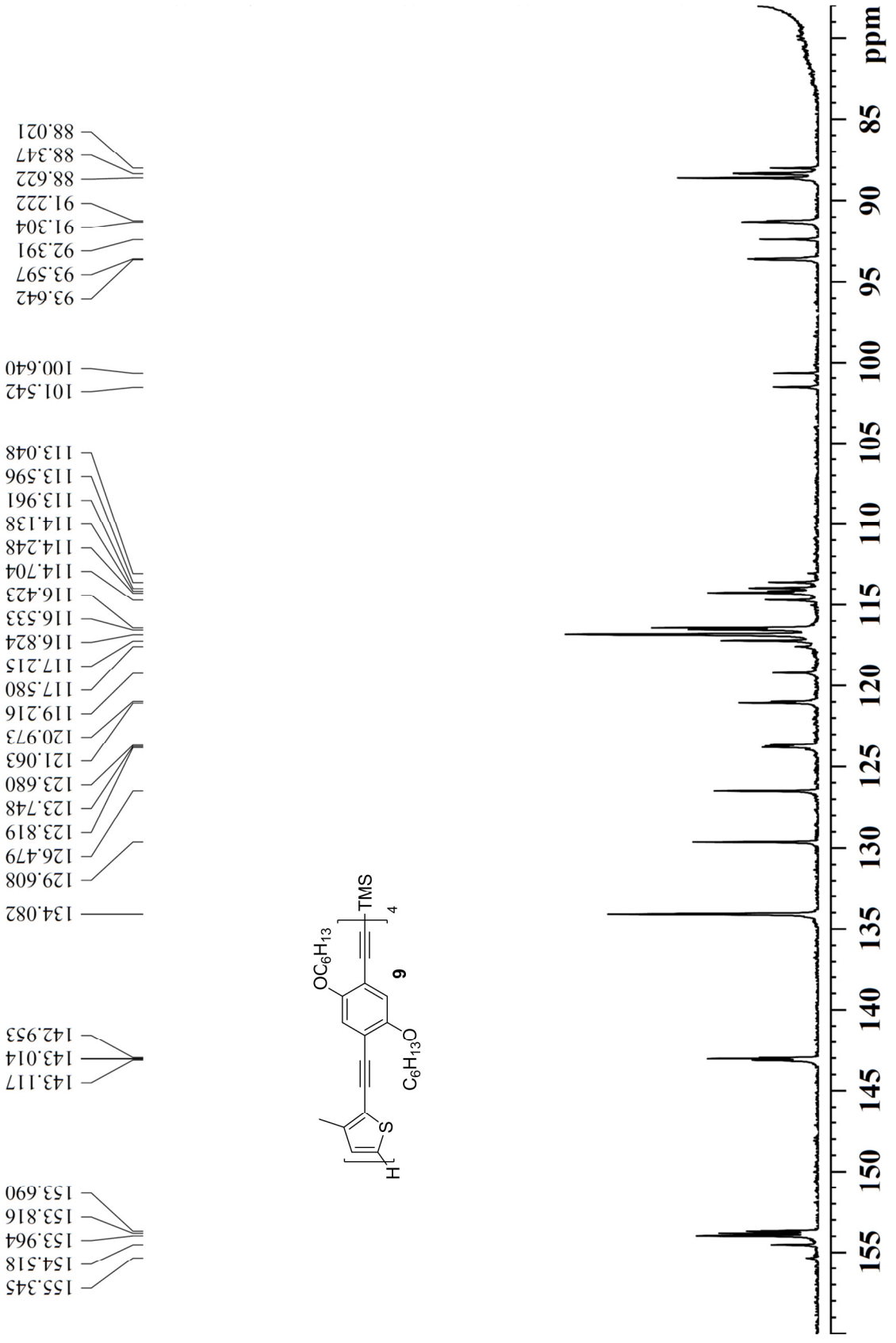
155.345
154.518
153.964
153.816
153.690
143.117
143.014
142.953
134.082
129.608
126.479
123.819
123.748
123.680
121.063
120.973
119.216
117.580
117.215
116.824
116.533
116.423
114.704
114.248
114.138
113.961
113.596
113.048
101.542
100.640
93.642
93.597
92.391
91.304
91.222
88.622
88.347
88.021
OC6H13
TMS
4
9
C6H13O
H
S
155
150
145
140
135
130
125
120
115
110
105
100
95
90
85
ppm

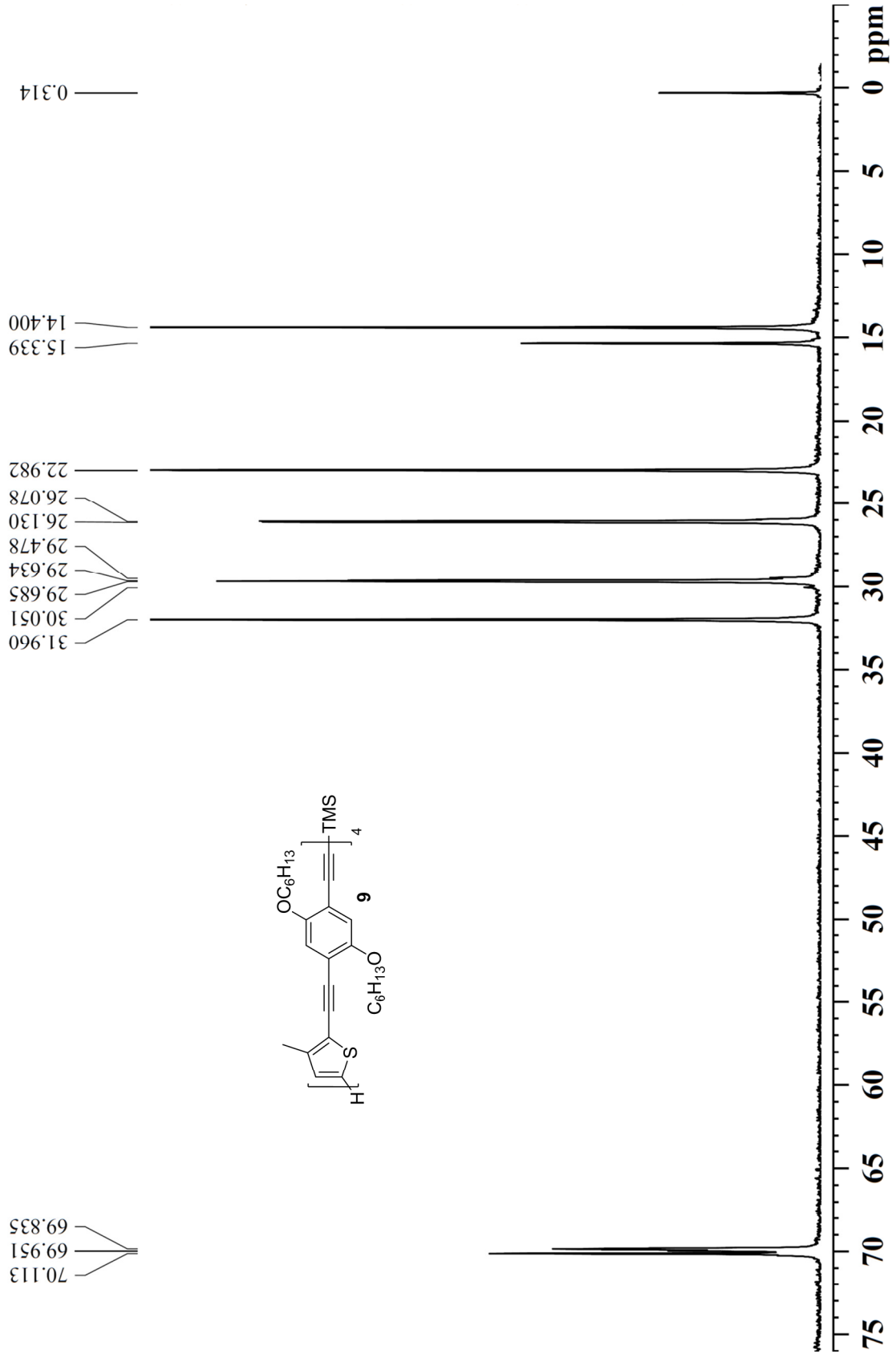
0.314
14.400
15.339
22.982
26.078
26.130
29.478
29.634
29.685
30.051
31.960
69.835
69.951
70.113
0 ppm
5
10
15
20
25
30
35
40
45
50
55
60
65
70
75
OC6H13
TMS
4
9
C6H13O
S
H

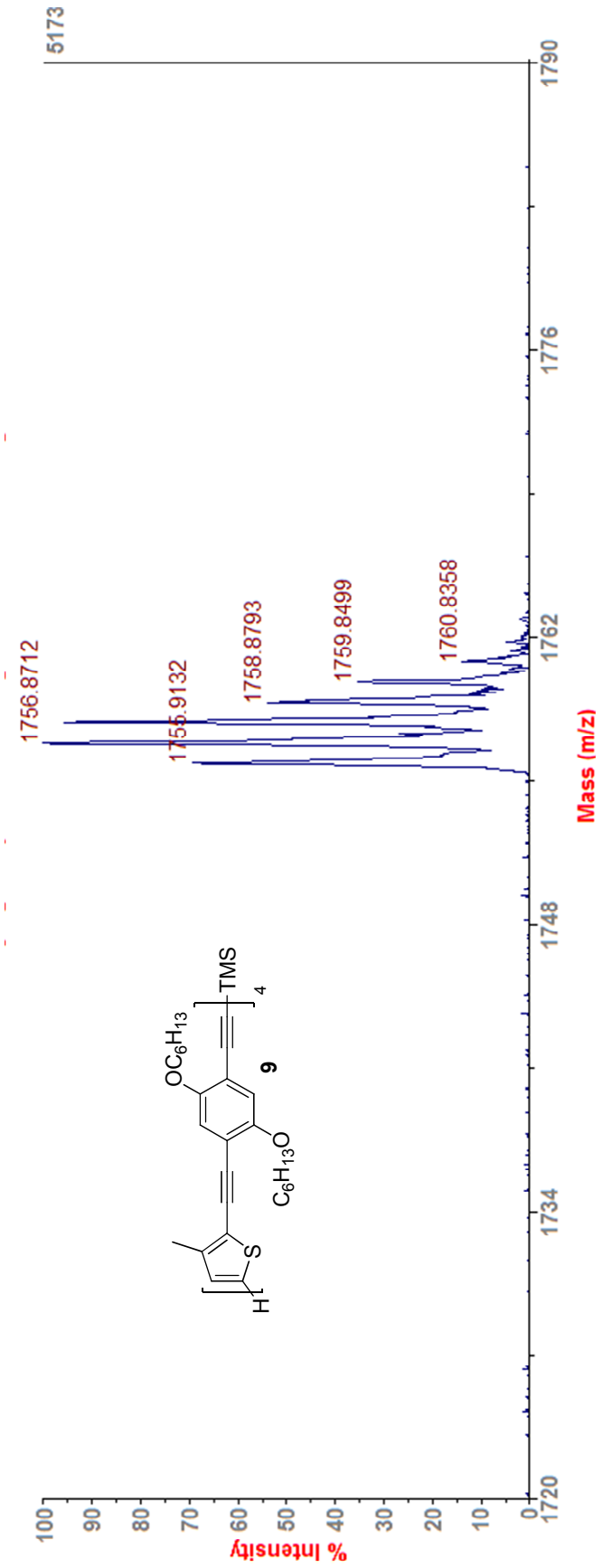
5173
1790
1776
1762
1748
1734
1720
1756.8712
1755.9132
1758.8793
1759.8499
1760.8358
Mass (m/z)
% Intensity
100
90
80
70
60
50
40
30
20
10
0
TMS
4
OC6H13
9
C6H13O
S
H

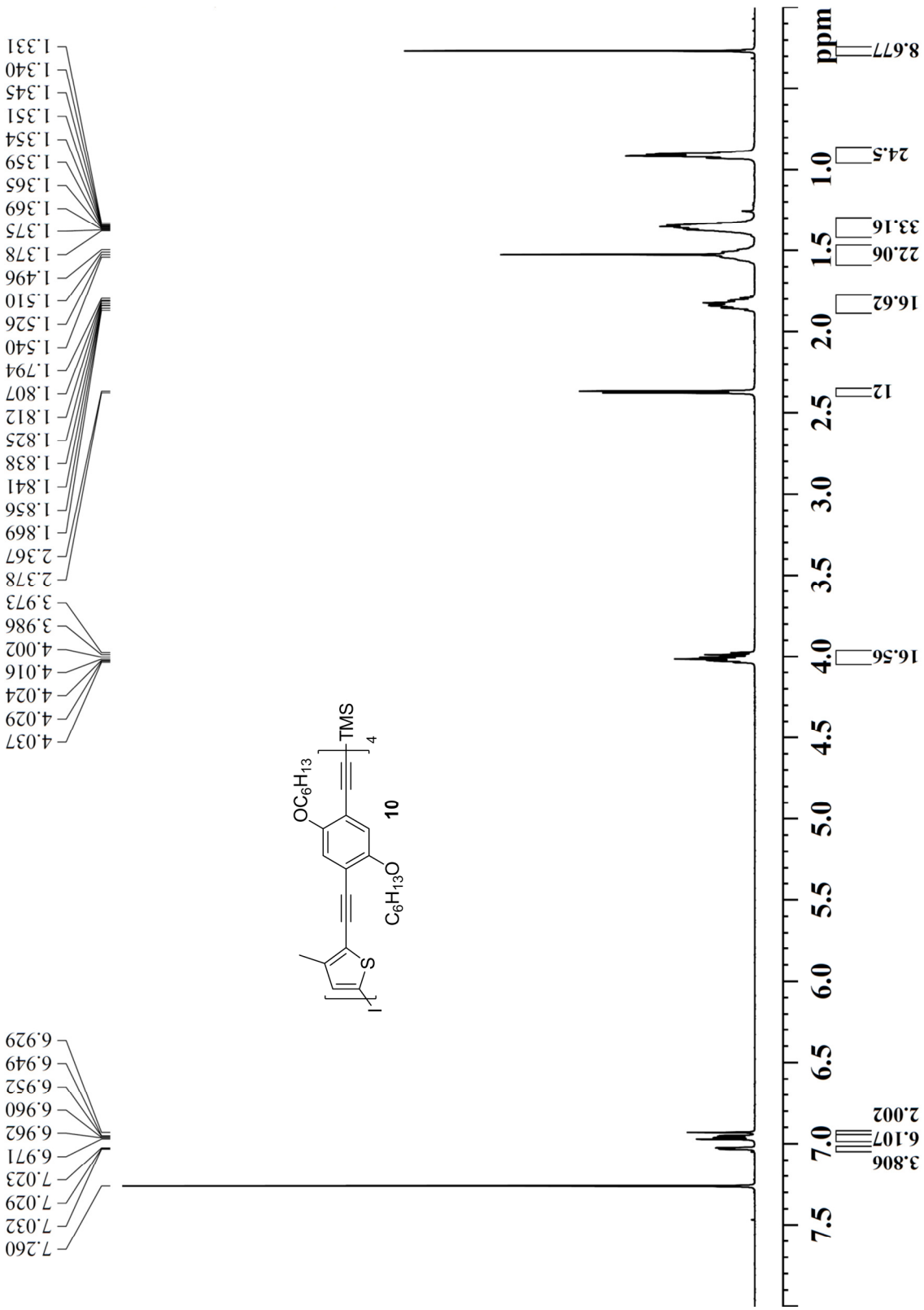
ppm
8.677
24.5
33.16
22.06
16.62
12
16.56
3.806
6.107
2.002
7.260
7.032
7.029
7.023
6.971
6.962
6.960
6.952
6.949
6.929
4.037
4.029
4.024
4.016
4.002
3.986
3.973
2.378
2.367
1.869
1.856
1.841
1.838
1.825
1.812
1.807
1.794
1.540
1.526
1.510
1.496
1.378
1.375
1.369
1.365
1.359
1.354
1.351
1.345
1.340
1.331
TMS
4
OC6H13
C6H13O
10
S
I

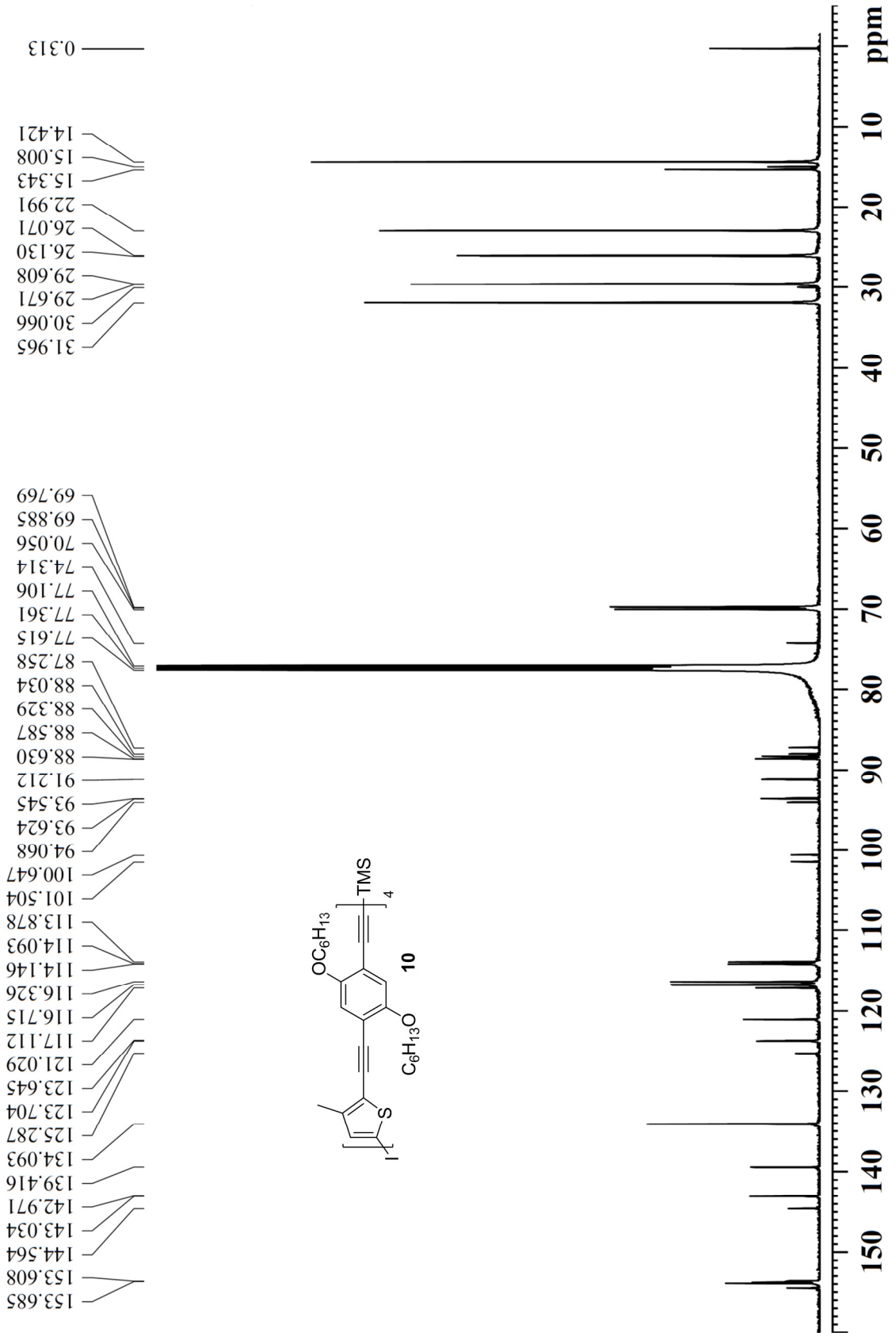
153.685
153.608
144.564
143.034
142.971
139.416
134.093
125.287
123.704
123.645
121.029
117.112
116.715
116.326
114.146
114.093
113.878
101.504
100.647
94.068
93.624
93.545
91.212
88.630
88.587
88.329
88.034
87.258
77.615
77.361
77.106
74.314
70.056
69.885
69.769
31.965
30.066
29.671
29.608
26.130
26.071
22.991
15.343
15.008
14.421
0.313
ppm
10
150
140
130
120
110
100
90
80
70
60
50
40
30
20
10
TMS
4
OC6H13
C6H13O
S
I

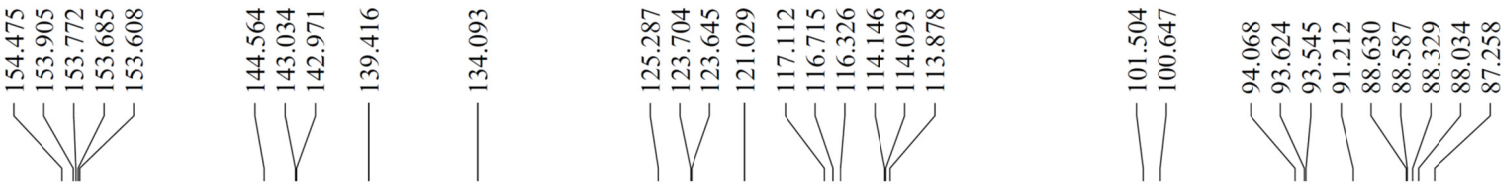
154.475
153.905
153.772
153.685
153.608
144.564
143.034
142.971
139.416
134.093
125.287
123.704
123.645
121.029
117.112
116.715
116.326
114.146
114.093
113.878
101.504
100.647
94.068
93.624
93.545
91.212
88.630
88.587
88.329
88.034
87.258

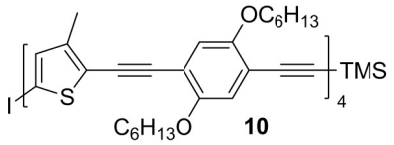
OC6H13
TMS
I
S
4
C6H13O

10

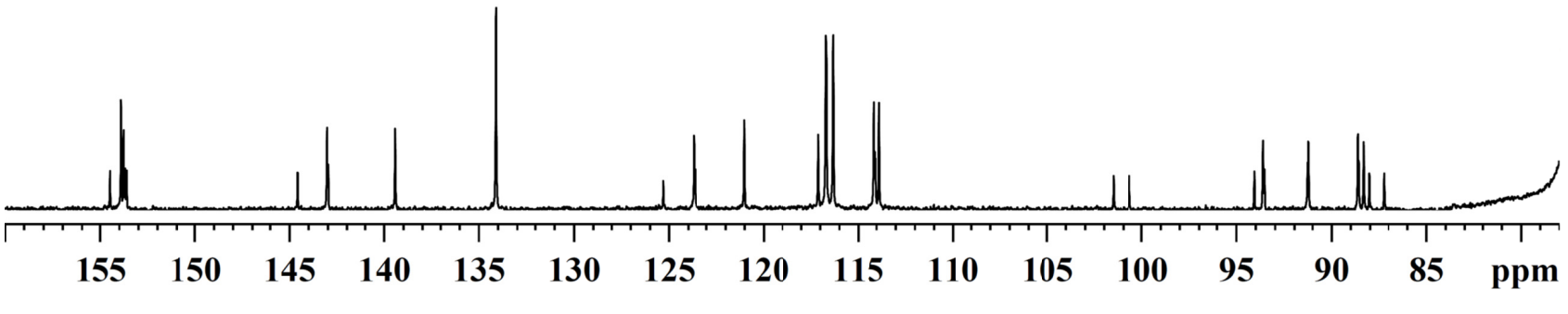
155
150
145
140
135
130
125
120
115
110
105
100
95
90
85
ppm

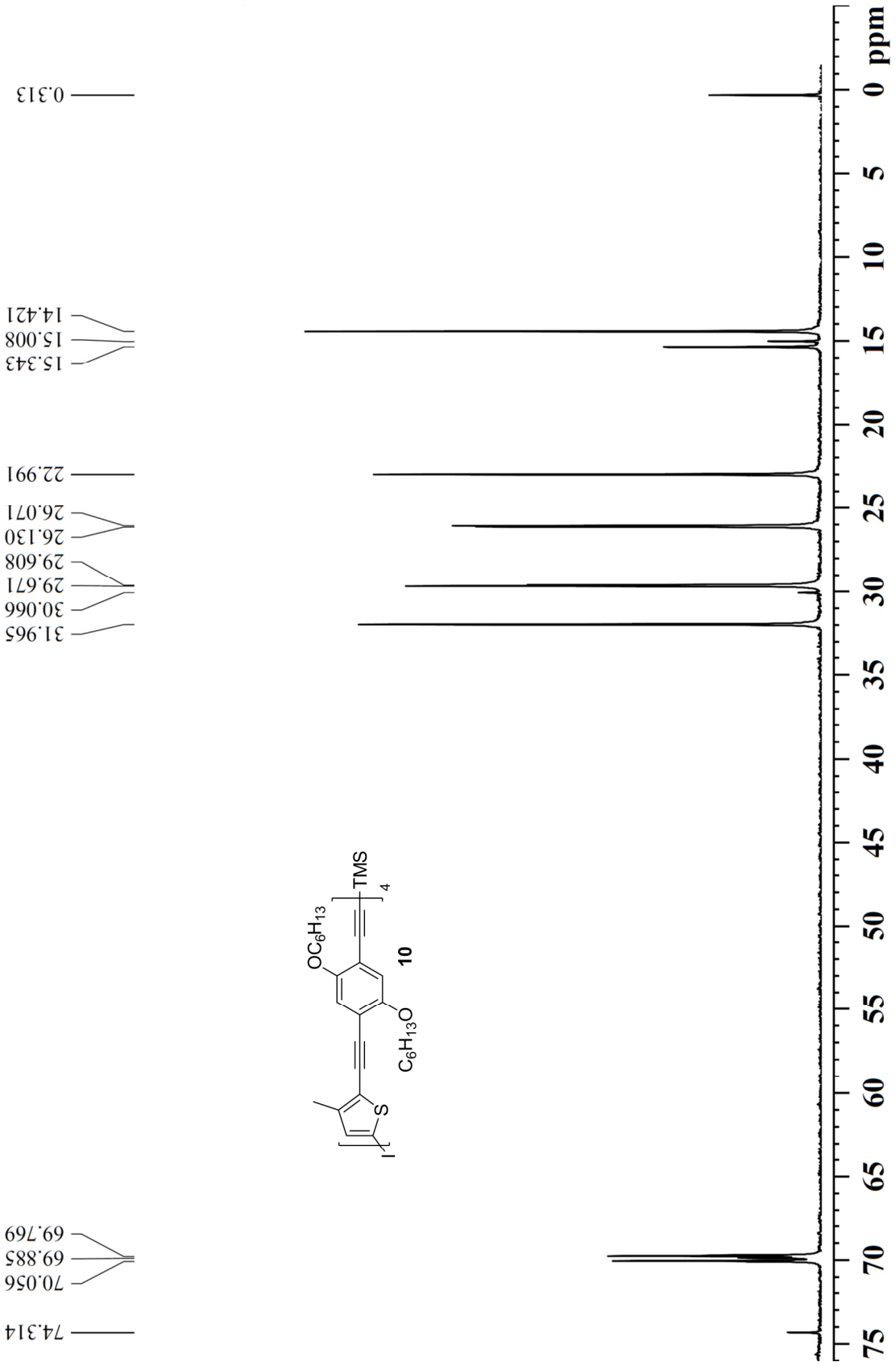
0.313
14.421
15.008
15.343
22.991
26.071
26.130
29.608
29.671
30.066
31.965
74.314
70.056
69.885
69.769
TMS
4
OC6H13
C6H13O
10
S
I
0 ppm
5
10
15
20
25
30
35
40
45
50
55
60
65
70
75

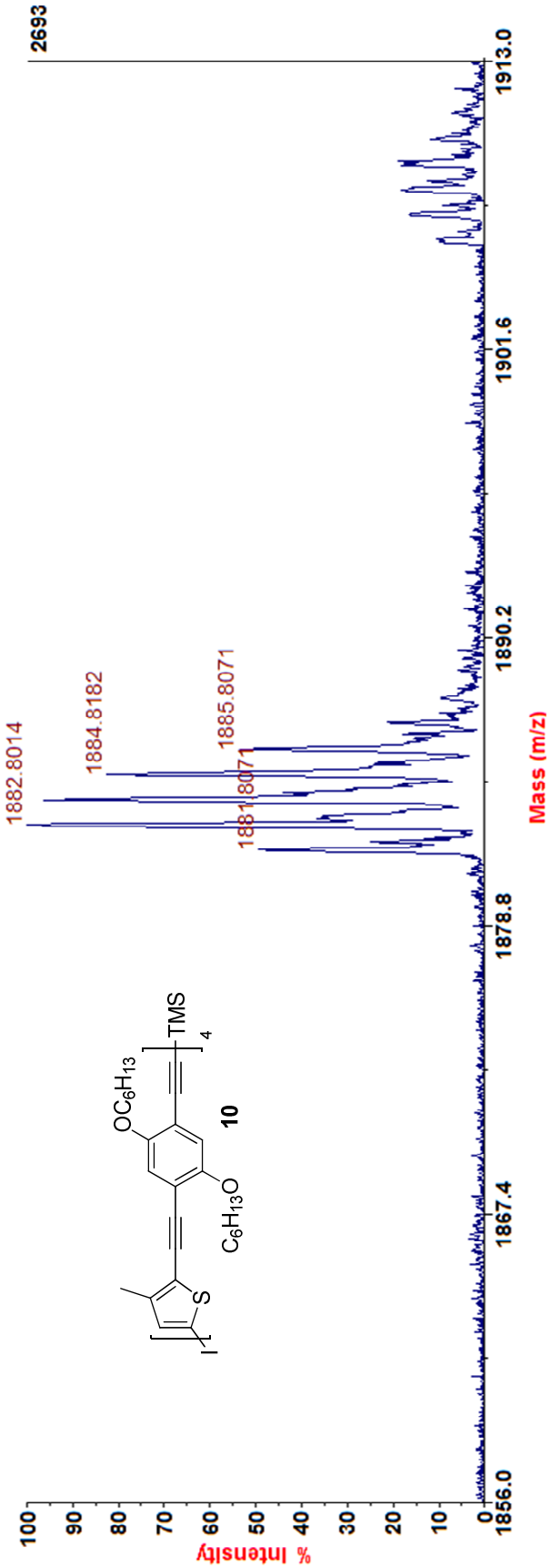
2693
1913.0
1901.6
1890.2
1878.8
1867.4
1856.0
Mass (m/z)
1882.8014
1884.8182
1885.8071
1881.8071
100
90
80
70
60
50
40
30
20
10
0
% Intensity
OC6H13
TMS
4
10
C6H13O
S
I

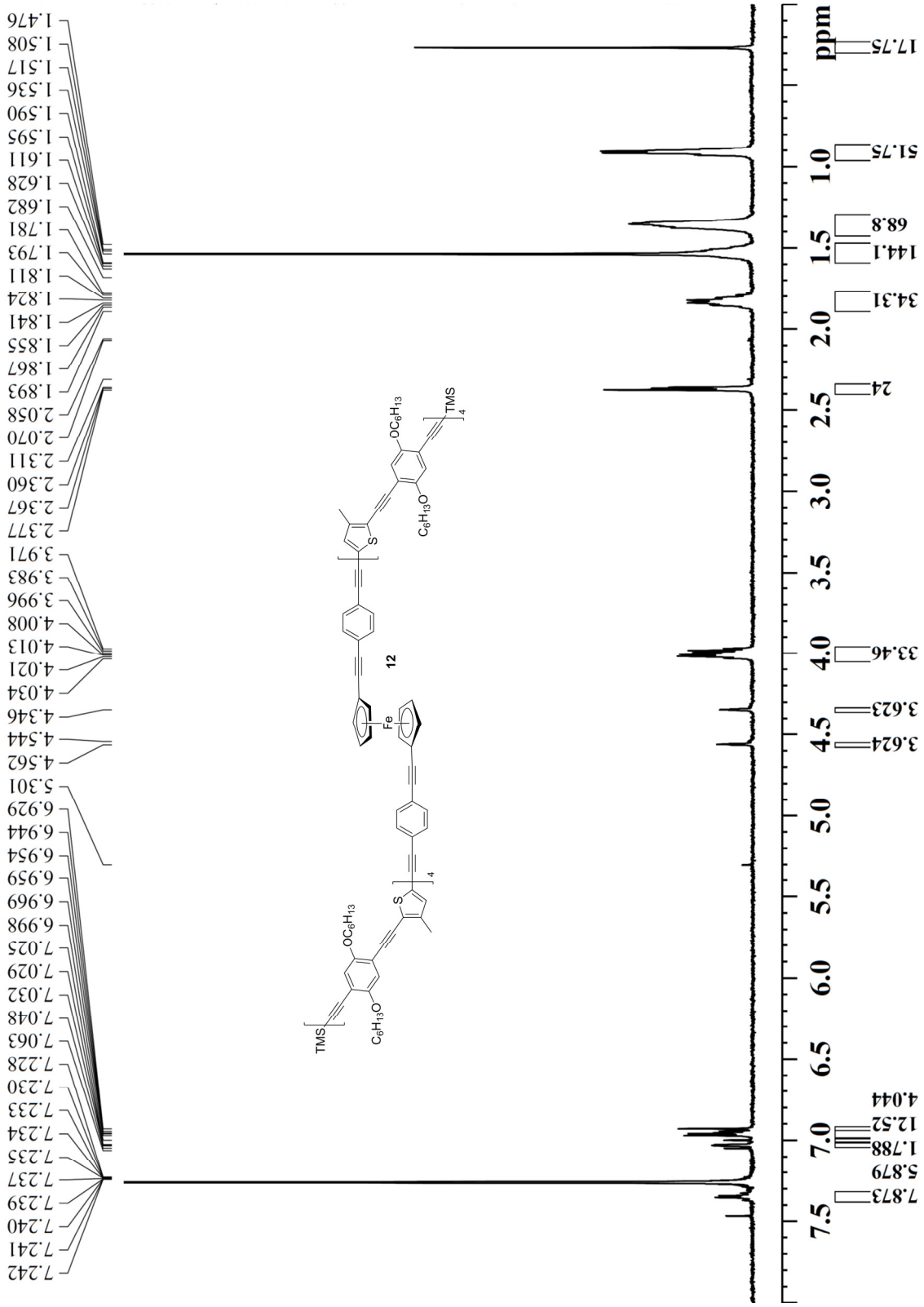
ppm
7.873
5.879
1.788
12.52
4.044
33.46
3.623
3.624
24
34.31
144.1
68.8
51.75
17.75
12
TMS
OC6H13
C6H13O
Fe
S

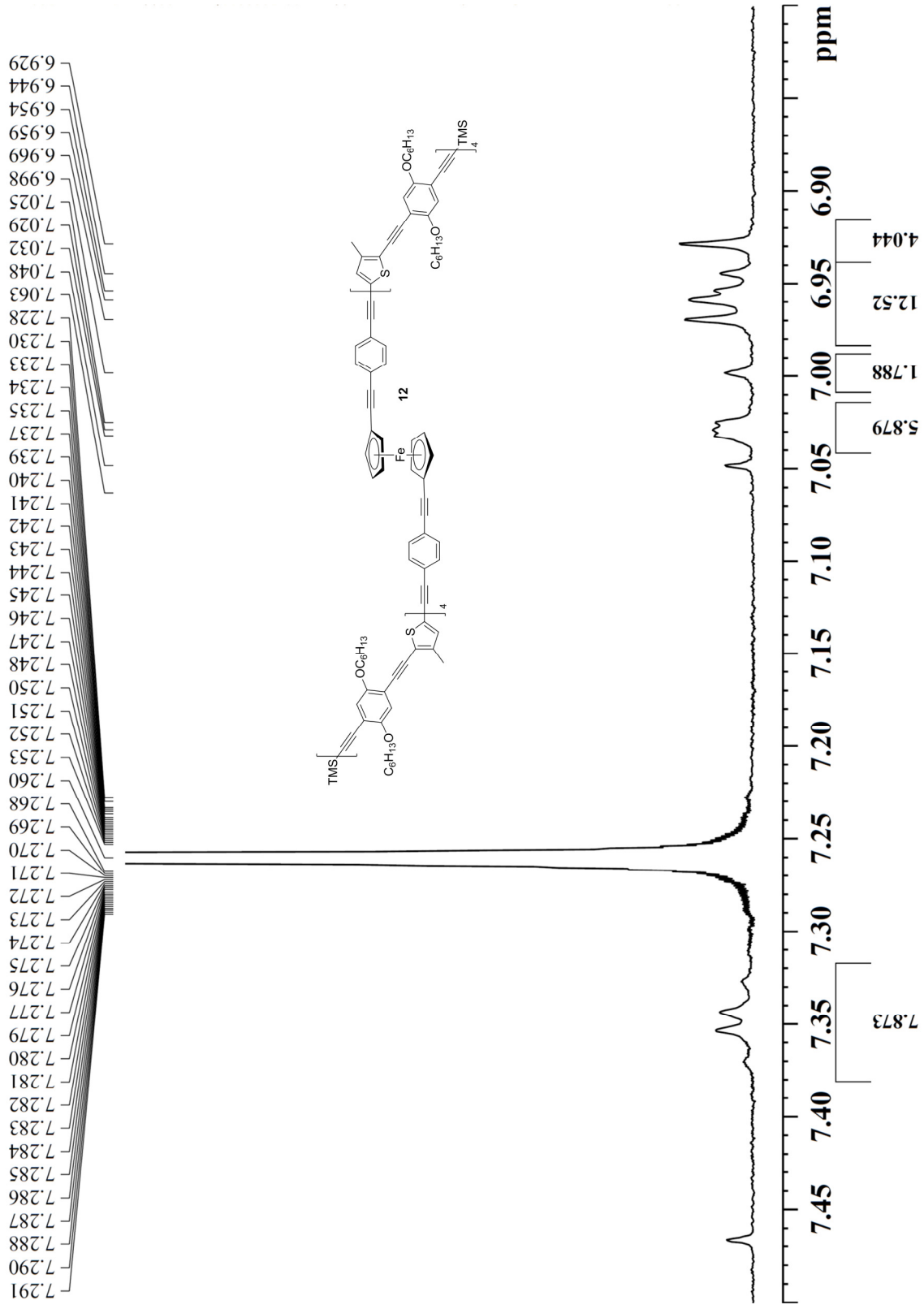
ppm
7.45
7.40
7.35
7.30
7.25
7.20
7.15
7.10
7.05
7.00
6.95
6.90
7.873
5.879
1.788
12.52
4.044
12
TMS
C6H13O
OC6H13
S
Fe
4
6.929
6.944
6.954
6.959
6.969
6.998
7.025
7.029
7.032
7.048
7.063
7.228
7.230
7.233
7.234
7.235
7.237
7.239
7.240
7.241
7.242
7.243
7.244
7.245
7.246
7.247
7.248
7.250
7.251
7.252
7.253
7.260
7.268
7.269
7.270
7.271
7.272
7.273
7.274
7.275
7.276
7.277
7.279
7.280
7.281
7.282
7.283
7.284
7.285
7.286
7.287
7.288
7.290
7.291

4.346
4.562
4.544
12
TMS
OC6H13
C6H13O
S
Fe
4.55
4.50
4.45
4.40
4.35
ppm
3.624
3.623

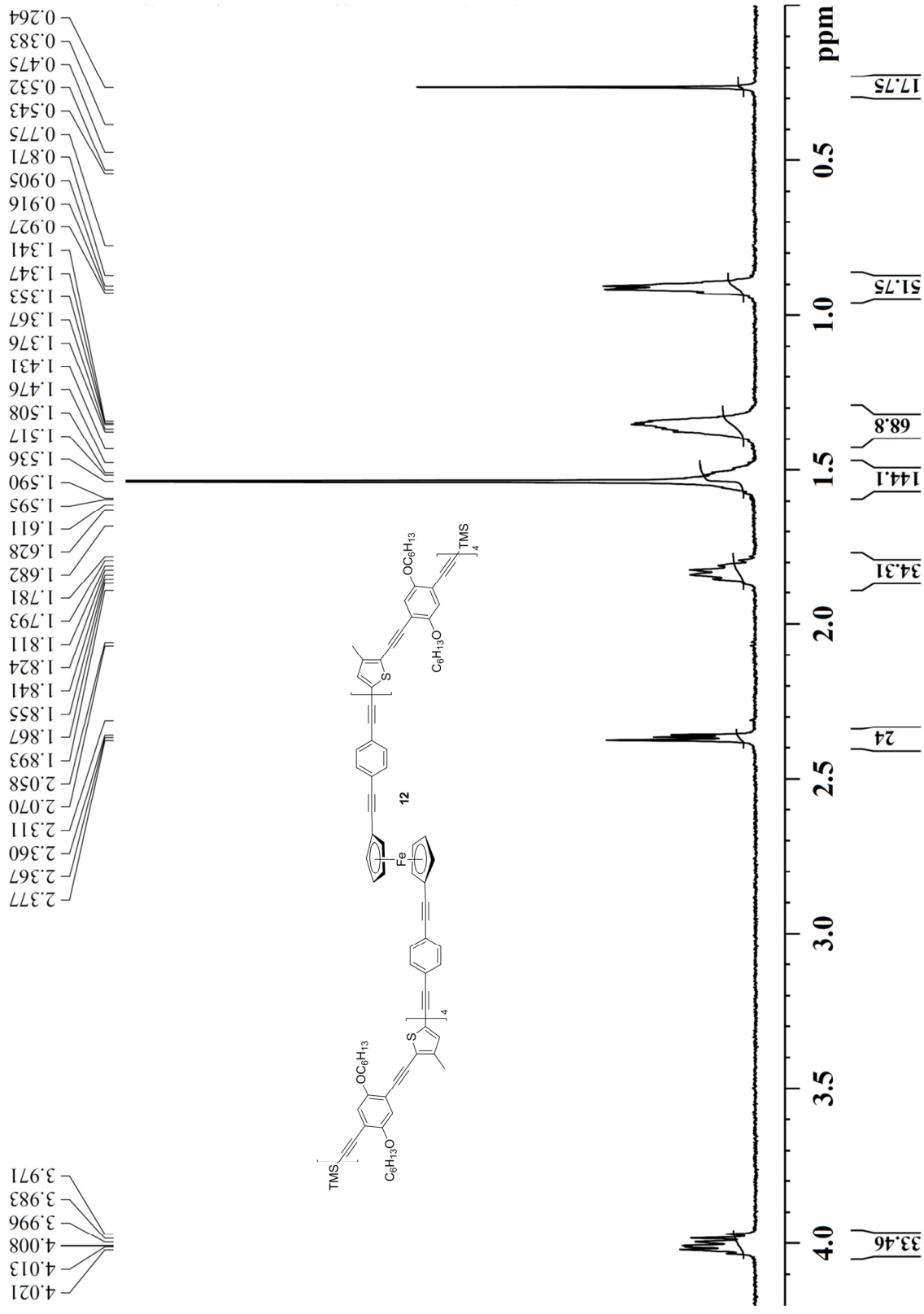
ppm
4.0
3.5
3.0
2.5
2.0
1.5
1.0
0.5
33.46
24
34.31
144.1
68.8
51.75
17.75
12
TMS
OC6H13
C6H13O
S
Fe
4
0.264
0.383
0.475
0.532
0.543
0.775
0.871
0.905
0.916
0.927
1.341
1.347
1.353
1.367
1.376
1.431
1.476
1.508
1.517
1.536
1.590
1.595
1.611
1.628
1.682
1.781
1.793
1.811
1.824
1.841
1.855
1.867
1.893
2.058
2.070
2.311
2.360
2.367
2.377
3.971
3.983
3.996
4.008
4.013
4.021

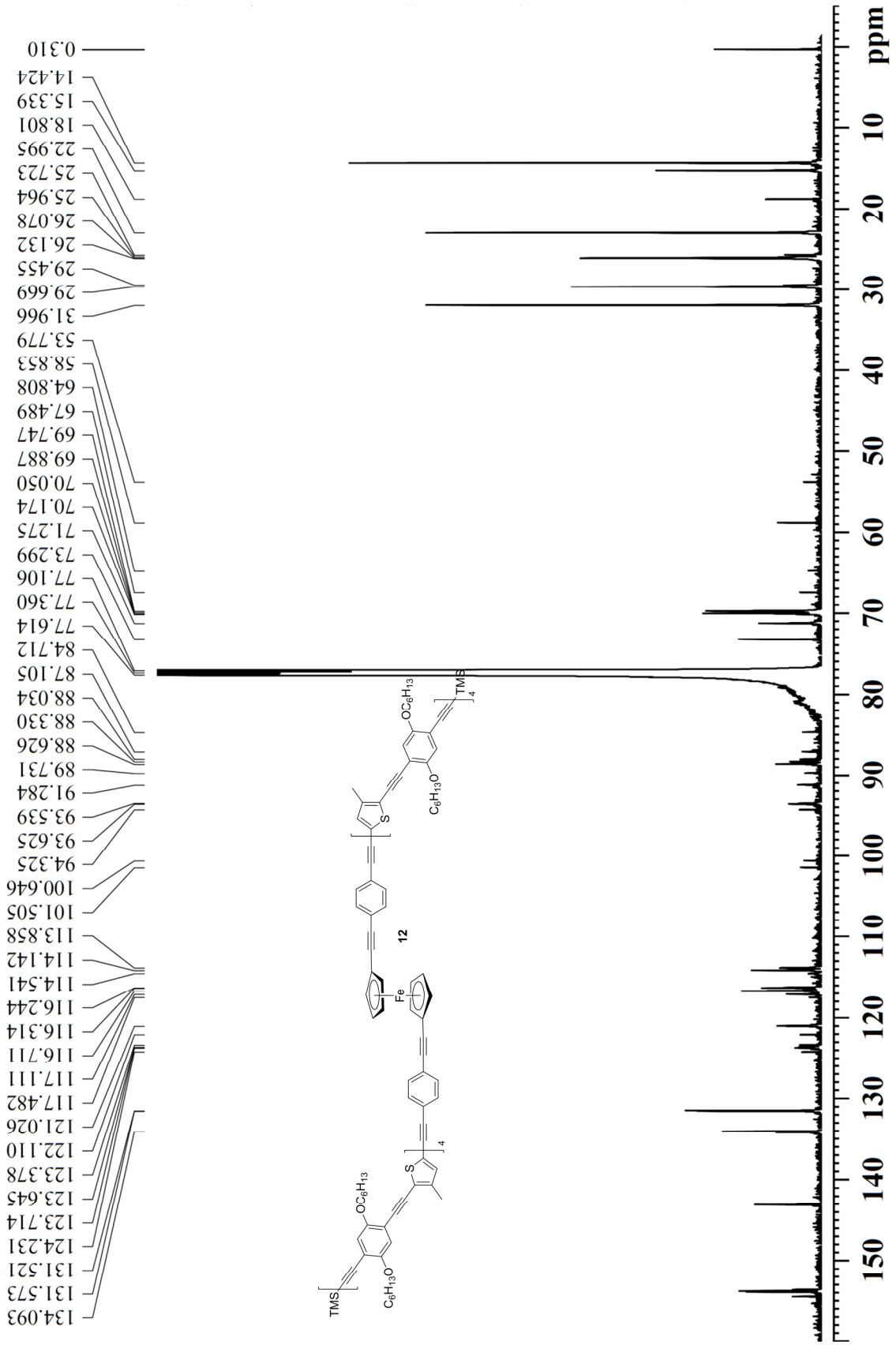
0.310
14.424
15.339
18.801
22.995
25.723
25.964
26.078
26.132
29.455
29.669
31.966
53.779
58.853
64.808
67.489
69.747
69.887
70.050
70.174
71.275
73.299
77.106
77.360
77.614
84.712
87.105
88.034
88.330
88.626
89.731
91.284
93.539
93.625
94.325
100.646
101.505
113.858
114.142
114.541
116.244
116.314
116.711
117.111
117.482
121.026
122.110
123.378
123.645
123.714
124.231
131.521
131.573
134.093
ppm
10
20
30
40
50
60
70
80
90
100
110
120
130
140
150
12
TMS
$C_6H_{13}O$
OC_6H_{13}
S
Fe
4

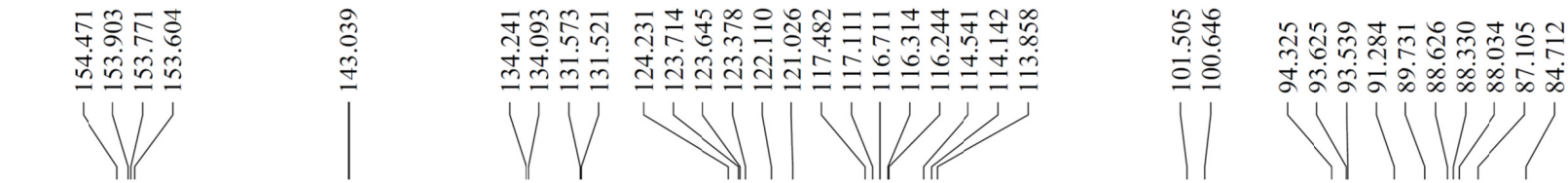
154.471
153.903
153.771
153.604
143.039
134.241
134.093
131.573
131.521
124.231
123.714
123.645
123.378
122.110
121.026
117.482
117.111
116.711
116.314
116.244
114.541
114.142
113.858
101.505
100.646
94.325
93.625
93.539
91.284
89.731
88.626
88.330
88.034
87.105
84.712

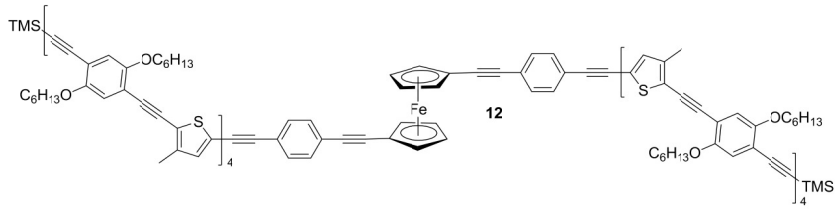
TMS
OC6H13
C6H13O
S
4
Fe
12
S
OC6H13
C6H13O
TMS
4

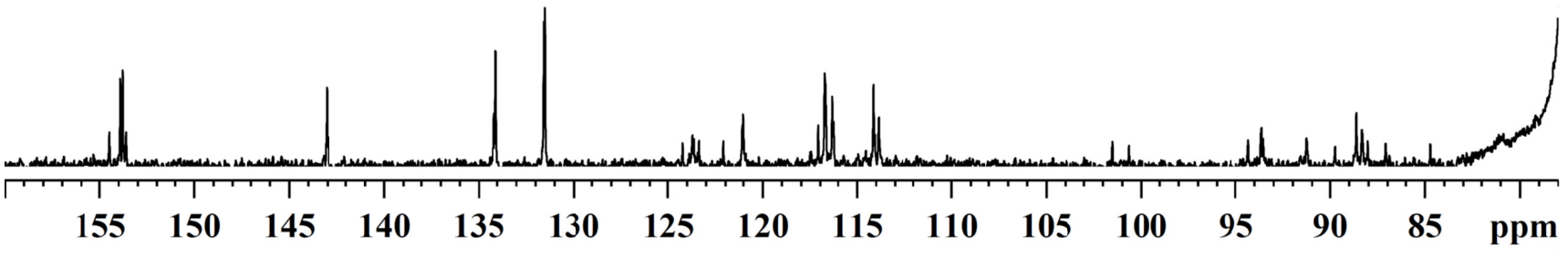
155
150
145
140
135
130
125
120
115
110
105
100
95
90
85
ppm

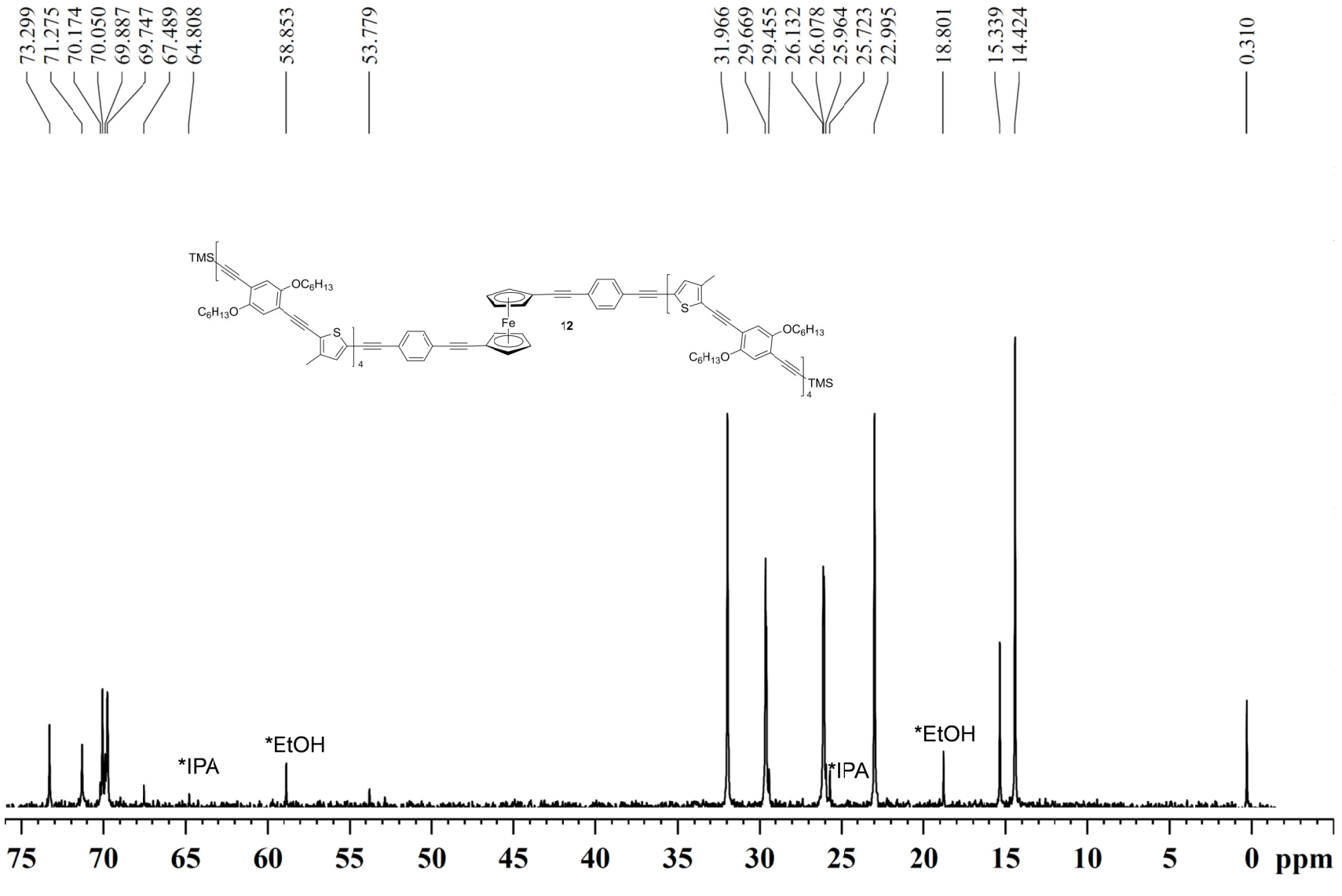
73.299
71.275
70.174
70.050
69.887
69.747
67.489
64.808
58.853
53.779
31.966
29.669
29.455
26.132
26.078
25.964
25.723
22.995
18.801
15.339
14.424
0.310
TMS
OC6H13
C6H13O
S
4
Fe
12
*IPA
*EtOH
*IPA
*EtOH
75
70
65
60
55
50
45
40
35
30
25
20
15
10
5
0
ppm

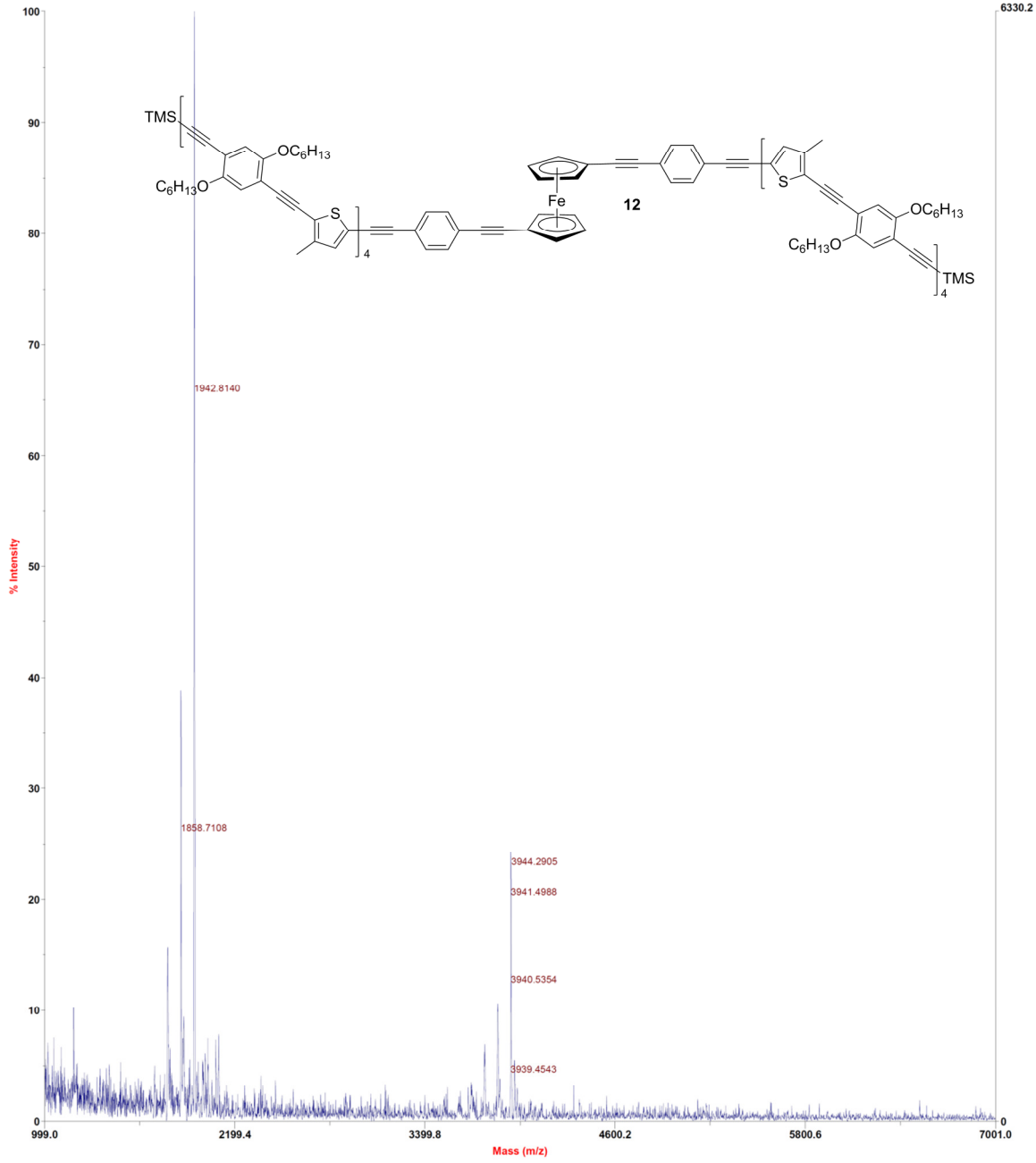
TMS
OC6H13
C6H13O
S
4
Fe
12
S
OC6H13
C6H13O
TMS
4
6330.2
1942.8140
1858.7108
3944.2905
3941.4988
3940.5354
3939.4543
% Intensity
Mass (m/z)
999.0
2199.4
3399.8
4600.2
5800.6
7001.0

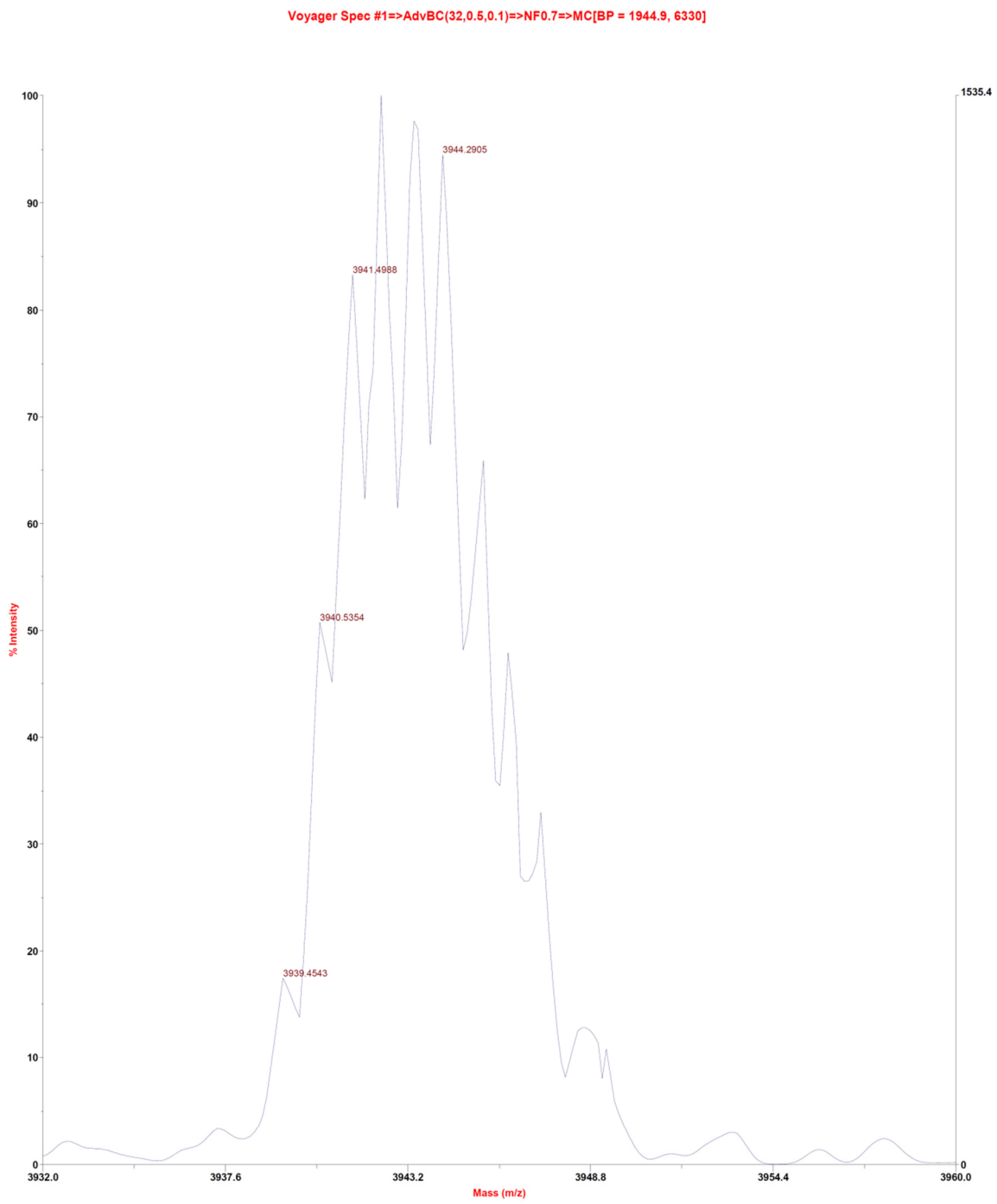
Voyager Spec #1=>AdvBC(32,0.5,0.1)=>NF0.7=>MC[BP = 1944.9, 6330]
1535.4
100
90
80
70
60
50
40
30
20
10
0
% Intensity
3944.2905
3941.4988
3940.5354
3939.4543
3932.0
3937.6
3943.2
3948.8
3954.4
3960.0
Mass (m/z)

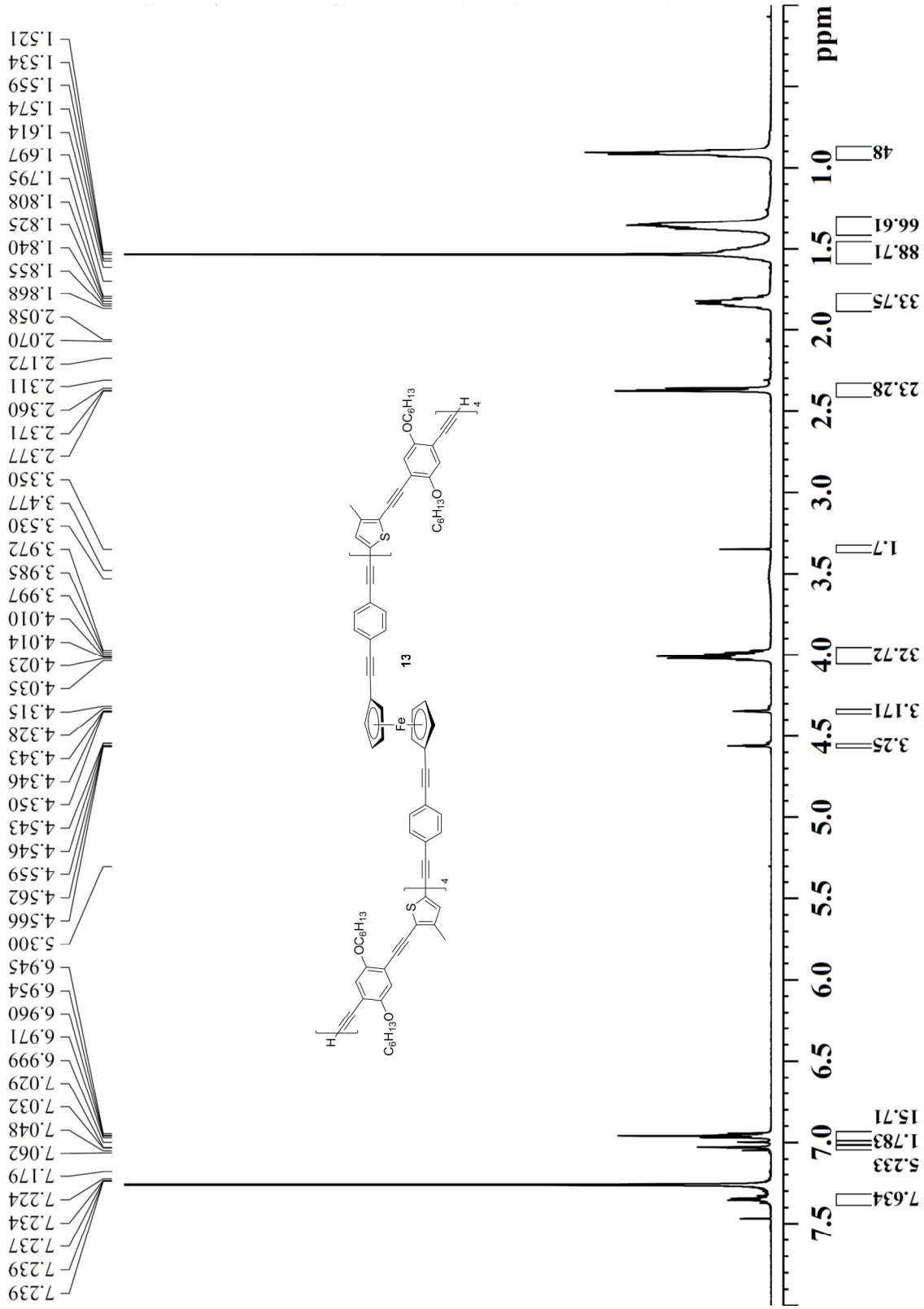
ppm
7.5
7.0
6.5
6.0
5.5
5.0
4.5
4.0
3.5
3.0
2.5
2.0
1.5
1.0
7.634
5.233
1.783
15.71
3.25
3.171
32.72
1.7
23.28
33.75
88.71
66.61
48
13
Fe
S
OC6H13
C6H13O
H
4

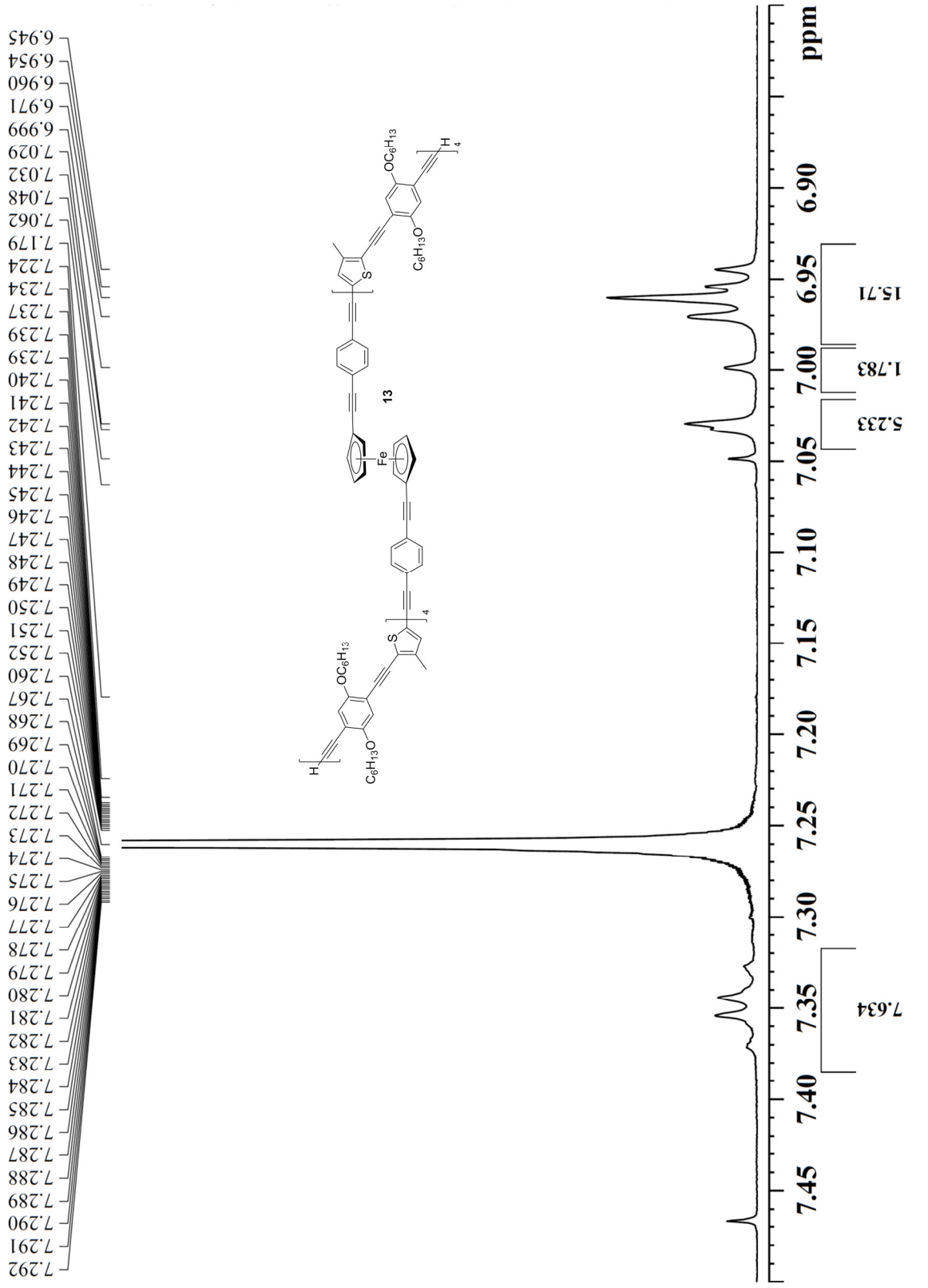
ppm
7.45
7.40
7.35
7.30
7.25
7.20
7.15
7.10
7.05
7.00
6.95
6.90
7.634
5.233
1.783
15.71
13
Fe
S
H
4
OC6H13
C6H13O
6.945
6.954
6.960
6.971
6.999
7.029
7.032
7.048
7.062
7.179
7.224
7.234
7.237
7.239
7.239
7.240
7.241
7.242
7.243
7.244
7.245
7.246
7.247
7.248
7.249
7.250
7.251
7.252
7.260
7.267
7.268
7.269
7.270
7.271
7.272
7.273
7.274
7.275
7.276
7.277
7.278
7.279
7.280
7.281
7.282
7.283
7.284
7.285
7.286
7.287
7.288
7.289
7.290
7.291
7.292

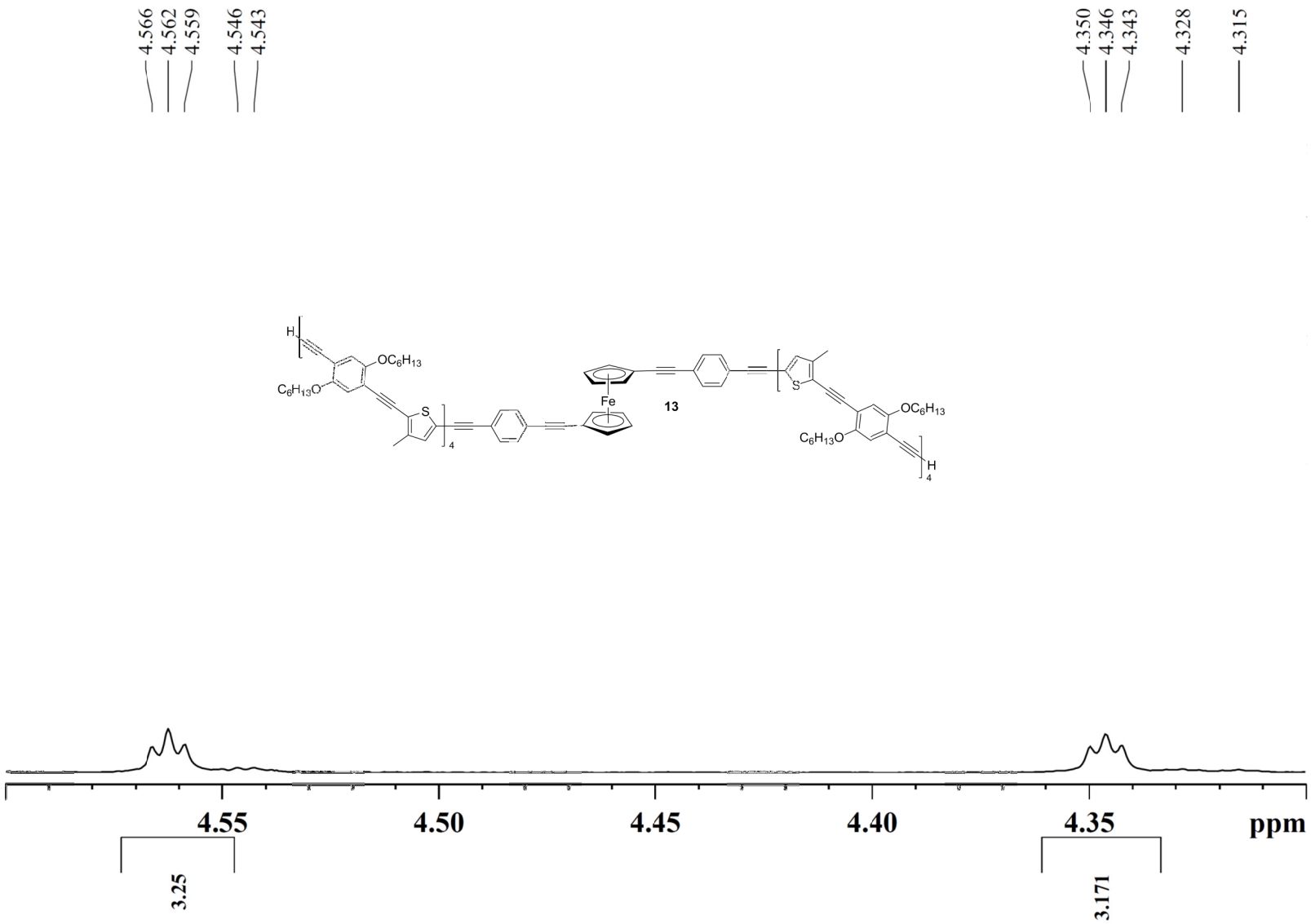
4.566
4.562
4.559
4.546
4.543
4.350
4.346
4.343
4.328
4.315
H
OC6H13
C6H13O
S
4
Fe
13
S
OC6H13
C6H13O
H
4
4.55
4.50
4.45
4.40
4.35
ppm
3.25
3.171

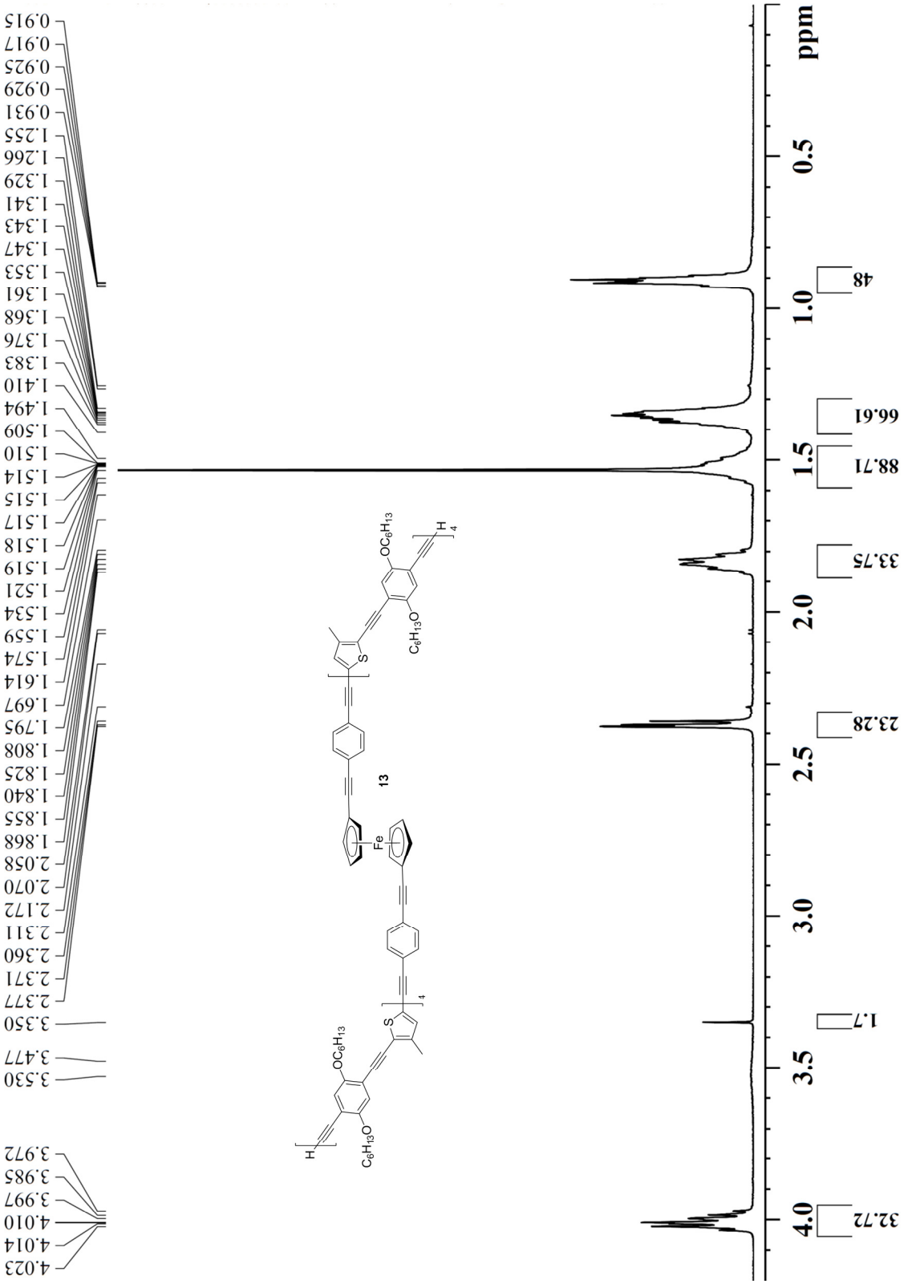
ppm
0.5
1.0
1.5
2.0
2.5
3.0
3.5
4.0
48
66.61
88.71
33.75
23.28
1.7
32.72
13
Fe
S
OC_6H_{13}
$C_6H_{13}O$
H
4
0.915
0.917
0.925
0.929
0.931
1.255
1.266
1.329
1.341
1.343
1.347
1.353
1.361
1.368
1.376
1.383
1.410
1.494
1.509
1.510
1.514
1.515
1.517
1.518
1.519
1.521
1.534
1.559
1.574
1.614
1.697
1.795
1.808
1.825
1.840
1.855
1.868
2.058
2.070
2.172
2.311
2.360
2.371
2.377
3.350
3.477
3.530
3.972
3.985
3.997
4.010
4.014
4.023

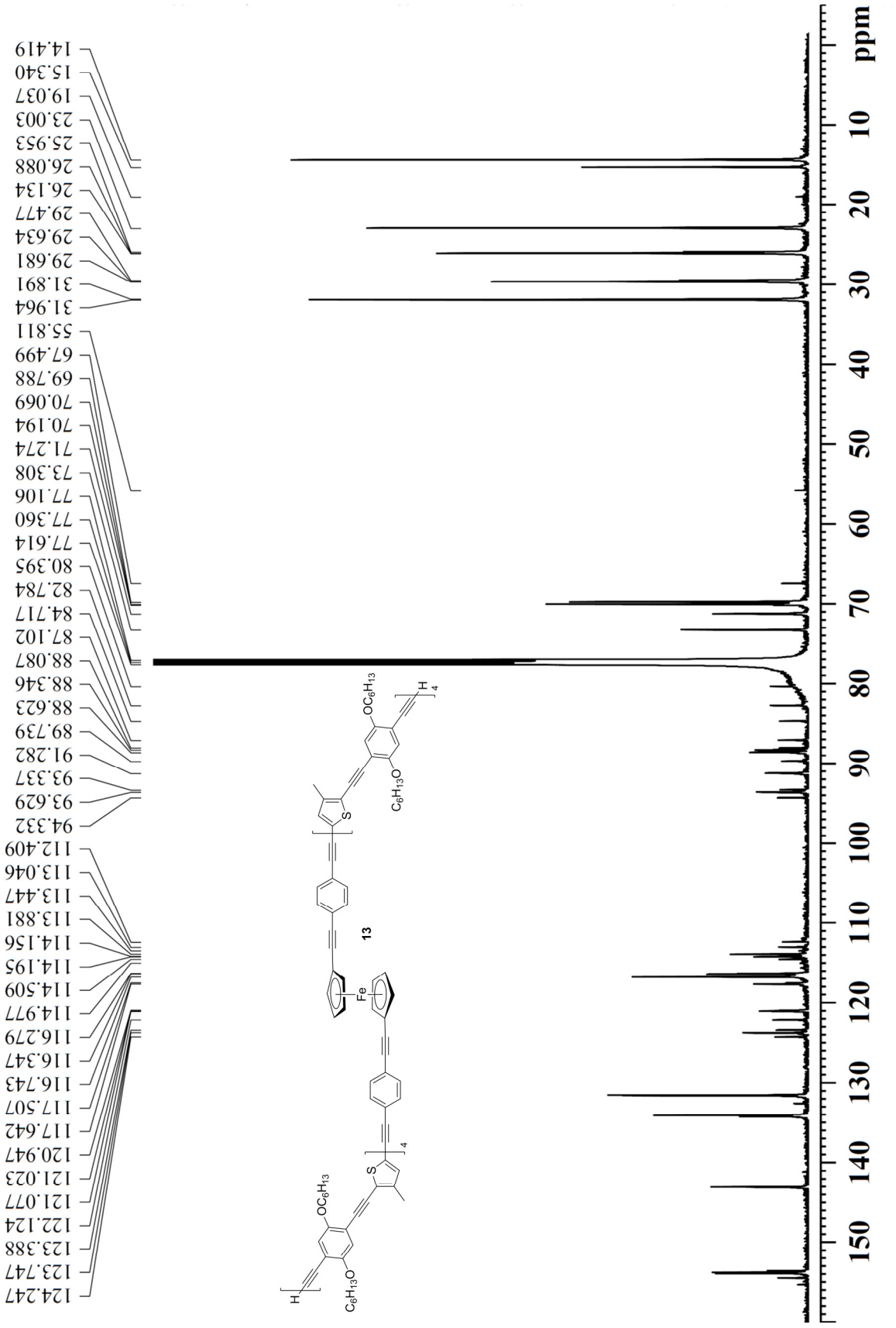
14.419
15.340
19.037
23.003
25.953
26.088
26.134
29.477
29.634
29.681
31.891
31.964
55.811
67.499
69.788
70.069
70.194
71.274
73.308
77.106
77.360
77.614
80.395
82.784
84.717
87.102
88.087
88.346
88.623
89.739
91.282
93.337
93.629
94.332
112.409
113.046
113.447
113.881
114.156
114.195
114.509
114.977
116.279
116.347
116.743
117.507
117.642
120.947
121.023
121.077
122.124
123.388
123.747
124.247
ppm
150
140
130
120
110
100
90
80
70
60
50
40
30
20
10
13
Fe
S
S
OC6H13
C6H13O
OC6H13
C6H13O
H
4
4

155.316
154.478
153.924
153.788
153.602

143.040

134.245
134.090
132.588
131.580
131.527
124.247
123.747
123.388
122.124
121.077
121.023
120.947
117.642
117.507
116.743
116.347
116.279
114.977
114.509
114.195
114.156
113.881
113.447
113.046
112.409

94.332
93.629
93.337
91.282
89.739
88.623
88.346
88.087
87.102
84.717
82.784
80.395

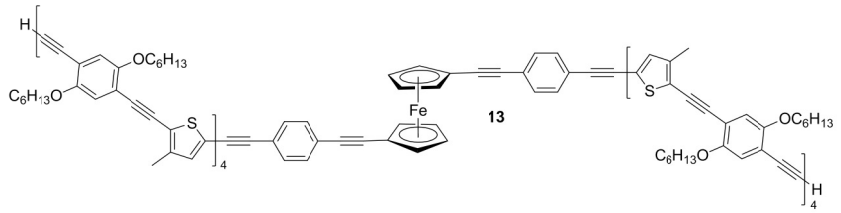

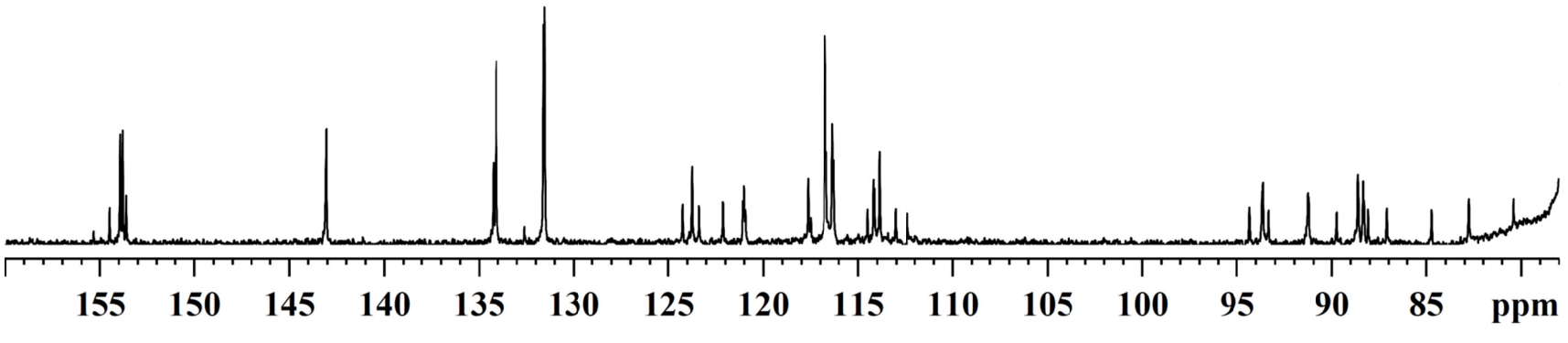

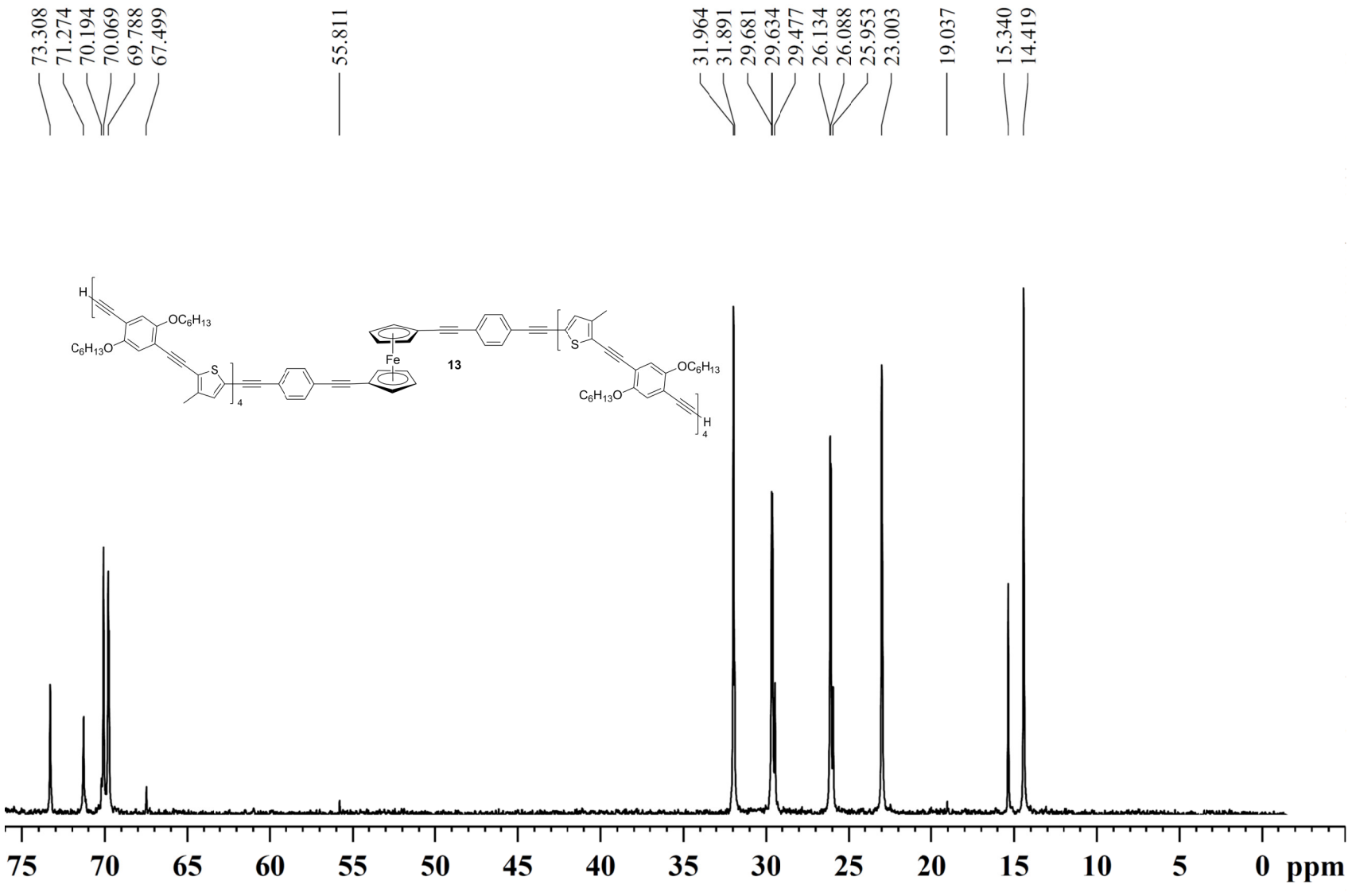
73.308
71.274
70.194
70.069
69.788
67.499
55.811
31.964
31.891
29.681
29.634
29.477
26.134
26.088
25.953
23.003
19.037
15.340
14.419
H
OC6H13
C6H13O
S
4
Fe
13
S
OC6H13
C6H13O
H
4
75
70
65
60
55
50
45
40
35
30
25
20
15
10
5
0
ppm

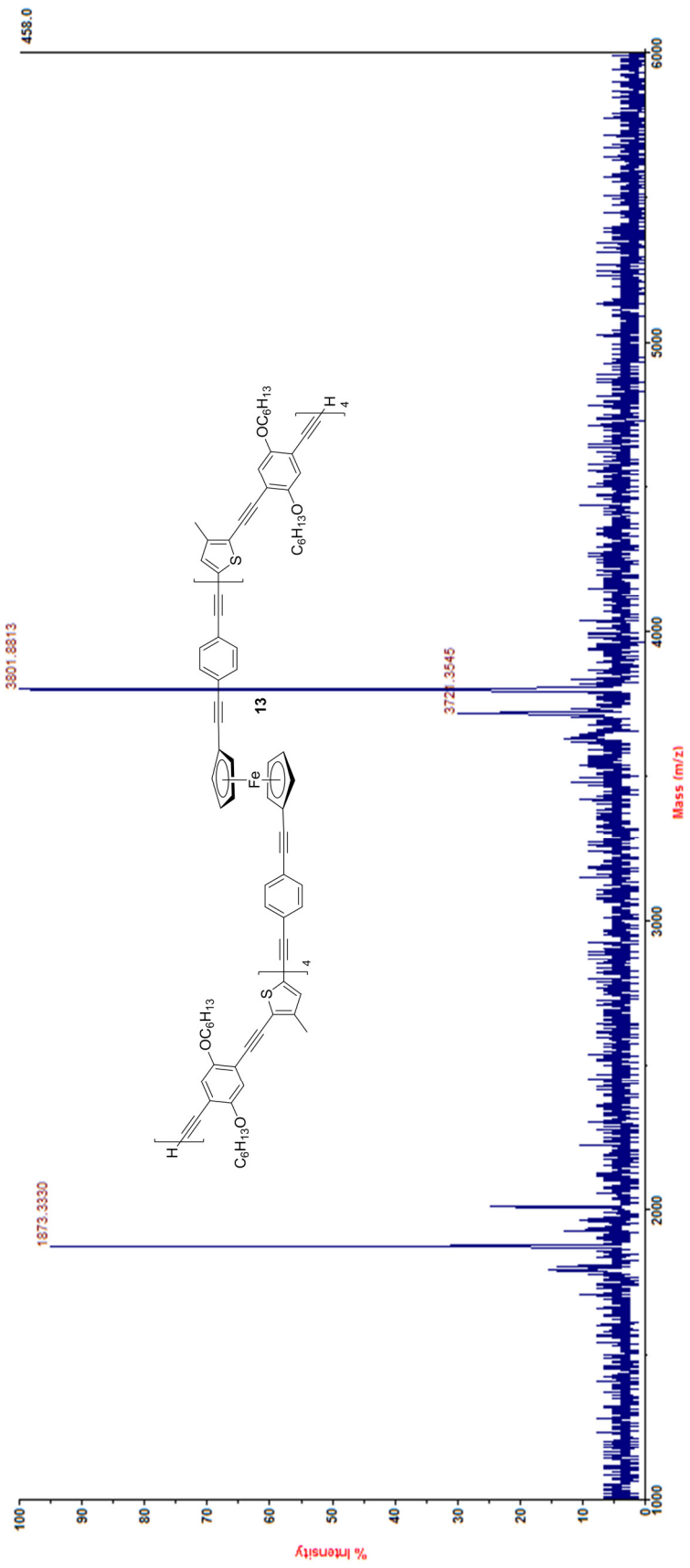
458.0
3801.8813
3721.3545
1873.3330
13
Fe
S
OC_6H_{13}
$C_6H_{13}O$
H
4
% Intensity
Mass (m/z)
100
90
80
70
60
50
40
30
20
10
0
1000
2000
3000
4000
5000
6000

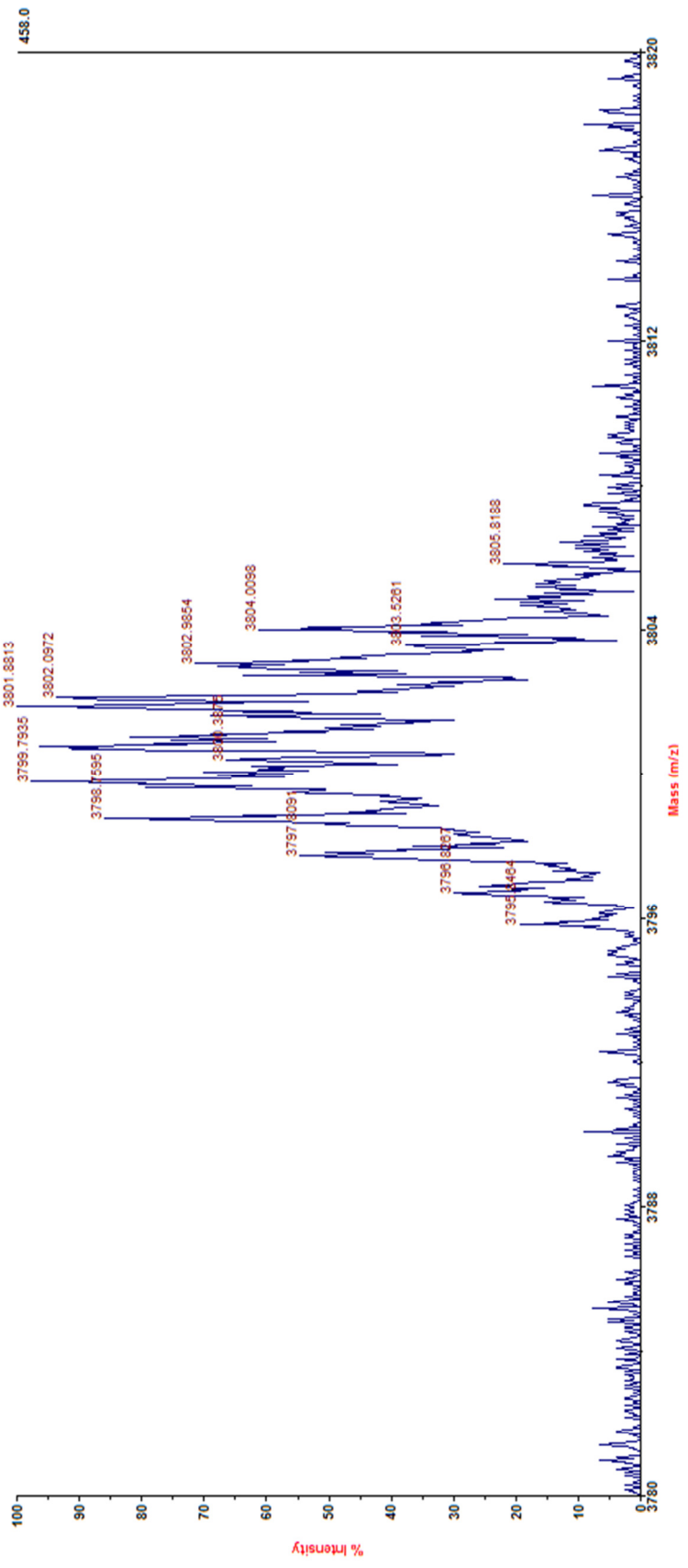
458.0
3820
3812
3804
3796
3788
3780
Mass (m/z)
% Intensity
100
90
80
70
60
50
40
30
20
10
0
3801.8813
3802.0972
3802.9854
3804.0098
3803.5261
3805.8188
3799.7935
3798.7595
3797.8091
3796.8637
3795.9484

Ryan R. Kohlmeyer

Education

May 2013 University of Wisconsin-Milwaukee, Ph.D. in Chemistry
Advisor: Prof. Jian Chen
Thesis: Functional Organic Nanomaterials

May 2007 University of Wisconsin-Whitewater, B.S. in Chemistry and minor in Mathematics, *Summa Cum Laude*

Academic Awards and Honors

Spring 2011 UWM Sosnovsky Award of Excellence in Graduate Research
Spring 2011 UWM Dissertation Fellowship Award
Fall 2008 UWM Research Fellowship Award
Fall 2008 UWM Chancellor's Award
Fall 2006 UWW Paul E. Wenaas Scholarship
Fall 2004 UWW John W. Brooks Scholarship

Research Interests

Functional materials for clean energy (e.g. batteries and photovoltaic devices) and smart material systems (shape-changing and shape-memory materials).

Research Experience

- Non-covalent functionalization/solubilization of carbon nanotubes/graphene.
- Carbon nanotube/graphene aerogels.
- Single-chirality separation of single-walled carbon nanotubes (e.g. (6,5) and (10,5) tubes).
- Synthesis of π-conjugated polymers and monodisperse oligomers.
- Shape-memory polymer composites and shape-changing polymer composites.
- High dielectric constant polymer composites.
- Graphene ceramic composite coatings.
- Fabrication and performance characterization of organic photovoltaic devices.
- Thin film fabrication techniques: spin coating, thermal vacuum deposition, solution casting, and interface dip coating.
- Analytical techniques: surface area and porosity analysis using BET and BJH methods, cyclic voltammetry, DSC, two- and four-point conductivity measurement, and mechanical testing.
- Imaging techniques: SEM/EDS, AFM, TEM, and polarized optical microscopy.
- Spectroscopy techniques: Raman, UV-Vis-NIR, fluorescence, FTIR, NMR, and mass spectrometry.
- Computational chemistry: Gaussian09 and Accelrys Materials Studio 5.5.

Teaching Experience

- Occasional substitute lecturer for Organic Chemistry II course, UWM.
- Mentor to three undergraduate researchers for one semester each since 2008, UWM.
- Teaching Assistant, fall 2007-spring 2008, UWM.
- Research Assistant, summer 2008-present, UWM.

Publications

(1) "Preparation of Stable Carbon Nanotube Aerogels with High Electrical Conductivity and Porosity." Kohlmeyer, R. R.; Lor, M.; Deng, J.; Liu, H.; Chen, J. ***Carbon*** 2011, 49, 2352-2361.

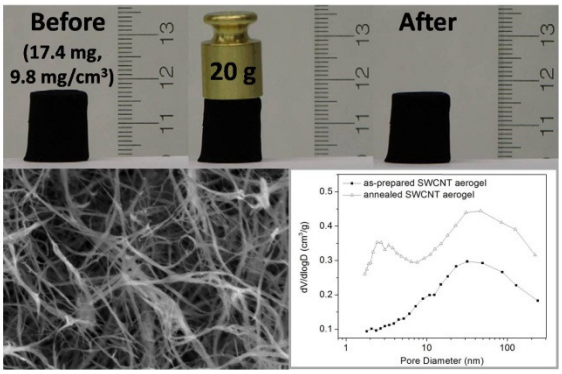

Stable carbon nanotube (CNT) aerogels were produced by forming a three-dimensional assembly of CNTs in solution to create a stable gel using a chemical cross-linker, followed by a CO_2 supercritical drying. Thermally annealed CNT aerogels are mechanically stable and stiff, highly porous (~99%), and exhibit excellent electrical conductivity (~1-2 S/cm) and large specific surface area (~590-680 m^2/g). Such CNT aerogels may find applications in fuel cells, super capacitors, 3D batteries, and advanced catalyst supports.

(2) "Remote, Local, and Chemical Programming of Healable Multishape Memory Polymer Nanocomposites." Kohlmeyer, R. R.; Lor, M.; Chen, J. ***Nano Lett.*** 2012, 12, 2757-2762.

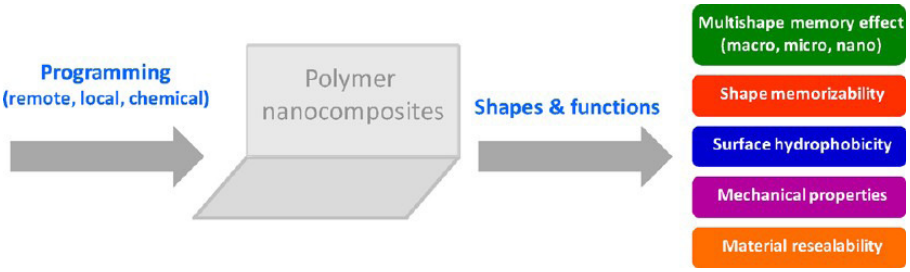

We show that the combination of remote, local, and chemical programming of the multishape memory effects offers unparalleled shape and function control in carbon nanotube–Nafion composites.

(3) "Wavelength-Selective, IR Light-Driven Hinges Based on Liquid Crystalline Elastomer Composites." Moua, M.[*]; Kohlmeyer, R. R.[*]; Chen, J. ***Angew. Chem. Int. Ed.*** 2013, In press.
-This work was highlighted by Chemical & Engineering News [***C&EN*** 2013, 91(11), 39].

[*] Authors contributed equally to this work.

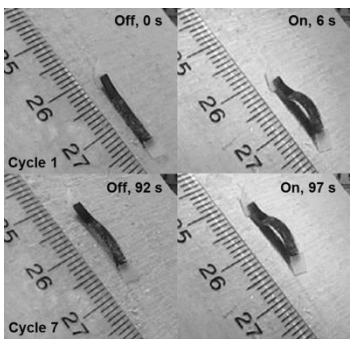

Wavelength-selective, IR light-driven bilayer hinges based on liquid crystalline elastomer (LCE) composites show fast, reversible bending with a large strain. Such composite bilayer hinges enable various remote-controlled soft robotic devices including active origami structures that can reversibly fold and unfold, Venus flytrap-inspired grippers that can pick up delicate objects even from the bottom of water, and inchworm walkers that can crawl up a hill at a 50° incline.

(4) "Electrical and Dielectric Properties of Hydroxylated Carbon Nanotube-Elastomer Composites." Kohlmeyer, R. R.; Javadi, A.; Pradhan, B.; Pilla, S.; Setyowati, K.; Chen, J.; Gong, S. ***J. Phys. Chem. C*** 2009, 113, 17626-17629.

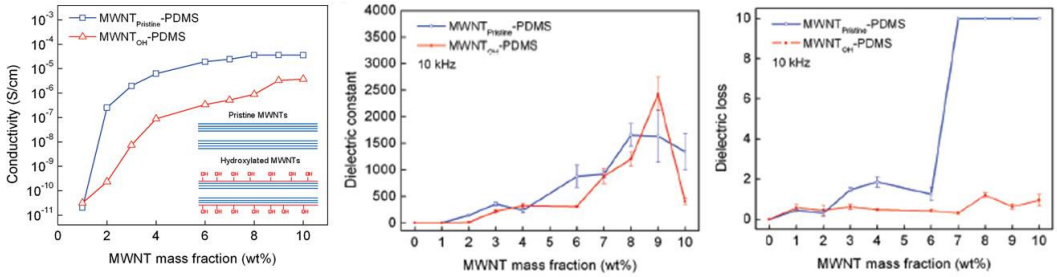

We demonstrate for the first time the feasibility of using core-shell MWNTs as a filler to increase the dielectric constant and reduce the dielectric loss of nanotube-polymer composites. High dielectric constant composites may find applications in super capacitors for energy storage.

(5) "Fabrication of In-Plane Aligned Carbon Nanotube-Polymer Composite Thin Films." Pradhan, B.; Kohlmeyer, R. R.; Chen, J. ***Carbon*** 2010, 48, 217-222.

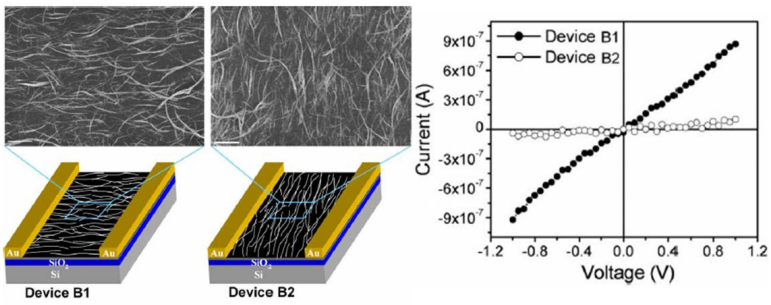

In-plane aligned carbon nanotube (CNT)-polymer composite thin films with submicrometer thickness on unmodified SiO_2 surfaces are fabricated using the spin coating alignment technique, which is simple, integratable to the manufacture process of organic devices, and applicable to various matrix polymers (e.g. polycarbonate and polythiophene). Controlled manipulation of the nanotube alignment in a polymer matrix is an effective method to tune the electrical conductivity of a 5 wt.% single-walled carbon nanotube-polycarbonate composite film spanning nearly four orders of magnitude. The ability to manipulate CNT orientation and conductivity is critical for engineering of various organic devices such as photovoltaics, light-emitting diodes, and thermoelectrics.

(6) "Advanced Carbon Nanotube/Polymer Composite Infrared Sensors." Pradhan, B.; Kohlmeyer, R. R.; Setyowati, K.; Owen, H. A.; Chen, J. ***Carbon*** 2009, 47, 1686-1692.

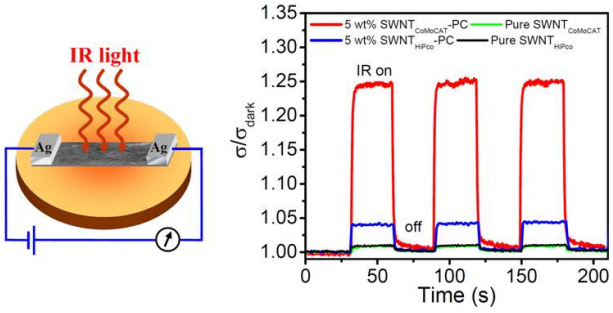

We show that both single-walled carbon nanotube (SWCNT) types and nanotube matrix polymer-nanotube junctions have profound impact on electro-optical properties of SWCNT/polymer composites. Higher semiconducting nanotube concentration in a SWCNT material is critical to enhance the photo effect of IR light on SWCNT/polymer nanocomposites, whereas CNT-P-CNT junctions play a dominant role in the thermal effect of IR light on supported SWCNT/polymer composite films.

(7) "Electron Doping of Small-Diameter Carbon Nanotubes with Exohedral Fullerenes." Pradhan, B.; Kohlmeyer, R. R.; Setyowati, K.; Chen, J. ***Appl. Phys. Lett.*** 2008, 93, 223102.

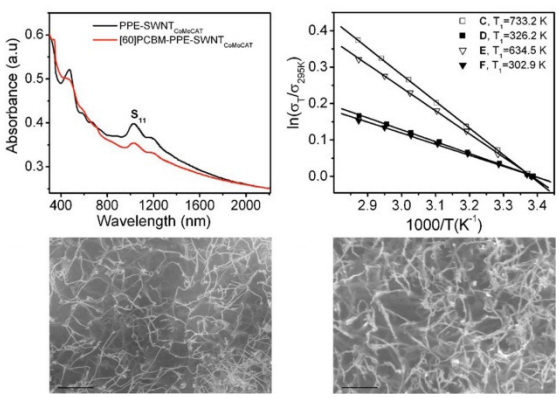

We report the charge transfer between small-diameter semiconducting single-walled CNTs (SWNTs) and fullerenes such as 1-(3-methoxycarbonyl)propyl-1-phenyl[6,6]C_{61} ([60]PCBM). The resulting [60]PCBM-doped SWNTs demonstrate significantly enhanced electrical conductivity while still retaining characteristics of semiconducting nanotubes. Polymer nanocomposites based on air-stable, *n*-doped SWNTs show a (15-22)-fold enhancement in electrical conductivity compared with nanocomposites based on undoped SWNTs at the same nanotube loading level. The fundamental understanding of the interaction between SWNTs and fullerenes is critical to the development of CNT-fullerene-based photovoltaic devices.

(8) "Efficient Transport of Gold Atoms with a Scanning Tunneling Microscopy Tip and a Linker Molecule." Boscoboinik, J. A.; Kohlmeyer, R. R.; Chen, J; Tysoe, W. T. ***Langmuir*** 2011, 27, 9337-9344.

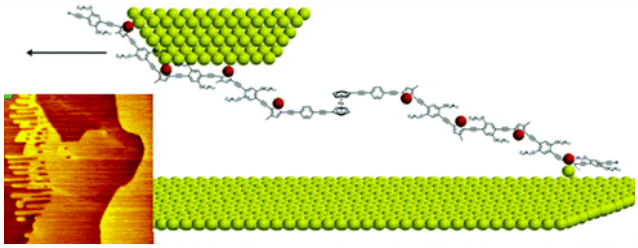

A π-conjugated thiophene-containing hinge molecule is shown to be highly efficient in the transport of gold atoms using a gold scanning tunneling microscopy (STM) tip. The binding between the thiophene-containing molecule and gold atoms is strong enough for the tip to pick up and transport gold atoms, but weak enough to drop them when the tip changes direction or encounters a step-up.

Presentations

(1) "Preparation and Characterization of Nanocarbon Aerogels." Kohlmeyer, R. R.; Moua, M.; Chen, J. Poster Presentation. 2012 MRS Fall Meeting. Boston, MA, November 25-30, **2012**.

(2) "Nanoengineering Stable Carbon Nanotube Aerogels." Kohlmeyer, R. R.; Lor, M.; Chen, J. Poster Presentation. 4th Annual Argonne Postdoctoral Research Symposium (also open to graduate students). Argonne National Laboratory, October 27, **2011**.